

# **On the Characterisation of Structural Damping in Wind Turbine Blade Composite Materials**

*An Approach Using Dynamic Mechanical Analysis  
and Experimental Modal Analysis*

**Euan Brough<sup>1,2</sup>**

**Supervisors: David H. Nash<sup>1</sup>, Abbas Mehrad Kazemi-Amiri<sup>2</sup>**

<sup>1</sup> Department of Mechanical and Aerospace Engineering,  
University of Strathclyde, Glasgow, G1 1XQ, U.K.

<sup>2</sup> Department of Electronic and Electrical Engineering,  
University of Strathclyde, Glasgow, G1 1XQ, U.K.

March 2025

To my family.

# Abstract

In wind turbine blade design, carbon fibre composites are increasingly employed in larger, more modern blades for their superior strength and stiffness; however, their inherent anisotropic nature under dynamic loads leads to complex and poorly understood damping mechanisms. Despite the advantages of these materials, current experimental approaches have failed to capture the directional variations in damping behaviour. This has led to an identifiable knowledge gap, which has resulted in non-optimised damping performance for wind turbine blades. This thesis addresses these shortfalls by developing two complementary experimental methodologies, which enable a more detailed damping characterisation. The first was an integrated approach that used a new FEA-assisted DMA framework, combining Dynamic Mechanical Analysis (DMA) with Finite Element Analysis (FEA) in order to quantify strain energy distributions. The second employed Experimental Modal Analysis (EMA) and a developed experimental test rig to characterise the damping properties of carbon fibre composite samples.

This research initially employed a FEA-assisted DMA methodology, integrating FEA with DMA by incorporating experimental DMA data and FEA strain results of the composite specimens into a new model. Traditional DMA methods historically have only provided an overall damping measure and did not quantify the anisotropic contributions inherent in carbon fibre composites,

necessitating the hybrid FEA approach. This integration enabled strain energy results to be extracted using an ANSYS model that replicated the experimental setup, thereby allowing the decomposition of bulk damping properties into directional components. The directional damping quantities obtained from the model then enabled the complex material behaviour to be predicted using existing models. Extensive DMA testing of unidirectional (fibre-aligned) and transverse samples, of 60 mm length (50 mm span) across varying thicknesses, validated the expected damping mechanisms associated with material anisotropy. The findings demonstrated that damping behaviours in the fibre-aligned direction differed significantly from those in the transverse direction, with shear contributions playing a vital role in energy dissipation. Additionally, the damping component measured in the fibre direction was observed to be approximately 10% lower than that of the thinnest samples (2 mm), with similar trends evident in the transverse results, further corroborating the influence of shear effects. Although this thesis primarily focused on damping in the fibre direction, which was the principal loading direction for the carbon fibre in the spar caps of turbine blades, the analysis also highlighted the importance of considering damping in other orientations, which enabled a more complete understanding of the composite's dynamic response.

In parallel, EMA was undertaken as a complementary technique to DMA, as the two methods captured different aspects of damping: DMA provided a stress–strain based measure of damping properties, in the form of  $\tan(\delta)$ , whereas EMA delivered a vibrational-based, bulk damping ratio  $\zeta$ . In contrast to DMA, which provides damping at the material level using shorter specimens, where contributions from non-fibre directions are much more pronounced, EMA testing involved geometries with a much larger aspect ratio. This structural-level configuration made off-axis damping contributions negligible, thereby simplifying the isolation of fibre-directional behaviour. DMA

offered detailed insights into local damping properties and strain energy distribution, whereas EMA provided a complementary structural perspective by capturing the modal responses of the specimens. EMA testing was performed on larger samples (up to 2 m in length) using a custom-designed rig that incorporated a vacuum chamber with automated sample excitation and nodal suspension with limited environmental control. The setup included an automated pneumatic impact hammer, accelerometers, strain gauges and a calibrated National Instruments data acquisition system, which provided both strain and acceleration data. This was then processed to yield mode shapes, modal frequencies, and damping ratio values. The rig was specifically designed to minimise external energy losses, seen in conventional EMA applications, that could be inadvertently recorded as damping in traditional EMA methodologies.

Following the experimental investigations, the DMA and EMA results were compared using an analytical model designed to convert one form of damping measurement into the other. However, the implementation of this model revealed that the correlation between the two sets of results was weaker than had been anticipated. This discrepancy was mainly attributed to differences in environmental conditions and the fact that DMA testing was not performed at the specimens' first natural frequency due to the limitations of the equipment used. Consequently, while confidence was maintained in the reliability of both methodologies, it was concluded that a direct conversion between these two distinct damping quantities was not feasible using standard analytical conversion methodologies.

By integrating computational modelling with experimental testing, this research characterised the directional damping mechanisms in carbon fibre composites used in wind turbine blades. The novel FEA-assisted DMA

approach quantified strain energy distributions and directional damping responses, clearly demonstrating anisotropy and the critical role of shear effects. EMA complemented these findings by providing structural-level damping measurements. Together, these methodologies provide actionable pathways by enabling targeted design and material selection specifically to enhance damping performance. Improved damping reduces vibrational amplitudes, leading to lower structural fatigue and thus extending blade lifespan. Additionally, the detailed directional damping characterisation informs more accurate numerical models, increasing the reliability of simulations used in blade design processes. Ultimately, this supports the development of optimised blades that are not only lighter, thereby reducing material usage and costs, but also more resilient, leading to improved structural performance, increased energy output efficiency, reduced maintenance frequency, and greater overall sustainability in wind turbine technology.

# Declaration

This thesis is the result of the author's original research. It has been composed by the author and has not been previously submitted for examination, which has led to the award of a degree.

The copyright of this thesis belongs to the author under the terms of the United Kingdom Copyright Acts as qualified by the University of Strathclyde Regulation 3.50. Due acknowledgement must always be made of the use of any material contained within or derived from this thesis.

Signed: Euan Brough

Date: 10/12/2024

# List of Figures

1.1	Coordinates of wind turbine blade . . . . .	3
2.1	Cross-sectional view of a wind turbine blade . . . . .	15
2.2	Cross-section of a wind turbine blade (ANSYS APDL Model). The purple section represents the spar caps where the Carbon UD material is used . . . . .	21
2.3	Diagram of a pultrusion manufacturing process . . . . .	23
2.4	Hysteresis Loop . . . . .	32
2.5	KV Model Schematic - showing spring and dashpot . . . . .	34
2.6	TA DMA Q800 . . . . .	41
2.7	Half Power Bandwidth Approach . . . . .	45
3.1	Cutaway illustration and schematic of DMA system . . . . .	64
3.2	Graphical representation of the complex modulus, illustrating how the storage modulus ( $E'$ ), loss modulus ( $E''$ ), and the resultant complex modulus ( $E^*$ ) relate through the phase angle $\delta$ . 64	64
3.3	TA DMA Q800 - In Strathclyde University Lab . . . . .	70
3.4	Stress and Strain with Phase Lag. The phase lag ( $\delta$ ) is the phase difference between the peak stress ( $\sigma$ ) and the peak strain ( $\epsilon$ ) - measured in degrees. . . . .	73
3.5	DMA Q800 - Three Point Configuration with calibration sample .	80

## List of Figures

3.6	Comparison of Normal Distribution of the Original and Filtered Data - for 4 mm Carbon UD sample at 25 Hz . . . . .	82
3.7	Single DMA Result Produced by 10 Tests . . . . .	83
3.8	DMA Result - C denotes Carbon Fibre Composite . . . . .	84
3.9	First deformation mode of the 2 mm thick sample from modal analysis (free-free condition). . . . .	90
3.10	Boundary Conditions of the FEA model (in ANSYS APDL) for a 4 mm thick sample, showing (a) the isometric view, (b) an additional boundary-condition image, (middle) side view, and (c) von Mises stress distribution. . . . .	92
3.11	Strain distribution results for a three-point bend test showing maximum and minimum strain regions in different directional components ( $\epsilon_{11}$ , $\epsilon_{13}$ , and $\epsilon_{33}$ ) – 2 mm Sample . . . . .	97
3.12	Total displacement in the sample during the three-point bend test – 2 mm Sample . . . . .	98
3.13	Effect of sample thickness on strain energy distribution overlaid with UD DMA loss factor results at 1 Hz (from Figure 3.8) - Note: Strain energy % in 23 direction is too small to plot on this figure. Tabulated data available in Appendix E . . . . .	99
3.14	Damping characteristics as a function of frequency for unidirectional carbon composites with up to 0.1 mm thickness variation . . . . .	103
3.15	Illustration of the coordinate system used. . . . .	108
3.16	Processed Contributions of Damping Results against Frequency - UD Model (UD samples were solely responsible for the creation of this figure) . . . . .	112
3.17	Transverse Layout - according to fibre direction coordinate system	116

## List of Figures

3.18 Raw Damping Results from Transverse Method - C denotes Carbon Fibre Composite, T denotes Transverse Sample . . . . .	117
3.19 Processed Contributions of Damping Results against Frequency	119
3.20 Processed Contributions of Damping Results against Frequency - Combined Model (Both UD and Transverse samples were used in the creation of this figure) . . . . .	127
3.21 Damping Characteristics for $\eta_{11}$ across all models, including the Directional Simplified Model (DSM UD), the full UD Model, and the Combined Model (Comb) - C UD represents Carbon Unidirectional . . . . .	130
3.22 Damping Characteristics for $\eta_{22}$ across all models, including the Directional Simplified Model (DSM Transverse), the full Transverse Model, and the Combined Model C T represents Carbon Transverse. . . . .	131
3.23 Comparison of Generated Results and Input DMA Data for UD Composite Material. The generated values represent model predictions, while the DMA data reflects experimental results. . .	134
3.24 Comparison of Generated Results and Input DMA Data for Transverse Composite Material. The generated values represent model predictions, while the DMA data reflects experimental results. . . . .	135
3.25 $\eta_{11}$ Damping Characteristics - Comparison of the Combined Model (Comb), Combined Model without the 2 mm sample, DSM UD Model, and DSM UD Model without the 2 mm sample. .	138
3.26 $\eta_{22}$ Damping Characteristics - Removing 2 mm Sample: Comparison of the Combined Model (Comb), DSM Transverse Model, and adjusted models after removing the thinnest sample (2.0 mm). . . . .	139

## List of Figures

3.27 $\eta_{11}$ Damping Characteristics - Comparison of the Combined Model (Comb), DSM UD Model, and Adjusted Models (4 mm sample removed). . . . .	141
3.28 $\eta_{22}$ Damping Characteristics - Comparison of the Combined Model (Comb), DSM Transverse Model, and Adjusted Models (4 mm sample removed). . . . .	142
4.1 Isometric View Of EMA Rig . . . . .	170
4.2 Ultrasonic scans of composite samples. The top image (a) shows a defect-free sample, while the bottom image (b) shows a sample with defects (circled). The sample in (b) was removed from the testing pool. . . . .	174
4.3 Modular frame design for the EMA test rig. (a) shows the frame only, while (b) shows the frame with the panel inserted. . . . .	176
4.4 Modal FEA results showing the first flexural mode under free-free boundary conditions with element size of 0.25 mm. This image highlights nodal (low displacement - dark blue) and anti-nodal (high displacement- red) regions. . . . .	177
4.5 Sample showing support locations based on mode 1 deformation - blue locations represent minimum deflection of mode shape . . . . .	178
4.6 (a) Updated suspension mechanism, (b) Zoomed view of the suspension point. . . . .	179
4.7 Frequency response function (FRF) of the unfiltered signals from the three accelerometers mounted along the test specimen. Peaks correspond to the first and second flexural modes, identified at 11.9 Hz and 64.3 Hz, respectively. . . . .	180
4.8 Comparison of excitation methods (a) and the schematic of the selected pneumatic-assisted excitation method (b). . . . .	183

## List of Figures

4.9	Full hammer setup for the EMA test rig. . . . .	186
4.10	CAD model of the vacuum chamber for the EMA test rig. . . . .	187
4.11	(a) Full vacuum chamber setup; (b) End-on view of the vacuum chamber; (c) Vacuum Pump on isolation pads . . . . .	189
4.12	NI cDAQ (NI 9189) with accelerometer module (NI 9234) . . . . .	190
4.13	Placement of accelerometers and strain gauges at anti-nodal points for optimal data capture. Dark blue represents minimum deformation and transitions to red, representing maximum deformation. . . . .	192
4.14	Impact test data showing the force applied by the hammer and the responses of Accelerometer 1, 2, and 3. . . . .	192
4.15	(a) NI 9237 strain gauge module for connecting strain gauges; (b) Wiring diagram for quarter-bridge setup with NI 9944 bridge completion module. . . . .	193
4.16	Nodal model showing accelerometer and force cell locations. . . . .	195
4.17	Stabilisation diagram generated using Polymax (PLSCF) method - for 2 m x 20 cm x 5 mm sample - dark circles represent stable modes . . . . .	196
4.18	Mode shape visualisation at the first modal frequency 11.7 Hz . . . . .	198
4.19	Heat map showing the consistency of the sample geometry for the 2 m x 20 cm x 5 mm UD pultruded carbon fibre composite. . . . .	200
4.20	Statistical evaluation of the sample's geometry, showing the thickness distribution (a) and summary of geometric data (b). . . . .	201
4.21	Mode shape of the stable first flexural mode identified using the Polymax (pLSCF) method. . . . .	203
4.22	Effect of applied force, strain, and temperature on damping ratios for the 5 mm carbon fibre composite sample in air and vacuum environments . . . . .	205

## List of Figures

4.23 NMIS CNC Machine, with carbon fibre milling tool and CFRP 2 m CFRP sample . . . . .	207
4.24 Heat map showing the consistency of the sample geometry for the 2 m x 20 cm x 2.5 mm milled UD pultruded carbon fibre composite. . . . .	208
4.25 Statistical evaluation of the milled sample's geometry, showing the thickness distribution (a) and summary of geometric data (b). . . . .	209
4.26 (a) Stabilisation diagram generated using the deterministic Polymax (pLSCF) method; (b) Mode shape of the stable mode identified after applying filtering criteria for the 2.5 mm sample. (Both were produced with MACEC) . . . . .	211
4.27 Effect of applied force, strain, and temperature on damping ratios for the 2.5 mm milled carbon fibre composite in air and vacuum environments. . . . .	213
4.28 Heat map showing the consistency of the sample geometry for the 1.2 m x 20 cm x 5 mm UD pultruded carbon fibre composite. . . . .	215
4.29 Statistical evaluation of the 1.2 m sample's geometry, showing the thickness distribution (a) and summary of geometric data (b). . . . .	217
4.30 (a) Stabilisation diagram generated using the deterministic Polymax (pLSCF) method; (b) Mode shape of the stable mode identified for the 1.2 m sample (Both Generated from MACEC) . . . . .	219
4.31 Effect of applied force, strain, and temperature on damping ratios for the shortened 1.2 m carbon fibre composite in air and vacuum. . . . .	221
4.32 Damping ratio comparison between 1.2 m and 2 m samples in vacuum, plotted against the applied force. The 1.2 m sample consistently exhibits higher damping ratios. . . . .	224

## List of Figures

4.33	Damping ratio comparison between 1.2 m and 2 m samples in vacuum, plotted against strain. The 1.2 m sample shows a higher damping ratio than the 2 m sample across the strain range.	225
4.34	Average damping ratios of the 1.2 m and 2 m UD pultruded carbon fibre composite samples tested under vacuum conditions.	226
4.35	Final approach for added masses: Copper masses drilled and clamped through the composite sample to ensure secure attachment and stable frequency modification.	228
4.36	Damping ratio for the 1.2 m x 20 cm x 5 mm composite sample in air and vacuum with added masses, showing applied force, strain, and temperature variations.	229
4.37	Extrapolated damping trend across frequencies based on average damping ratios from 1.2 m and 2 m samples under vacuum with Added Mass Configuration	230
4.38	EMA setup highlighting striker, DAQ, and complete vacuum chamber configuration.	233
I.1	Comparison of the FRFs for the selected and poor suspension mechanisms, highlighting differences in mode identification and additional undesired modes.	336
J.1	Graph for evaluating $\varepsilon_2$ based on $\frac{L_{stiff}}{2R}$ and $\frac{2R}{e_{final}}$	344
J.2	Graph for determining $\Delta_2$ for cylindrical shells under external pressure	345

# List of Tables

1.1	Mechanical properties of UD carbon and glass fibre composites	5
2.1	Comparison of EMA and OMA	49
2.2	Comparison of Experimental Methods for Damping Evaluation	51
3.1	DMA Test Setup Parameters	80
3.2	Modal Frequencies for Various Sample Thicknesses	90
3.3	Boundary Conditions for the Three-Point Bend Test in FEA	93
3.4	Detailed FEA Model Configuration for DMA Testing	95
3.5	UD Test – Strain values and corresponding displacements for 100 microstrains across selected thicknesses.	101
3.6	Target Thickness ( $T_T$ ) against the resultant sample dimensions	102
3.7	Comparison of Central Deformation with respect to Equations 3.7 and 3.8	102
3.8	Strain Energy (SE) Distribution Relative to Total Energy for Different Thicknesses - UD Samples	111
3.9	Strain Energy (SE) Distribution Relative to Total Energy for Different Thicknesses - Transverse Samples	118
3.10	Strain Energy (SE) Distribution Relative to Total Energy for Different Thicknesses - All Samples	123
3.11	Comparison of Loss Factors at Various Frequencies	146

## List of Tables

4.1	Design considerations for the EMA test rig. . . . .	172
4.2	Force testing results for the pneumatic-assisted striking system. . . . .	185
4.3	Data acquisition hardware for EMA testing. . . . .	194
4.4	Comparison of FEA-predicted frequency and EMA-obtained modal frequency. . . . .	203
4.5	Comparison of FEA-predicted frequency and EMA-obtained modal frequency for the 2.5mm sample. . . . .	212
4.6	Comparison of FEA-predicted frequency and EMA-obtained modal frequency for the 1.2m sample. . . . .	220
4.7	Summary of EMA Damping Results . . . . .	234
4.8	Summary of EMA Damping Results . . . . .	237
B.1	Summary of DMA0 Sample Dimensions . . . . .	294
B.2	Summary of DMA90 Sample Dimensions . . . . .	295
E.1	UD Test - Strain values and corresponding displacements for different microstrains and selected thicknesses. . . . .	321
G.1	DAQ Connection Details . . . . .	325

# Contents

<b>Abstract</b>	<b>ii</b>
<b>Declaration</b>	<b>vi</b>
<b>List of Figures</b>	<b>vii</b>
<b>List of Tables</b>	<b>xiv</b>
<b>Contents</b>	<b>xvi</b>
<b>Acknowledgements</b>	<b>xxiii</b>
<b>Nomenclature</b>	<b>xxiv</b>
<b>1 Introduction</b>	<b>1</b>
1.1 Structural Damping in Wind Turbine Blades . . . . .	2
1.2 Research Motivation . . . . .	5
1.3 Objectives and Scope . . . . .	6
1.4 Thesis Structure . . . . .	9
1.5 Scientific Contributions . . . . .	11
1.6 List of Outputs . . . . .	12
1.6.1 Publications . . . . .	12
1.6.2 Presentations . . . . .	13

## Contents

<b>2</b>	<b>Fundamentals of Damping</b>	<b>14</b>
2.1	Introduction & Literature Review . . . . .	14
2.2	Damping in Isotropic and Anisotropic Materials . . . . .	18
2.3	Composite Materials and Their Role in Damping for Offshore Wind Turbine Blades . . . . .	20
2.3.1	Interfacial Damping and the Role of Fibre-Matrix Interface Quality . . . . .	25
2.4	Damping Mechanisms and Models in Wind Turbine Blades . . .	28
2.4.1	Appropriate Damping Models . . . . .	28
2.4.2	Critical Evaluation of Damping Models for Composite Wind Turbine Blades . . . . .	36
2.5	Current Experimental Approaches used for Damping Evaluation in Composite Materials . . . . .	38
2.5.1	Dynamic Mechanical Analysis (DMA) . . . . .	39
2.5.2	Logarithmic Decrement . . . . .	42
2.5.3	Half-Power Bandwidth Method . . . . .	43
2.5.4	Operational Modal Analysis (OMA) . . . . .	45
2.5.5	Experimental Modal Analysis . . . . .	47
2.5.6	Critical Comparison of Experimental Damping Evaluation Methods . . . . .	50
2.6	Expected Benefits from Improving Structural Damping Characterisation . . . . .	53
2.6.1	Historical Model Development for Multi-Orientation Composite Laminates . . . . .	54
2.6.2	Benefits for Wind Turbine Blade Design . . . . .	58
2.7	Chapter Summary . . . . .	59
<b>3</b>	<b>Dynamic Mechanical Analysis for Damping Estimation</b>	<b>62</b>

## Contents

3.1	DMA Introduction . . . . .	62
3.2	Background of DMA . . . . .	66
3.2.1	History of DMA in Composite Materials . . . . .	67
3.2.1.1	Early Experimental Approaches . . . . .	67
3.2.1.2	Development of Standardised Testing and Equipment . . . . .	68
3.2.1.3	Refinement in Analysis Techniques . . . . .	68
3.2.1.4	Advancements in Commercial DMA Equipment	69
3.2.2	Principles and Material Response in DMA . . . . .	71
3.2.2.1	Significance of Loss Factor and Its Relationship with Other Damping Metrics . . . . .	75
3.2.3	Limitations and Challenges of DMA . . . . .	76
3.3	Standard DMA method – influential factors on test results . . . . .	77
3.3.1	Experimental Setup and Test Procedure . . . . .	78
3.3.2	Influence of Sample Geometry on DMA Results . . . . .	81
3.4	FEA Assisted DMA . . . . .	86
3.4.1	Using FEA to Investigate the Influence of Setup Changes in DMA . . . . .	86
3.4.2	Analysing Strain Energy Components . . . . .	88
3.4.3	FEA - Static Viability . . . . .	89
3.4.4	FEA - Initial Setup . . . . .	90
3.4.4.1	Influence of Sample Thickness on Strain Energy Results . . . . .	98
3.4.4.2	Influence of Strain Variation on Strain Energy Results . . . . .	100
3.4.4.3	Influence of Minor Thickness Variations within Samples on Strain Energy Results . . . . .	101
3.5	FEA assisted DMA testing – Methodological development . . . . .	104

## Contents

3.5.1	Proposed Approach for FEA assisted DMA . . . . .	105
3.5.1.1	Synergy of FEA and DMA: UD Modelling approach . . . . .	110
3.5.1.2	Synergy of FEA and DMA: Transverse Modelling approach . . . . .	115
3.5.1.3	Synergy of FEA and DMA: Combined UD-Transverse Modelling Approach . . . . .	122
3.5.1.4	Development of the Directional Simplified Model	129
3.5.2	Evaluation of the Results . . . . .	132
3.5.2.1	Comparison of Generated Results and Input DMA Data . . . . .	133
3.5.2.2	Evaluating Model Robustness by Removing Data Extremes . . . . .	136
3.6	DMA Discussion . . . . .	145
3.7	DMA Conclusion . . . . .	147
<b>4</b>	<b>Experimental Modal Analysis for Damping Estimation</b>	<b>148</b>
4.1	EMA Introduction . . . . .	148
4.2	EMA Background . . . . .	151
4.2.1	History of EMA in Composite Materials . . . . .	152
4.2.2	Application of EMA . . . . .	154
4.2.3	Excitation Methods Used in EMA . . . . .	155
4.2.4	Post-Processing Methods . . . . .	156
4.2.4.1	Polymax (pLSCF) Method . . . . .	159
4.2.4.2	Justification for Selecting pLSCF in This Study .	161
4.2.5	The MACEC Modal Analysis Toolbox . . . . .	162
4.2.5.1	Modal Analysis Methods in MACEC . . . . .	162
4.2.5.2	Why MACEC Was Chosen for This Study . . . .	163

## Contents

4.2.6	Advantages and Limitations of EMA . . . . .	164
4.2.7	Main Aims of Conducting EMA . . . . .	168
4.3	Development of EMA Test Rig and Accompanying Methodology .	169
4.3.1	Requirements . . . . .	170
4.3.2	Material Inspection Prior to Testing . . . . .	173
4.3.3	Testing Frame and Suspension Mechanism . . . . .	175
4.3.4	Sample Excitation Method . . . . .	181
4.3.5	Vacuum Chamber . . . . .	186
4.3.6	Data Acquisition . . . . .	190
4.3.7	Post-Processing . . . . .	195
4.4	EMA Results . . . . .	198
4.4.1	Results from EMA Testing of UD Pultruded Carbon Fibre Composite (2 m x 20 cm x 5 mm) . . . . .	199
4.4.1.1	Sample Geometry Consistency . . . . .	199
4.4.1.2	Modal Testing, Stabilisation Diagram, and Frequency Validation . . . . .	202
4.4.1.3	Damping Analysis . . . . .	204
4.4.2	Results from EMA Testing of Milled UD Pultruded Carbon Fibre Composite (2 m x 20 cm x 2.5 mm) . . . . .	207
4.4.2.1	Sample Geometry Consistency . . . . .	207
4.4.2.2	Modal Testing, Stabilisation Diagram, and Frequency Validation . . . . .	210
4.4.2.3	Damping Analysis . . . . .	212
4.4.3	Results from EMA Testing of UD Pultruded Carbon Fibre Composite - Shortened (1.2 m x 20 cm x 5 mm) . . . . .	215
4.4.3.1	Sample Geometry Consistency . . . . .	215
4.4.3.2	Modal Testing, Stabilisation Diagram, and Frequency Validation . . . . .	218

## Contents

4.4.3.3	Damping Analysis . . . . .	220
4.4.4	Comparison of Vacuum Damping Results for 1.2 m and 2 m Samples - Vacuum Conditions . . . . .	223
4.4.5	Comparison of Damping Results Across Frequencies . . . . .	226
4.4.6	Impact of Frequency Variation on Damping Behaviour through Added Mass . . . . .	227
4.5	Comparison Between DMA and EMA Results . . . . .	231
4.6	Discussion and Conclusion . . . . .	239
4.6.1	Key Findings . . . . .	239
4.6.2	Evaluation of the EMA Test Rig . . . . .	240
4.6.3	Sample Size - Thickness & Consistency . . . . .	241
4.6.4	Comparison with DMA Results . . . . .	242
<b>5</b>	<b>Conclusions</b>	<b>244</b>
5.1	Research Structure . . . . .	244
5.2	Summary of Main Contributions . . . . .	246
5.3	Key Conclusions . . . . .	248
5.4	Implications for Wind Turbine Blade Design . . . . .	249
5.5	Limitations of the Present Study . . . . .	249
5.6	Future Work . . . . .	253
	<b>Bibliography</b>	<b>256</b>
<b>A</b>	<b>Derivations of Damping Models</b>	<b>283</b>
<b>B</b>	<b>DMA Sample Dimensions</b>	<b>294</b>
<b>C</b>	<b>MATLAB Code: FEA 1-5 mm Sample Test</b>	<b>296</b>
<b>D</b>	<b>ANSYS APDL Code: Baseline Implementation</b>	<b>302</b>

## Contents

<b>E Strain Energy Study</b>	<b>321</b>
<b>F Equation Derivation</b>	<b>322</b>
<b>G EMA Test Protocol with Vacuum Chamber</b>	<b>324</b>
<b>H MATLAB Code: EMA Data Acquisition</b>	<b>328</b>
<b>I FRF Response of Suspension Mechanisms</b>	<b>336</b>
<b>J Vacuum Chamber Validation Calculations</b>	<b>337</b>
<b>K MATLAB Code: EMA Post-processing via MACEC using pLSCF Method</b>	<b>349</b>

# Acknowledgements

I want to express my deepest gratitude to those who have supported and contributed to the completion of my PhD thesis. Firstly, I extend my sincere thanks to my supervisors, Prof. David H. Nash and Dr. Abbas Mehrad Kazimi Amiri, for the invaluable guidance, expertise, encouragement, and the great moments shared throughout this research. I am also profoundly grateful to my supervisors at Siemens Gamesa Renewable Energy (SGRE), Lars Hedegaard, Philippe Couturier, and Vitor Reis, for their support during this time. Special thanks to my PhD colleagues, whose technical advice and assistance have been crucial to the successful completion of this thesis.

I would also like to acknowledge the support of the Wind & Marine Energy Systems & Structures Centre for Doctoral Training (EP/S023801/1). Additionally, I am grateful to the Electronic and Electrical Engineering (EEE) Department and the Mechanical and Aerospace Engineering (MAE) Department for providing the resources and facilities essential for this research. Further to this, I would also like to thank James Gillespie, Alasdair Kerr, and the team of MAE technicians for their assistance in assembling my experimental modal analysis rig and supporting the test manufacturing process.

Finally, my heartfelt appreciation goes to my family, friends and especially Carolyn, for their unwavering support, patience, and understanding throughout this challenging journey. Their presence has been a constant source of strength and motivation.

Thank you all for your support and encouragement.

# Nomenclature

## General Symbols and Operators

$\delta$	Deformation or deflection
$\dot{x}, \ddot{x}$	Velocity and acceleration
$\epsilon$	Strain
$\sigma$	Stress
$F(t)$	Time-dependent force function in dynamic systems
$L$	Span length in bending tests
$t$	Thickness of a sample
$N$	Number of layers in composite laminates (or number of terms in summations)
$c, s$	Cosine and sine of fibre orientation angles, respectively

## Contents

### Material and Damping Properties

$\eta$	Loss factor
$\xi$	Damping ratio
$\nu$	Poisson's ratio
$\Delta$	Logarithmic Decrement
$\tan \delta$	Tangent of the phase angle (equivalent to loss factor)
$\eta_{\text{DMA}}$	Loss factor obtained from Dynamic Mechanical Analysis
$\eta_{ij}$	Decomposed Loss factor in direction $i$ and $j$
$\psi$	Specific damping capacity (SDC)

### Moduli in Viscoelastic Materials

$E'$	Storage modulus (elastic component)
$E''$	Loss modulus (viscous component)
$E^*$	Complex modulus, defined as $E^* = E'(1 + i \tan \delta)$

### Energy Components

$U$	Total Strain Energy
$U_{ij}$	Strain energy components in directions $i$ and $j$
$\Delta U$	Energy dissipation per cycle

## Contents

### Model Matrices and Components

$C$	Damping matrix in dynamic systems
$K$	Stiffness matrix in dynamic systems
$M$	Mass matrix in dynamic systems
$Q$	Reduced stiffness matrix for composite laminates
$T_{ij}$	Transformation matrix for global and fibre coordinate systems
$Q_{ij}$	Transformed stiffness matrix components for each layer $k$ in directions $i$ and $j$
$C_{ij}$	Compliance matrix for reduced stiffness calculations
$W_k$	Weighting factor for the $k^{th}$ term in summations in damping models

### Indices

11	Axial direction
22	Transverse direction
33	Out-of-plane direction
12, 13, 23	In-plane and out-of-plane shear directions

## **Abbreviations and Acronyms**

APDL	ANSYS Parametric Design Language
DMA	Dynamic Mechanical Analysis
EMA	Experimental Modal Analysis
FEA	Finite Element Analysis
FRF	Frequency Response Function
MDOF	Multi degree-of-freedom
pLSCF	Poly-reference Least-Squares Complex Frequency- Domain
SDOF	Single degree-of-freedom
SE	Strain Energy
SDC	Specific Damping Capacity
TTS	Time-Temperature Superposition

# Chapter 1

## Introduction

The global transition towards renewable energy has driven remarkable growth in the wind energy sector, with wind turbines playing a pivotal role in this shift. Wind energy has emerged as one of the most promising technologies for reducing carbon emissions, and its expansion is expected to accelerate significantly [1, 2]. Between 2000 and 2023, global wind turbine capacity grew at an annual rate of nearly 20%, climbing to 1,021 GW by 2023, representing a roughly 50% increase over 2019 levels [3]. Current forecasts project that this capacity will exceed 1,200 GW sometime in 2025 [4, 5]. Global efforts to meet emission reduction targets further highlight the need to optimise wind turbine technology, particularly under the Paris Agreement [6].

The blades are central to wind turbines' efficiency and longevity. They are exposed to extreme environmental conditions, including wind loads, cyclic stresses, and temperature fluctuations [7, 8]. These factors contribute to structural fatigue, making the design and reliability of wind turbine blades critical to overall turbine performance [1, 9]. One of the major challenges in blade design is managing the dynamic responses of these large, flexible

## Chapter 1. Introduction

structures since operational loads can trigger wind-induced vibrations [10, 11].

Damping, an intrinsic property of mechanical systems, plays an important role in dissipating vibrational energy and reducing the amplitude of oscillatory motions over time [12]. This dissipation is essential for mitigating resonant vibrations, enhancing structural stability, and extending the service life of wind turbine blades [7]. In wind turbines, damping mechanisms must be well understood to reduce the dynamic responses and peak displacements caused by wind-induced and operational loads [13]. Structural damping is a singular term that represents the overall ability of a complex structure to dissipate vibrational energy through internal friction and material hysteresis. It is often quantified by the damping ratio, a dimensionless parameter that compares the system's actual damping to the critical damping, the minimum damping needed to eliminate oscillations without overshoot. This parameter is required for evaluating and optimising the performance of wind turbine blades and towers. Increasing the structural damping can reduce vibrational stresses in sections of the blades and tower, optimising energy output and prolonging the turbine's operational lifespan [14].

### **1.1 Structural Damping in Wind Turbine Blades**

Wind turbine blades can experience vibrations due to their size, flexibility, and exposure to turbulent wind conditions. Flapwise, torsional and edgewise modes dominate the blade dynamic design [15] and can be seen on a blade in Figure 1.1, modified from [16]. Among these, edgewise vibration presents an important challenge, mainly because aerodynamic damping is limited in this direction [17]. This is because edgewise motions cause only minimal changes in the blade's angle of attack relative to the wind, resulting in insufficient aerodynamic forces to dissipate vibrational energy effectively in

## Chapter 1. Introduction

that direction. Structural damping, therefore, becomes the primary means of mitigating these vibrations. Without sufficient damping, turbine blades can be susceptible to resonance and amplified oscillations, which can compromise the blade's structural integrity and lead to premature failure [18, 19].

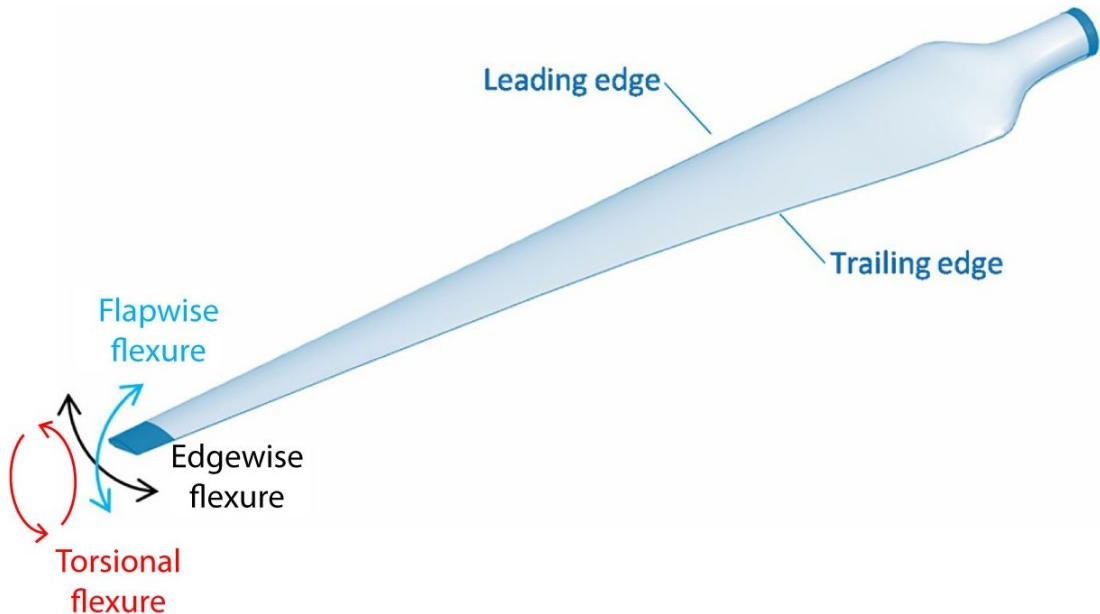


Figure 1.1: Coordinates of wind turbine blade (modified from [16]).

Recent advancements in blade materials, particularly the introduction of carbon fibre composites (CFRP) in spar caps of offshore wind turbine blades, have added complexity to damping characterisation. Traditionally, glass-reinforced plastic (GFRP) composites have been used exclusively in wind turbines due to their favourable properties and well-established dynamic behaviour [20]. However, carbon fibre composites, offering superior strength, stiffness and fatigue resistance, are increasingly employed in offshore wind turbine applications, which demand reliable operation in extreme and remote environments [21]. Despite their mechanical advantages, particularly in terms of strength-to-weight ratio, the damping characteristics of carbon fibre composites remain insufficiently understood, and accurate representation of

## Chapter 1. Introduction

their behaviour presents an ongoing challenge [22].

In particular, the spar caps of wind turbine blades, which carry the majority of the flapwise bending loads, have undergone a material transition from unidirectional glass fibre (UD-GF) to unidirectional carbon fibre (UD-CF) composites. The superior longitudinal stiffness and tensile strength of carbon fibres primarily drive this shift. An example of such materials used in wind turbine applications is provided by the AVATAR reference blade design project [23], whose material properties are summarised in Table 1.1. According to this data, UD-CF exhibits a longitudinal modulus  $E_{11}$  of 115 GPa, nearly three times higher than the 41.63 GPa of UD-GF, while also being significantly lighter (1578 compared with 1915 kg/m<sup>3</sup>) and stronger in tension ( $\sigma_{11}^{\text{Ten}} = 1317.6$  MPa compared with 876.1 MPa). These advantages enable the design of longer, stiffer and lighter blades, improving aerodynamic efficiency and reducing gravitational loading. However, carbon composites are generally more anisotropic and exhibit lower inherent damping than glass fibre, making accurate damping characterisation increasingly important in modern blade designs.

Table 1.1: Mechanical properties of UD carbon and glass fibre composites used in AVATAR blade design [23].

Symbol	Units	UD CF	UD GF
$E_{11}$	GPa	115.00	41.63
$E_{22}$	GPa	7.56	14.93
$\nu_{12}$	–	0.300	0.241
$G_{12}$	GPa	3.96	5.05
$\rho$	kg/m <sup>3</sup>	1578	1915
$\sigma_{11}^{\text{Ten}}$	MPa	1317.6	876.1
$\sigma_{11}^{\text{Comp}}$	MPa	620.1	625.8
$\sigma_{22}^{\text{Ten}}$	MPa	21.88	74.03
$\sigma_{22}^{\text{Comp}}$	MPa	76.25	189.4
$\tau_{12}$	MPa	45.53	56.58

## 1.2 Research Motivation

The need to characterise structural damping in carbon fibre composites has increased with the growing use of these materials in modern wind turbine blades [24]. Significant discrepancies have been observed between predicted and actual damping performance, particularly in the case of carbon fibre composites [22]. Leading companies such as Siemens Gamesa Renewable Energy (SGRE) have initiated efforts to improve damping simulations and sponsor this work. However, although internal friction is recognised as the primary mechanism by which carbon fibre composites dissipate energy, accurately quantifying this damping under dynamic loading conditions

## Chapter 1. Introduction

remains challenging.

This research aims to bridge the knowledge gap by developing novel experimental and computational methods to assess and optimise the damping properties of carbon fibre laminates and their directional contributions in wind turbine blades. A primary challenge addressed in this thesis is the precise characterisation of damping in these composites, especially under operational conditions where cyclic loading induces fatigue mechanisms that compromise performance and durability [8, 25]. Moreover, the continual variation in wind loading can increase the risk of fatigue failure.

By incorporating damping design constraints into the blade design process, fatigue loads in sections of the blades can be reduced, thereby improving the overall durability and efficiency of wind turbines [26]. This is particularly important for offshore applications, where the structural integrity of the blades must be maintained over extended periods [27]. Continuing to integrate carbon fibre composites into modern blade designs requires a more comprehensive understanding of their damping behaviour to ensure wind turbines' long-term performance and safety.

**Research Statement:** How can the damping of anisotropic composites be accurately characterised through experimental methods, taking into account their directional property dependence, and therefore be effectively represented in numerical models to enhance wind turbine blade design?

### 1.3 Objectives and Scope

The primary objective of this thesis is to provide a comprehensive investigation into the damping mechanisms present in wind turbine blade materials, with a particular emphasis on carbon fibre composites. This

## Chapter 1. Introduction

research aims to bridge the gap between experimental and computational approaches to understand how these materials dissipate energy when subjected to dynamic loading conditions. By doing so, it seeks to contribute valuable insights into optimising material performance in wind turbine applications.

Central to this investigation is DMA, an industry-standard technique for exploring the viscoelastic properties of materials across a range of frequencies and temperatures, providing a detailed understanding of energy dissipation and material response. For the experimental component, a DMA Q800 instrument is employed to conduct a frequency sweep of the sample using a three-point bending test, with the force applicator positioned on the middle arm. The standard DMA methodology is explored with a focus on the shortcomings associated with this methodology, and methods to overcome these are presented.

Building on conventional DMA techniques, this thesis introduces a novel FEA-assisted DMA method, incorporating strain energy considerations into the analysis. This hybrid approach is designed to enhance the reliability of predictions regarding the material's damping behaviour under real-world operational conditions, specifically focusing on the first flexural mode of wind turbine blades. By integrating FEA into the DMA process, this thesis aims to offer a more comprehensive view of how strain energy and anisotropic materials influence damping. The newly developed FEA-assisted DMA method has provided insight into carbon composites' dynamic behaviour and energy dissipation. (Refer to Chapter 3: Dynamic Mechanical Analysis for Damping Estimation).

As a complementary approach to small-scale DMA testing, medium-scale EMA is used to examine the damping properties of a laminated panel. EMA is

## Chapter 1. Introduction

a widely recognised method for estimating the dynamic characteristics of structures, including natural frequencies, mode shapes, and damping ratios, through direct physical testing. The process involves exciting the structure using techniques like impact hammers or shakers and recording the structural responses via sensors such as accelerometers or strain gauges. The modal parameters derived from these responses are important for understanding the structure's dynamic behaviour under operational conditions. In this study, EMA provides insights into the material's dynamic response, complementing the DMA findings. (Refer to Chapter 4: Experimental Modal Analysis for Damping Estimation).

Together, these methods provide a robust framework for evaluating the vibrational characteristics of wind turbine blades and their interaction with material-damping properties. Investigating EMA and FEA-assisted DMA is particularly valuable for analysing materials used in structures like wind turbines, where the interplay between material properties and structural dynamics is complex and significantly affects overall performance. DMA is especially valuable because it can precisely measure the viscoelastic properties of materials in a controlled lab environment across a range of frequencies and temperatures, thereby capturing the dynamic response under realistic loading conditions. This dual-method approach considers damping from both a stress–strain and a vibrational dissipation perspective, offering a comprehensive understanding of system behaviour. Using both testing methodologies, distinct damping metrics are captured that can be applied as necessary to address specific analysis requirements.

This thesis's scope extends beyond characterising composite materials' damping properties through experimental testing and computational modelling. By investigating the dynamic behaviour of carbon fibre composites

## Chapter 1. Introduction

used in wind turbine blades, this research provides valuable insights into how these materials dissipate energy under operational conditions, thereby contributing to the optimisation of structural damping for renewable energy applications. The results include both loss factors and damping ratios for the composite under investigation, which can be integrated into larger-scale blade models. These outputs offer designers quantitative metrics that enable targeted material selection or development, such as incorporating higher-damping materials where necessary to mitigate vibrations. They also open up the potential for optimised, lighter blades without compromising structural integrity. As a result, there is potential to reduce maintenance costs, prolong turbine lifespans, and improve energy output efficiency by mitigating harmful vibrations through a more considered design. Ultimately, this work supports efforts to boost the reliability of wind turbine technology in the global transition towards renewable energy, thereby contributing to an emissions reduction.

### 1.4 Thesis Structure

This thesis comprises five chapters, each addressing specific research components related to damping mechanisms in wind turbine blade materials. A conventional literature review chapter is not present within this thesis. However, Chapters 2 to 4 provide a review of the relevant literature specific to that topic.

The chapters are organised as follows:

- **Chapter 1: Introduction** - Outlines the research motivation, objectives, and scope, emphasising the significance of investigating damping mechanisms in wind turbine blades, particularly carbon fibre

## Chapter 1. Introduction

composites. It sets the scene for the subsequent experimental and computational analyses.

- **Chapter 2: Damping Fundamentals** - Provides a comprehensive overview of the fundamental damping concepts, including various damping mechanisms (structural, material, and aerodynamic). It also covers the theoretical background of damping in composite materials and its role in energy dissipation.
- **Chapter 3: Dynamic Mechanical Analysis** - Outlines the experimental setup and procedures for conducting DMA tests, and discusses the resulting data, which examines the viscoelastic properties and energy dissipation of carbon fibre composites across different frequencies and temperatures. It also introduces a novel FEA-assisted DMA method that incorporates strain energy distribution to enhance the quantification of damping characteristics.
- **Chapter 4: Experimental Modal Analysis** - Uses EMA to estimate the dynamic characteristics of wind turbine blade materials, including natural frequencies, mode shapes, and damping ratios. The results of the EMA experiments are presented and compared with the DMA findings to provide a comprehensive understanding of the material's dynamic behaviour under operational conditions. Additionally, EMA and DMA results were compared using an analytical conversion approach
- **Chapter 5: Discussion, Conclusions, and Future Work** - Synthesises the findings from the DMA and EMA experiments, discussing the implications of the results for the design and optimisation of wind turbine blades. It also outlines potential areas for future research, particularly in developing more advanced damping models and improved material characterisation techniques.

## 1.5 Scientific Contributions

- Conducted a study and reviewed a range of experimental approaches for characterising damping in carbon fibre composites. EMA and DMA were identified as the most appropriate techniques for further investigation based on their suitability for the material system and target application. See Chapter 2 for more details.
- Developed a new FEA-assisted DMA methodology for determining damping within anisotropic materials when comparing testing using standard DMA machines (in an adapted but conventional approach) to overcome shear influence contributions. This was done through implementing strain energy results from an FEA model replicating the experimental setup to determine the proportion of energy dissipated in each direction. See Chapter 3 for more details.
- Investigated the role of strain energy in the damping characteristics of carbon fibre composites, offering insights into directional energy dissipation mechanisms and demonstrating how fibre-specific damping can be accurately simulated/modelled using the novel FEA-assisted DMA model. See Chapter 3 for more details.
- Developed an improved experimental EMA test rig to limit external energy loss mechanisms and better characterise damping behaviour. This involved the design, construction, and validation of a custom rig incorporating a vacuum chamber and nodal suspension system. The setup enabled the isolation and estimation of structural damping by removing aerodynamic effects, allowing for the characterisation of damping within complex composite structures. See Chapter 4 for more details.

## Chapter 1. Introduction

- Provided recommendations for how best to experimentally quantify damping in anisotropic composite materials within the limits discussed in Chapter 3 & 4. This data will be used for the future optimisation of wind turbine blades using advanced material characterisation techniques, including FEA-assisted DMA and EMA.

## 1.6 List of Outputs

The outputs generated during this research, including peer-reviewed publications and conference presentations, are listed here.

### 1.6.1 Publications

The following is a list of publications related to the research presented in this thesis. These publications highlight the development of experimental and computational methods for assessing the damping characteristics of composite materials used in wind turbine blades, focusing on both DMA and EMA.

1. **Brough, E., Nash, D. H., Kazemi-Amiri, A. M., Couturier, P., & Reis, V. L. (2023).** Development of a Test Rig for Improved Estimation of Structural Damping of Wind Turbine Composite Materials. In *Proceedings of ASME 2023 Aerospace Structures, Structural Dynamics, and Materials Conference*, SSDM 2023, Article V001T01A026. ASME. <https://doi.org/10.1115/SSDM2023-108462>.
2. **Brough, E., Kazemi-Amiri, A. M., & Nash, D. H. (under review).** On the Damping Characterisation of Composite Material Systems in Wind Turbine Blades: A Novel Approach Using FEA-Assisted DMA. Submitted to *Composites Structures*.

3. **Brough, E., Kazemi-Amiri, A. M., & Nash, D. H. (to be submitted).**  
On the Damping Characterisation of Composite Material Systems in Wind Turbine Blades: A Novel EMA and Rig Framework to Resolve Experimental Limitations.

## 1.6.2 Presentations

The following presentations were delivered as part of this research, disseminating key findings and contributions to the field of composite material damping for wind turbine applications:

- **SSDM 2023:** Development of a Test Rig for Improved Estimation of Structural Damping of Wind Turbine Composite Materials. Presented at the ASME Aerospace Structures, Structural Dynamics, and Materials Conference, San Diego, CA, June 2023.
- **FutureWind 2023:** Structural Damping Characterisation of Materials Used within Wind Turbine Blades. Presented at the Future Wind Conference, University of Edinburgh, UK, March 2023.
- **WESC 2023:** Development of Test Rig for Accurate Estimation of Structural Damping of Wind Turbine Blade Composites Through Experimental Modal Analysis. Presented at the Wind Energy Science Conference, Glasgow, UK, May 2023.
- **ISSI 2024:** An Integrated DMA and EMA Approach for Damping Characterisation of Composite Materials. Presented at the International Symposium on Structural Integrity, Dongguan, China, November 2024.

# Chapter 2

## Fundamentals of Damping

### 2.1 Introduction & Literature Review

Damping, a key property of mechanical systems, dissipates vibrational energy, reducing the amplitude of oscillatory motions over time [28]. Effective dissipation of vibrational energy is essential across a wide range of applications, particularly for mitigating resonant vibrations, enhancing structural stability, and extending the lifespan of mechanical systems [13, 29]. In the specific context of wind turbine blades, damping is an important factor, especially in modern, larger offshore turbines, where the scale of the blades amplifies dynamic loads and increases the potential for structural fatigue. As turbine blades grow larger, the introduction of advanced composite materials, such as carbon fibre composites, plays a crucial role in managing these dynamic challenges [30, 31]. Specifically, unidirectional (UD) carbon fibre reinforcements, which provide high stiffness and strength along the fibre direction, are strategically placed in critical sections, mainly the spar caps, of the blades to enhance their structural strength [30–32]. A cross-sectional view of carbon UD placement in a wind turbine blade, taken from [21], can be seen

in Figure 2.1.

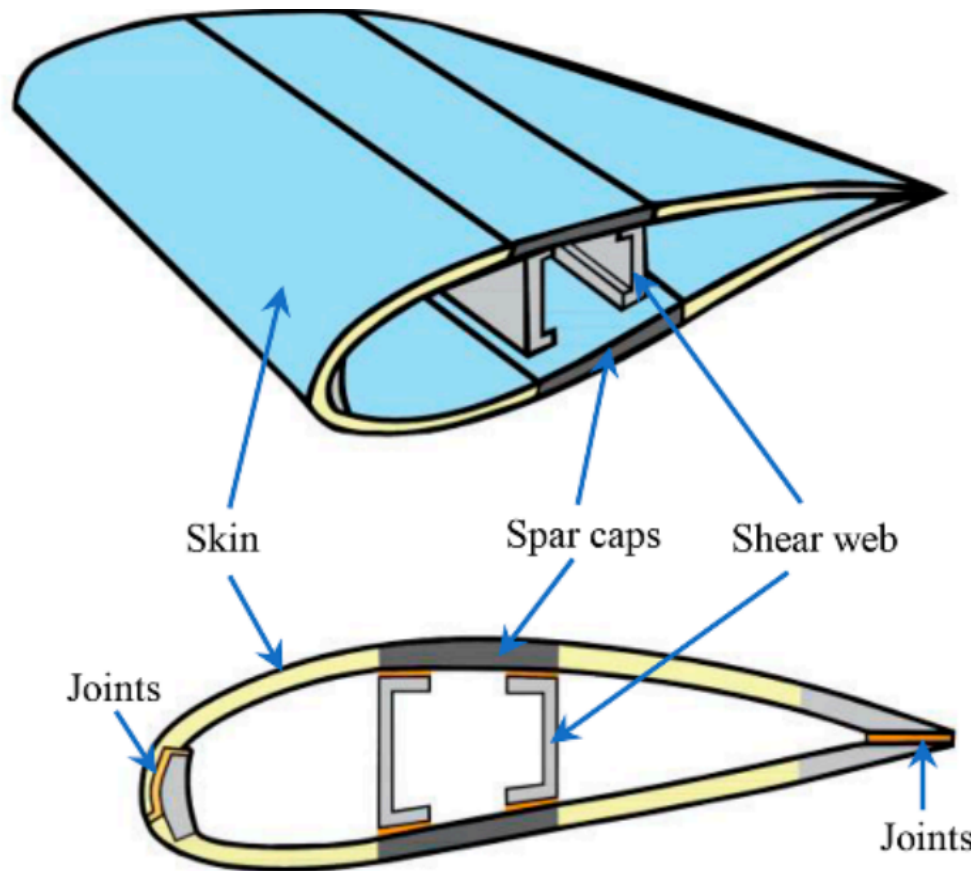


Figure 2.1: Cross-sectional view of a wind turbine blade. Carbon UD reinforcements may be in spar caps (image taken from [21]).

These advanced materials contribute to the structural strength and influence the turbine blades' overall behaviour [30, 33]. In fibre-reinforced composites, structural damping primarily arises from several interacting mechanisms, including matrix viscoelasticity, interfacial friction between fibres and the surrounding resin, microcracking, and fibre-matrix debonding under cyclic loading [34, 35]. Unlike metals, where damping is often associated with dislocation movement [36], composite materials exhibit more complex, anisotropic damping behaviour. This complexity stems from the combined influence of fibre orientation, fibre volume fraction, matrix properties,

## Chapter 2. Fundamentals of Damping

interfacial bonding quality, and manufacturing techniques such as curing conditions and fibre sizing [33, 35, 37, 38]. For example, damping in the fibre direction tends to be lower due to the high stiffness of carbon fibres, while transverse and shear directions, where the matrix plays a more dominant role, typically show higher damping levels. These direction-dependent interactions necessitate careful characterisation and modelling, as the energy dissipation mechanisms vary not only with material composition but also with the direction of applied loading. Accurately predicting damping behaviour in composite structures, therefore, requires methods that account for their anisotropic and microstructural nature.

The effectiveness of a material's damping capacity depends on its intrinsic properties, geometric configuration, environment and the frequency of excitations [39, 40]. Materials with high damping capacity, such as viscoelastic materials, are favoured in applications susceptible to vibrational issues [41]. These materials exhibit a phase lag between stress and strain during cyclic loading, enabling efficient energy dissipation and improving the overall damping performance of structures, including wind turbine blades [40, 42]. While both GFRP and carbon fibre composites exhibit anisotropic behaviour, carbon fibre composites possess a less extensively characterised damping response with lower damping, necessitating the use of more advanced modelling and experimental techniques to predict their behaviour accurately [43].

Effective damping characterisation is required for controlling the dynamic responses of wind turbines to various forces, including wind-induced and gravitational loads. A significant design challenge is managing edgewise vibrations, oscillations occurring perpendicular to the primary blade span [44]. Unlike in-plane (flapwise) vibrations, which are partially damped by

## Chapter 2. Fundamentals of Damping

aerodynamic effects, edgewise vibrations receive minimal aerodynamic damping, leaving them more prone to resonant oscillations [17]. These vibrations can increase material stress and fatigue risks that may compromise structural integrity. By fine-tuning damping properties through advanced material selection and design strategies, these critical vibrations can be mitigated, decreasing fatigue risk and ultimately extending the operational lifespan of turbine components [45,46].

The use of advanced materials like carbon fibre composites has introduced additional complexities due to their less established history in understanding and optimising the damping behaviour of wind turbine blades. While composites offer significant strength-to-weight advantages, their anisotropic nature presents unique damping challenges that necessitate sophisticated modelling and experimental techniques [34]. Future advancements in damping technology will likely centre on optimising material compositions and structural configurations to fine-tune damping responses across diverse operational scenarios, ensuring reliable performance under varying environmental conditions [43,47].

To effectively manage vibrations, understanding how energy is dissipated in materials like composites used in turbine blades is essential at both the microscopic (material structure) and macroscopic (structural assembly) levels [48]. This comprehensive knowledge is vital to optimising key components, enabling them to withstand complex dynamic loads during operation [49]. This chapter introduces these fundamental damping concepts, setting the stage for a detailed discussion of experimental methodologies in subsequent chapters, with a focus on the role of composite materials in modern wind turbine blade design.

## **2.2 Damping in Isotropic and Anisotropic Materials**

The study of damping in materials requires an in-depth understanding of their structural makeup, particularly distinguishing between isotropic and anisotropic materials [50]. Isotropic materials are characterised by uniform properties in all directions, meaning their mechanical behaviour, including damping, is constant regardless of the applied stress or strain direction. Common examples include metals, such as aluminium and steel, and certain polymers with uniform molecular structure [51]. These materials are typically easier to model and predict because their behaviour does not change with loading direction, simplifying the application of classical damping models, covered in Section 2.6.

Anisotropic materials, also known as anisotropic materials, exhibit properties that vary depending on the direction of the applied force [52]. This category includes composites like carbon fibre and glass fibre materials, which are widely used in advanced engineering applications due to their directional strength and stiffness characteristics [53]. The mechanical performance of these materials is tailored by adjusting the orientation of fibres or layers, making them highly efficient in handling loads in specific directions but, in turn, adding complexity to their damping behaviour. The directional dependence of stiffness and strength in anisotropic materials, such as CFRP, introduces significant challenges in predicting accurate damping behaviour [54]. Traditional damping models, typically developed for isotropic materials, often fall short when applied to these composites as they do not consider anisotropy [55]. This is due to many of the models treating composites as a 2D material and not fully considering their anisotropy. As a

## Chapter 2. Fundamentals of Damping

result, there is a requirement for models accounting for the variability in damping capacity across different fibre orientations and structural layers [43, 56].

In isotropic materials, energy dissipation due to damping is relatively predictable because of the uniformity of their structure [57]. Classical damping models, such as viscous or hysteretic damping, can be reliably applied to calculate energy dissipation based on established mechanical principles [58]. The homogeneity of these materials means that damping characterisation is simpler with more predictable results, making them suitable for applications where uniform performance is important, such as in metallic structural components.

Anisotropic materials, on the other hand, present more complex challenges in damping characterisation [59]. The anisotropic nature means that the damping capacity can vary significantly depending on the direction of load application, fibre orientation in composites, and the interaction between different material components [54, 60]. For instance, in a carbon fibre composite, damping behaviour can differ drastically along the fibres compared to across them. Carbon fibres' orientation and interlaminar regions' behaviour are crucial in determining the blade's overall damping characteristics [55, 60]. These interlaminar interactions can alter the vibrational response of the blade, making it essential to account for such complexities in damping models [56].

A comprehensive review of damping in both isotropic and anisotropic materials enhances the understanding of material behaviour under dynamic loading. It informs the selection and design of materials for specific applications. This is particularly important in fields where material efficiency and durability are paramount, such as renewable energy, aerospace, and civil engineering, where optimising damping characteristics can significantly

extend the operational lifespan of critical components. The insights gained from studying the damping behaviour of both isotropic and anisotropic materials are essential for improving the performance of complex engineering systems, such as wind turbine blades, which will be explored in greater detail in subsequent sections.

## **2.3 Composite Materials and Their Role in Damping for Offshore Wind Turbine Blades**

Composite materials, created by combining two or more constituent materials with distinct physical or chemical properties, are highly valued in engineering applications for their ability to deliver tailored properties that meet specific performance requirements [61, 62]. Combining the advantages of each component, composite materials often exhibit increased strength, stiffness, and durability while maintaining a reduced weight. These features are particularly desirable for applications in offshore wind turbines, where high strength-to-weight and stiffness-to-weight ratios are critical for optimal performance [21, 63, 64].

Carbon fibre composites, particularly those made with a vinyl ester matrix, have garnered significant interest due to their exceptional mechanical properties. Carbon fibres contribute high strength and stiffness, while the vinyl ester matrix enhances chemical resistance, durability, and efficient load transfer between fibres [21, 65]. This combination makes these composites highly suitable for the challenging conditions faced by wind turbine blades, which must endure dynamic loading, fatigue, and environmental factors such as moisture, UV exposure, and temperature fluctuations [63, 65]. Their use is now common in large offshore wind turbine blades in their spar caps, where

## Chapter 2. Fundamentals of Damping

their strength and stiffness are critical to withstanding the high loads experienced during operation. Figure 2.2 illustrates a cross-section of a wind turbine blade, highlighting the location and role of the spar caps.

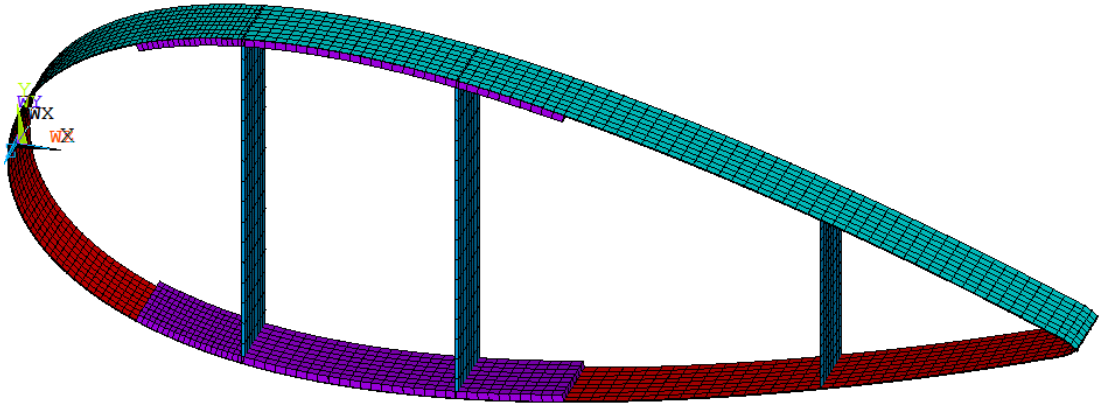


Figure 2.2: Cross-section of a wind turbine blade (ANSYS APDL Model). The purple section represents the spar caps where the Carbon UD material is used

The material of interest within this study is a unidirectional carbon fibre vinyl ester composite enhanced with nitrile sizing. The components of this composite are:

- **Carbon Fibre:** The high-strength, high-stiffness fibres are oriented in a single direction, optimising reinforcement where the load is most significant. This unidirectional configuration allows the material to exhibit high performance in specific directions [66].
- **Vinyl Ester Matrix:** The matrix is a durable resin with excellent mechanical properties and chemical resistance. It plays a crucial role in transferring loads between the fibres and maintaining the structural integrity of the composite [66].
- **Nitrile Sizing:** A treatment applied to the carbon fibres to enhance adhesion to the vinyl ester matrix, nitrile sizing also serves to reduce moisture ingress, thus improving the long-term durability of the

## Chapter 2. Fundamentals of Damping

composite in harsh environments [66,67].

The unidirectional carbon fibre vinyl ester composite used in this study was manufactured using pultrusion. In this continuous process, fibres are pulled through a resin bath and then a heated die to impregnate and cure them into a constant cross-sectional shape [68]. Different infusion methods can lead to vastly different material quality upon setting [69, 70]. It is also important to note that the method of manufacture may influence the composite's damping characteristics, as increased defects or inconsistencies introduced during processing can result in higher damping levels. This process ensures precise fibre alignment, which enhances the mechanical properties, such as strength and stiffness, along the fibre direction [71]. Pultrusion offers advantages like high fibre volume fraction, resulting in superior load-bearing capabilities, consistent quality due to the uniform nature of the process, and cost-efficiency in producing large quantities of composite materials [72]. These characteristics make pultruded composites particularly suitable for wind turbine blades, where strength, durability, and efficient load transfer are crucial. A diagram of a pultrusion process, taken from [68], is shown in Figure 2.3.

## Chapter 2. Fundamentals of Damping

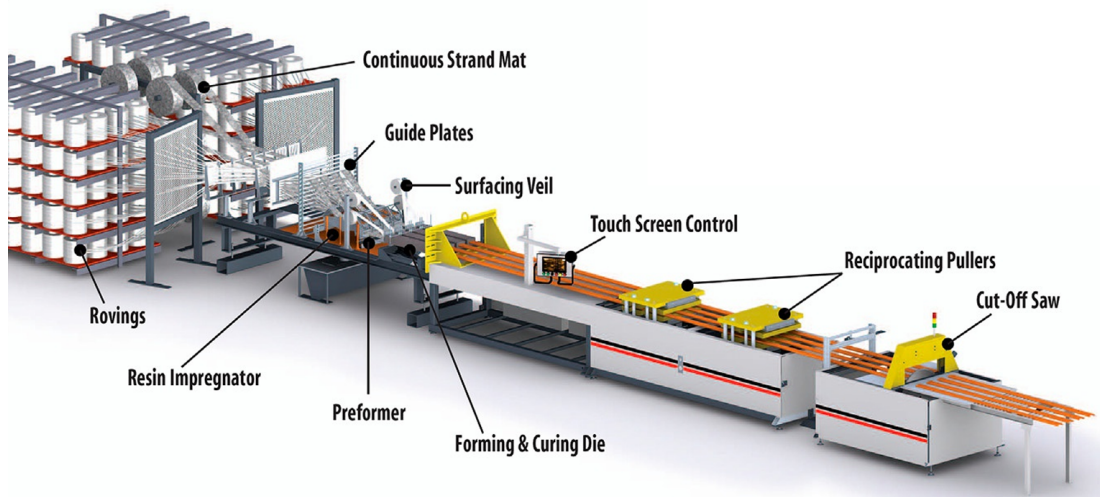


Figure 2.3: Diagram of a pultrusion manufacturing process. Continuous fibres are impregnated with resin and pulled through a heated die to form a cured composite with a constant cross-section (taken from [68]).

The unidirectional nature of carbon fibres, which aligns the fibres in the load-bearing direction, enhances both stiffness and damping. By controlling the directionality of the fibres, the composite can be optimised for specific load-bearing scenarios in offshore wind turbine blades. This increases the blade's strength and reduces its deformation under operational loading conditions [64]. Additionally, nitrile sizing improves the interface between the carbon fibres and the matrix, enhancing load transfer and minimising the ingress of moisture, which can degrade material properties over time. This treatment is particularly beneficial in the harsh environments offshore turbines are subjected to, where saltwater, UV radiation, and fluctuating temperatures present significant challenges for material durability [65].

The anisotropic nature of carbon fibre composites, where properties vary with the direction of applied force, presents both opportunities and modelling challenges. Damping in CFRP arises primarily from internal friction within the matrix and at fibre–matrix interfaces. Earlier studies, such as Hashin [73] and

## Chapter 2. Fundamentals of Damping

Saravanos [74], established a foundational understanding of how fibre alignment leads to high stiffness but low damping along the 11-direction, with greater dissipation seen in matrix-dominated directions.

This foundational understanding was further supported by key review works. Treviso et al. highlighted how early analytical models often treated composite materials as quasi-isotropic, neglecting the influence of fibre orientation and matrix viscoelasticity. Their review established that accurate damping prediction requires models that incorporate directional stiffness and energy dissipation [75]. Qiu et al. experimentally validated that damping increases with fibre misalignment from the loading direction, supporting the classical view that transverse and shear directions exhibit higher damping [76]

Recent studies have refined this perspective using advanced experimental and modelling techniques. Qiu et al. [76] demonstrated that processing defects and air damping can significantly distort damping measurements if not controlled, recommending vacuum-based testing as a reliable approach. Rouhi Moghanlou et al. [77] quantitatively confirmed the trade-off between fibre alignment and damping—higher angles relative to the load increase damping but reduce structural stiffness.

More recent investigations have expanded this understanding significantly. Mohanty et al. [78] demonstrated a multiscale framework in which micromechanical models and experimental data are jointly used to predict direction-dependent damping, validating how matrix–fibre bonding and fibre orientation affect modal loss. Li et al. [79] further showed that even small deviations in fibre orientation or interfacial quality can have measurable effects on damping behaviour, especially in repair contexts. These studies confirm that damping anisotropy is not just inherent to composite architecture but is also influenced by processing and operational conditions.

## Chapter 2. Fundamentals of Damping

Moreover, Chamoli et al. [17] demonstrated how directionally dependent damping characteristics directly impact the effectiveness of active vibration suppression in wind turbine blades. Their work, which integrates pitch control strategies and interval observers, highlights the importance of understanding edgewise damping behaviour for system-level dynamic stability and load mitigation in large offshore turbines.

Together, these developments highlight a shift from empirical observations toward predictive modelling and system-level damping control, which is especially critical in offshore wind turbine blades. A thorough understanding of directionally dependent damping allows for finer tailoring of structural responses to site-specific load conditions, enabling safer and more efficient turbine blade designs.

### **2.3.1 Interfacial Damping and the Role of Fibre-Matrix Interface Quality**

Interfacial damping mechanisms significantly influence the damping characteristics of fibre-reinforced composite materials, crucially determining their dynamic behaviour, fatigue resistance, and vibration attenuation capabilities. Unlike metals, where damping is typically driven by dislocation mechanisms [36], composites exhibit energy dissipation primarily at the fibre-matrix interfaces through complex microstructural interactions [35, 80].

In polymer-matrix composites, such as carbon fibre-vinyl ester composites used in large wind turbine blades, damping arises from a combination of viscoelastic matrix behaviour, fibre-matrix friction, adhesion hysteresis, and microstructural degradation mechanisms such as microcracking and debonding under cyclic loading [81]. Of these, interfacial phenomena, particularly adhesion hysteresis and friction, are especially critical, as the

## Chapter 2. Fundamentals of Damping

quality of the fibre-matrix interface directly influences them.

Adhesion hysteresis involves the cyclic formation and breaking of interfacial bonds under dynamic loading, which dissipates energy. Strong interfacial adhesion, supported by chemical compatibility, enhances damping by increasing the energy required to reform these bonds. For example, hydrogen bonding in nanocrystalline cellulose (CNC)-reinforced polyamide (PA610) composites has been shown to significantly enhance damping via this mechanism [82].

Interfacial friction, meanwhile, results from relative motion between fibres and matrix, especially near microcracks or regions of partial debonding. This frictional mechanism dissipates energy and is influenced by fibre-matrix bond strength, radial stresses, and the extent of debonding. While moderate debonding may initially enhance damping through increased friction, extensive interface degradation can compromise structural integrity [83].

In the present study's composite system, a unidirectional carbon fibre reinforced vinyl ester matrix, nitrile sizing is used to enhance interfacial bonding. This sizing improves chemical compatibility with the matrix and reduces moisture ingress. From a micromechanical perspective, these effects strengthen interfacial adhesion and increase friction resistance, thereby enhancing energy dissipation under cyclic loading. Such interface improvements are especially valuable in fibre-dominated directions where the matrix contributes less to damping.

At the nanoscale, models and experiments converge on the importance of increased interfacial area and enhanced bonding. Reinforcement with nanoscale fillers, such as CNC, amplifies adhesion hysteresis and interfacial elasticity, yielding improved damping without sacrificing stiffness [82].

## Chapter 2. Fundamentals of Damping

Multiple factors influence interfacial damping effectiveness:

- **Fibre Volume Fraction:** Higher fibre contents reduce matrix-dominated damping pathways, especially in transverse and shear directions.
- **Fibre Orientation and Interface Anisotropy:** Anisotropic fibre arrangements lead to directional variations in interface quality and associated damping [83].
- **Environmental Effects:** Moisture and temperature changes alter interface chemistry, impacting adhesion and friction [35].

Experimental findings consistently reinforce the importance of high-quality interfaces. Enhanced interfacial bonding has been shown to increase damping performance, particularly through increased hydrogen bonding and effective stress transfer. Conversely, environmental degradation of interfaces reduces damping efficacy, underscoring the need for robust interface design throughout a composite's service life [82].

Interface engineering strategies such as surface treatments, coupling agents, and sizing technologies offer pathways to improve damping without compromising structural integrity. These approaches must be balanced against long-term durability requirements, particularly in demanding environments such as offshore wind energy. Through targeted improvements in interfacial adhesion and frictional mechanisms, composite structures can achieve superior damping performance. This is of critical importance for components like wind turbine blades, where vibration control, fatigue resistance, and environmental resilience are essential for reliable operation.

## 2.4 Damping Mechanisms and Models in Wind Turbine Blades

Understanding and accurately representing damping is pivotal in predicting the dynamic behaviour of mechanical systems, particularly in the context of wind turbine blade design, where the implications on performance and longevity are significant. Damping mechanisms in materials and systems are critical as they contribute uniquely to energy dissipation, which is crucial for the stability and efficiency of wind turbines.

Damping mechanisms vary based on the material and system, each contributing uniquely to energy dissipation. Understanding these mechanisms is essential for predicting and optimising the damping behaviour of materials and structures, particularly in engineering applications involving dynamic loading and vibrations.

### 2.4.1 Appropriate Damping Models

- **Viscous Damping and Rayleigh Damping:** Viscous damping describes a resistive force proportional to the velocity of a vibrating system and is commonly used to model energy dissipation in mechanical and structural systems. It is mathematically expressed as [84, 85]:

$$F_d = c \cdot \dot{x} \quad (2.1)$$

where  $F_d$  is the damping force,  $c$  is the viscous damping coefficient, and  $\dot{x}$  is the velocity. The damping ratio  $\zeta$ , defined as the ratio of actual damping to critical damping, characterises the system response:

- $\zeta < 1$ : Underdamped – oscillatory decay

## Chapter 2. Fundamentals of Damping

- $\zeta = 1$ : Critically damped – fastest non-oscillatory return to equilibrium
- $\zeta > 1$ : Overdamped – slow non-oscillatory return

While viscous damping is straightforward and effective in modelling systems with fluid interactions (e.g., hydraulic dampers or shock absorbers), real-world structural systems, such as wind turbine blades, often require a more generalised approach to account for damping across a range of vibration modes. For this purpose, **Rayleigh damping** is frequently employed.

Rayleigh damping models the damping matrix  $C$  as a linear combination of the mass and stiffness matrices:

$$C = \alpha M + \beta K \quad (2.2)$$

where  $M$  is the mass matrix,  $K$  is the stiffness matrix, and  $\alpha$ ,  $\beta$  are mass- and stiffness-proportional damping coefficients, respectively. This formulation preserves the symmetry of system matrices and is particularly suitable for implementation in finite element analyses.

The damping ratio for a vibration mode  $i$  with natural frequency  $\omega_i$  is given by:

$$\zeta_i = \frac{1}{2}(\alpha/\omega_i + \beta\omega_i) \quad (2.3)$$

This expression leads to a frequency-dependent damping behaviour: mass-proportional damping ( $\alpha$ ) dominates at low frequencies (e.g., rigid body motion), while stiffness-proportional damping ( $\beta$ ) becomes more influential at higher frequencies. The result is a U-shaped damping curve with a minimum at an intermediate frequency.

## Chapter 2. Fundamentals of Damping

Various strategies exist for selecting  $\alpha$  and  $\beta$ , including:

- **Two-frequency matching:** Ensures the desired damping ratio at two selected frequencies.
- **Critical mode focus:** Targets the dominant mode at the expense of others.
- **Stiffness-only damping ( $\alpha = 0$ ):** Often used when low-frequency damping is less critical.

Despite its limitations, particularly its unphysical frequency dependence, Rayleigh damping remains widely used due to its simplicity, numerical efficiency, and ease of implementation in time-domain simulations. It is especially valuable in large-scale structural dynamics applications such as wind turbine blade design, seismic response analysis, and aerospace vibration control, where approximated but stable damping representation across multiple modes is necessary [86, 87].

- **Hysteretic (Structural) Damping:** This model accounts for energy dissipation due to internal friction within the material, characterised by a phase lag between stress and strain. The relationship is often represented using a complex modulus:

$$\sigma = E^* \cdot \epsilon \quad \text{with} \quad E^* = E(1 + i\eta) \quad (2.4)$$

where  $\sigma$  is the stress,  $E^*$  denotes complex modulus,  $\epsilon$  is the strain,  $E$  is the elastic modulus,  $\eta$  is the loss factor, and  $i$  is the imaginary unit. Hysteretic damping results in a hysteresis loop in the stress-strain curve, indicating energy dissipation as heat [88]. The energy dissipated per cycle is given by [84]:

$$\Delta E = \pi k h X^2 \quad (2.5)$$

## Chapter 2. Fundamentals of Damping

where  $\Delta E$  is the energy dissipated per cycle,  $k$  is the stiffness,  $h$  is the hysteretic damping coefficient, and  $X$  is the amplitude of motion. This energy dissipation is independent of the loading frequency and proportional to the square of the amplitude [84]. This model is particularly relevant for materials like metals and composites, where energy dissipation occurs due to micro-structural movements. Designing the structure of wind turbine blades to operate within the linear stress-strain range is a common practice to ensure safe and predictable performance. However, real-world conditions such as stress concentrations, material and manufacturing imperfections, damage and cracks in the blade material and adhesive behaviour can lead to elastoplastic behaviour [89]. A hysteretic damping loop can be seen in Figure 2.4.

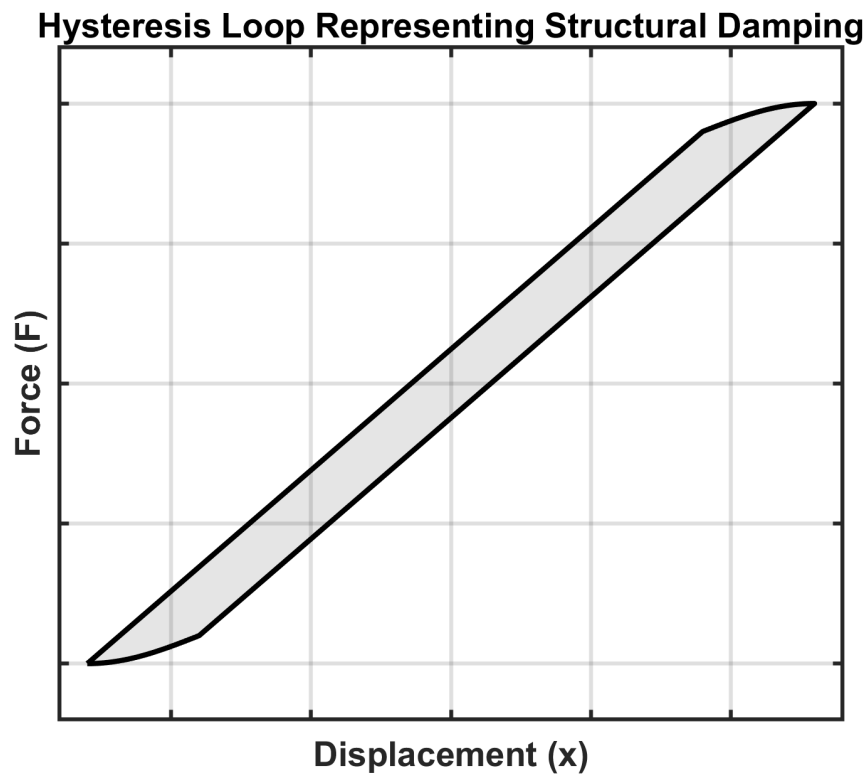


Figure 2.4: Hysteresis Loop

- **Coulomb (Dry Friction) Damping:** This model accounts for energy dissipation due to dry friction when two surfaces slide against one another. Coulomb damping is characterised by a friction force proportional to the normal force between the surfaces  $N$  and opposes the direction of motion. The differential equation governing the free vibration of an SDOF (Single Degree-Of-Freedom) slider with Coulomb damping is [84, 86]:

$$m\ddot{x} + kx = -\mu N \text{sgn}(\dot{x}) \quad (2.6)$$

where  $m$  is the mass,  $k$  is the stiffness,  $\mu$  is the coefficient of friction, and  $\text{sgn}(\dot{x})$  is the sign function of the velocity. Unlike viscous damping, Coulomb damping results in a linear amplitude decay and does not

## Chapter 2. Fundamentals of Damping

affect the system's natural frequency. The Coulomb damping model is particularly relevant for systems involving dry sliding friction, such as joints and blade root connections.

- **Aerodynamic Damping:** This damping mechanism results from air or fluid flow interaction with structures. In wind turbines, it plays a significant role due to the constant airflow impacting the turbine blades, enhancing stability and reducing vibrations [90]. The fluctuating aerodynamic force per unit length is given by:

$$F_d = \frac{1}{2}\rho(\bar{U} - \dot{x})^2 C_d c(r) - \frac{1}{2}\rho\bar{U}^2 C_d c(r) \quad (2.7)$$

where  $\rho$  is the air density,  $\bar{U}$  is the mean wind speed,  $\dot{x}$  is the blade flapwise velocity,  $C_d$  is the drag coefficient, and  $c(r)$  is the local blade chord length. When  $\dot{x}$  (the blade flapwise velocity) is small compared to  $\bar{U}$  (the mean wind speed), the term  $(\bar{U} - \dot{x})^2$  can be approximated by neglecting the second-order small term  $\dot{x}^2$ . This expression then simplifies to:

$$F_d \approx \rho\bar{U}\dot{x}C_d c(r) \quad (2.8)$$

indicating that the damping force is proportional to the fluid density, velocity, drag coefficient, and chord length. This form of damping is crucial for reducing resonant oscillations that occur due to wind fluctuations at frequencies close to the blade's natural frequency. When the blade is at an angle that maximises lift, aerodynamic damping can be effectively zero, relying solely on structural damping to limit deflections [91]. Aerodynamic and hydrodynamic damping are critical in maintaining the wind turbines' dynamic stability and structural integrity by mitigating oscillations and associated loads. [90]

- **Viscoelastic Damping (VED):** Viscoelastic damping is important in materials that exhibit both viscous and elastic characteristics, such as blade fibre-reinforced composites. Among the proposed models to describe the viscoelastic behaviour [92], the two key models are the Kelvin-Voigt (KV) model and the Maxwell model.

**Kelvin-Voigt (KV) Model:** This model combines a spring and a dashpot in parallel to represent the viscoelastic behaviour as seen in Figure 2.5.

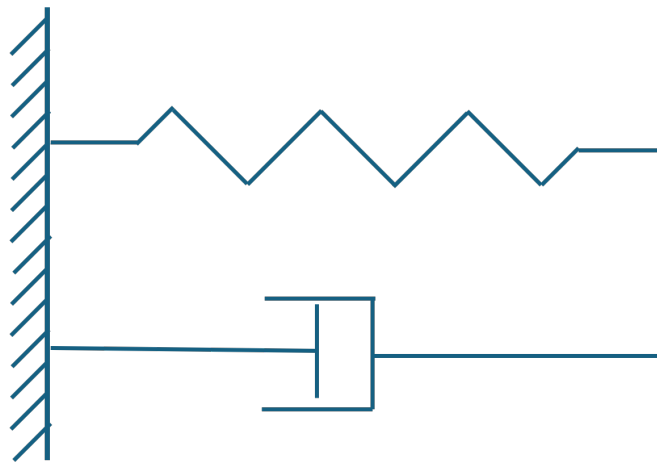


Figure 2.5: KV Model Schematic - showing spring and dashpot

The constitutive equations for the Kelvin-Voigt model are [93, 94]:

$$\epsilon = \frac{\sigma_1}{E}, \quad \dot{\epsilon} = \frac{\sigma_2}{c}, \quad \sigma = \sigma_1 + \sigma_2 \quad (2.9)$$

where  $\sigma$  is the total stress,  $\sigma_1$  is the stress in the spring,  $\sigma_2$  is the stress in the dashpot,  $E$  is the elastic modulus,  $c$  is the viscosity coefficient,  $\epsilon$  is the strain and  $\dot{\epsilon}$  is the strain rate. By eliminating  $\sigma_1$  and  $\sigma_2$ , the following constitutive law is obtained:

$$\sigma = E\epsilon + c\dot{\epsilon} \quad (2.10)$$

## Chapter 2. Fundamentals of Damping

This model effectively describes materials where the damping is proportional to the strain rate.

**Maxwell Model:** This model consists of a spring and dashpot in series, representing the viscoelastic behaviour of materials that exhibit both elastic and viscous properties. The constitutive equations for the Maxwell model are [93]:

$$\epsilon_1 = \frac{\sigma}{E}, \quad \dot{\epsilon}_2 = \frac{\sigma}{c}, \quad \epsilon = \epsilon_1 + \epsilon_2 \quad (2.11)$$

By differentiating and combining these equations, we obtain:

$$\sigma + \frac{c}{E}\dot{\sigma} = c\dot{\epsilon} \quad (2.12)$$

where  $\epsilon$  is the total strain,  $\epsilon_1$  is the strain in the spring,  $\dot{\epsilon}_2$  is the strain rate in the dashpot,  $\sigma$  is the stress,  $E$  is the elastic modulus, and  $c$  is the viscosity coefficient. This model is beneficial for describing stress relaxation in materials where an initial elastic deformation is followed by a slow, time-dependent viscous flow.

These models provide the foundation for modelling and estimating the damping behaviour of structures and materials. They are critical for designing and optimising engineering systems, particularly in applications involving blades' dynamic loading and vibrations. While this contribution primarily focuses on the material damping, in reality, for a turbine blade, the total damping can be a combination of the structural damping of the blade materials, friction damping of the joints and connections, as well as aerodynamic damping depending on the vibration mode and the relative position of the blade to the airflow [91].

## 2.4.2 Critical Evaluation of Damping Models for Composite Wind Turbine Blades

While the previous section outlined a range of damping models used in structural dynamics, their application to composite wind turbine blades requires more nuanced consideration. Each model offers differing degrees of physical realism, computational simplicity, and relevance to the underlying energy dissipation mechanisms in composite materials.

**Viscous and Rayleigh Damping:** Although viscous damping is mathematically convenient and widely adopted in dynamic simulations, its assumption of a linear velocity-dependent force does not physically represent the microstructural damping mechanisms present in fibre-reinforced composites, such as interfacial friction and matrix viscoelasticity [95]. To overcome some of these limitations, Rayleigh damping is often used in finite element analyses due to its computational simplicity. It is formulated as a linear combination of the mass and stiffness matrices. However, Rayleigh damping introduces an artificial frequency dependence that does not align with experimentally observed material damping behaviour, potentially causing significant over- or underestimation of damping outside the calibration frequency range. As a result, it is often inadequate for accurately modelling the broadband dynamic response of composite wind turbine blades unless carefully calibrated for the specific frequency range of interest [96].

**Hysteretic Damping:** Hysteretic (or structural) damping captures energy dissipation through internal friction and micro-slip at fibre–matrix interfaces, which is a dominant mechanism in laminated composites where interlaminar shear and ply debonding occur [81]. This mechanism is often modelled using a complex modulus or loss factor, which avoids velocity-dependent

## Chapter 2. Fundamentals of Damping

assumptions and effectively describes phase lag under cyclic loading [74]. However, hysteretic models do not account for the frequency-dependent damping observed in viscoelastic resin systems, where polymer chain dynamics can significantly influence the damping behaviour. Additionally, such models tend to underestimate nonlinear dissipation at high strain levels due to matrix cracking and other damage mechanisms [97].

**Coulomb Damping:** Coulomb (dry friction) damping is primarily associated with energy dissipation at mechanical interfaces—such as blade root joints and other contact regions—rather than within the bulk of composite materials [98, 99]. In wind turbine and aerospace blades, friction at these interfaces can significantly influence overall system damping, as small relative motions at contact surfaces induce nonlinear, amplitude-dependent energy losses [98]. Studies have shown that neglecting such interface damping can result in substantial underestimation of energy dissipation, leading to non-conservative predictions of vibration response and fatigue life in critical regions such as blade roots [99]. Although advanced finite element models can simulate the complex stick–slip transitions and evolving contact areas at these joints, practical implementation in large composite structures remains challenging due to the inherently nonlinear and variable nature of frictional behaviour [98].

**Aerodynamic Damping:** Aerodynamic damping is highly relevant for operational wind turbine blades. It is inherently mode-dependent and relies on the interaction between structural velocity and airflow. Its magnitude and sign can vary with wind speed, blade pitch, and mode shape, occasionally providing negative damping. While it is critical for full-system models, aerodynamic damping is not material-specific and is generally not captured in laboratory-scale material characterisation efforts like DMA.

**Viscoelastic Damping Models (KV and Maxwell):** These models provide a more realistic representation of time-dependent, frequency-dependent material behaviour, particularly for the resin matrix in fibre-reinforced composites. The KV model effectively captures immediate elastic and delayed viscous response, suitable for simulating in-phase and out-of-phase stresses in DMA experiments. The Maxwell model, on the other hand, is better suited for capturing stress relaxation and long-term creep but may not reflect the typical cyclic loading behaviour of blades. More advanced generalised viscoelastic models or Prony series expansions may be required for high-fidelity representation over broad frequency ranges.

**Summary:** In practice, wind turbine blade models often combine multiple damping representations to approximate real-world behaviour. Rayleigh damping may be used for numerical stability, while hysteretic or viscoelastic models better capture laminate-specific energy dissipation. Aerodynamic and Coulomb damping account for additional system-level effects.

## **2.5 Current Experimental Approaches used for Damping Evaluation in Composite Materials**

In this section, the experimental techniques currently used to evaluate damping in composite materials are reviewed. These approaches treat systems as either single-degree-of-freedom (SDOF) or multi-degree-of-freedom (MDOF) systems, providing insights into both the energy dissipation mechanisms and dynamic behaviour of the materials. By employing a range of experimental methods from controlled laboratory tests like DMA to medium-scale EMA, these techniques establish critical benchmarks that not only capture the intricacies of material damping but also

## Chapter 2. Fundamentals of Damping

support the validation and refinement of computational models for enhanced design optimisation.

### 2.5.1 Dynamic Mechanical Analysis (DMA)

DMA is a widely employed technique for characterising the viscoelastic properties of polymeric and composite materials under oscillatory loading [100]. It provides a frequency- and temperature-dependent understanding of material behaviour by applying a sinusoidal force and measuring the resultant displacement. This allows for evaluation of key mechanical parameters, including the storage modulus ( $E'$ ), which represents the elastic response; the loss modulus ( $E''$ ), which quantifies energy dissipation; and the complex modulus ( $E^*$ ), which combines both components:

$$E^* = E' + iE'' \quad (2.13)$$

The damping capacity of the material is often expressed as the loss factor:

$$\tan \delta = \frac{E''}{E'} \quad (2.14)$$

These parameters offer critical insight into the stiffness, damping, and energy dissipation mechanisms within a material across a range of frequencies and temperatures. DMA is particularly useful in the study of fibre-reinforced polymers, where damping behaviour is affected by matrix viscoelasticity, fibre–matrix interaction, and fibre orientation.

A variety of test modes can be used depending on the geometry and application context of the material, including single and dual cantilever,

## Chapter 2. Fundamentals of Damping

three-point bending, tension, compression, and shear. Each mode provides different strain distributions and is chosen based on the dominant deformation mechanisms of interest. For instance, three-point bending is commonly employed for assessing flexural damping, especially in laminated or beam-like structures.

The technique is typically carried out using dedicated DMA equipment that records high-resolution force and displacement data, often using optical encoders or capacitance-based sensors to capture small oscillatory deflections. The resulting phase lag between the applied force and material response allows for the precise calculation of damping behaviour. DMA is especially advantageous due to its high sensitivity, ability to simulate in-service dynamic loading, and suitability for small, controlled samples.

Figure 2.6 shows a typical DMA system, adapted from [101].

## Chapter 2. Fundamentals of Damping

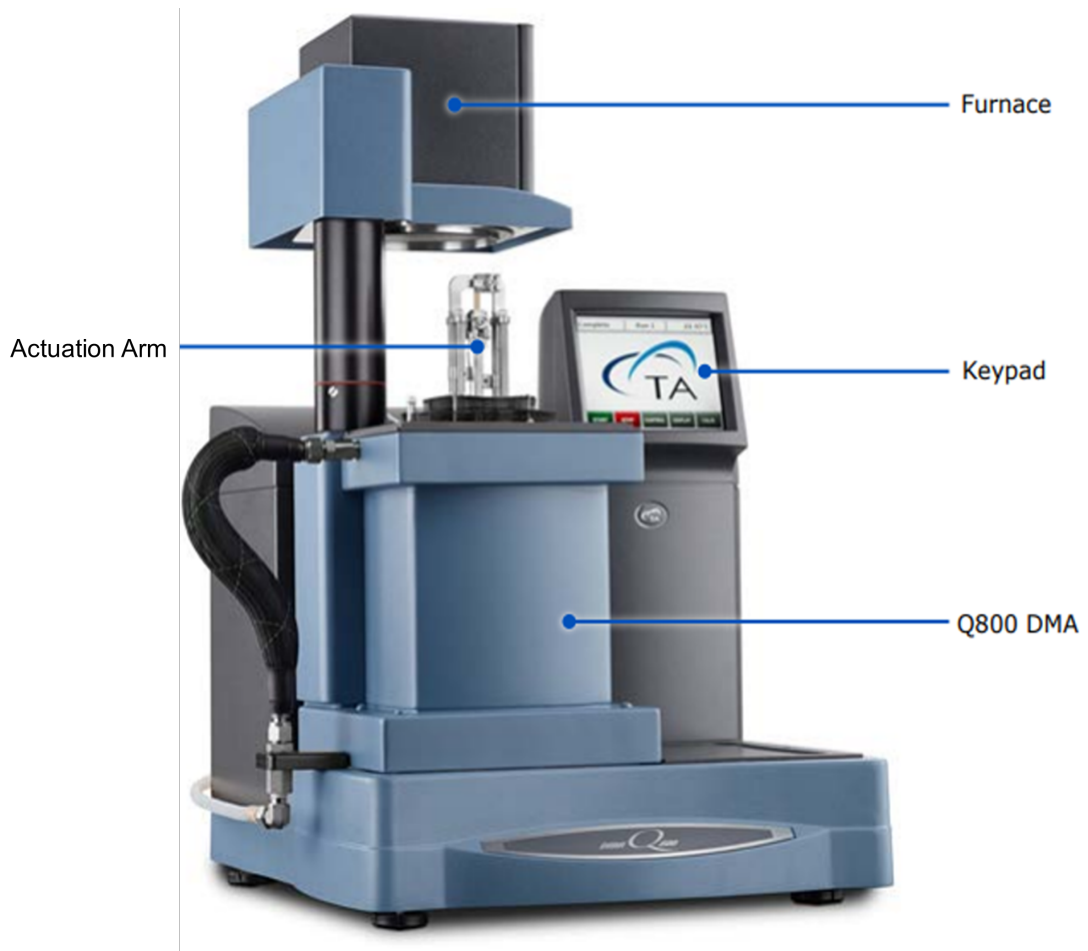


Figure 2.6: TA Instruments DMA Q800 (adapted from [101]).

The displacement data, combined with the known applied force, enables precise calculation of stress and strain. The phase lag between applied force and resultant displacement reveals the material's viscoelastic nature. The in-phase component of the response determines the storage modulus ( $E'$ ), while the out-of-phase component defines the loss modulus ( $E''$ ). The complex modulus ( $E^*$ ) combines these two elements to describe the material's total resistance to deformation, and the ratio  $E''/E'$  gives the damping loss factor ( $\tan \delta$ ), a key metric for quantifying energy dissipation.

DMA is therefore considered one of the most suitable methods for quantifying

material damping, particularly in fibre-reinforced composites.

## 2.5.2 Logarithmic Decrement

Logarithmic decrement is a classical time-domain technique used to estimate the damping ratio of a system that can be approximated as a SDOF oscillator. It evaluates how the amplitude of free vibrations decays over time following an initial displacement or impulse. This decay occurs due to internal and external energy dissipation mechanisms.

The method involves measuring the amplitude of two successive peaks,  $x_n$  and  $x_{n+1}$ , in the displacement-time response of the system. The logarithmic decrement,  $\Delta$ , is then calculated using the natural logarithm of their ratio [41]:

$$\Delta = \ln \left( \frac{x_n}{x_{n+1}} \right) \quad (2.15)$$

Once  $\Delta$  is known, the damping ratio,  $\zeta$ , can be approximated for lightly damped systems using the following expression:

$$\zeta \approx \frac{\Delta}{\sqrt{4\pi^2 + \Delta^2}} \quad (2.16)$$

This approach is particularly suited for systems with low damping (i.e., underdamped responses), where oscillations persist over several cycles, allowing multiple peak comparisons to improve accuracy. It is relatively simple to implement and requires only displacement measurements, making it appealing for field testing or systems without access to advanced instrumentation.

However, the accuracy of the method deteriorates in highly damped systems, where oscillations decay too rapidly to yield sufficient data, or in noisy

## Chapter 2. Fundamentals of Damping

environments where peak detection becomes unreliable. Furthermore, it assumes linear behaviour and that the system conforms well to an SDOF approximation, conditions not always met in composite structures with complex damping characteristics.

Due to the influence of boundary conditions and external losses in experimental setups, particularly when dealing with composite specimens, this method was not adopted for further evaluation within this thesis.

### 2.5.3 Half-Power Bandwidth Method

The half-power bandwidth method is a frequency-domain approach used to estimate the damping ratio of a system by analysing its Frequency Response Function (FRF) in the vicinity of a resonance peak [102]. It is grounded in the observation that damping affects the sharpness—or bandwidth—of the resonance peak: greater damping results in a broader peak, while lower damping produces a sharper response.

The method determines the damping ratio,  $\zeta$ , by identifying the frequencies  $f_1$  and  $f_2$  at which the system's response amplitude falls to  $\frac{1}{\sqrt{2}}$  (approximately 70.7%) of the peak amplitude, corresponding to a reduction of 3 dB in power. These points define the so-called “half-power” frequencies around the resonant frequency  $f_n$ . The damping ratio is then approximated by:

$$\zeta \approx \frac{f_2 - f_1}{2f_n} = \frac{\Delta f}{2f_n} \quad (2.17)$$

This method is particularly suitable for lightly damped systems with well-separated modal peaks, where resonance curves are clearly defined and not influenced by modal overlap. It is widely used in experimental modal testing due to its simplicity and minimal computational requirements.

## Chapter 2. Fundamentals of Damping

To implement the method, a harmonic excitation is applied while sweeping across a frequency range encompassing  $f_n$ , and the FRF is measured. A high frequency resolution is essential to precisely identify  $f_1$ ,  $f_2$ , and  $f_n$ , especially in systems with narrow bandwidths or closely spaced modes.

Despite its utility, the half-power bandwidth method has several limitations. It assumes linear system behaviour and distinct, non-overlapping modes—conditions that may not hold in composite structures with distributed damping, geometric complexity, or non-linear responses. Moreover, if the frequency resolution is insufficient, the half-power points may be misidentified, leading to inaccurate damping estimates.

Due to the potential sensitivity of this method to external factors such as boundary condition effects and noise, which can distort the measured FRF, this approach was not selected for further analysis within this thesis. Nonetheless, it remains a foundational tool in dynamic testing for preliminary modal characterisation. An illustration of the method is provided in Figure 2.7, which shows how the damping ratio is inferred from the width of the resonance peak.

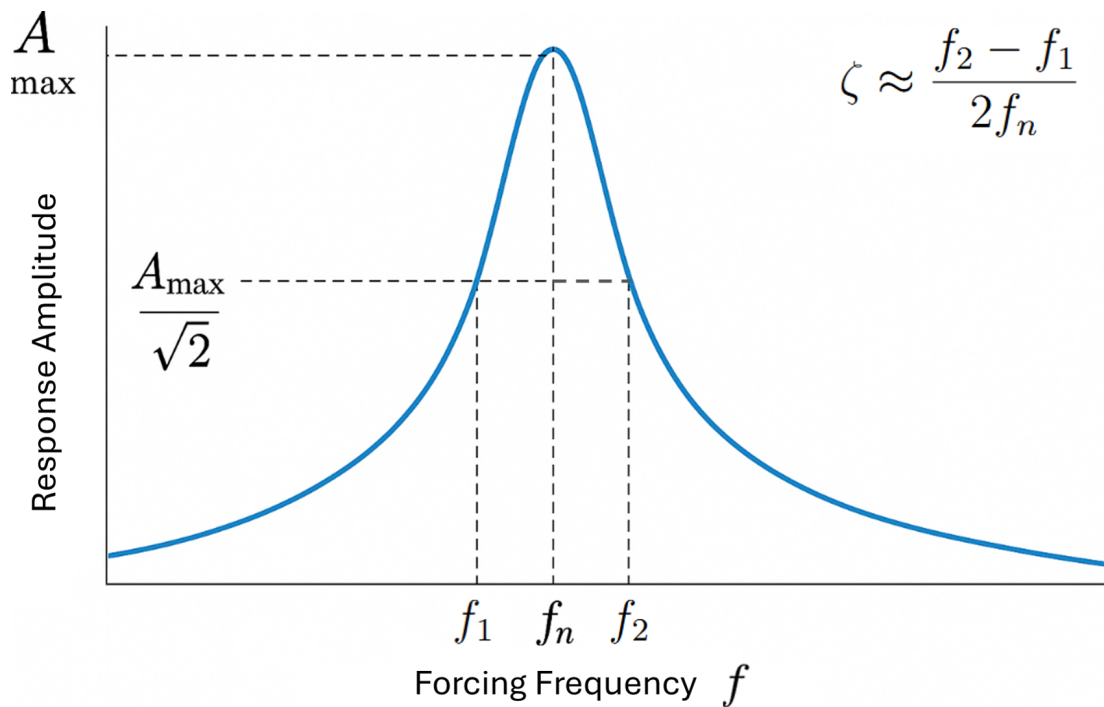


Figure 2.7: Half-power bandwidth approach, illustrating damping estimation from resonance peak width (adapted from [103]).

The previously discussed models offer practical methods for quantifying the damping of an SDOF system, thereby aiding in the design and analysis of structures. The following models described may be used for MDOF systems.

### 2.5.4 Operational Modal Analysis (OMA)

OMA is a non-intrusive technique used to identify the modal properties, natural frequencies, damping ratios, and mode shapes of structures under their actual operating conditions. Unlike EMA, which will be discussed next, OMA relies exclusively on the structure’s response to ambient or operational excitations, which are unmeasured and assumed to be broadband and stochastic in nature [104].

OMA is particularly useful for systems that are difficult or impractical to excite

## Chapter 2. Fundamentals of Damping

artificially, such as wind turbine blades in situ, large civil structures, or machinery in continuous operation [105]. The method assumes that the excitation (e.g., wind, wave loading, or ground motion) excites a sufficiently wide frequency range and that the structure behaves as a linear, time-invariant system during the measurement period [106].

Only the output responses are recorded, typically using accelerometers or laser vibrometers, and modal parameters are extracted using advanced stochastic signal processing techniques. Common methods include:

- **Stochastic Subspace Identification (SSI):** A time-domain algorithm that estimates system matrices from output-only measurements, particularly effective in noisy environments or when modes are closely spaced [107].
- **Frequency Domain Decomposition (FDD):** A frequency-domain technique that uses singular value decomposition of the output spectral density matrix to isolate modal contributions [108].
- **Natural Excitation Technique (NExT):** Utilises the cross-correlation of ambient responses to reconstruct the system's impulse response, enabling further modal identification [109].

The extracted modal shapes are typically unscaled due to the unknown excitation, meaning modal masses cannot be directly calculated [110]. However, the method provides high-quality estimates of frequency and damping, especially when excitation is broad and the signal-to-noise ratio is sufficient [111].

OMA offers several advantages:

- Non-intrusive and cost-effective, requiring no artificial excitation [112].

## Chapter 2. Fundamentals of Damping

- Capable of capturing the true dynamic behaviour of a structure under realistic loading [113].
- Particularly suitable for continuous structural health monitoring of infrastructure and rotating machinery [114].

However, it also presents limitations. The reliance on unknown excitation introduces uncertainty, particularly in damping estimation. Modal properties may vary with excitation amplitude, and insufficient excitation bandwidth may result in undetected modes [110]. Therefore, careful sensor placement, noise filtering, and advanced algorithmic post-processing are essential for reliable results [111].

For wind turbine applications, OMA is often employed for in-field monitoring or in conjunction with EMA to validate dynamic models under operational conditions. Its ambient, output-only nature makes it a valuable tool in scenarios where replicating operational loads in a laboratory setting would be impractical or unrepresentative [113]. However, given that controlled input excitation is available in the present study, EMA is adopted instead. EMA enables more accurate and scalable characterisation of modal parameters, including mode shapes and damping ratios, by leveraging known input–output relationships. The following section details the EMA methodology used within this thesis.

### **2.5.5 Experimental Modal Analysis**

EMA is a comprehensive approach for characterising the dynamic behaviour of systems with multiple degrees of freedom (MDOF) [115]. It involves decomposing the overall structural response into individual natural modes of vibration, with each mode defined by a natural frequency, damping ratio, and mode shape, the spatial pattern of vibration corresponding to that

## Chapter 2. Fundamentals of Damping

frequency [56]. This modal decomposition is key for identifying potential resonant frequencies and understanding how different parts of a structure contribute to its overall dynamic behaviour. Such insights enable the design of structures that avoid critical operating conditions and enhance performance.

In practice, EMA requires controlled excitation of the structure using known input forces, such as those from impact hammers, electrodynamic shakers, or other actuators. The resulting vibrational response is measured using an array of sensors, such as accelerometers, strain gauges, or laser vibrometers, placed strategically across the structure. These measurements are then used to construct the Frequency Response Function (FRF), which expresses the relationship between the applied input force and the measured response (e.g., displacement or acceleration) across a frequency range [116].

The identification of modal parameters from the FRF is typically performed using frequency-domain techniques, including:

- **PolyMAX (or pLSCF):** A robust and widely used method for modal parameter extraction that fits polynomial models to the FRF data to isolate modes, even in the presence of closely spaced frequencies [117, 118].
- **Circle Fit and Peak-Picking:** Simpler frequency-domain methods suitable for well-separated, lightly damped modes, though less effective for complex systems [116].

While EMA is a powerful and well-established method, it requires careful calibration, sensor placement, and high-quality excitation signals. It may be limited by environmental noise, nonlinear behaviour, or difficulty exciting all relevant modes [119]. However, when executed correctly, EMA offers detailed and repeatable insight into structural dynamics, making it invaluable for

## Chapter 2. Fundamentals of Damping

structural design and validation in fields such as aerospace, civil engineering, and renewable energy.

In the context of this thesis, EMA was selected over OMA due to the availability of controlled excitation and the need for precise, scalable damping characterisation across a range of loading conditions. A summary comparison between EMA and OMA is presented in Table 2.1, highlighting the key differences in methodology, applicability, and limitations [110].

Table 2.1: Comparison of EMA and OMA

Feature	EMA	OMA
Excitation	Known, controlled (e.g., hammer, shaker)	Unknown, ambient (e.g., wind, vibration, traffic)
Measurements	Input and output	Output only
Conditions	Laboratory or controlled environment	In-service or field conditions
Mode Shape Scaling	Fully scaled; modal mass identifiable	Unscaled; modal mass not identifiable
Applications	Design validation, structural tuning, benchmarking	Structural health monitoring, large infrastructure
Advantages	High precision and full modal parameter recovery	Non-intrusive, realistic loading, field-compatible
Limitations	May not reflect real-world conditions; setup-intensive	Requires broadband excitation and advanced processing

**Note:** EMA is preferred when controlled input is available, whereas OMA is ideal when testing must be performed under operational conditions.

### **2.5.6 Critical Comparison of Experimental Damping Evaluation Methods**

The reviewed techniques span from material-level characterisation to full structural dynamic analysis, each offering distinct strengths and limitations in the context of damping evaluation for fibre-reinforced composites. A summary of these methods is provided in Table 2.2, highlighting their relative applicability to composite material research and wind turbine blade dynamics [100, 102, 104, 116, 120].

Table 2.2: Comparison of Experimental Methods for Damping Evaluation

Method	Strengths	Limitations
DMA	High-resolution viscoelastic property measurement; frequency and temperature control; ideal for assessing fibre-matrix interactions.	Limited to small specimens; fixed boundary conditions; excludes global structural effects.
Logarithmic Decrement	Simple and low-cost for lightly damped SDOF systems; suitable for quick field tests.	Assumes linearity; inaccurate for complex or highly damped systems; not suitable for distributed composite damping.
Half-Power Bandwidth	Enables damping estimation directly from FRFs; requires minimal post-processing.	Requires clearly defined resonance peaks; unreliable for overlapping modes or non-linear behaviour.
OMA	Captures in-service dynamic behaviour; scalable to large structures; non-intrusive.	Unscaled modal shapes; depends on excitation quality; limited accuracy in damping ratio estimation.
EMA	Enables full modal parameter recovery using controlled excitation; scalable to complex structures; supports validation of numerical models.	Laboratory-based; requires careful setup and instrumentation; may not replicate operational loading.

**Note:** Methods are evaluated with respect to their applicability to composite damping characterisation and relevance to wind turbine blade materials.

**Selection Rationale for DMA and EMA:**

DMA was selected for its unparalleled ability to isolate and quantify material-level damping mechanisms, such as matrix viscoelasticity and fibre–matrix interfacial slip, under controlled frequency and temperature

## Chapter 2. Fundamentals of Damping

conditions [100]. This aligns with the thesis's emphasis on intrinsic damping phenomena in composite materials. While DMA is limited in representing structural boundary effects, these shortcomings are addressed through its combination with system-scale methods.

EMA was preferred over OMA and simpler SDOF approaches due to its ability to yield fully scaled modal parameters and detailed mode shapes via known input–output relationships. This precision is essential for validating finite element models and understanding the dynamic performance of composite blade sections. Although laboratory-bound, EMA's controlled excitation minimises uncertainties arising from ambient disturbances, providing more repeatable and generalisable insights.

Logarithmic decrement and half-power bandwidth methods were excluded from further use due to their limited resolution and inability to account for the multi-scale, frequency-dependent nature of damping in fibre-reinforced composites [102]. These methods overly simplify the complex interplay of dissipation mechanisms in laminated structures.

In summary, the complementary use of DMA and EMA bridges the micro-scale damping behaviour of composites with their macro-scale structural response. These two methods were therefore selected for further evaluation within Chapters 3 and 4, where they are examined in greater detail. This integrated methodology supports both the optimisation of composite materials and the development of reliable predictive models for wind turbine blade dynamics.

## **2.6 Expected Benefits from Improving Structural Damping Characterisation**

A key focus of this thesis has been the characterisation of the damping behaviour of unidirectional (UD) carbon fibre composites used in SGRE's offshore wind turbine blades. While the primary emphasis is on these specific materials, the experimental methodologies developed are broadly applicable to other composite systems.

This section shifts the focus from direct material characterisation to how the experimentally derived damping data, obtained using techniques such as DMA and EMA, can be integrated into established theoretical models. These models, including those by Ni–Adams, Adams–Maheri, and Tsai–Chang, use directional damping inputs to predict the behaviour of multi-orientation laminate systems under dynamic loading conditions.

The distinct nature of each experimental method influences how damping is captured. EMA, as applied in this thesis, primarily measured damping in the fibre direction due to the exceptionally high aspect ratio of the specimens—up to 400 for the 2 m long samples described in Chapter 4. This geometric configuration concentrates strain energy almost exclusively along the fibre axis, resulting in negligible contributions from transverse and through-thickness directions. By contrast, the DMA tests presented in Chapter 3 used much smaller specimens, with aspect ratios as low as 12.5 for 2 mm thick and 50 mm long samples. This allowed for a more distributed strain energy profile, capturing significant damping contributions from off-axis and matrix-dominated directions. Together, these methods provide complementary insight into the directional dependency of damping behaviour within the composite.

## Chapter 2. Fundamentals of Damping

By incorporating these experimental findings into established numerical frameworks, the models can more accurately predict energy dissipation in layered laminates, leading to improved design and optimisation of composite layups for enhanced performance and fatigue resistance in wind turbine blades.

The models referenced in this section are presented below, with full derivations provided in Appendix A.

### 2.6.1 Historical Model Development for Multi-Orientation Composite Laminates

**Ni-Adams Model:** The Ni-Adams model was one of the early attempts to capture the damping behaviour of multi-layer composite laminates developed in 1984 [121]. This model extends basic damping approaches by incorporating not only in-plane properties but also flexural and interlaminar effects. In the Ni-Adams formulation, the overall damping in the fibre, transverse, and shear directions (denoted as  $\psi_x$ ,  $\psi_y$ , and  $\psi_{xy}$ , respectively) is expressed as a summation over half the number of layers. Each term in these summations combines the transformed reduced stiffness components (represented by  $\bar{Q}$ ) with cosine and sine functions (denoted by  $c$  and  $s$ ) that account for the fibre orientation. Scaling factors such as  $\psi_L$ ,  $\psi_T$ , and  $\psi_{LT}$  are introduced to represent the specific damping capacities derived from unidirectional experimental data. This model provides a systematic framework for converting directional stiffness and damping measurements into predictive damping values, thereby accounting for the layered structure of composite laminates. The key equations describing energy dissipation are given by:

## Chapter 2. Fundamentals of Damping

$$\psi_x = \frac{8\psi_L}{C_{11}^* N^3} \sum_{k=1}^{N/2} [c^2(\bar{Q}_{11}^k C_{11}^* + \bar{Q}_{12}^k C_{12}^* + \bar{Q}_{16}^k C_{16}^*)] \times [c^2 C_{11}^* + cs C_{16}^*] W_k \quad (2.18)$$

$$\psi_y = \frac{8\psi_T}{C_{11}^* N^3} \sum_{k=1}^{N/2} [s^2(\bar{Q}_{11}^k C_{11}^* + \bar{Q}_{12}^k C_{12}^* + \bar{Q}_{16}^k C_{16}^*)] \times [s^2 C_{11}^* - cs C_{16}^*] W_k \quad (2.19)$$

$$\psi_{xy} = \frac{8\psi_{LT}}{C_{11}^* N^3} \sum_{k=1}^{N/2} [cs(\bar{Q}_{11}^k C_{11}^* + \bar{Q}_{12}^k C_{12}^* + \bar{Q}_{16}^k C_{16}^*)] \times [2cs C_{11}^* - (c^2 - s^2) C_{16}^*] W_k \quad (2.20)$$

where:

- $\psi_x$ ,  $\psi_y$ , and  $\psi_{xy}$  are the predicted total damping values in the longitudinal (fibre), transverse, and in-plane shear directions of the laminate, respectively;
- $\psi_L$ ,  $\psi_T$ , and  $\psi_{LT}$  are the specific damping capacities measured from unidirectional (UD) composite tests in the corresponding directions;
- $\bar{Q}_{ij}^k$  are the transformed reduced stiffness components of the  $k$ th ply in the laminate, accounting for fibre orientation;
- $C_{ij}^*$  are the effective stiffness terms of the overall laminate, determined from the stiffness matrix of the full layup;
- $N$  is the total number of plies in the laminate;
- $W_k$  is a weighting factor for the  $k$ th ply, typically associated with its thickness or distance from the laminate mid-plane;

## Chapter 2. Fundamentals of Damping

- $c = \cos \theta_k$  and  $s = \sin \theta_k$ , where  $\theta_k$  is the fibre orientation angle of the  $k$ th ply; the term  $cs$  denotes the product  $\cos \theta_k \cdot \sin \theta_k$
- The notation  $cs$  denotes the product  $\cos \theta_k \cdot \sin \theta_k$

**Adams-Maheri Model:** The Adams-Maheri model builds on the Ni-Adams approach by further refining the representation of damping in composite laminates [122] developed in 1994. In this model, additional terms are incorporated to account for the effects of boundary conditions and specific experimental setups. While retaining the fundamental idea of summing contributions from the transformed stiffness components, the Adams-Maheri formulation also integrates the original (untransformed) stiffness components, denoted as  $Q$ , into the energy dissipation equations. This modification enhances the model's ability to accurately represent the interactions between composite layers under realistic testing conditions. As a result, the equations for  $\psi_x$ ,  $\psi_y$ , and  $\psi_{xy}$  derived in the Adams-Maheri model offer improved predictive capabilities by more closely aligning with empirical observations of damping in anisotropic composite materials. The energy dissipation equations for the Adams-Maheri model are as follows:

$$\psi_x = \frac{8\psi_L}{C_{11}^* N^3} \sum_{k=1}^{N/2} [c^2(c^2 C_{11}^* + s^2 C_{12}^* + cs C_{16}^*)] \times (Q_{11}^k C_{11}^* + Q_{12}^k C_{12}^* + Q_{16}^k C_{16}^*) W_k \quad (2.21)$$

$$\psi_y = \frac{8\psi_T}{C_{11}^* N^3} \sum_{k=1}^{N/2} [s^2(s^2 C_{11}^* + c^2 C_{12}^* - cs C_{16}^*)] \times (Q_{11}^k C_{11}^* + Q_{12}^k C_{12}^* + Q_{16}^k C_{16}^*) W_k \quad (2.22)$$

## Chapter 2. Fundamentals of Damping

$$\psi_{xy} = \frac{8\psi_{LT}}{C_{11}^* N^3} \sum_{k=1}^{N/2} [cs(2csC_{11}^* - 2csC_{12}^* - (c^2 - s^2)C_{16}^*)] \times (Q_{11}^k C_{11}^* + Q_{12}^k C_{12}^* + Q_{16}^k C_{16}^*) W_k \quad (2.23)$$

where the same terms apply as in the Ni-Adams model.

**Tsai-Chang Model:** The Tsai-Chang model, developed in 2009, represents a further advancement in the damping characterisation of composite laminates by addressing the complexities of multi-layer, multi-orientation systems [123]. The Tsai-Chang model includes comprehensive terms to account for in-plane stresses across different fibre orientations. This is achieved by extending the summations over the transformed stiffness components and introducing additional terms that capture both longitudinal and transverse effects. The resulting formulation provides a more holistic view of energy dissipation in layered composites, thereby enabling more accurate simulations of material behaviour under cyclic loading. This enhanced model is particularly valuable for predicting the dynamic response of complex composite systems, ultimately guiding the optimisation of composite layups in applications such as wind turbine blades. The model equations are:

$$\begin{aligned} \psi_x = \frac{8\psi_L}{C_{11}^* N^3} \sum_{k=1}^{N/2} [c^2 C_{11}^* + s^2 C_{12}^* + cs C_{16}^*] \times [c^2 (\bar{Q}_{11}^k C_{11}^* + \bar{Q}_{12}^k C_{12}^* + \bar{Q}_{16}^k C_{16}^*) \\ + s^2 (\bar{Q}_{12}^k C_{11}^* + \bar{Q}_{22}^k C_{12}^* + \bar{Q}_{26}^k C_{16}^*) + 2cs (\bar{Q}_{16}^k C_{11}^* + \bar{Q}_{26}^k C_{12}^* + \bar{Q}_{66}^k C_{16}^*)] W_k \end{aligned} \quad (2.24)$$

## Chapter 2. Fundamentals of Damping

$$\begin{aligned} \psi_y = & \frac{8\psi_T}{C_{11}^* N^3} \sum_{k=1}^{N/2} [s^2 C_{11}^* + c^2 C_{12}^* - cs C_{16}^*] \times [s^2 (\bar{Q}_{11}^k C_{11}^* + \bar{Q}_{12}^k C_{12}^* + \bar{Q}_{16}^k C_{16}^*) \\ & + c^2 (\bar{Q}_{12}^k C_{11}^* + \bar{Q}_{22}^k C_{12}^* + \bar{Q}_{26}^k C_{16}^*) + 2cs (\bar{Q}_{16}^k C_{11}^* + \bar{Q}_{26}^k C_{12}^* + \bar{Q}_{66}^k C_{16}^*)] W_k \end{aligned} \quad (2.25)$$

$$\begin{aligned} \psi_{xy} = & \frac{8\psi_{LT}}{(C_{11}^* N)^3} \sum_{k=1}^{N/2} [2cs C_{11}^* - 2cs C_{12}^* - (c^2 - s^2) C_{16}^*] \times [cs (\bar{Q}_{11}^k C_{11}^* + \bar{Q}_{12}^k C_{12}^* + \bar{Q}_{16}^k C_{16}^*) \\ & - cs (\bar{Q}_{12}^k C_{11}^* + \bar{Q}_{22}^k C_{12}^* + \bar{Q}_{26}^k C_{16}^*) - (c^2 - s^2) (\bar{Q}_{16}^k C_{11}^* + \bar{Q}_{26}^k C_{12}^* + \bar{Q}_{66}^k C_{16}^*)] W_k \end{aligned} \quad (2.26)$$

where the same terms apply as previous models.

### 2.6.2 Benefits for Wind Turbine Blade Design

Leveraging the detailed insights provided by the experimental damping characterisation developed in this thesis and incorporating them into existing models enables the optimisation of wind turbine blade designs. By accurately predicting how damping behaviour varies across individual composite layers, specifically for the unidirectional (UD) carbon fibre composites used in SGRE's offshore wind turbine blades, it is possible to tailor composite layups to address specific dynamic challenges. This approach allows for the strategic adjustment of fibre orientation, resin selection, and layer stacking sequences to effectively control vibrations, reduce fatigue loads, and redistribute stresses within critical regions of the blade.

Moreover, the damping results obtained in this research, as well as the existing 2D models, form the foundation for the development of

## Chapter 2. Fundamentals of Damping

comprehensive three-dimensional numerical models. These existing models, which incorporate the directional damping characteristics measured via DMA and EMA, can be integrated into finite element analysis tools to simulate the complex behaviour of multi-layer, multi-orientation composites under realistic cyclic loading conditions. Such predictive capabilities are essential for guiding design modifications that enhance blade performance and durability, particularly in the demanding offshore environment.

Furthermore, these advanced models facilitate the investigation of trade-offs between material performance and manufacturing constraints, ensuring that improvements in dynamic behaviour are achieved without compromising cost-effectiveness or manufacturability. Overall, the models and experimental findings presented support the development of more efficient, reliable, and optimised wind turbine blades, ultimately contributing to longer service lives, reduced maintenance requirements, and improved energy production.

### 2.7 Chapter Summary

This chapter has established a comprehensive framework for understanding damping in wind turbine blade materials by integrating theoretical principles, advanced materials, and experimental approaches. Key points covered include:

- **Fundamental Concepts:** An overview of damping as a key property for dissipating vibrational energy, enhancing structural stability, and extending the operational lifespan of mechanical systems, with a particular focus on wind turbine blades.
- **Material Transitions:** A discussion on the evolution from traditional materials, such as glass fibre-reinforced polymers, to advanced

## Chapter 2. Fundamentals of Damping

composites like carbon fibre composites, highlighting the challenges posed by their anisotropic behaviour.

- **Damping Mechanisms:** An examination of various damping models, including viscous, hysteretic, Coulomb, aerodynamic, and viscoelastic damping, that describe energy dissipation at both the microscopic and macroscopic levels.
- **Experimental Techniques:** A review of methods (DMA, logarithmic decrement, half-power bandwidth, and EMA) employed to evaluate damping properties, including their key parameters, advantages, and limitations. Both DMA and EMA were the selected techniques for further investigation within this thesis.
- **Advanced Damping Models:** A detailed presentation of existing models such as the Ni–Adams, Adams–Maheri, and Tsai–Chang models, which facilitate the prediction of the dynamic behaviour of multi-orientation composite laminates.
- **Integration with Computational Models and Future Research:** An outline of how the damping results from this thesis will contribute to the development of three-dimensional computational models, thereby guiding future design improvements and research directions.
- **Application to Wind Turbine Blade Design:** Insights on how the advanced damping models and experimental findings can be utilised to predict damping properties, optimise composite layups, enhance vibration control, reduce fatigue loads, and ultimately extend the lifespan of wind turbine blades.

Overall, this chapter has provided the essential theoretical and experimental foundation required for the subsequent analysis and optimisation of damping

## Chapter 2. Fundamentals of Damping

in wind turbine blades, setting the stage for further investigations into enhanced material performance and structural reliability in demanding offshore environments.

## **Chapter 3**

# **Dynamic Mechanical Analysis for Damping Estimation**

### **3.1 DMA Introduction**

DMA is a widely adopted experimental technique used to characterise the viscoelastic behaviour of materials [100, 124]. Developed in the 1960s in response to the emerging need for dynamic testing of polymers and other viscoelastic materials, DMA was developed to overcome the limitations of static testing methods and to capture material responses over a range of frequencies and temperatures. Today, DMA is extensively employed in sectors such as renewable energy, aerospace, and civil engineering, where both mechanical stability and efficient energy dissipation are critical for long-term durability, to evaluate the performance of materials like polymers, metals, and composites under dynamic loading conditions. By observing the phase lag between applied stress and resultant strain, DMA helps engineers predict how materials will behave when exposed to forces over time, making it invaluable for structures subjected to repetitive loading [125–128].

### Chapter 3. Dynamic Mechanical Analysis for Damping Estimation

In operation, DMA works by applying a controlled oscillatory force to a material sample and measuring the resulting deformation. The force is applied in a sinusoidal manner, and the corresponding displacement is recorded with an optical displacement sensor, as shown in Figure 3.1, taken from [101]. By analysing the phase difference between the applied force and the measured deformation, the instrument separates the response into two components: the in-phase component, which is used to calculate the storage modulus ( $E'$ ) representing the elastic (recoverable) deformation, and the out-of-phase component, which is used to determine the loss modulus ( $E''$ ) reflecting the energy dissipated as heat during cyclic loading [101, 129, 130]. The ratio of these two moduli, known as the loss factor ( $\eta$ ), provides a direct measure of a material's damping capability, which is particularly important in applications where controlling vibration and energy dissipation is of high importance [131]. Figure 3.2 shows the relationship between these parameters.

### Chapter 3. Dynamic Mechanical Analysis for Damping Estimation

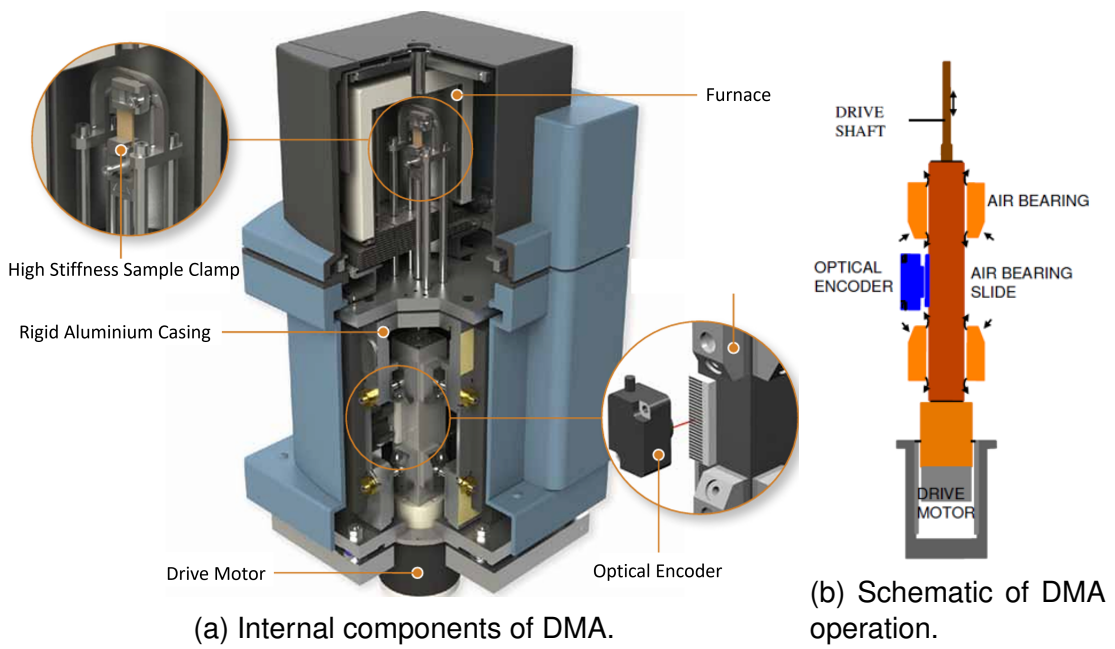


Figure 3.1: (a) Cutaway illustration showing key internal components of the DMA system and (b) high-level schematic of DMA operation (adapted from [101]).

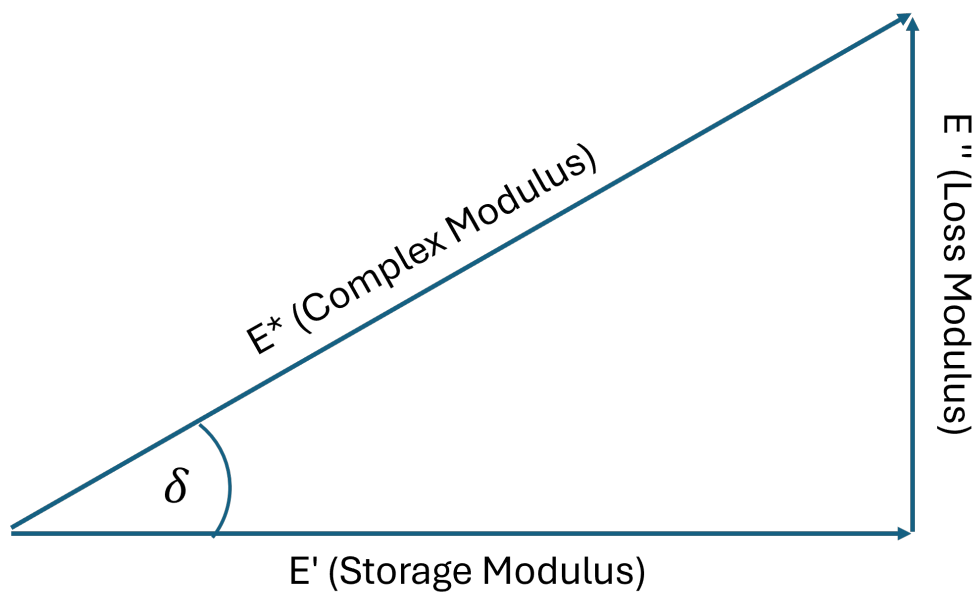


Figure 3.2: Graphical representation of the complex modulus, illustrating how the storage modulus ( $E'$ ), loss modulus ( $E''$ ), and the resultant complex modulus ( $E^*$ ) relate through the phase angle  $\delta$ .

### Chapter 3. Dynamic Mechanical Analysis for Damping Estimation

In the context of this work, DMA is particularly valuable for evaluating the viscoelastic properties of materials used in wind turbine blades. For isotropic materials such as metals or certain polymers, DMA can accurately capture dynamic performance under varying loads [132]. However, applying DMA to anisotropic materials like carbon fibre-reinforced polymers (CFRP) is more complex because properties vary with load orientation. Typically, carbon fibre composites exhibit high stiffness and lower damping along the fibre direction, while the matrix-dominated transverse direction demonstrates higher energy dissipation with less stiffness [133, 134].

Because conventional DMA often measures bulk properties without fully isolating directional dependencies, the output may represent a combined damping response rather than an individual contribution from each principal direction [135]. This can introduce inaccuracies when predicting real-world behaviour in CFRP, where anisotropy heavily influences performance. Consequently, advanced experimental setups or supplementary computational techniques are required to capture the full scope of anisotropic damping and yield more reliable characterisations of how these materials respond to dynamic loading [136–138].

This thesis integrates Dynamic Mechanical Analysis (DMA) with Finite Element Analysis (FEA) to address the limitations of conventional DMA in capturing directional damping properties. FEA supplements the experimental data by quantifying the strain energy distribution within the test sample under DMA operating conditions, thereby enabling a more comprehensive characterisation of material behaviour. This combined experimental and numerical approach enhances predictions of composite performance under real-world dynamic conditions [139] and is particularly valuable for wind turbine blades, where directional strength and damping are important for

## Chapter 3. Dynamic Mechanical Analysis for Damping Estimation

long-term structural stability and performance.

In summary, DMA is a powerful tool for evaluating the dynamic mechanical properties of materials. The development was driven by the need to understand the complex behaviour of viscoelastic materials under cyclic loading, and while it has become a standard technique, there are limitations in assessing anisotropic materials which can be mitigated by integrating computational methods such as FEA as use of DMA on it's own would lead to over predictions of the damping capacity of the material in its fibre direction. This chapter introduces DMA, discusses the historical context and relevance in dynamic characterisation, acknowledges limitations when it comes to the characterisation of anisotropic materials, and presents a novel approach for enhancing damping estimation in composite materials for applications in wind turbine blade design.

### **3.2 Background of DMA**

DMA is a widely used technique for characterising the viscoelastic behaviour of materials. By applying oscillatory forces to a specimen and measuring its response, DMA provides insights into how materials behave under dynamic loading conditions, including storing and dissipating energy [29, 137]. DMA plays a pivotal role in evaluating materials' mechanical performance, especially in relation to their stiffness, damping, and energy dissipation characteristics. As industries continue to innovate in materials science, DMA remains an essential tool for characterising materials performance under real-world conditions [40, 42].

This section outlines the principles of DMA, explores applications in both research and industry and examines the key challenges and limitations when

testing complex materials such as composites.

### **3.2.1 History of DMA in Composite Materials**

The development of DMA has played a significant role in advancing our understanding of the viscoelastic properties of polymers and composite materials. Over the decades, it has become an essential tool for both academic research and industrial applications.

#### **3.2.1.1 Early Experimental Approaches**

The 1950s marked the introduction of fundamental principles related to polymer viscoelasticity [140]. During this time, researchers began to explore how polymeric materials responded to stress over time, laying the groundwork for the viscoelastic theory. In his seminal work, Ferry [141] introduced the concept of frequency-dependent material behaviour, which led to the development of the terms storage modulus and loss modulus. These ideas were foundational to the later development of DMA as they allowed researchers to quantify how materials store and dissipate energy under oscillatory loading.

Ferry's contributions, alongside works such as *Introduction to Polymer Viscoelasticity* by Aklonis et al. [140], helped establish the time-temperature superposition principle and other key concepts that remain central to DMA applications. These early experiments provided insights into how the mechanical properties of polymers change with varying frequencies and temperatures, which later formed the basis for modern DMA techniques.

### **3.2.1.2 Development of Standardised Testing and Equipment**

In the 1980s, the widespread commercialisation of DMA equipment allowed for the technique to be more accessible and widely applied across both academic and industrial sectors. TA Instruments released the first commercial implementation in the form of the 980 DMA, introduced in 1976 [142]. These developments led to the establishment of standardised testing modes, such as three-point bending, dual cantilever, and tension, which improved the accuracy and reliability of mechanical property measurements for various materials, including composites.

The commercialisation of DMA in the 1980s not only made the technique more widely accessible but also facilitated its integration with other complementary testing methods. Techniques such as Differential Scanning Calorimetry (DSC), Thermogravimetric Analysis (TGA), and ThermoMechanical Analysis (TMA) began to be employed alongside DMA, allowing for a more comprehensive characterisation of polymeric and composite materials under dynamic loading conditions [143–145].

### **3.2.1.3 Refinement in Analysis Techniques**

As the use of DMA became more widespread, researchers refined its analytical capabilities by incorporating advanced techniques such as time-temperature superposition (TTS). TTS, initially explored by Ferry and later expanded upon by Menard [146], enables the extrapolation of material behaviour over extended periods by shifting data from various temperatures to a reference temperature to create a comprehensive master curve. This method is particularly useful for predicting the long-term mechanical performance of polymers and composites, especially under sustained loads or cyclic stresses, by providing critical insights into fatigue and creep

## Chapter 3. Dynamic Mechanical Analysis for Damping Estimation

behaviours under real-world operating conditions [146].

However, while the approach demonstrated by Georgantzinis et al. [147] offers a precise quantification of energy loss due to damping under dynamic loading, it has limitations in capturing the directional damping behaviour of anisotropic composite materials. To overcome this, strain energy considerations have been integrated into DMA, providing essential data that enhance our evaluation of composite durability and dynamic mechanical properties [132]. By combining TTS with strain energy modelling, these refinements enable a more thorough understanding of material longevity and energy dissipation performance.

### **3.2.1.4 Advancements in Commercial DMA Equipment**

As DMA technology evolved, commercial equipment has advanced in precision and functionality, enabling more complex and reliable material testing for research and industrial applications. One of the most common models, the TA Instruments Q800, introduced a suite of features aimed at enhancing the accuracy and flexibility of DMA testing [148]. The Q800 utilises non-contact, linear drive technology and air-bearing support, providing precise control over stress and strain in modes such as tension, shear, and compression. These features, combined with its broad operational temperature range of  $-150^{\circ}\text{C}$  to  $600^{\circ}\text{C}$ , have made the Q800 suitable for various applications, including studies focused on high-performance materials in aerospace and renewable energy sectors [148–150]. The DMA Q800 can be seen in Figure 3.3.

### Chapter 3. Dynamic Mechanical Analysis for Damping Estimation



Figure 3.3: TA DMA Q800 - In Strathclyde University Lab

The Q850 model, which followed the Q800, builds on these capabilities with expanded environmental controls, including humidity options and an extended temperature range, enhancing the adaptability for specific applications [151, 152]. While the Q850 offers additional features, the Q800 remains a well-regarded instrument in both academic and industrial settings due to generating accurate and reproducible data across a variety of testing conditions. In the present work, the TA Q800 was selected due to its availability and established performance record, providing a reliable basis for characterising the dynamic mechanical properties of composite materials under diverse testing scenarios [132].

### 3.2.2 Principles and Material Response in DMA

DMA is an essential experimental technique for investigating the viscoelastic behaviour of materials under dynamic loading [138]. The fundamental operational principle behind DMA involves applying oscillatory forces to a material and measuring the mechanical response. A vital outcome of this process is the phase lag ( $\delta$ ) between the applied stress and the resulting strain. This phase lag reveals the material's capacity to both store energy (elastic response) and dissipate it (viscous response), making it critical for understanding damping, stiffness, and energy dissipation in various engineering applications [153].

**Key Parameters in DMA** Several key parameters are utilised to describe a material's viscoelastic behaviour:

- **Storage Modulus ( $E'$ ):** This represents the elastic portion of the deformation, quantifying how much energy is stored in the material during each loading cycle. A high storage modulus indicates greater stiffness, a desirable trait in structural applications where materials must resist deformation under load [40, 129].
- **Loss Modulus ( $E''$ ):** This reflects the viscous, non-recoverable deformation, corresponding to the energy dissipated as heat during cyclic loading. Materials with a higher loss modulus are better suited to applications where damping and energy dissipation are critical, such as in vibration control [42, 129].
- **Loss Factor ( $\eta$ ):** Also known as the damping factor, the loss factor is the ratio of the loss modulus to the storage modulus ( $\eta = \frac{E''}{E'}$ ). It measures a material's ability to convert mechanical energy into heat. A high loss factor indicates good damping performance, particularly in materials

### Chapter 3. Dynamic Mechanical Analysis for Damping Estimation

exposed to dynamic loads, such as wind turbine blades or automotive components [129, 153].

- **Phase Lag ( $\delta$ ):** The phase lag between the applied stress and the resulting strain provides direct insight into a material's viscoelastic properties. In a purely elastic material, stress and strain occur in phase ( $\delta = 0^\circ$ ), while in a purely viscous material, the strain lags the stress by  $90^\circ$ . Most viscoelastic materials display a phase lag between these extremes, reflecting a combination of energy storage and energy dissipation (typically as heat). This parameter is crucial for assessing how efficiently a material responds to dynamic forces and, in anisotropic materials such as composites, it can vary with direction, often exhibiting lower phase lag (closer to  $0^\circ$ ) along the fibre direction and higher phase lag (approaching  $90^\circ$ ) in the transverse direction [40].

**Stress-Strain Behaviour and Measurement Process** The stress-strain behaviour observed during DMA testing is essential for understanding how materials perform under real-world cyclic loading conditions. Viscoelastic materials exhibit both recoverable (elastic) and non-recoverable (viscous) deformations when subjected to oscillatory forces. It is possible to quantify how effectively a material stores and dissipates energy by analysing the phase lag ( $\delta$ ) between stress and strain, as shown in Figure 3.4

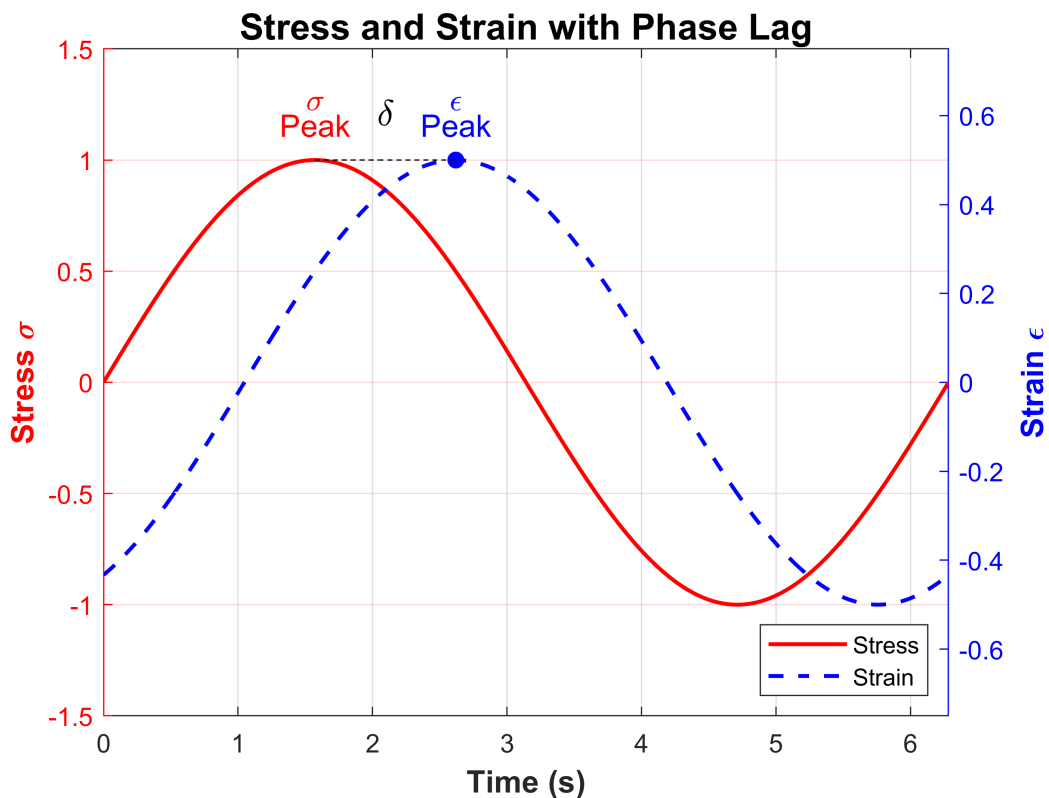


Figure 3.4: Stress and Strain with Phase Lag. The phase lag ( $\delta$ ) is the phase difference between the peak stress ( $\sigma$ ) and the peak strain ( $\epsilon$ ) - measured in degrees.

The TA Instruments Q800 DMA system employed in this research provides a high degree of control over stress application and strain measurement, which is vital for accurately characterising the viscoelastic properties of the composite materials under investigation. Specifically:

- **Controlled Stress Application:** The system’s electromagnetic drive mechanism delivers precisely regulated oscillatory forces, ensuring that stress is applied consistently across a wide range of materials [101].
- **Versatile Testing Configurations:** The Q800 accommodates various clamping geometries, such as three-point bending and tensile setups, thus enabling experimental conditions that closely mimic real-world

applications [101].

- **High-Resolution Displacement Measurement:** An integrated optical encoder captures minute displacements with exceptional resolution, which is critical for accurately measuring strain in materials exhibiting low deformation or high stiffness [101].

The dynamic modulus of a material, derived from the applied stress and resulting strain, helps to characterise the response under cyclic loading [125–127]. The phase lag ( $\delta$ ), which was graphically represented in Figure 3.4, is fundamental in evaluating a material's damping capacity. The  $\tan \delta$  (tangent of the phase lag) is often used to directly measure a material's ability to dissipate energy [40, 154].

A central parameter in DMA is the loss factor ( $\eta$ ), defined as:

$$\eta = \tan \delta = \frac{E''}{E'} \quad (3.1)$$

In line with this definition, the complex modulus can be considered as the summation of the storage and loss modulus. Loss factor is central to different models for describing the viscoelastic material behaviour, such as those mentioned in Section 2.4 [92, 94]. A higher loss factor signifies greater damping capability, which is important for materials subjected to repetitive stresses, like those experienced by wind turbine blades.

In summary, DMA provides an overview of how materials store and dissipate energy by analysing key dynamic parameters such as the storage modulus, loss modulus, loss factor, and phase lag. However, it is important to acknowledge that conventional DMA methods have limitations, particularly when applied to anisotropic materials like CFRP. The output typically represents a summation of multi-directional damping components rather than

## Chapter 3. Dynamic Mechanical Analysis for Damping Estimation

isolating directional properties, which is not the desired intent of the experimental methodology. Overcoming these challenges necessitates advanced experimental setups or supplementary computational techniques to assess material behaviour under dynamic conditions accurately.

### 3.2.2.1 Significance of Loss Factor and Its Relationship with Other Damping Metrics

The loss factor ( $\eta$ ) is critical for evaluating how effectively a material can convert mechanical energy into heat, reducing vibrations and improving the stability of structures under dynamic loads. Several other essential metrics of damping are closely related to the loss factor and help provide a fuller understanding of a material's damping characteristics [92, 153].

The relationship between the loss factor and other damping metrics is expressed as [41, 92, 153, 155]:

$$\eta = \frac{\psi}{2\pi} = \frac{E''}{E'} = \frac{\Delta}{\pi} = \tan \delta \approx \delta \quad (3.2)$$

where:

$\eta$  = Loss Factor

$\psi$  = Specific Damping Capacity

$E''$  = Loss Modulus

$E'$  = Storage Modulus

$\Delta$  = Logarithmic Decrement

$\tan \delta$  = Ratio of Loss Modulus to Storage Modulus

$\delta$  = Phase Angle

## Chapter 3. Dynamic Mechanical Analysis for Damping Estimation

These parameters are beneficial for selecting materials that exhibit optimal damping properties in dynamic engineering applications.

**Specific Damping Capacity ( $\psi$ ):** The ratio of the energy dissipated per cycle to the maximum potential energy stored in the system, providing a measure of a material's ability to damp vibrations [153].

**Logarithmic Decrement ( $\Delta$ ):** A measure of the rate at which free vibrations decay in a system, related to the loss factor by  $\eta = \Delta/\pi$ . A higher logarithmic decrement indicates greater damping capacity [92].

**Phase Angle ( $\delta$ ):** The phase angle represents the lag between stress and strain in a viscoelastic material, another useful measure of damping. For small damping values,  $\eta \approx \tan \delta \approx \delta$  [153].

**Moduli ( $E'$  and  $E''$ ):** The storage modulus ( $E'$ ) indicates the material's elastic properties, while the loss modulus ( $E''$ ) describes the energy dissipation as heat. The ratio of these values gives the loss factor, which is a primary indicator of damping [42].

### 3.2.3 Limitations and Challenges of DMA

While DMA is effective for characterising the viscoelastic behaviour of materials, it is not without its limitations, particularly when applied to anisotropic materials such as carbon fibre composites. For example, the accuracy of DMA results is highly dependent on sample geometry and preparation techniques; any inaccuracies in sample preparation can lead to significant inconsistencies in the measured properties [137]. Moreover, conventional DMA setups often have a limited operational range, meaning they may not fully replicate the complex conditions encountered in real-world

## Chapter 3. Dynamic Mechanical Analysis for Damping Estimation

applications, such as high-strain, high-temperature, or extreme frequency environments. The interpretation of DMA data also poses challenges; nonlinear viscoelastic behaviour, common in composites under certain loading conditions, requires advanced analytical techniques to be accurately understood [42]. Additionally, environmental factors including humidity, temperature fluctuations, and UV exposure can significantly affect material properties, complicating efforts to simulate actual service conditions [136].

Furthermore, conventional DMA methods fail to capture the full spectrum of directional damping behaviour for anisotropic materials like CFRP, where mechanical properties vary with direction. This is compounded by the fact that standard 3-point bending setups do not effectively isolate shear forces, especially in thick or multi-layered samples. This results in an incomplete characterisation of the material's response [40, 137].

### **3.3 Standard DMA method – influential factors on test results**

The primary objective of this research was to evaluate the reliability of DMA in determining the structural damping properties of materials used in wind turbines [156]. This section focuses on characterising the structural damping of a selected material. It was important to note that completely isolating structural damping was challenging due to the possibility of minor aerodynamic influences during testing, as tests could not be conducted in vacuum conditions due to the air bearing. Therefore, aerodynamic effects were not accounted for in this test process. Initially, the study explores how various factors, particularly sample geometry, influence DMA damping results, aiming to identify potential limitations in the methodology. By understanding

these variations and previously discussed limitations, the objective was to develop a more complete/physically realistic method for determining the damping properties of anisotropic materials using DMA.

### **3.3.1 Experimental Setup and Test Procedure**

The DMA tests were conducted using a three-point bend setup to accommodate the high-modulus nature of the carbon fibre composite samples. This mode was selected due to machine limitations in other configurations, such as tensile or dual-cantilever modes, where the stiffness of the samples exceeded the force capacity of the DMA Q800. Although a four-point bend test would have provided a more uniform stress distribution, the required fixture was unavailable and non-standard. The three-point bend test was therefore chosen as a practical compromise and is also more accessible for other research groups wishing to replicate the methodology. While this setup proved suitable for capturing general damping behaviour, it was found to include strain energy dissipations in directions other than the fibre axis, limiting its ability to resolve fibre-direction damping contributions — a limitation further discussed previously in Section 3.2.3. This effect will be evaluated within this section, and this limitation will be attempted to be overcome in Section 3.4.

As detailed in the manufacturer's three-point test procedure, the DMA machine was calibrated before each use against a TA Instruments-provided standard sample, as shown in Figure 3.5. All samples were manufactured by IMA Dresden [157], with tight tolerances of  $\pm 0.01$  mm on width and thickness to minimise geometric variability. The span of 50 mm and specimen length of 60 mm were fixed by the clamp dimensions, ensuring a consistent loading condition. These parameters were selected to ensure that the resulting

### Chapter 3. Dynamic Mechanical Analysis for Damping Estimation

stiffness and deflections remained within the DMA's measurable range.

The applied strain was fixed at 100 microstrains to remain well within the linear viscoelastic range of the material, as well as allowing for the 100 microstrain to be achieved across the full thickness range. This low strain amplitude minimises non-linear effects, such as matrix microcracking or interface degradation, which could otherwise skew damping measurements. The frequency range was varied from 0.01 to 15 Hz, a range chosen to capture low-frequency behaviour relevant to wind turbine blade dynamics while staying well within the DMA's frequency control limits. 15 Hz was also selected as it was a frequency region that would overlap with EMA testing, which will be discussed in Chapter 4. Temperature was held constant at 30 °C to isolate frequency-dependent effects without introducing thermal softening or relaxation phenomena common at elevated temperatures. This temperature was selected to ensure that experiments could be continually carried out within the test lab and that the temperature would not exceed the test value. This control enabled direct assessment of frequency-dependent damping characteristics.

Ten tests were conducted for each sample configuration to assess repeatability and to ensure that any trends observed were statistically robust. Table 3.1 summarises the test setup parameters. Additional details on individual sample dimensions can be found in Appendix B.

### Chapter 3. Dynamic Mechanical Analysis for Damping Estimation



Figure 3.5: DMA Q800 - Three Point Configuration with calibration sample

Table 3.1: DMA Test Setup Parameters

<b>Parameter</b>	<b>Value/Description</b>
Test Mode	Three-Point Bend
Strain Applied	100 microstrains
Temperature Range	Constant (30 °C)
Frequency Range	Varied (Range = 0.01 - 15 Hz)
Sample Thicknesses Tested	2-4 mm (0.5 mm increments)
Sample Length Tested	60 mm
Sample Width Tested	5 mm
Material Nature	Carbon Fibre - UD
Number of Tests per Sample	10

## Chapter 3. Dynamic Mechanical Analysis for Damping Estimation

All samples were prepared and manufactured by IMA in Germany [157], with a focus on achieving high accuracy in thickness and width (tolerances of  $\pm 0.01$  mm were maintained). The length of the samples was kept consistent at 60 mm, determined by the span of the three-point bend clamp (50 mm). Consistent dimensions across samples were crucial for reliable results, ensuring observed variations in damping are due to material characteristics rather than geometric factors. Detailed sample dimensions are provided in Appendix B and are measured to tolerances of  $\pm 0.01$  mm.

### 3.3.2 Influence of Sample Geometry on DMA Results

An important aspect of the study involved investigating how the geometry of the samples, particularly their thickness, influenced the damping results obtained from DMA. Samples ranging from 2 mm to 4 mm thickness were tested to assess how thickness variation impacts the damping properties measured by DMA.

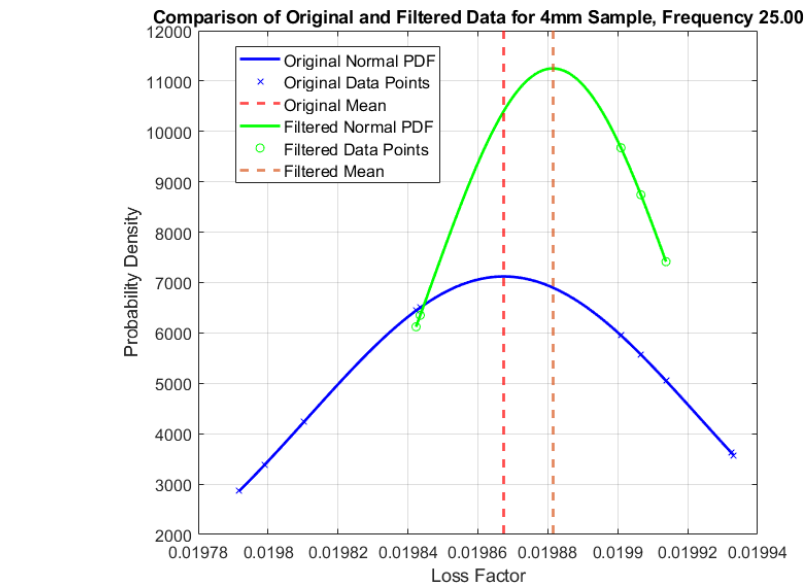
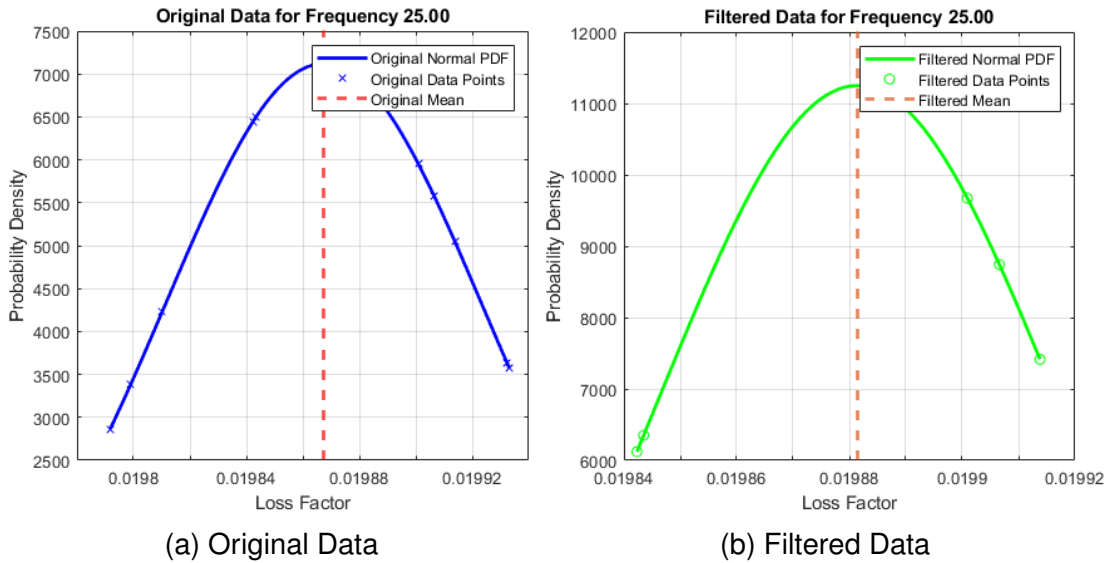
After conducting the tests, the results were post-processed to remove outliers and create a normal distribution for each sample under each environmental condition. This step ensured the reliability and accuracy of the damping data. The processed data was then analysed to understand the impact of sample geometry on damping properties and to validate the theoretical models developed in the study. Any data point that was more than two standard deviations away from the mean was excluded to remove outliers. The equation used for this process is given by:

$$x_i \in \{x \mid |x - \mu| \leq 2\sigma\} \quad (3.3)$$

where  $x_i$  is a data point,  $\mu$  is the mean, and  $\sigma$  is the standard deviation of the loss factor in each frequency. This criterion helped to mitigate the impact

### Chapter 3. Dynamic Mechanical Analysis for Damping Estimation

of abnormal values and ensure a more robust representation of the material's damping properties. The data filtering process can be seen in Figure 3.6c.

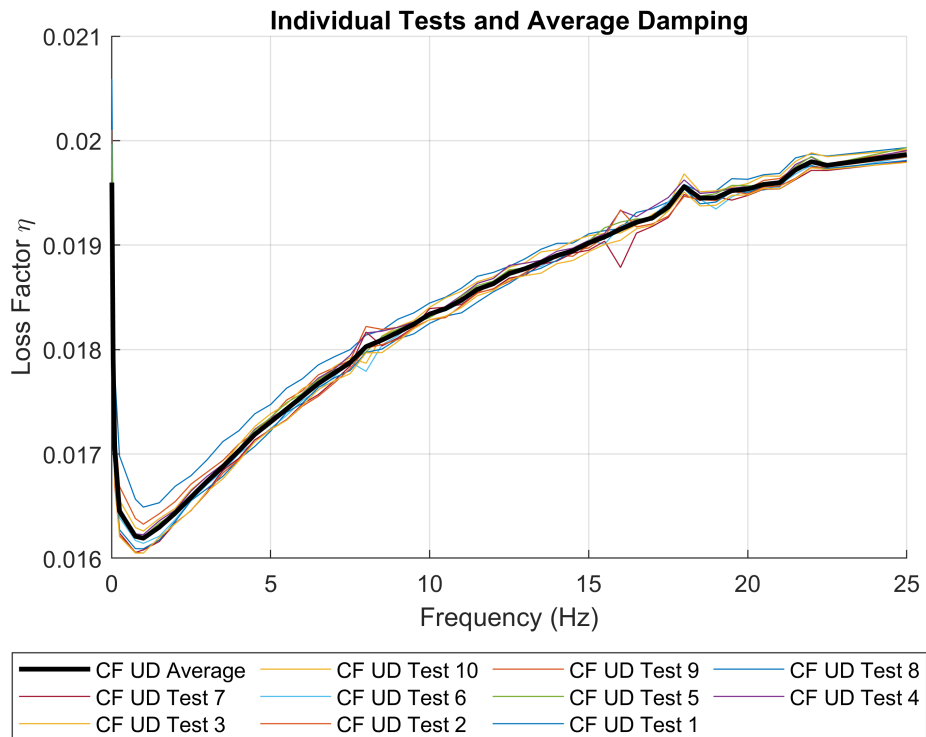


(c) Comparison of Normal Distribution of the Original and Filtered Data

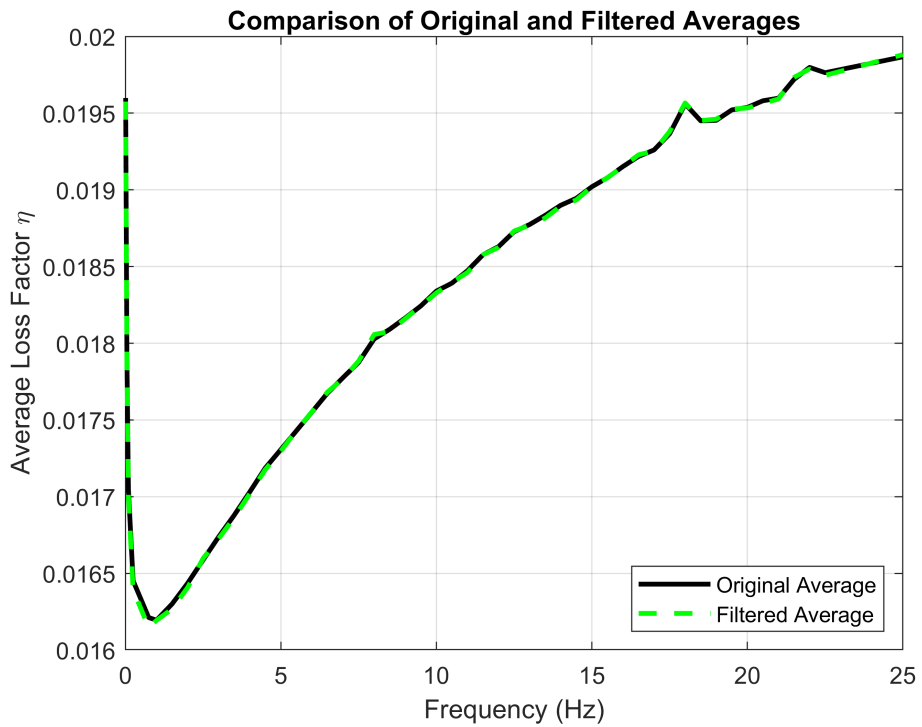
Figure 3.6: Comparison of Normal Distribution of the Original and Filtered Data - for 4 mm Carbon UD sample at 25 Hz

Figure 3.6 shows that removing outliers refines the dataset, allowing updated averages for each experimental condition to be recalculated (see Figure 3.7).

### Chapter 3. Dynamic Mechanical Analysis for Damping Estimation



(a) Average of 10 Test Results



(b) Average Results vs Filtered Average Result

Figure 3.7: Single DMA Result Produced by 10 Tests

### Chapter 3. Dynamic Mechanical Analysis for Damping Estimation

Figure 3.7 shows that the average produced from implementing the normal distribution stage is very similar to the original average. However, this step was introduced to safeguard against significant errors corrupting otherwise reliable data. For the remainder of this thesis, the post-processed data will be that which is presented.

Upon producing a methodology where each sample test result can be post-processed and displayed, it was then possible to do this for the range of thicknesses intended, as seen in Table 3.1. The samples tested within this section were produced at IMA Germany and were of higher quality than another in-house milled set that will be discussed later within this thesis [157]. The result of the thickness investigation can be viewed in Figure 3.8.

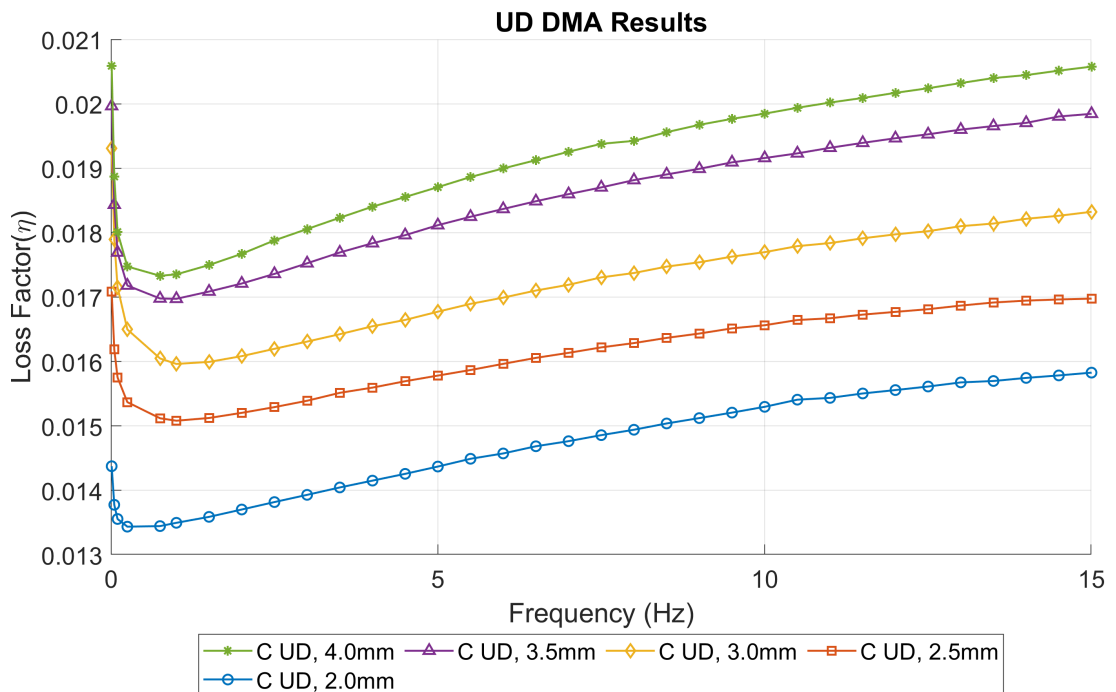


Figure 3.8: DMA Result - C denotes Carbon Fibre Composite

As seen in Figure 3.8, there is a major variation within the results produced,

### Chapter 3. Dynamic Mechanical Analysis for Damping Estimation

which shows a trend of increasing damping as the thickness of the specimen increases. These variations are well outside the margin of error of approximately  $\pm 3\%$ ; therefore, the effect of thickness can be considered a driving factor in obtainable results.

Despite the repeatable results achieved by the standard DMA method, several significant shortcomings were identified. Notably, the technique is highly sensitive to variations in sample geometry, particularly thickness. This investigation indicates that as specimen thickness increases, the measured damping properties deviate substantially from expected values—variations that far exceed the experimental margin of error (approximately  $\pm 3\%$ ). This discrepancy is likely attributable to two main factors. Firstly, energy dissipation at the supports and load application points introduces additional damping from friction that is not intrinsic to the material and cannot be fully controlled, even though the manufacturer states the supports are low-friction [101]. Secondly, and more critically, shear deformation becomes increasingly significant in thicker specimens. As the span-to-thickness ratio decreases, transverse shear deformation plays a greater role in strain energy dissipation, violating the pure bending assumptions inherent in classical DMA interpretations. This effect is particularly relevant in composite laminates, where fibre–matrix interactions and interlaminar shear deformation can amplify damping contributions from directions other than the primary fibre axis [34, 158]. In three-point bending tests of laminated beams, it has been shown that shear-related energy dissipation increases with thickness and reduces the accuracy of axial property estimation if unaccounted for [159]. Consequently, the measured damping reflects not only axial energy losses but also shear-related contributions, particularly in the 13 direction, and the transverse 22 direction. This confirms the need for directional decomposition of DMA results in anisotropic materials such as CFRP.

## Chapter 3. Dynamic Mechanical Analysis for Damping Estimation

These limitations affect industry, particularly in wind turbine blade design applications, where representative damping characterisation is important in ensuring structural integrity and long-term performance. Inaccurate damping measurements can lead to design inefficiencies, resulting in higher CAPEX (Capital Expenditure) costs, increased maintenance costs, reduced efficiency, or even premature component failure. Clearly, by identifying and understanding these shortcomings, this work lays the foundation for developing a more robust DMA methodology. To this end, FEA was utilised to simulate DMA testing conditions and quantify strain energy dissipations directional contributions. The insights gained from these simulations have been integrated into the proposed methodology, which aims to improve the predictive accuracy of DMA testing for anisotropic materials like CFRP. Ultimately, these advancements are expected to benefit a wide range of industries by enabling more precise material selection and optimisation, thereby enhancing the performance and reliability of high-stress components in sectors such as aerospace, automotive, and renewable energy.

### **3.4 FEA Assisted DMA**

Given the limitations of standard DMA processes, directional damping contributions are suspected to influence the DMA results significantly. In order to better understand how sample behaviours under deformation, FEA analysis was required.

#### **3.4.1 Using FEA to Investigate the Influence of Setup Changes in DMA**

The investigation utilised detailed FEA employing ANSYS Parametric Design Language (APDL) to address specific questions: How does energy dissipate

### Chapter 3. Dynamic Mechanical Analysis for Damping Estimation

in DMA test samples? And why do results vary with different sample thicknesses? This analysis will improve the modelling and understanding of the test environment that samples experience during DMA testing by quantifying the directional contributions to energy dissipation, thereby clarifying how the material's damping properties vary with orientation.

The central focus of the present study was to analyse the strain energy within the samples. Strain energy was directly linked to a material's capacity to absorb and dissipate energy, which is key to accurate damping characterisation [160]. Understanding how strain energy was distributed under varying conditions was instrumental to explaining the damping properties of laminate composite materials.

The FEA methodology was designed to achieve two main goals: understanding strain energy dissipation in samples with differing thicknesses and clarifying how these variances affect DMA results. By employing a static analysis approach, the FEA model can determine the strain components, closely mirroring the loads experienced in physical DMA tests. This detailed approach allows the model to accurately simulate deformations corresponding with real DMA results across various material thicknesses, providing deeper insight into the material's response to dynamic loading.

An important output of the FEA model is the precise calculation of strain energy for each finite element within the sample. This computation offers insights into the stress-strain response of each element and aggregates these responses to determine the total strain energy at peak deformation. The formula used for this calculation is detailed below [160, 161]:

$$\text{Total Strain Energy, } U = \sum_n \sum_l \sum_{i=11,22,33,12,13,23} \frac{1}{2} \sigma_{il}^n \epsilon_{il}^n V_l^n \quad (3.4)$$

## Chapter 3. Dynamic Mechanical Analysis for Damping Estimation

This equation accounts for total strain energy across various directional components (represented by indices  $n$  and  $l$  for element and layer, respectively). Here,  $\sigma$  and  $\epsilon$  denote stress and strain in the corresponding directions, with  $V$  representing the elemental volume. This detailed approach provides a clear picture of how materials dissipate energy under dynamic conditions and sheds light on the fundamental characteristics that govern their damping properties.

The total strain energy may also be represented as [162]:

$$U_{\text{total}} = U_{11} + U_{12} + U_{13} + U_{22} + U_{23} + U_{33} \quad (3.5)$$

where the strain energy per unit volume in each direction is represented by [162]:

$$u_{ij} = \frac{1}{2}\sigma_i\epsilon_i \quad \text{and} \quad U = \sum u_i V \quad (3.6)$$

This formulation underscores the comprehensive nature of strain energy distribution analysis. By evaluating the contributions of different strain components, it can be seen how energy is dissipated within the material.

### 3.4.2 Analysing Strain Energy Components

From previous work in Section 3.3.2, it was proposed that different thicknesses may result in varied strain energy contributions due to the anisotropic nature of carbon fibre materials. To test this hypothesis, a series of strain energy analyses were conducted. This involved evaluating the directional strain energy components within the FEA model and comparing them across different sample thicknesses, which will be further explored in Section 3.4.4.1

## Chapter 3. Dynamic Mechanical Analysis for Damping Estimation

The results revealed that as the sample thickness increases, the individual directional strain energy distribution varies. This is attributed to the carbon fibre material's anisotropic properties, which cause different energy dissipation patterns in response to the loading. By understanding these patterns, it is possible to characterise the material's damping properties better.

### **3.4.3 FEA - Static Viability**

Although DMA applies oscillatory loading, the mechanical response can be approximated using static FEA if the excitation frequencies are significantly lower than the sample's natural frequencies.

To justify this simplification, modal analysis was performed for each sample geometry. While the actual DMA setup uses three-point bending, with constrained vertical displacement at the supports and centrally applied loading, the modal analysis was conducted under free-free boundary conditions. This removes artificial stiffening due to constraints and provides a conservative estimate of the sample's fundamental natural frequency.

The analysis confirmed that the first six modes were rigid-body motions, with the first deformation mode (flexural) appearing as the seventh. Across the tested thicknesses, the first deformation frequencies ranged from 569 Hz to 2519 Hz, as shown in Table 3.2.

Table 3.2: Modal Frequencies for Various Sample Thicknesses

Thickness (mm)	Mode 1 Frequency (Hz)
1.0	569.03
1.5	852.60
2.0	1135.1
2.5	1416.0
3.0	1695.2
3.5	1972.2
4.0	2246.8
4.5	2518.6

Given that DMA excitation frequencies in this study were limited to 20 Hz, more than an order of magnitude below the first natural frequencies, dynamic effects are negligible. Static FEA is therefore a valid approximation for evaluating the response under these loading conditions.

Figure 3.9 shows the first deformation mode for a representative 2 mm thick sample.

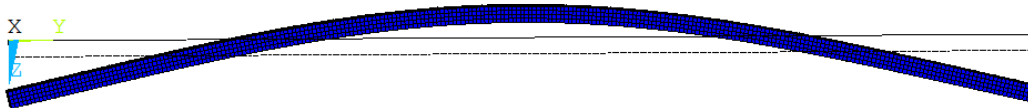


Figure 3.9: First deformation mode of the 2 mm thick sample from modal analysis (free-free condition).

### 3.4.4 FEA - Initial Setup

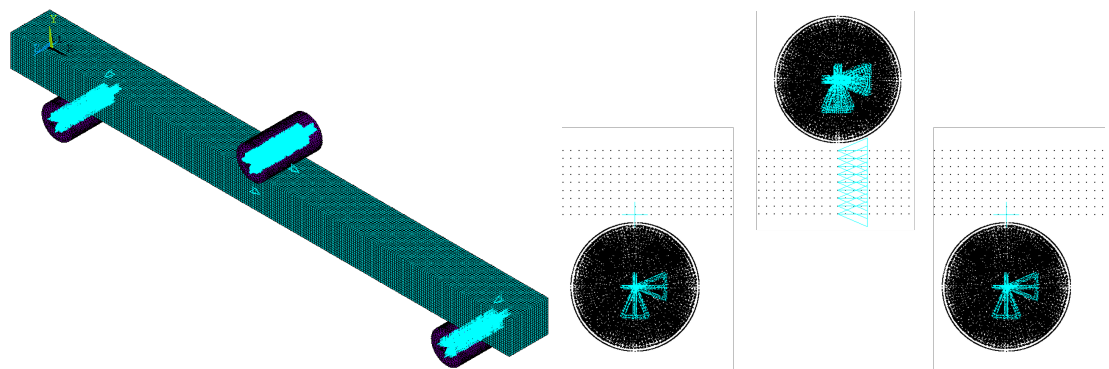
The ANSYS APDL static model setup was required to replicate DMA test conditions. Given that static FEA analysis was sufficient due to the low-frequency nature of the DMA testing, this section details the creation of the ANSYS model to match the experimental setup. Key considerations included:

### Chapter 3. Dynamic Mechanical Analysis for Damping Estimation

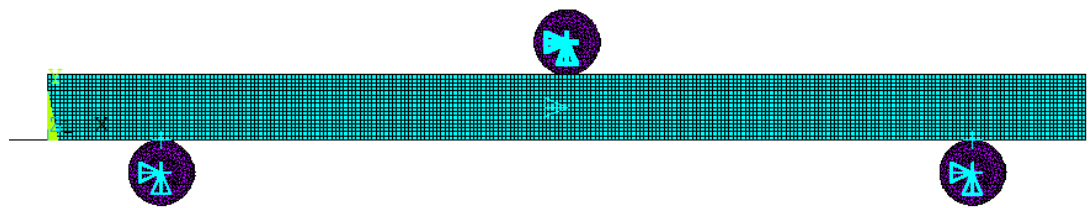
- **Material Definitions:** Incorporating material properties of the sample and incompressible supports as manufacturers provide.
- **Geometry Setup:** Establishing the dimensions and shape of the sample and supports in the FEA model.
- **Meshing:** Configuring the element size and type for optimal resolution and computational efficiency.
- **Boundary Conditions:** Setting up constraints and loads to replicate the DMA testing environment.
- **Contact Modeling:** Defining the interaction between the sample and supports to simulate physical contact behaviours, including frictional coefficients.
- **In-compressible Supports:** Modeling the supports to be rigid and incompressible, reflecting real-world testing apparatus.
- **Deformation Calculation:** Applying deformation based on targeted strain and displacement as per the DMA manufacturer's relationship.
- **Analysis Type:** Employing a non-linear static simulation suitable for the low-frequency nature of the DMA testing.

Material properties of the sample were included as provided by the manufacturer and integrated as element SOLID185. The cylindrical supports, modelled as incompressible solids using the element SOLID187, reflected the rigidity of the real-world testing conditions. Figure 3.10 shows the model and boundary conditions and is detailed in Table 3.3.

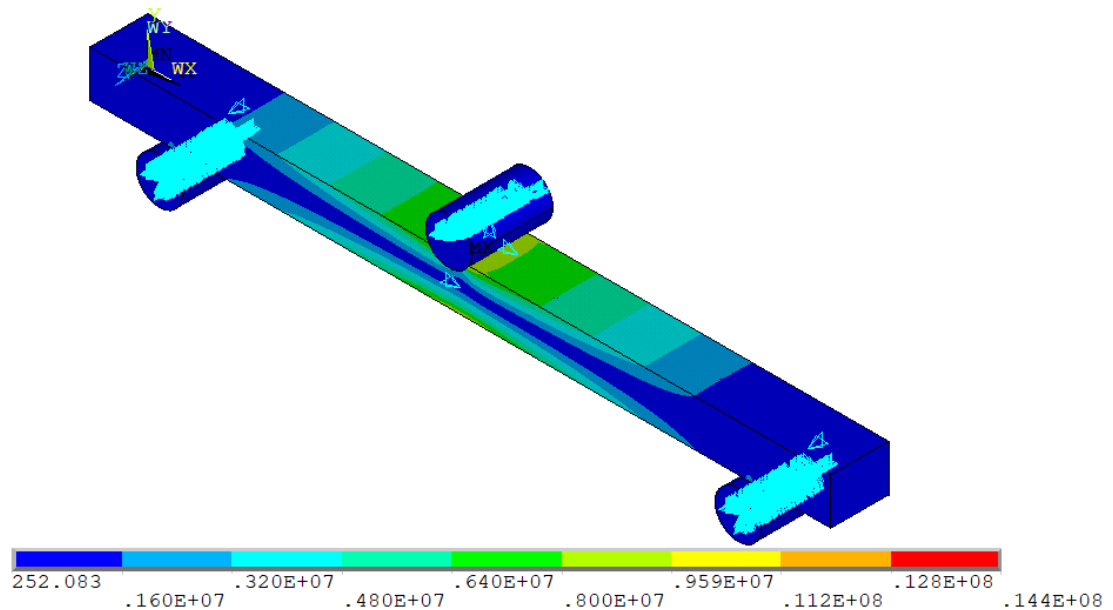
### Chapter 3. Dynamic Mechanical Analysis for Damping Estimation



(a) Boundary Condition on Elemental Model - Isometric View (b) Additional View of the Boundary Conditions - Supports



(c) Boundary Condition on Elemental Model - Side View



(d) Boundary Conditions with von Mises stress distribution visible, illustrating how the sample deflects under load.

Figure 3.10: Boundary Conditions of the FEA model (in ANSYS APDL) for a 4 mm thick sample, showing (a) the isometric view, (b) an additional boundary-condition image, (middle) side view, and (c) von Mises stress distribution.

### Chapter 3. Dynamic Mechanical Analysis for Damping Estimation

Table 3.3: Boundary Conditions for the Three-Point Bend Test in FEA

<b>Component</b>	<b>X-Axis Constraint</b>	<b>Y-Axis Constraint</b>	<b>Z-Axis Constraint</b>
Supports	Fully constrained (immovable)	Fully constrained (immovable)	Fully constrained (immovable)
Beam at Supports	Constrained at two outer node locations (immovable)	Unconstrained (free)	Constrained at a single node at each support (immovable)
Beam (Mid-span)	Constrained (immovable)	Unconstrained (free)	Unconstrained (free)
Top Support	Constrained (immovable)	Controlled displacement applied	Constrained (immovable)

An accurate simulation of the physical interaction between the sample and the supports was achieved by defining contact pairs in the FEA model. Surface contacts were established at the bottom and top of the sample, while corresponding target surfaces were defined on the top of the two fixed bottom supports and the underside of the central cylinder. This setup allowed the physical components to interact within the model. SOLID170 elements were designated for the target surfaces and SOLID174 elements for the contact surfaces, enabling precise calculations of deformation and reaction under the applied load.

Deformation was calculated by selecting a target microstrain level (100 microstrain) at the mid-length of the sample, using the DMA machine's relationship. The DMA Q800's software converts targeted strain values into corresponding deformations on the central displacement arm using the following formulae depending on the aspect ratio of the sample:

### Chapter 3. Dynamic Mechanical Analysis for Damping Estimation

$$\delta_d = \epsilon_x \frac{5L^2 + 12t^2(1 + \nu)}{60t} \quad (3.7)$$

where:

$\delta_d$  is the deformation (in metres) at the mid-length of the sample,  $\epsilon_x$  is the applied strain (in microstrain),  $L$  is the span length of the sample (in meters),  $t$  is the thickness of the sample (in metres), and  $\nu$  is Poisson's ratio.

For samples where  $\frac{L}{t} > 10$ :

$$\delta_d = \epsilon_x \frac{L^2}{12t} \quad (3.8)$$

This derived equation can now determine the deflection applied to the sample. Therefore, deflection must be applied to the FEA method to characterise the stress and strain components correctly.

Table 3.4 summarises the detailed FEA model configuration.

### Chapter 3. Dynamic Mechanical Analysis for Damping Estimation

Table 3.4: Detailed FEA Model Configuration for DMA Testing

<b>Aspect of FEA Model</b>	<b>Description</b>
Material Properties	Orthotropic properties for the carbon sample were defined using MP commands and implemented via SOLID185. Properties were provided by the manufacturer and assumed temperature-invariant, linear elastic behaviour.
Supports	Span and actuator supports were modelled using SOLID187 with a Poisson's ratio of 0.4999 to simulate near-incompressibility and avoid numerical singularities.
Contact Modelling	Two contact pairs were created between the beam and supports (bottom) and between the beam and central actuator (top). Contact behaviour was modelled using CONTA174 and TARGE170 elements, with normal behaviour governed by the augmented Lagrangian method and a friction coefficient of 0.0001 to reflect a very low friction contact (as described by TA [101] and ANSYS [163]). Contact surfaces were generated via ESURF.
Boundary Conditions	Z-displacement was fixed at the supports. To prevent rigid body motion, X-displacement was constrained at the beam mid-span (both top and bottom nodes). These constraints replicate the experimental DMA setup (see Table 3.3).
Meshing	The carbon sample was meshed using structured hexahedral SOLID185 elements generated via vdrag/vmesh, with an element size of 0.25 mm. Cylindrical support volumes were meshed separately using SOLID187 elements with the same size. Mesh convergence was confirmed by halving the sample mesh size and observing less than a 5% change in displacement and strain, consistent with ASME V&V 20 guidance [164].
Deformation Calculation	A target strain of $100 \mu\epsilon$ (within the linear viscoelastic range and applicable across all thicknesses) was converted to actuator displacement using Equation 3.8. This was applied vertically to the actuator using D, ALL, UY, -C_DISP.

### Chapter 3. Dynamic Mechanical Analysis for Damping Estimation

To visualise the distribution of strain and overall displacement in a three-point bend test, Figure 3.11 presents the strain components in different directions within the sample ( $\epsilon_{11}$ ,  $\epsilon_{13}$ , and  $\epsilon_{33}$ ) along with the total displacement as seen in Figure 3.12. These images illustrate the maximum and minimum strain regions in each directional component, providing detailed insight into how strain energy is distributed during bending. The total displacement image highlights the cumulative deformation across the sample, offering a comprehensive view of its response to the applied load. This analysis of strain and displacement patterns is essential for understanding the material's behaviour under dynamic loading conditions, aiding in the characterisation of its damping properties.

### Chapter 3. Dynamic Mechanical Analysis for Damping Estimation

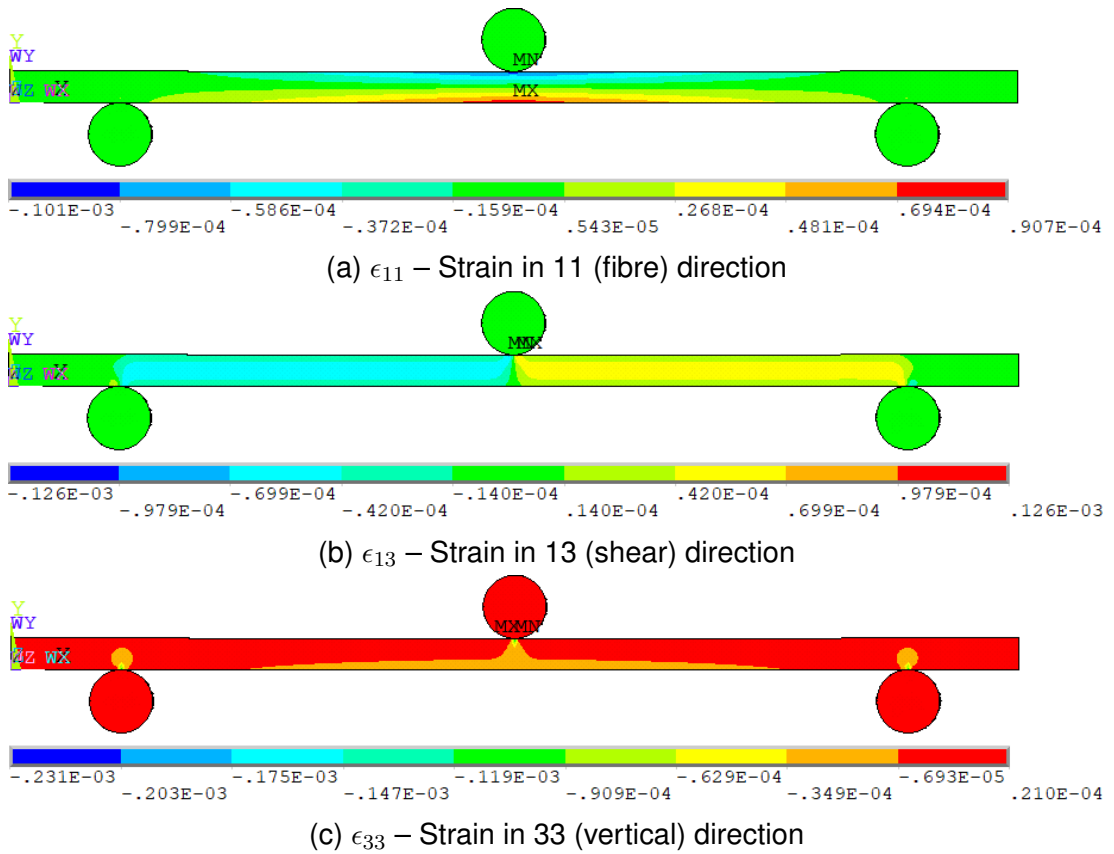


Figure 3.11: Strain distribution results for a three-point bend test showing maximum and minimum strain regions in different directional components ( $\epsilon_{11}$ ,  $\epsilon_{13}$ , and  $\epsilon_{33}$ ) – 2 mm Sample

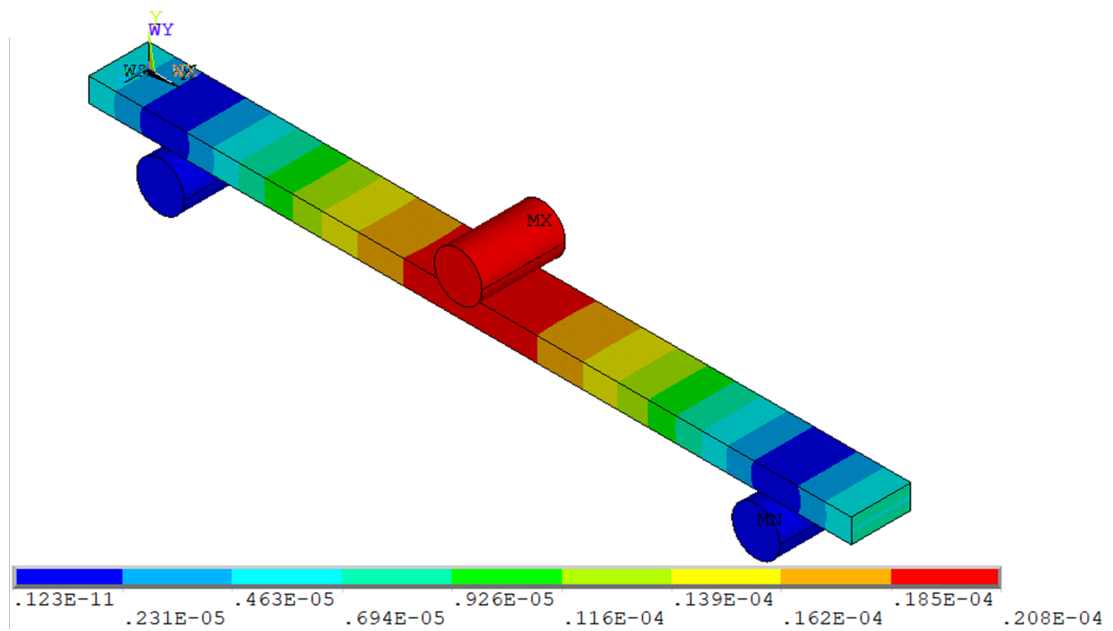


Figure 3.12: Total displacement in the sample during the three-point bend test – 2 mm Sample

#### 3.4.4.1 Influence of Sample Thickness on Strain Energy Results

A Matlab script, seen in Appendix C, was used to run the ANSYS code, seen in Appendix D in batch mode, allowing strain energy analysis for a range of sample thicknesses. The stress and strain data from each element in the sample were recorded and processed according to Equation 3.4. The Matlab code also post-processed the data to produce the strain energy for each specimen used in the FEA analysis. The strain energy components and 1 Hz damping results from various thicknesses can be seen in Figure 3.13.

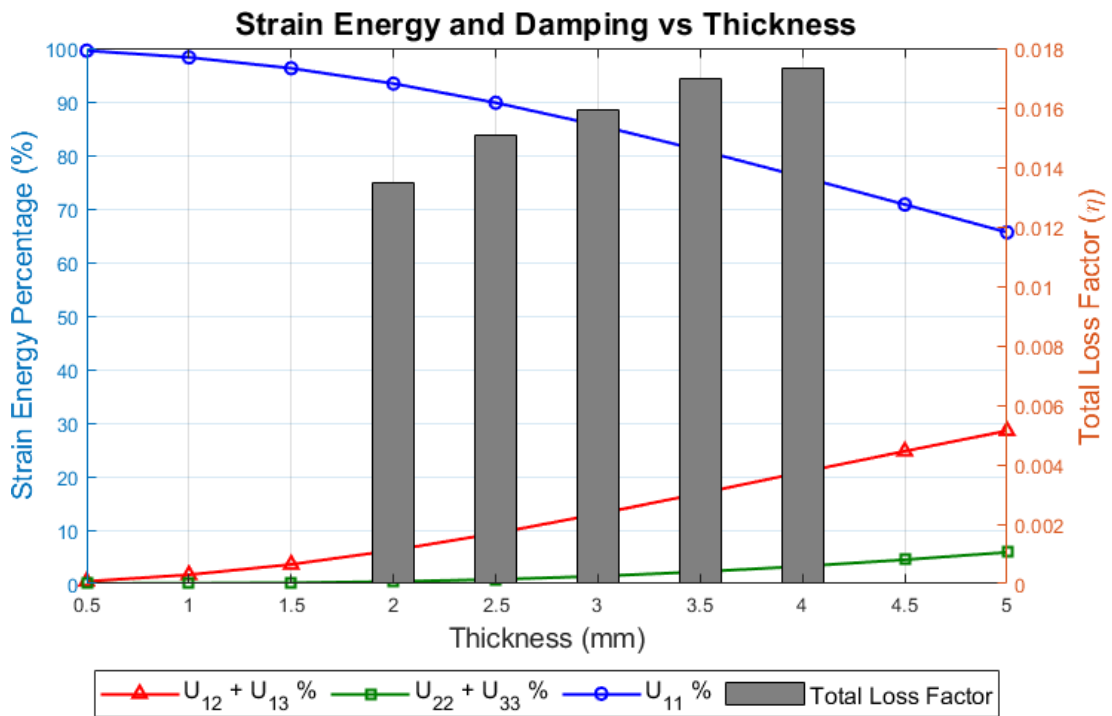


Figure 3.13: Effect of sample thickness on strain energy distribution overlaid with UD DMA loss factor results at 1 Hz (from Figure 3.8) - Note: Strain energy % in 23 direction is too small to plot on this figure. Tabulated data available in Appendix E

By analysing Figure 3.13, it is possible to see the impact of the strain energy distribution when the thickness of the sample is changed, particularly the aspect ratio. The fibre direction's (11) strain energy contribution is at its maximum at lower thicknesses and reduces as the sample thickness increases (within the region of interest). This reduction aligns with the anticipated mechanical behaviour when increased thickness can lead to a greater distributed strain energy profile across the composite material layers. It can also be seen that the thickness at which this strain energy was at a maximum was 0.5 mm thick (+/- 0.25 mm); however, the manufacture of such proved difficult with these thin samples. Therefore, a balance was struck between the ideal design indicated by the strain energy analysis and the

## Chapter 3. Dynamic Mechanical Analysis for Damping Estimation

practical limitations of manufacturing processes.

In addition to the proportion of strain energy seen in the fibre direction, the shear and transverse components of energy were also recorded as part of the bulk DMA output. As the samples' thickness increased, so too did the proportion of energy in the other directions, especially when considering the vertical transverse direction (33). The observed shift towards non-fibre directions as thickness increased may result in implications for the material's anisotropic behaviour and should be considered when designing for specific loading conditions.

### **3.4.4.2 Influence of Strain Variation on Strain Energy Results**

A main consideration when creating the FEA model was to ensure that the deformation of the sample was subjected under DMA conditions. This process was possible using the equation 3.8. To implement this, an appropriate target strain level was required, which will be discussed. It was also important that the sample stayed within the linear viscoelastic range as well as be within the force limitations of the DMA machine itself.

After considering these two factors, it was found that the maximum microstrain usable for all samples in question would be 200 microstrain due to force limitations. An investigation was then conducted to see the strain energy variance based on the small fluctuations (in the region of 50-250 microstrain) in the applied strain. Modifying the input strain on the ANSYS model found that these minor strain variations had a negligible difference in the strain energy percentage distributions.

The full results of this study, with strain energy percentages, can be viewed in Appendix F. Upon viewing the results and noting the negligible difference in energy dissipation, a value of 100 microstrains was used for this study. This

### Chapter 3. Dynamic Mechanical Analysis for Damping Estimation

strain energy distribution for this scenario can be seen in Table 3.5

Table 3.5: UD Test – Strain values and corresponding displacements for 100 microstrains across selected thicknesses.

Thickness (mm)	0.50	1.00	1.50	2.00	2.50	3.00	3.50	4.00	4.50	5.00
Span (mm)	50									
Microstrain	100									
$U_{11}$ (%)	99.53	98.28	96.25	93.38	89.81	85.60	80.93	75.94	70.81	65.61
$U_{22} + U_{33}$ (%)	0.04	0.07	0.16	0.39	0.79	1.39	2.22	3.24	4.47	5.85
$U_{12} + U_{13}$ (%)	0.43	1.66	3.59	6.23	9.40	13.01	16.85	20.83	24.73	28.54
Displacement ( $\mu\text{m}$ )	41.67	20.83	13.89	10.42	8.33	6.94	5.95	5.21	4.63	4.17

**Note:** Strain components ( $U_{11}$ ,  $U_{22} + U_{33}$ ,  $U_{12} + U_{13}$ ) are shown as percentages of total strain energy. Displacement corresponds to maximum deflection for each thickness under 100  $\mu\text{strain}$  at a 50 mm span.

From the results, it was found that slight variations in strain within the limitation of the capability of the machine was found to have a negligible impact upon the results. Therefore, a single value of 100 microstrain was selected to ensure consistency and ensure the machine was not operating too close to its limitations.

#### 3.4.4.3 Influence of Minor Thickness Variations within Samples on Strain Energy Results

The initial in-house batch of carbon samples exhibited minor geometric inconsistencies, with thickness variations of less than 0.05 mm along their length. To assess whether such deviations significantly affect strain-based results, a subset of these samples was selected for further investigation. Their geometric data are summarised in Table 3.6.

### Chapter 3. Dynamic Mechanical Analysis for Damping Estimation

Table 3.6: Target Thickness ( $T_T$ ) against the resultant sample dimensions

$T_T$ (mm)	t along sample (mm)					$\bar{t}$ (mm)
	0%	25%	50%	75%	100%	
1	0.54	0.60	0.63	0.64	0.62	0.61
2	1.52	1.56	1.59	1.62	1.62	1.58
3	2.56	2.59	2.63	2.65	2.66	2.62
4	3.90	3.93	3.96	3.98	4.00	3.95
5	4.89	4.89	4.83	4.82	4.81	4.85

As can be seen, the in-house samples were not aligned well with their target thicknesses, with the measurements being calculated from measurements at multiple locations. In addition, all specimens satisfy  $L/t > 10$ , Equation 3.8 was still deemed the most appropriate for estimating central displacement under loading.

To evaluate the validity of this equation, Table 3.7 compares predicted central displacements from both the long and short-span analytical solutions, using the measured average thicknesses.

Table 3.7: Comparison of Central Deformation with respect to Equations 3.7 and 3.8

Average Thickness (mm)	Central Displacement (Eq. 3.7) ( $\mu\text{m}$ )	Central Displacement (Eq. 3.8) ( $\mu\text{m}$ )	Percentage Difference (%)
0.61	34.39	34.38	0.04
1.58	13.21	13.17	0.30
2.62	8.02	7.96	0.82
3.95	5.37	5.27	1.84
4.85	4.42	4.30	2.74

\* For thicknesses  $\geq 5$  mm, Eq. 3.7 is considered more appropriate.

### Chapter 3. Dynamic Mechanical Analysis for Damping Estimation

Table 3.7 highlights that the two analytical expressions produce nearly identical displacement values at lower thicknesses, with divergence increasing progressively beyond 3.5 mm. This reflects the rising influence of non-uniform stress distribution as thickness increases. Since all tested samples remain below 5 mm in average thickness, Equation 3.8 was used throughout the remainder of the analysis.

DMA testing was then performed on these same samples. Figure 3.14 presents the damping factor ( $\eta$ ) over the frequency range of interest, alongside high-precision IMA samples shown previously in Figure 3.8.

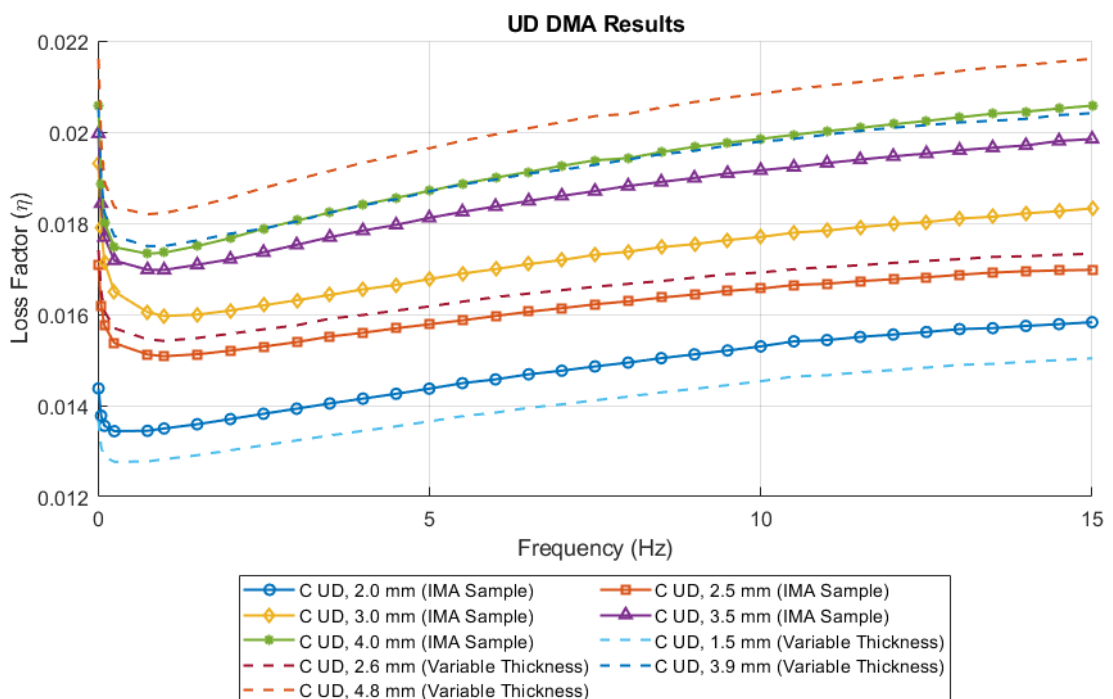


Figure 3.14: Damping characteristics as a function of frequency for unidirectional carbon composites with up to 0.1 mm thickness variation

As shown in Figure 3.14, the damping response for samples with variable thicknesses (1.5, 2.6, 3.9, and 4.8 mm) was compared against closely matched IMA specimens. For the closest pairs—namely 2.6 mm vs. 2.5 mm

## Chapter 3. Dynamic Mechanical Analysis for Damping Estimation

and 3.9 mm vs. 4.0 mm, the deviation in loss factor across the frequency spectrum remained below 2%. This suggests that modest geometric variations (within  $\pm 0.2$  mm) do not significantly affect damping behaviour when average thickness is accounted for. In contrast, larger deviations, such as 1.5 mm and 4.8 mm, exhibited more substantial differences.

These results reaffirm the sensitivity of damping properties to thickness, especially under three-point bending conditions, where cross-sectional stiffness and energy dissipation are strongly geometry-dependent. Despite this, the influence of minor thickness deviations was found to be negligible when the average value is used in analysis. For consistency, all subsequent sections (starting from Section 3.5) rely exclusively on IMA samples with tight tolerances ( $\pm 0.01$  mm), ensuring a robust foundation for correlating FEA strain energy data with experimentally observed damping.

### **3.5 FEA assisted DMA testing – Methodological development**

This section outlines the methodology developed to integrate FEA results with damping measurements obtained from DMA. Building on the test configuration detailed in Table 3.1, the approach uses strain energy data extracted from simulations of the IMA-manufactured samples to decompose the global damping response into its directional components.

By relating the measured loss factors to the distribution of strain energy across the principal material directions, this method enables the extraction of geometry-independent damping parameters. These directional loss factors, weighted by their corresponding energy contributions, provide a more detailed understanding of anisotropic damping behaviour and support more accurate

predictive modelling of composite structures.

### 3.5.1 Proposed Approach for FEA assisted DMA

With the FEA model validated, attention was focused on the analysis of directional damping components. The aim was to understand the interaction between the components of strain energy and their collective influence on the observed damping characteristics. Conducting the DMA simulation through FEA facilitates the isolation and quantification of the different directional components of damping. The most significant factor in this study was the damping of fibre direction due to its important role in the overall damping behaviour of the composite material in the blade's spar cap. This integrated analysis aims to enhance the understanding of material damping, particularly as it applied to the unique properties of composite structures.

To demonstrate the relationship between the directional damping components and the overall system damping, the total strain energy in the system (as shown in Equation 3.4) is considered as the sum of the strain energies in the principal material directions [160, 165]. Accordingly, the specific damping capacity is defined as:

$$\psi = \frac{\Delta U}{U_{\text{total}}} \quad (3.9)$$

where:  $\psi$  is the specific damping capacity,  $\Delta U$  is the energy dissipated per cycle (in Joules),  $U_{\text{total}}$  is the total strain energy in the system (in Joules).

$$\begin{aligned} \Delta U = & \psi_{11}U_{11} + \psi_{12}U_{12} + \psi_{13}U_{13} \\ & + \psi_{22}U_{22} + \psi_{23}U_{23} + \psi_{33}U_{33} \end{aligned} \quad (3.10)$$

where:  $\psi_{ij}$  are the directional specific damping capacities,  $U_{ij}$  are the strain

### Chapter 3. Dynamic Mechanical Analysis for Damping Estimation

energy components in the principal material directions  $i, j$ , with  $i, j = 1, 2, 3$ .

$$U_{\text{total}} = U_{11} + U_{12} + U_{13} + U_{22} + U_{23} + U_{33} \quad (3.11)$$

resulting in:

$$\psi = \frac{\psi_{11}U_{11} + \psi_{12}U_{12} + \psi_{13}U_{13} + \psi_{22}U_{22} + \psi_{23}U_{23} + \psi_{33}U_{33}}{U_{11} + U_{12} + U_{13} + U_{22} + U_{23} + U_{33}} \quad (3.12)$$

Given the relationship between the directional specific damping capacity  $\psi_{ij}$  and loss factor  $\eta_{ij}$  (appropriate when  $\tan(\delta) < 0.1$ ), shown in Equation 3.2, [153]  $\psi_{ij} = 2\pi\eta_{ij}$  it is possible to rearrange this formula to use loss factor directly. By substituting  $\psi_{ij}$  with  $2\pi\eta_{ij}$  and considering the damping results obtained from the DMA testing as the total loss factor, this gives:

$$\eta_{\text{DMA}} = \frac{\eta_{11}U_{11} + \eta_{12}U_{12} + \eta_{13}U_{13} + \eta_{22}U_{22} + \eta_{23}U_{23} + \eta_{33}U_{33}}{U_{11} + U_{12} + U_{13} + U_{22} + U_{23} + U_{33}} \quad (3.13)$$

This equation demonstrates that the overall damping factor ( $\eta_{\text{DMA}}$ ) is a function of both the individual damping coefficients ( $\eta_{ij}$ ) and the strain energy distribution in each principal direction ( $U_{ij}$ ). The damping coefficients represent the material's ability to dissipate energy in each direction, whilst the strain energy components reflect the energy distribution under dynamic loading.

By considering the proportion of strain energy in each principal direction (expressed as a percentage of the total strain energy - resulting in a denominator of 1), the equation can be further refined to:

$$\eta_{\text{DMA}} = \eta_{11}U_{\%11} + \eta_{12}U_{\%12} + \eta_{13}U_{\%13} + \eta_{22}U_{\%22} + \eta_{23}U_{\%23} + \eta_{33}U_{\%33} \quad (3.14)$$

### Chapter 3. Dynamic Mechanical Analysis for Damping Estimation

where the variables are as follows:

$$\begin{aligned}\eta_{11} & \text{ (Axial loss factor),} \\ \eta_{12} = \eta_{13} & \text{ (In-Plane Shear loss factor),} \\ \eta_{22} = \eta_{33} & \text{ (Transverse normal loss factor),} \\ \eta_{23} & \text{ (Out-of-plane Shear loss factor).}\end{aligned}$$

Simplifying the equation to highlight the predominant damping mechanisms yields:

$$\eta_{\text{DMA}} = \eta_{11}(U_{\%11}) + \eta_{12}(U_{\%12} + U_{\%13}) + \eta_{22}(U_{\%22} + U_{\%33}) + \eta_{23}(U_{\%23}) \quad (3.15)$$

To resolve the unknown loss factors ( $\eta_{11}, \eta_{12}, \eta_{22}, \eta_{23}$ ), a minimum of four data sets from samples with varying thicknesses was required as input. Each set contributes a unique equation to the linear system. While four sets form a baseline, additional data improves the model's accuracy through error minimisation techniques like least squares fitting, which help mitigate measurement and testing variations.

Within this and all future sections of this thesis, a coordinate system definition was required to understand the directional components of damping being discussed. As there are multiple setups, the coordinate systems being referred to will always be in line with the fibre direction of the sample, displayed in Figure 3.15.

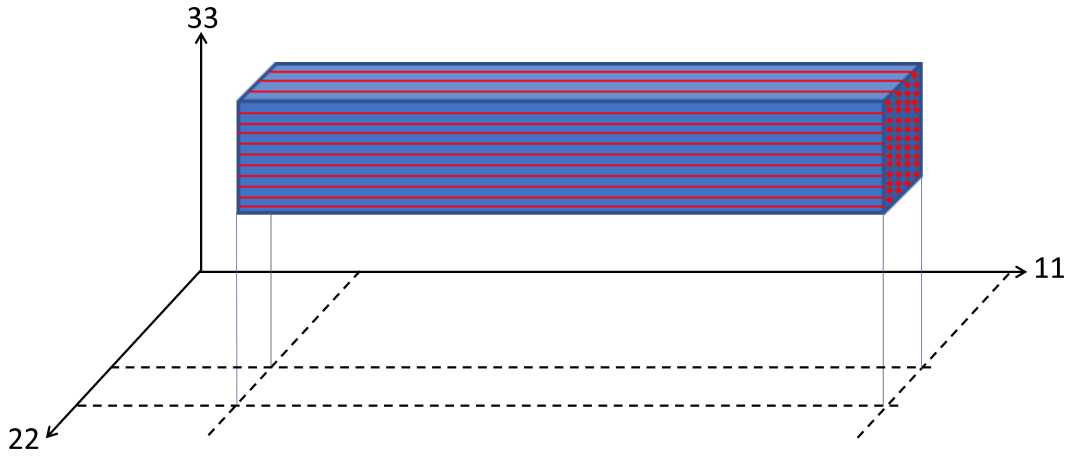


Figure 3.15: Illustration of the coordinate system used.

Formulating these basic equations in matrix form, the model may be represented as:

$$\eta_{\text{DMA}} = \mathbf{U}_{\%} \eta \quad (3.16)$$

where,

$$\eta_{\text{DMA}} = \left\{ \eta_{\text{DMA}}^{(1)} \eta_{\text{DMA}}^{(2)} \eta_{\text{DMA}}^{(3)} \eta_{\text{DMA}}^{(n)} \right\}^T$$

$$\mathbf{U}_{\%} = \left[ \mathbf{U1} \quad \mathbf{U2} \quad \mathbf{U3} \quad \mathbf{U4} \right]$$

$$\mathbf{U1} = \begin{Bmatrix} U_{\%11}^{(1)} \\ U_{\%11}^{(2)} \\ U_{\%11}^{(3)} \\ U_{\%11}^{(n)} \end{Bmatrix} \quad \mathbf{U2} = \begin{Bmatrix} U_{\%12}^{(1)} + U_{\%13}^{(1)} \\ U_{\%12}^{(2)} + U_{\%13}^{(2)} \\ U_{\%12}^{(3)} + U_{\%13}^{(3)} \\ U_{\%12}^{(n)} + U_{\%13}^{(n)} \end{Bmatrix}$$

### Chapter 3. Dynamic Mechanical Analysis for Damping Estimation

$$\mathbf{U3} = \begin{Bmatrix} U_{\%22}^{(1)} + U_{\%33}^{(1)} \\ U_{\%22}^{(2)} + U_{\%33}^{(2)} \\ U_{\%22}^{(3)} + U_{\%33}^{(3)} \\ U_{\%22}^{(n)} + U_{\%33}^{(n)} \end{Bmatrix} \quad \mathbf{U4} = \begin{Bmatrix} U_{\%23}^{(1)} \\ U_{\%23}^{(2)} \\ U_{\%23}^{(3)} \\ U_{\%23}^{(n)} \end{Bmatrix}$$

$$\eta = \left\{ \eta_{11} \quad \eta_{12} \quad \eta_{22} \quad \eta_{23} \right\}^T$$

It is noted that  $\eta_{\text{DMA}}$  represents the damping results obtained from the DMA machine for unidirectional samples where the fibres can be aligned either in the normal principal direction (11) or the transverse normal direction which are hereafter referred to as UD and transverse tests, respectively. The  $U_{\%}$  contains the strain energy percentage data obtained from the FEA. Here, the objective is to determine the decomposed DMA's lumped loss factor result to determine the directional damping components that are independent of the sample geometry.

The full equation can be seen in Equation 3.17

$$\begin{Bmatrix} \eta_{\text{DMA}}^{(1)} \\ \eta_{\text{DMA}}^{(2)} \\ \eta_{\text{DMA}}^{(3)} \\ \eta_{\text{DMA}}^{(n)} \end{Bmatrix} = \begin{bmatrix} U_{\%11}^{(1)} & U_{\%12}^{(1)} + U_{\%13}^{(1)} & U_{\%22}^{(1)} + U_{\%33}^{(1)} & U_{\%23}^{(1)} \\ U_{\%11}^{(2)} & U_{\%12}^{(2)} + U_{\%13}^{(2)} & U_{\%22}^{(2)} + U_{\%33}^{(2)} & U_{\%23}^{(2)} \\ U_{\%11}^{(3)} & U_{\%12}^{(3)} + U_{\%13}^{(3)} & U_{\%22}^{(3)} + U_{\%33}^{(3)} & U_{\%23}^{(3)} \\ U_{\%11}^{(n)} & U_{\%12}^{(n)} + U_{\%13}^{(n)} & U_{\%22}^{(n)} + U_{\%33}^{(n)} & U_{\%23}^{(n)} \end{bmatrix} \begin{Bmatrix} \eta_{11} \\ \eta_{12} \\ \eta_{22} \\ \eta_{23} \end{Bmatrix} \quad (3.17)$$

The subsequent sections expand upon developing models that are based on the formulation in Equation 3.16 and using the UD, transverse and the combined UD-transverse loss factors obtained from DMA testing incorporating the associated strain energy percentage data from the FE analysis. The need to create these different models to develop a robust methodology for determining the directional damping characterisation will also

be substantiated.

### 3.5.1.1 Synergy of FEA and DMA: UD Modelling approach

The integration of DMA and FEA data, as detailed in Section 3.4.1, has enabled the construction of a detailed model that reflects the anisotropic nature of damping within composite materials. This novel model is built on several critical observations:

- The thickness of the sample emerges as a key factor, with substantial effects on the damping characteristics. This has been evidenced by the variation in damping values with changes in sample thickness, underscoring the need for precise thickness selection and control in sample preparation.
- The ability to now determine the matrix material damping contribution (as seen in  $\eta_{22}$  and  $\eta_{33}$ ). Even though in testing, the percentage of energy dissipated in these directions was very small compared to the fibre direction (with these being predominantly near the support and load application points), the larger damping magnitudes result in real influence. Strain Distribution is shown in Appendix E
- The study also acknowledges that minor inconsistencies in thickness (in the region of +/- 0.01 mm), likely arising from manufacturing tolerances, are not expected to skew the energy dissipation patterns drastically. This assumption is predicated on the premise that the average thickness was measured accurately.
- Strain range deviations within the functional limits of the testing apparatus have been found to have a minimal effect on the energy distribution among the various directions of strain. This reinforces the robustness of the composite material's damping properties under

### Chapter 3. Dynamic Mechanical Analysis for Damping Estimation

different operational strains.

- The consistency of environmental conditions during testing, specifically temperature and frequency, has proven to be necessary for reliable data. This research highlights the necessity for a controlled testing environment to limit the impact of extraneous variables on the damping results. Furthermore, although this study did not explore the influence of humidity, it could be a non-negligible factor in material damping; however, the Q800 did not possess the ability to control this property.

By considering the raw DMA results shown previously in Figure 3.8 and the strain energy distributions from FEA for the measured geometries (as seen in Appendix B), it is possible to solve for the different magnitudes of damping in the composite material through using Equation 3.16.

Using Equation 3.16, it was possible to quantify the variations in damping characteristics in different directions. The least-squares method was then applied to align the multiple data sets with the model. To solve Equation 3.16, the lsqin Matlab function, with a positive directional loss factor constraint, was applied and swept for each frequency. The strain energy contributions can be seen in Table 3.8

Table 3.8: Strain Energy (SE) Distribution Relative to Total Energy for Different Thicknesses - UD Samples

Thickness (mm)	SE (%) 11	SE (%) 22+33	SE (%) 12+13	SE (%) 23
2.49	98.86	0.26	0.86	0.01
3.00	98.50	0.28	1.22	0.01
3.50	98.06	0.30	1.63	0.01
3.99	97.51	0.37	2.11	0.01
4.50	96.85	0.48	2.67	0.01

### Chapter 3. Dynamic Mechanical Analysis for Damping Estimation

As can be seen in Table 3.8, the percentage of energy in the 11 direction is most prominent in the thinner samples and reduced slightly as the samples thickened. The percentage of energy in the transverse normal (22+33) and shear 23 directions was almost negligible in this analysis.

The results are shown in Figure 3.16, which concisely illustrate how each damping component plays out over the tested frequency range.

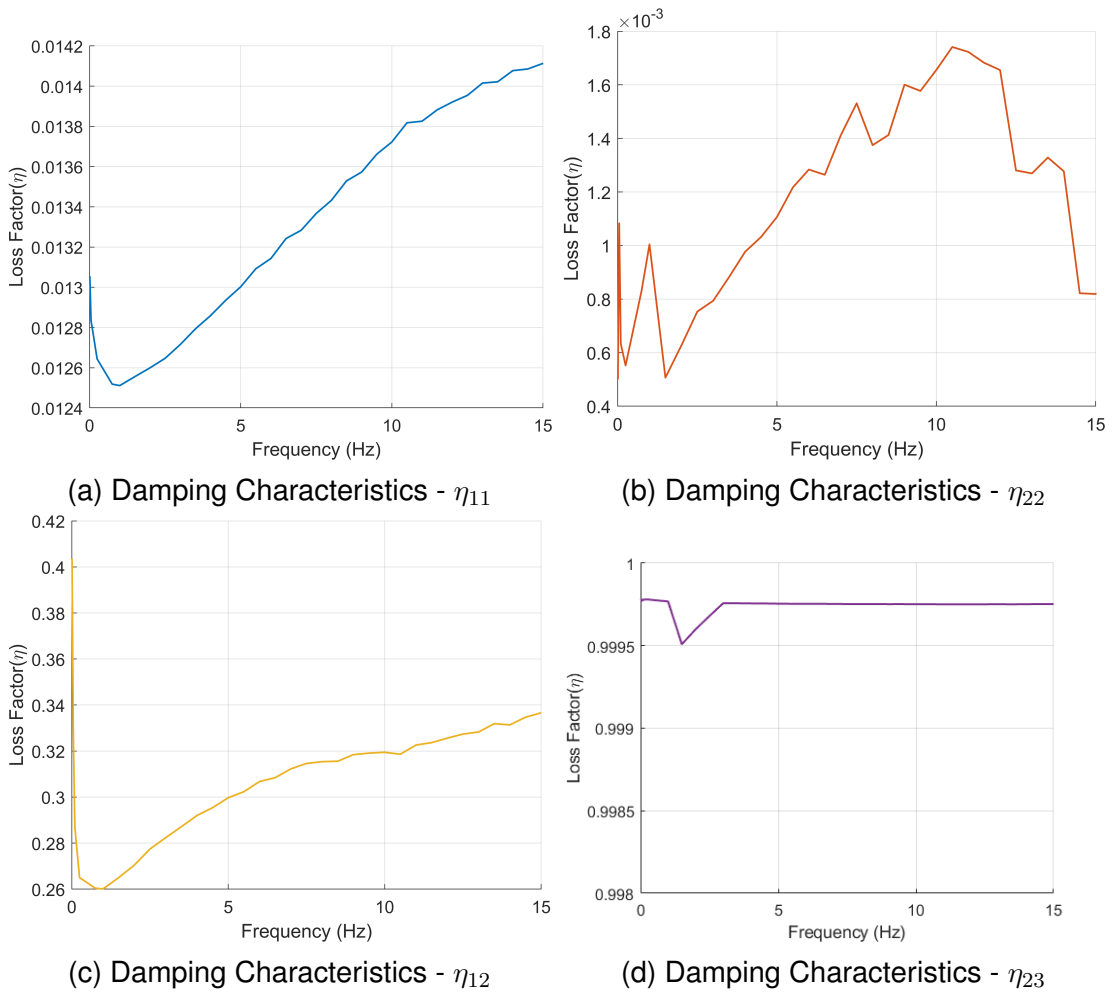


Figure 3.16: Processed Contributions of Damping Results against Frequency - UD Model (UD samples were solely responsible for the creation of this figure)

The results of the UD Model loss factor components are presented in

### Chapter 3. Dynamic Mechanical Analysis for Damping Estimation

Figure 3.16, which provides a clear visual representation of how each damping component varies across the tested frequency range.

The key observations are as follows:

- **Fibre Direction Damping ( $\eta_{11}$ ):** The fibre direction loss factor,  $\eta_{11}$ , has a logical trend and is within the expected magnitude for this material (as validated against internal SGRE testing), showing a minimum loss factor of approximately 0.0125, at 1 Hz.
- **Shear Damping ( $\eta_{12}$ ):** The shear loss factor,  $\eta_{12}$ , also follows a logical pattern, likely influenced by the non-negligible strain contribution from the 13 direction. This results in a minimum loss factor of 0.26 at 1 Hz.
- **Transverse Loss Factor ( $\eta_{22}$ ):** The transverse loss factor,  $\eta_{22}$ , has a near-negligible shear percentage, accounting for less than 1% of the total strain energy. This low proportional contribution also introduces uncertainty into the accuracy of these results.
- **Shear Damping ( $\eta_{23}$ ):** The shear loss factor,  $\eta_{23}$ , result is significantly larger in magnitude than the fibre direction and transverse contributions, despite representing less than 0.1% of the total strain energy. This raised concerns about the model's ability to accurately predict  $\eta_{23}$  data. There is also a very slight drop present within the results, however, this fluctuation is approximately 0.1% and is therefore considered negligible.

#### **Improved Representation Through Directional Damping Quantification**

A key strength of the integrated DMA/FEA methodology lies in its ability to resolve individual directional damping components ( $\eta_{11}, \eta_{22}, \eta_{12}, \eta_{23}$ ) by accounting for the anisotropic strain energy distribution within the composite samples. Unlike traditional DMA testing, which typically outputs a scalar damping metric averaged across the sample response, this combined

### Chapter 3. Dynamic Mechanical Analysis for Damping Estimation

approach uses finite element strain energy ratios to decompose the measured global damping into physically meaningful directional contributions.

This enables a direct comparison between modes of energy dissipation - for instance, the model quantitatively shows that  $\sim 97\%$  of strain energy is concentrated in the fibre direction for thin UD samples (see Table 3.8), while less than 1% is attributable to transverse and through-thickness directions. Yet, due to the significantly higher local loss factors in the transverse and shear modes, their influence on total damping cannot be neglected - a distinction not easily captured in conventional methods.

The measurable advantage is therefore the ability to:

- Disaggregate global damping into directional loss factors ( $\eta_{ij}$ ) - a capability not present in standalone DMA or EMA.
- Attribute damping contributions to specific deformation mechanisms, validated through FEA strain energy partitioning.
- Compare damping directionality across geometries and frequencies, as visualised in Figure 3.16, enhancing the understanding of material behaviour under complex loading.

By quantifying damping anisotropy with other industrial data (provided by SGRE), this method supports more informed material design choices for applications where specific directional damping behaviour is critical, such as in wind turbine blades or aerospace laminates. This distinction in damping behaviours, now validated across methods and industrial benchmarks, is crucial for designing and optimising composite materials where directional damping properties dominate performance requirements. The analysis highlights that the fibre direction (11) and shear-related (12 and 13) damping dominate. At the same time, the transverse and out-of-plane shear

## Chapter 3. Dynamic Mechanical Analysis for Damping Estimation

contributions are minimal, introducing some uncertainty due to their low proportional strain energy. Incorporating a transverse mechanical analysis could enhance the understanding of these lesser contributions, providing additional clarity and potentially uncovering information not previously available. This approach would further confirm the observed damping tendencies of the material and improve the reliability of the model predictions for all directional components.

### **3.5.1.2 Synergy of FEA and DMA: Transverse Modelling approach**

Transverse testing is particularly important due to the relatively minor contributions of the transverse (22) and shear (23) components to the overall strain energy, less than 0.1% and 0.01%, respectively. These findings raise the question of whether the UD method alone is sufficient to characterise the composite material's damping properties or if transverse behaviour plays a significant, yet underappreciated, role.

By running transverse sample tests, it was anticipated that the lower contributions observed in the UD Model could be enhanced, thereby increasing confidence in the model. It was decided that the fibre direction would align with the sample width, as machining the transverse direction in the thickness orientation would be significantly more challenging. This fibre orientation was selected to experimentally isolate and amplify the transverse (22) and out-of-plane shear (23) damping components, which were found to contribute minimally in the unidirectional configuration. While aligning fibres perpendicular to the span is not typical in standard structural loading configurations, this arrangement was chosen as a practical and controlled way to represent the transverse direction in the material coordinate system. Attempting to machine and test specimens with fibres oriented along the thickness direction (through-thickness configuration) would introduce

### Chapter 3. Dynamic Mechanical Analysis for Damping Estimation

significant manufacturing difficulties and could lead to geometrical inconsistencies or premature failure due to limited fibre support. Therefore, the transverse layout in this study was designed not to mimic a common structural application, but to enable the evaluation of material behaviour along the 22 and 23 directions within a feasible testing setup. This directional isolation supports the goal of resolving the full anisotropic damping tensor by combining insights from both fibre-aligned and fibre-perpendicular samples.

The third configuration would be of interest for testing, but this is not within the current test plan. The layout for the transverse test is shown in Figure 3.17, retaining the original coordinate system with respect to the fibre direction.

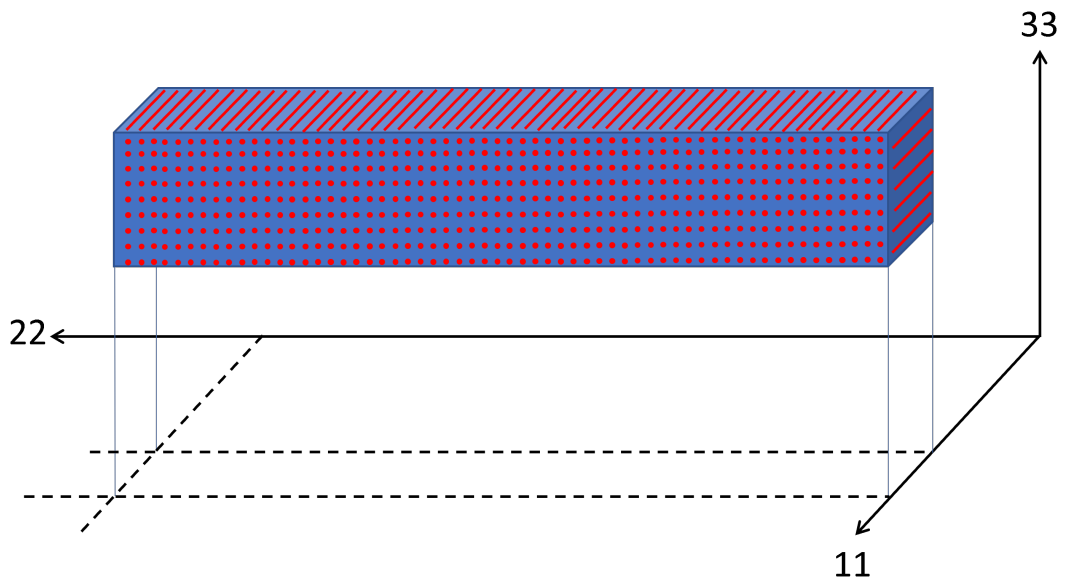


Figure 3.17: Transverse Layout - according to fibre direction coordinate system

As part of the study, five transverse IMA samples were tested using the same experimental methodology. The DMA tests were conducted, and the initial findings are presented as raw damping results in Figure 3.18.

### Chapter 3. Dynamic Mechanical Analysis for Damping Estimation

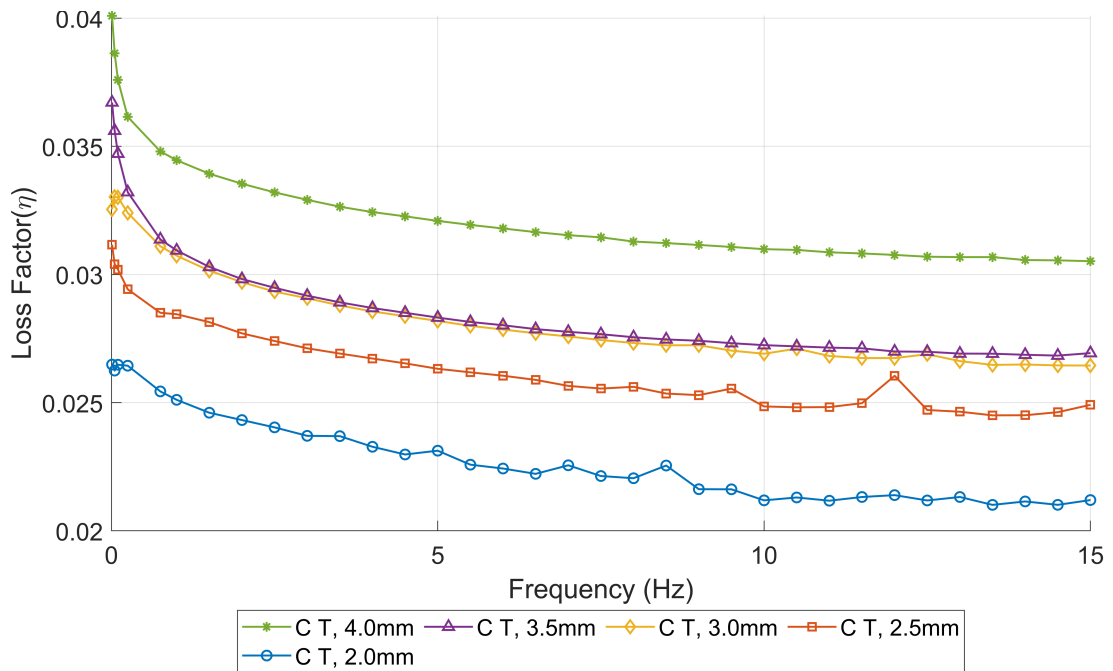


Figure 3.18: Raw Damping Results from Transverse Method - C denotes Carbon Fibre Composite, T denotes Transverse Sample

The next step in this process involved using FEA to determine the strain energy contributions of transverse samples undergoing DMA testing. To achieve this, the original FEA model used for the UD samples was reused with a single key modification: the fibre orientation in the material definition was rotated such that the fibre direction aligned with the width direction of the specimen, thereby replicating the transverse test configuration. This adjustment reflects the practical orientation of the transverse DMA specimens, in which the fibres were aligned perpendicular to the loading axis. Aside from this material axis rotation, all other model parameters, including geometry, boundary conditions (as in Table 3.3), mesh density, load application, and solver settings, remained consistent with the original UD model. This ensured that any changes observed in the strain energy distribution were solely due to the change in fibre orientation, not other modelling variables.

### Chapter 3. Dynamic Mechanical Analysis for Damping Estimation

Once the FEA simulations were complete, the same strain energy post-processing methodology was applied. Directional strain energy components ( $U_{11}, U_{22}, U_{33}, U_{12}, U_{13}, U_{23}$ ) were extracted from each model and normalised against the total strain energy to yield percentage contributions. This data is presented in Table 3.9 and can be directly compared to the results from the UD model (Table 3.8). These values play a critical role in identifying the energy dissipation mechanisms dominant in transverse configurations and validating the applicability of the damping decomposition model across different orientations.

Table 3.9: Strain Energy (SE) Distribution Relative to Total Energy for Different Thicknesses - Transverse Samples

Thickness (mm)	SE (%) 11	SE (%) 22+33	SE (%) 12+13	SE (%) 23
2.47	0.09	99.21	0.02	0.78
2.99	0.11	98.85	0.02	1.15
3.50	0.13	98.42	0.02	1.58
3.94	0.15	97.99	0.02	2.01
4.45	0.18	97.43	0.03	2.56

The updated Transverse Model can be seen in Equation 3.18.

$$\begin{Bmatrix} \eta_{\text{DMA}, T}^{(2)} \\ \eta_{\text{DMA}, T}^{(2.5)} \\ \eta_{\text{DMA}, T}^{(3)} \\ \eta_{\text{DMA}, T}^{(3.5)} \\ \eta_{\text{DMA}, T}^{(4)} \end{Bmatrix} = \begin{bmatrix} U_{\%11,T}^{(2)} & U_{\%12,T}^{(2)} + U_{\%13,T}^{(2)} & U_{\%22,T}^{(2)} + U_{\%33,T}^{(2)} & U_{\%23,T}^{(2)} \\ U_{\%11,T}^{(2.5)} & U_{\%12,T}^{(2.5)} + U_{\%13,T}^{(2.5)} & U_{\%22,T}^{(2.5)} + U_{\%33,T}^{(2.5)} & U_{\%23,T}^{(2.5)} \\ U_{\%11,T}^{(3)} & U_{\%12,T}^{(3)} + U_{\%13,T}^{(3)} & U_{\%22,T}^{(3)} + U_{\%33,T}^{(3)} & U_{\%23,T}^{(3)} \\ U_{\%11,T}^{(3.5)} & U_{\%12,T}^{(3.5)} + U_{\%13,T}^{(3.5)} & U_{\%22,T}^{(3.5)} + U_{\%33,T}^{(3.5)} & U_{\%23,T}^{(3.5)} \\ U_{\%11,T}^{(4)} & U_{\%12,T}^{(4)} + U_{\%13,T}^{(4)} & U_{\%22,T}^{(4)} + U_{\%33,T}^{(4)} & U_{\%23,T}^{(4)} \end{bmatrix} \begin{Bmatrix} \eta_{11} \\ \eta_{12} \\ \eta_{22} \\ \eta_{23} \end{Bmatrix} \quad (3.18)$$

Following the strain energy analysis, the processed contributions of damping

### Chapter 3. Dynamic Mechanical Analysis for Damping Estimation

results against frequency are presented, illustrating the damping behaviour over the selected range of frequencies and material orientations, as shown in Figure 3.19.

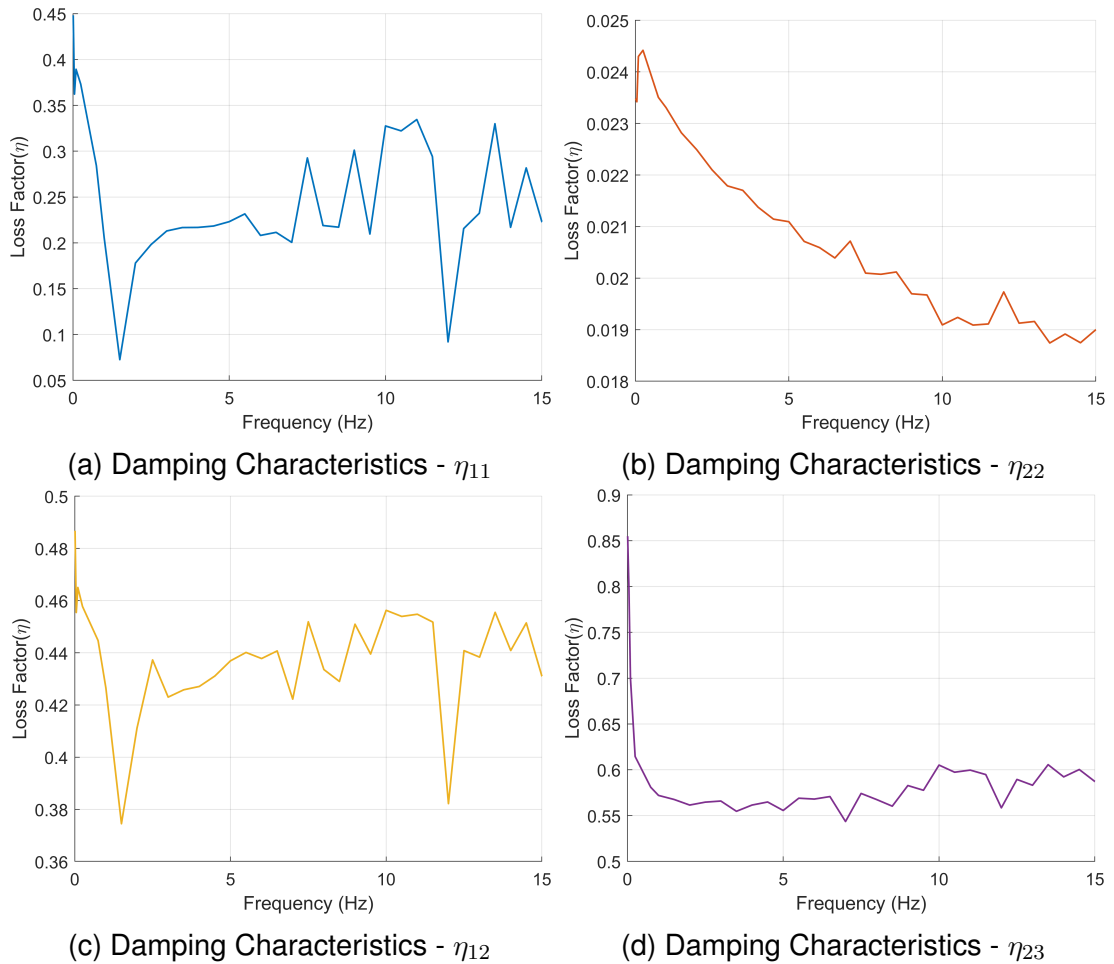


Figure 3.19: Processed Contributions of Damping Results against Frequency

The results of the Transverse Model loss factor components are presented in Figure 3.19, which provides a clear visual representation of how each damping factor varies across the tested frequency range.

The key observations for the transverse damping results are as follows:

- **Fibre Direction Damping ( $\eta_{11}$ ):** The fibre direction loss factor,  $\eta_{11}$ , does

### Chapter 3. Dynamic Mechanical Analysis for Damping Estimation

not exhibit the expected trend. This behaviour is likely due to the strain energy in the 11 direction having a minimal influence, accounting for less than 0.2%. This low proportional contribution also introduces uncertainty into the results.

- **Shear Damping ( $\eta_{12}$ ):** The shear loss factor,  $\eta_{12}$ , in this case, also does not exhibit the expected trend. This was predicted to be due to a low strain energy contribution, which is approximately 0.02%.
- **Transverse Loss Factor ( $\eta_{22}$ ):** The transverse loss factor,  $\eta_{22}$ , on the other hand, showed a consistent trend within the Transverse Model results. This behaviour was most likely due to the increased strain energy in this direction. The result showed a minimum loss factor of 0.019 at 15 Hz and a value of approximately 0.0235 at 1 Hz.
- **Shear Damping ( $\eta_{23}$ ):** The shear loss factor,  $\eta_{23}$ , displayed a more logical damping trend, with its contribution increasing above 2.5% for the 4 mm sample. The result showed a loss factor of 0.58 at 15 Hz and 0.57 at 1 Hz.

As demonstrated in Figure 3.19, the results in the direction with the most prominent strain energy contribution, namely the sample length direction, appeared to be more consistent with expectations compared to Figure 3.16b. However, the fibre direction component,  $\eta_{11}$ , did not exhibit the expected trend, likely due to its minimal strain energy contribution, which introduced uncertainty into the results. Similarly, the shear component  $\eta_{12}$  showed a less predictable pattern, also attributed to a low strain energy contribution. On the other hand, the transverse loss factor,  $\eta_{22}$ , displayed a stable and logical trend within the Transverse Model results, likely due to the increased strain energy in this direction. Finally, the shear-related damping,  $\eta_{23}$ , showed a more consistent trend with a significant contribution for thicker samples.

### Chapter 3. Dynamic Mechanical Analysis for Damping Estimation

This section provides valuable insights into the transverse damping characteristics of the samples, offering a contrasting yet complementary perspective to the fibre direction damping results. The transverse orientation underscores the importance of directional strain energy contributions in accurately characterising damping behaviours across different material orientations.

The following summarises the key distinctions between the UD and transverse damping models:

- **Fibre Direction Damping ( $\eta_{11}$ ):** In the UD Model,  $\eta_{11}$  exhibited a logical trend with a minimum loss factor of 0.0125 at 1 Hz, reflecting the significant strain energy contribution in the fibre direction. In contrast, the Transverse Model showed no clear trend for  $\eta_{11}$ , likely due to its minimal strain energy contribution (less than 0.2%).
- **Shear Damping ( $\eta_{12}$ ):** The UD Model captured  $\eta_{12}$  more effectively, showing a minimum loss factor of 0.26 at 1 Hz, however, the Transverse Model failed to show a consistent trend for  $\eta_{12}$  due to its negligible strain energy contribution (approximately 0.02%).
- **Transverse Loss Factor ( $\eta_{22}$ ):**  $\eta_{22}$  is inconsistent in the UD Model, contributing less than 1% of the total strain energy. The Transverse Model,  $\eta_{22}$  followed a logical trend, with loss factors increasing from 0.019 at 15 Hz to 0.0235 at 1 Hz, reflecting the higher strain energy contribution in this direction.
- **Shear Damping ( $\eta_{23}$ ):**  $\eta_{23}$  in the UD Model was larger in magnitude but less reliable due to its minimal strain energy contribution (less than 0.1%). The Transverse Model showed a more logical trend for  $\eta_{23}$ , particularly for thicker samples, with loss factors of 0.58 at 15 Hz and 0.57 at 1 Hz.

## Chapter 3. Dynamic Mechanical Analysis for Damping Estimation

In summary, the UD Model captures damping behaviour more effectively in the fibre and shear directions ( $\eta_{11}$  and  $\eta_{12}$ ), while the Transverse Model excels in predicting transverse and shear-related damping ( $\eta_{22}$  and  $\eta_{23}$ ). These findings highlight the complementary nature of the two models and the importance of considering both orientations for a more comprehensive analysis.

To further enhance prediction accuracy and evaluate the validity of the individual models, a Combined Model integrating both UD and transverse sample results was developed. This combined approach allowed for a complete analysis of the material's damping behaviour, capturing the complex interplay between orientations and improving confidence in the predictions.

### **3.5.1.3 Synergy of FEA and DMA: Combined UD-Transverse Modelling Approach**

Within the previous sections, it has been demonstrated that the FEA-assisted DMA method provided valuable context to the standalone DMA results by incorporating strain energy contributions across different orientations. However, limitations in the energy contribution from certain directions, particularly those with very low strain energy percentages, reduced confidence in some of the directional damping predictions. Combining data from both the UD and Transverse Models addresses these limitations, leveraging the strengths of each model to provide a more robust analysis. The combined strain energy contributions across different thicknesses are presented in Table 3.10.

### Chapter 3. Dynamic Mechanical Analysis for Damping Estimation

Table 3.10: Strain Energy (SE) Distribution Relative to Total Energy for Different Thicknesses - All Samples

Sample Type	Thickness (mm)	SE (%) 11	SE (%) 22+33	SE (%) 12+13	SE (%) 23
UD	2.49	98.86	0.26	0.86	0.01
UD	3.00	98.50	0.28	1.22	0.01
UD	3.50	98.06	0.30	1.63	0.01
UD	3.99	97.51	0.37	2.11	0.01
UD	4.50	96.85	0.48	2.67	0.01
T	2.47	0.09	99.21	0.02	0.78
T	2.99	0.11	98.85	0.02	1.15
T	3.50	0.13	98.42	0.02	1.58
T	3.94	0.15	97.99	0.02	2.01
T	4.45	0.18	97.43	0.03	2.56

When analysing the data in Table 3.10, it is evident that the damping components in the UD direction ( $\eta_{11}$ ) and the transverse directions ( $\eta_{22}$  and  $\eta_{33}$ ) can be evaluated with higher confidence, as they account for the majority of the energy dissipation. The minor strain energy contributions from shear directions ( $\eta_{12} + \eta_{13}$  and  $\eta_{23}$ ) may still provide additional insights into the material's behaviour, despite their limited proportional contributions. By leveraging the complementary strengths of both datasets, this model offers a more comprehensive analysis of the damping behaviour. The resulting Combined Model is expressed in Equation 3.19.

$$\eta_{\text{DMA UD + T}} = \mathbf{U}_{\% \text{UD, T}} \eta_{\text{xy}} \quad (3.19)$$

where,

### Chapter 3. Dynamic Mechanical Analysis for Damping Estimation

$$\eta_{\text{DMA, UD+T}} = \left\{ \begin{array}{l} \eta_{\text{DMA, UD}}^{(2)} \\ \eta_{\text{DMA, UD}}^{(2.5)} \\ \eta_{\text{DMA, UD}}^{(3)} \\ \eta_{\text{DMA, UD}}^{(3.5)} \\ \eta_{\text{DMA, UD}}^{(4)} \\ \eta_{\text{DMA, T}}^{(2)} \\ \eta_{\text{DMA, T}}^{(2.5)} \\ \eta_{\text{DMA, T}}^{(3)} \\ \eta_{\text{DMA, T}}^{(3.5)} \\ \eta_{\text{DMA, T}}^{(4)} \end{array} \right\}$$

$$\mathbf{U}_{\% \text{UD,T}} = [\mathbf{U1} \quad \mathbf{U2} \quad \mathbf{U3} \quad \mathbf{U4}]$$

$$\mathbf{U1} = \left\{ \begin{array}{l} U_{\%11, \text{UD}}^{(2)} \\ U_{\%11, \text{UD}}^{(2.5)} \\ U_{\%11, \text{UD}}^{(3)} \\ U_{\%11, \text{UD}}^{(3.5)} \\ U_{\%11, \text{UD}}^{(4)} \\ U_{\%11, \text{T}}^{(2)} \\ U_{\%11, \text{T}}^{(2.5)} \\ U_{\%11, \text{T}}^{(3)} \\ U_{\%11, \text{T}}^{(3.5)} \\ U_{\%11, \text{T}}^{(4)} \end{array} \right\} \quad \mathbf{U2} = \left\{ \begin{array}{l} U_{\%12, \text{UD}}^{(2)} + U_{\%13, \text{UD}}^{(2)} \\ U_{\%12, \text{UD}}^{(2.5)} + U_{\%13, \text{UD}}^{(2.5)} \\ U_{\%12, \text{UD}}^{(3)} + U_{\%13, \text{UD}}^{(3)} \\ U_{\%12, \text{UD}}^{(3.5)} + U_{\%13, \text{UD}}^{(3.5)} \\ U_{\%12, \text{UD}}^{(4)} + U_{\%13, \text{UD}}^{(4)} \\ U_{\%12, \text{T}}^{(2)} + U_{\%13, \text{T}}^{(2)} \\ U_{\%12, \text{T}}^{(2.5)} + U_{\%13, \text{T}}^{(2.5)} \\ U_{\%12, \text{T}}^{(3)} + U_{\%13, \text{T}}^{(3)} \\ U_{\%12, \text{T}}^{(3.5)} + U_{\%13, \text{T}}^{(3.5)} \\ U_{\%12, \text{T}}^{(4)} + U_{\%13, \text{T}}^{(4)} \end{array} \right\}$$

### Chapter 3. Dynamic Mechanical Analysis for Damping Estimation

$$\mathbf{U3} = \begin{Bmatrix} U_{\%22,UD}^{(2)} + U_{\%33,UD}^{(2)} \\ U_{\%22,UD}^{(2.5)} + U_{\%33,UD}^{(2.5)} \\ U_{\%22,UD}^{(3)} + U_{\%33,UD}^{(3)} \\ U_{\%22,UD}^{(3.5)} + U_{\%33,UD}^{(3.5)} \\ U_{\%22,UD}^{(4)} + U_{\%33,UD}^{(4)} \\ U_{\%22,T}^{(2)} + U_{\%33,T}^{(2)} \\ U_{\%22,T}^{(2.5)} + U_{\%33,T}^{(2.5)} \\ U_{\%22,T}^{(3)} + U_{\%33,T}^{(3)} \\ U_{\%22,T}^{(3.5)} + U_{\%33,T}^{(3.5)} \\ U_{\%22,T}^{(4)} + U_{\%33,T}^{(4)} \end{Bmatrix} \quad \mathbf{U4} = \begin{Bmatrix} U_{\%23,UD}^{(2)} \\ U_{\%23,UD}^{(2.5)} \\ U_{\%23,UD}^{(3)} \\ U_{\%23,UD}^{(3.5)} \\ U_{\%23,UD}^{(4)} \\ U_{\%23,T}^{(2)} \\ U_{\%23,T}^{(2.5)} \\ U_{\%23,T}^{(3)} \\ U_{\%23,T}^{(3.5)} \\ U_{\%23,T}^{(4)} \end{Bmatrix}$$

$$\eta_{xy} = \left\{ \eta_{11} \ \eta_{12} \ \eta_{22} \ \eta_{23} \right\}^T$$

The full equation can be seen in Equation 3.20

$$\begin{Bmatrix} \eta_{DMA, UD}^{(2)} \\ \eta_{DMA, UD}^{(2.5)} \\ \eta_{DMA, UD}^{(3)} \\ \eta_{DMA, UD}^{(3.5)} \\ \eta_{DMA, UD}^{(4)} \\ \eta_{DMA, T}^{(2)} \\ \eta_{DMA, T}^{(2.5)} \\ \eta_{DMA, T}^{(3)} \\ \eta_{DMA, T}^{(3.5)} \\ \eta_{DMA, T}^{(4)} \end{Bmatrix} = \begin{bmatrix} U_{\%11,UD}^{(2)} & U_{\%12,UD}^{(2)} + U_{\%13,UD}^{(2)} & U_{\%22,UD}^{(2)} + U_{\%33,UD}^{(2)} & U_{\%23,UD}^{(2)} \\ U_{\%11,UD}^{(2.5)} & U_{\%12,UD}^{(2.5)} + U_{\%13,UD}^{(2.5)} & U_{\%22,UD}^{(2.5)} + U_{\%33,UD}^{(2.5)} & U_{\%23,UD}^{(2.5)} \\ U_{\%11,UD}^{(3)} & U_{\%12,UD}^{(3)} + U_{\%13,UD}^{(3)} & U_{\%22,UD}^{(3)} + U_{\%33,UD}^{(3)} & U_{\%23,UD}^{(3)} \\ U_{\%11,UD}^{(3.5)} & U_{\%12,UD}^{(3.5)} + U_{\%13,UD}^{(3.5)} & U_{\%22,UD}^{(3.5)} + U_{\%33,UD}^{(3.5)} & U_{\%23,UD}^{(3.5)} \\ U_{\%11,UD}^{(4)} & U_{\%12,UD}^{(4)} + U_{\%13,UD}^{(4)} & U_{\%22,UD}^{(4)} + U_{\%33,UD}^{(4)} & U_{\%23,UD}^{(4)} \\ U_{\%11,T}^{(2)} & U_{\%12,T}^{(2)} + U_{\%13,T}^{(2)} & U_{\%22,T}^{(2)} + U_{\%33,T}^{(2)} & U_{\%23,T}^{(2)} \\ U_{\%11,T}^{(2.5)} & U_{\%12,T}^{(2.5)} + U_{\%13,T}^{(2.5)} & U_{\%22,T}^{(2.5)} + U_{\%33,T}^{(2.5)} & U_{\%23,T}^{(2.5)} \\ U_{\%11,T}^{(3)} & U_{\%12,T}^{(3)} + U_{\%13,T}^{(3)} & U_{\%22,T}^{(3)} + U_{\%33,T}^{(3)} & U_{\%23,T}^{(3)} \\ U_{\%11,T}^{(3.5)} & U_{\%12,T}^{(3.5)} + U_{\%13,T}^{(3.5)} & U_{\%22,T}^{(3.5)} + U_{\%33,T}^{(3.5)} & U_{\%23,T}^{(3.5)} \\ U_{\%11,T}^{(4)} & U_{\%12,T}^{(4)} + U_{\%13,T}^{(4)} & U_{\%22,T}^{(4)} + U_{\%33,T}^{(4)} & U_{\%23,T}^{(4)} \end{bmatrix} \begin{Bmatrix} \eta_{11} \\ \eta_{12} \\ \eta_{22} \\ \eta_{23} \end{Bmatrix} \quad (3.20)$$

### Chapter 3. Dynamic Mechanical Analysis for Damping Estimation

Using this newly developed, more complete model, where the accuracy of the fibre directions and transverse directional damping components may be more accurately predicted.

Following the integration of strain energy data and the DMA testing results, the Combined Model was developed to process and compute the damping contributions against frequency. This model uses results from both the UD and transverse datasets, ensuring a more comprehensive representation of the material's behaviour. The resulting damping behaviour, spanning a range of frequencies and orientations, is presented in Figure 3.20.

### Chapter 3. Dynamic Mechanical Analysis for Damping Estimation

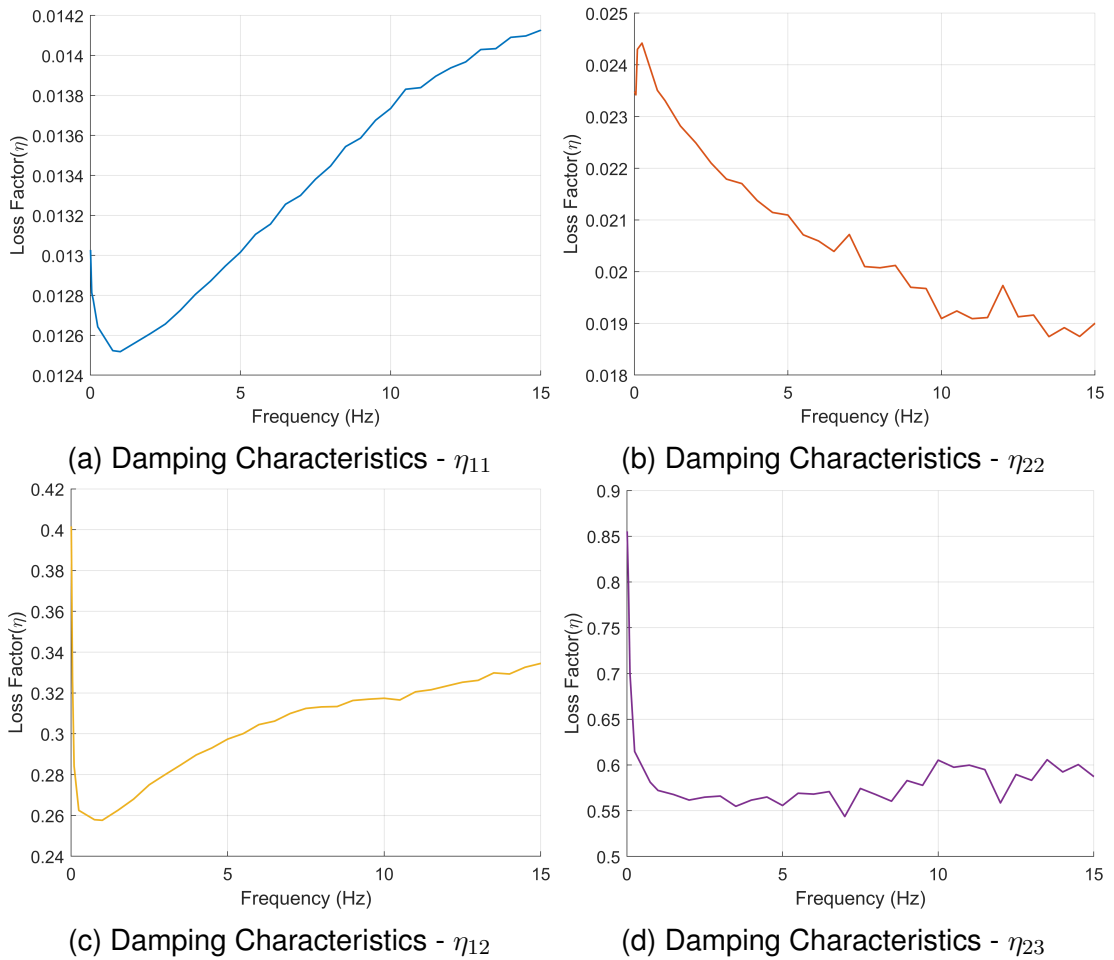


Figure 3.20: Processed Contributions of Damping Results against Frequency - Combined Model (Both UD and Transverse samples were used in the creation of this figure)

The results of the Combined Model loss factor components are presented in Figure 3.20, which provides a clear visual representation of how each damping component varies across the tested frequency range.

The key observations for the combined damping results are as follows:

- **Fibre Direction Damping ( $\eta_{11}$ ):** The fibre direction loss factor,  $\eta_{11}$ , closely mirrors the results from the UD Model alone.
- **Shear Damping ( $\eta_{12}$ ):** The shear loss factor,  $\eta_{12}$ , also closely mirrors the

### Chapter 3. Dynamic Mechanical Analysis for Damping Estimation

UD Model, with only a very minor reduction observed.

- **Transverse Loss Factor ( $\eta_{22}$ ):** The transverse loss factor,  $\eta_{22}$ , closely mirrors the results from the Transverse Model alone.
- **Shear Damping ( $\eta_{23}$ ):** The shear loss factor,  $\eta_{23}$ , also closely mirrors the Transverse Model, with only a very minor reduction observed.
- **Greater Consistency and Reduced Uncertainty:** By merging data from both UD and transverse samples, the Combined Model leverages two complementary sets of strain-energy distributions. This broader dataset reduces uncertainties, particularly for directions that previously exhibited negligible strain energy in the UD or T only models, thereby improving the reliability of the damping estimates.

The Combined Model results indicate that, although two of the four damping contributions in the standalone UD and Transverse Models exhibit significant deviations from expected trends, likely due to their very low strain energy contributions, these discrepancies are mitigated when the models are integrated into the combined approach. However, this improvement has only a minor effect on the overall predicted damping values (less than 1%). This suggests that the fibre direction ( $\eta_{11}$ ) and shear ( $\eta_{12}$ ) damping components are the most important for achieving results for the UD Model, while the transverse ( $\eta_{22}$ ) and shear-related ( $\eta_{23}$ ) components play a more significant role in the Transverse Model.

Given that the primary (normal) results show minimal variation when using the Combined Model, it was concluded that the standalone UD and Transverse Models are sufficient for estimating their respective normal damping components. The Combined Model, therefore, serves as a valuable validation tool, with its necessity depending on the level of precision required for specific

applications.

#### **3.5.1.4 Development of the Directional Simplified Model**

To allow for the widespread adoption of a methodology like the one presented in this thesis, it is essential to examine whether the underlying models can be simplified without compromising the accuracy of the results. To investigate the primary damping contributions further, a simplified model was developed for both the UD and Transverse cases, referred to as the Directional Simplified Models. These models consider only 1 sample set at a time and isolate the key directional inputs, focusing solely on their contribution to the corresponding damping behaviour.

For the UD case, only the strain energy inputs from the 11 and 13 directions were considered to calculate the damping in the 11 direction. Similarly, for the Transverse case, only the strain energy inputs from the 22 and 23 directions were used to calculate the damping in the 22 direction. By limiting the model to these primary contributions, this approach allows for a more focused analysis of the directional damping mechanisms. The results of this analysis provide insight into the sufficiency of individual directional contributions and help validate the importance of including additional strain directions in more comprehensive models.

The results of the Directional Simplified Models (DSM) for the UD and Transverse cases are presented in Figures 3.21 and 3.22, respectively. These figures compare the damping behaviour across frequencies for the directional simplified models, the original models, and the Combined Model.

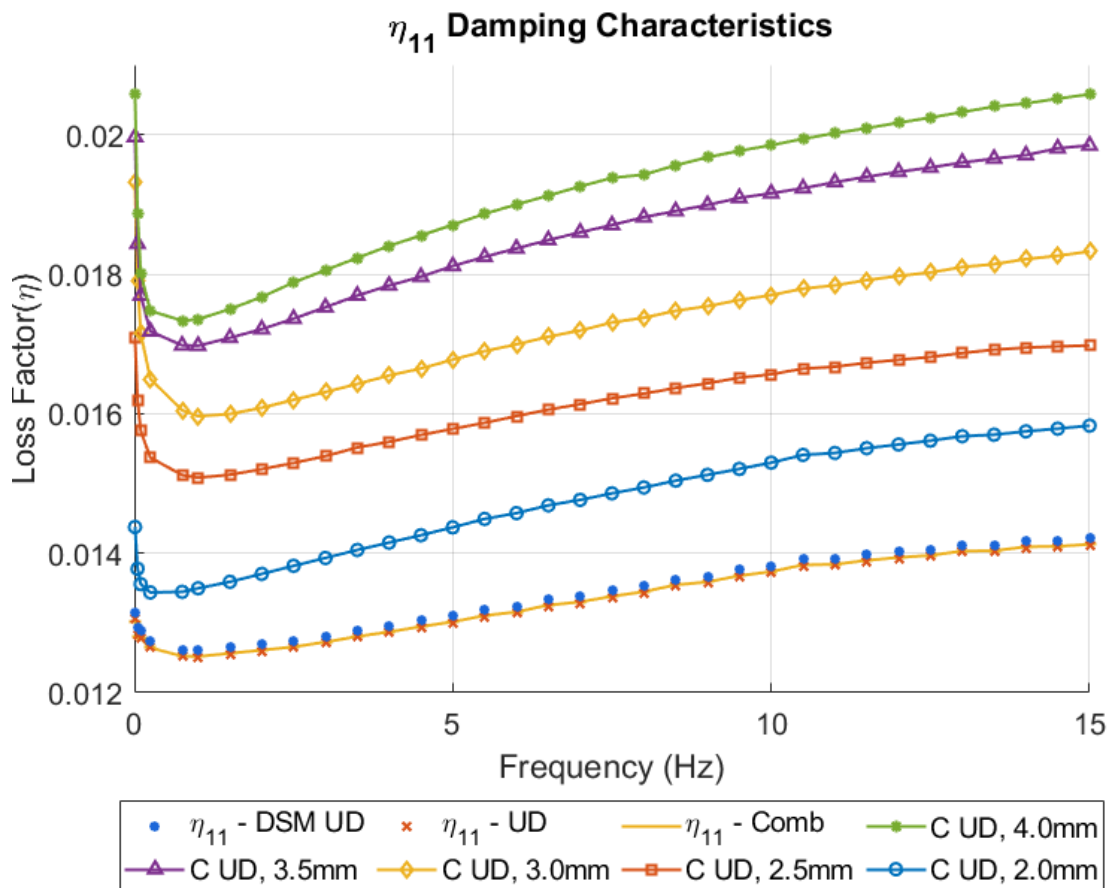


Figure 3.21: Damping Characteristics for  $\eta_{11}$  across all models, including the Directional Simplified Model (DSM UD), the full UD Model, and the Combined Model (Comb) - C UD represents Carbon Unidirectional

Figure 3.21 shows that the Directional Simplified Model for  $\eta_{11}$  provides results that are nearly identical to those of the full UD Model and the Combined Model. This indicates that the strain energy contributions from the 11 and 13 directions are sufficient to characterise the damping behaviour in the fibre direction. The consistency across models confirms that additional strain energy components, which may contribute minimally in the UD case, do not significantly influence the results for  $\eta_{11}$ . These findings highlight the robustness of the UD Model in accurately predicting damping in the fibre direction without requiring extensive additional data.

### Chapter 3. Dynamic Mechanical Analysis for Damping Estimation

Additionally, the average difference between the Combined Model, across all frequencies, and the 2 mm UD sample DMA results used as the initial input was calculated to be 10.38%. While this variation may appear notable, the implications are further explored and discussed in subsequent sections.

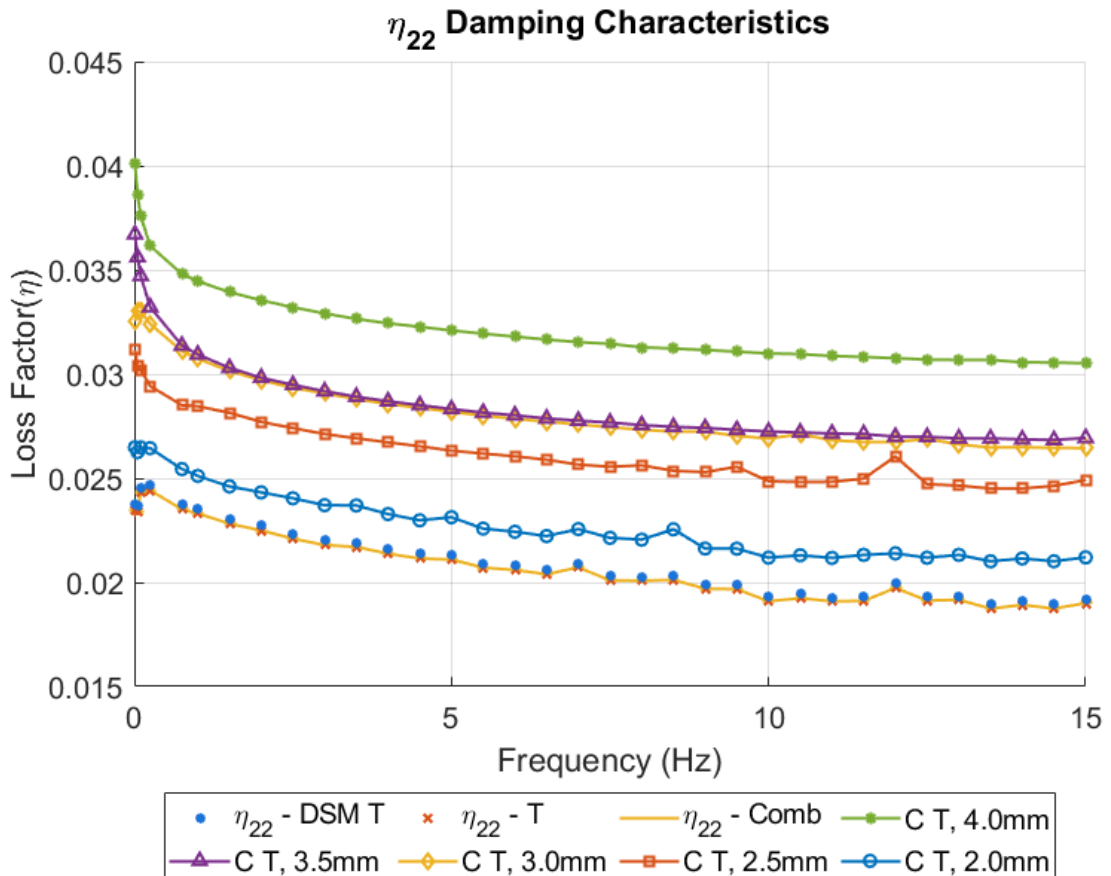


Figure 3.22: Damping Characteristics for  $\eta_{22}$  across all models, including the Directional Simplified Model (DSM Transverse), the full Transverse Model, and the Combined Model C T represents Carbon Transverse.

Figure 3.22 shows that the Directional Simplified Model for  $\eta_{22}$  produces results that closely align with the full Transverse Model and the Combined Model. This indicates that the strain energy contributions from the 22 and 23 directions are critical and sufficient to determine the damping behaviour in the transverse direction. The results validate the importance of these primary contributions

## Chapter 3. Dynamic Mechanical Analysis for Damping Estimation

in characterising  $\eta_{22}$  and suggest that incorporating additional strain energy components has minimal impact on the predictions for the transverse direction.

The results from Figures 3.21 and 3.22 demonstrate the ability of the Directional Simplified Models to accurately predict damping behaviour in the fibre and transverse directions, respectively (within 1% of the Combined Model). These findings suggest that for practical applications, the standalone simplified models may be sufficient for directional damping predictions, reducing computational complexity and maintaining accuracy. However, the Combined Model remains valuable as a validation tool to confirm the robustness of these simplified approaches.

### 3.5.2 Evaluation of the Results

The analysis conducted has demonstrated that the UD and Transverse Simplified Methods are suitable for accurately predicting damping behaviour in their respective directions. However, to ensure the robustness of the proposed methods and models, additional evaluations are required. These evaluations aim to validate the models further and assess their reliability across varying scenarios.

Firstly, the Combined Model results are used to generate predicted DMA results for the tested geometries. These predictions are then compared with the original experimental DMA data. This comparison helps identify any discrepancies and evaluate the Combined Model's ability to replicate experimental behaviour. Secondly, the effect of excluding the thinnest and thickest samples from the dataset was examined. This analysis assesses how sensitive the models were to variations in the range of input data. By removing these extreme cases, the results show the extent to which the model's predictions were influenced by the range of geometries included in

## Chapter 3. Dynamic Mechanical Analysis for Damping Estimation

the dataset.

Through these two approaches, the robustness of the simplified and Combined Models was validated, ensuring that the proposed methodology was both reliable and adaptable for various applications.

To evaluate the robustness of the Combined Model, the predicted damping results were generated for the exact geometries used in the DMA tests. These predictions were then compared against the original DMA data to assess how accurately the model replicates experimental observations.

The results of this comparison are presented in Figures 3.23 and 3.24, which display the damping characteristics for the UD and Transverse composite materials, respectively.

### **3.5.2.1 Comparison of Generated Results and Input DMA Data**

To evaluate the robustness of the Combined Model, the predicted damping results were generated for the exact geometries used in the DMA tests. These predictions were then compared against the original DMA data to assess how accurately the model replicates experimental observations.

The results of this comparison are presented in Figures 3.23 and 3.24, which display the damping characteristics for the UD and Transverse composite materials, respectively.

### Chapter 3. Dynamic Mechanical Analysis for Damping Estimation

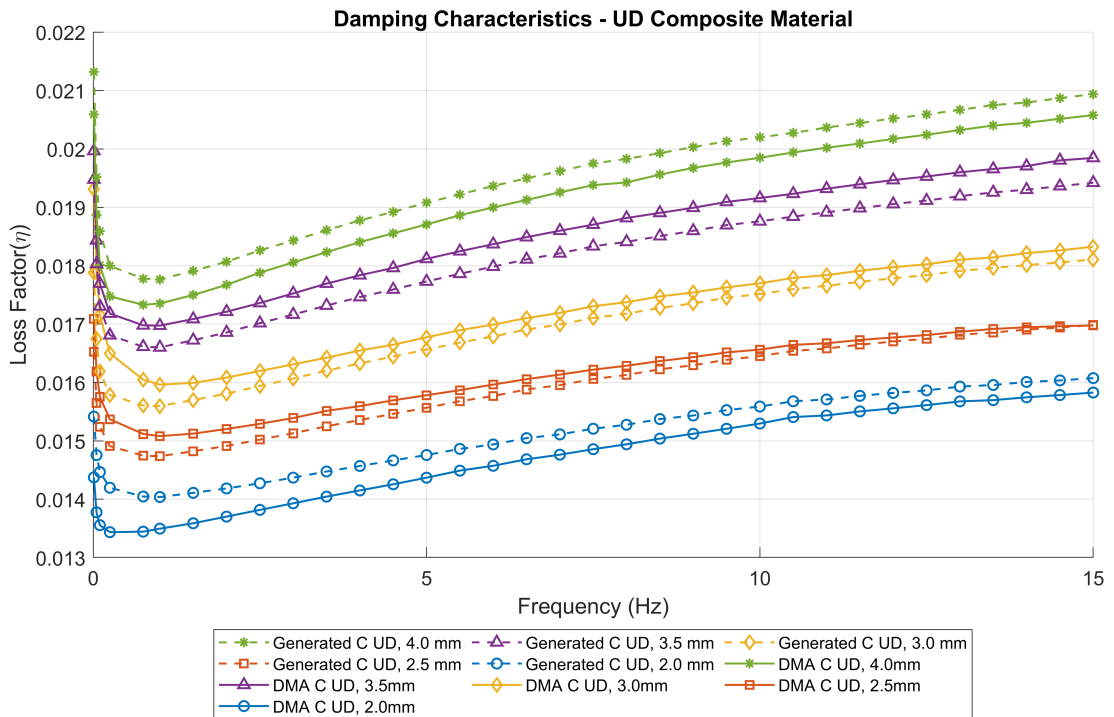


Figure 3.23: Comparison of Generated Results and Input DMA Data for UD Composite Material. The generated values represent model predictions, while the DMA data reflects experimental results.

For the UD composite material, the generated results closely follow the experimental DMA data, indicating that the Combined Model effectively captures the damping behaviour in the fibre direction. Maximum deviations are within approximately 0.0005 (less than 4% relative to the measured values). However, slight localised differences between the model predictions and the DMA results are visible at specific frequencies and thicknesses, including instances where the trends intersect and reverse in order.

### Chapter 3. Dynamic Mechanical Analysis for Damping Estimation

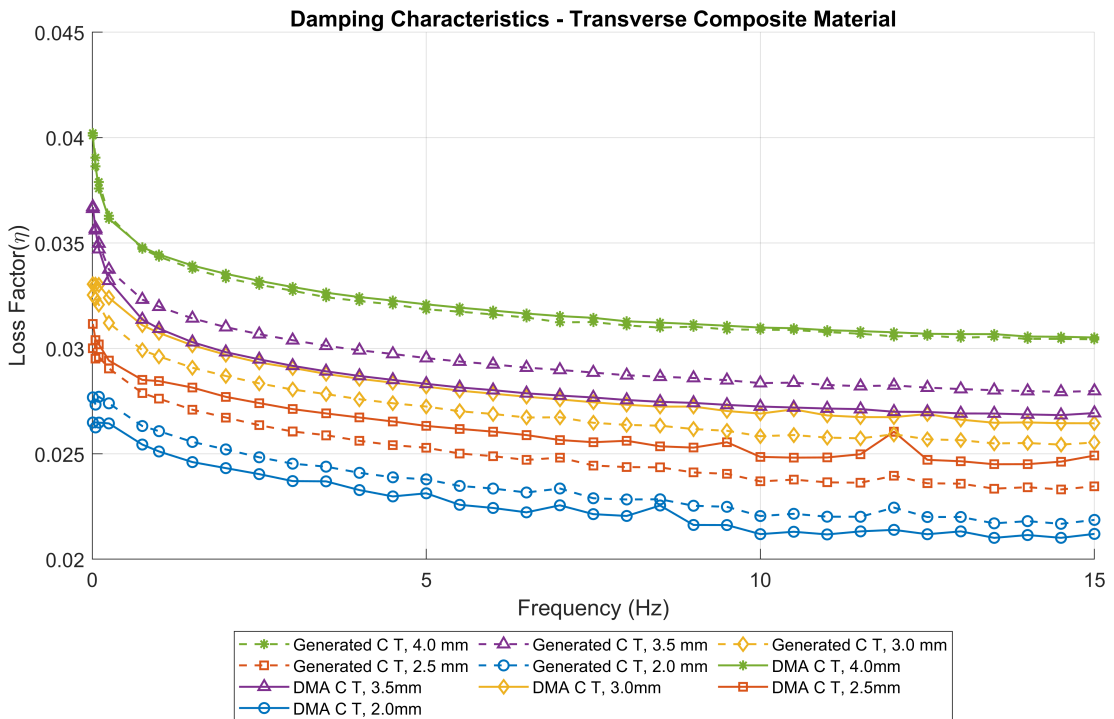


Figure 3.24: Comparison of Generated Results and Input DMA Data for Transverse Composite Material. The generated values represent model predictions, while the DMA data reflects experimental results.

For the Transverse composite material, the model predictions also align well with the experimental results, suggesting that the Combined Model adequately represents transverse damping behaviour. Maximum deviations are approximately 0.00125 (excluding one unexplained localised peak). Similar to the UD case, some crossing points and deviations across the frequency spectrum are observed.

These deviations can be attributed to a combination of factors. Firstly, experimental DMA results inherently include variability due to microstructural imperfections (e.g., fibre misalignment, resin-rich zones) and limitations in clamping or measurement sensitivity. Secondly, the FEA model assumes idealised material uniformity, which may not fully capture the

### Chapter 3. Dynamic Mechanical Analysis for Damping Estimation

frequency-dependent behaviour observed experimentally. Lastly, the model relies on a least squares fitting process, which may favour accuracy within set regions with more data points, potentially introducing small over- or underestimations elsewhere. These combined effects likely account for the minor discrepancies and observed trend crossings.

Despite these variations, the consistency in overall trend and magnitude between the model and experimental data validates the Combined Model's predictive capability. Building upon this, the next step was to assess the model's robustness by investigating the impact of removing the thinnest and thickest samples. This sensitivity analysis helped determine the model's stability when exposed to reduced input data ranges.

#### **3.5.2.2 Evaluating Model Robustness by Removing Data Extremes**

To validate the robustness and reliability of the developed Combined Model, an analysis was conducted by selectively removing extreme data points, specifically the thinnest (2.0 mm) and thickest (4.0 mm) samples from the dataset. This evaluation aimed to determine the sensitivity of the model's predictions to variations in the input dataset and assess whether the model remains consistent in predicting damping characteristics with a reduced range of thicknesses. The results of primary interest were the 11 (normal) and 22 (transverse) directions, and these were the focus of comparison. It should also be noted that within this section, the frequencies of interest were less than 10 Hz, closer to 1 Hz.

Extremities in data can disproportionately affect the modelling outcome due to their high leverage. By omitting these points, the goal was to evaluate the stability of the findings and ensure that the results were not overly dependent on these outliers. The model was recalibrated using the remaining data points,

### Chapter 3. Dynamic Mechanical Analysis for Damping Estimation

and the updated results were compared against the full dataset predictions. This approach provided insight into the influence of extreme data points on the overall accuracy of the model and its ability to generalise across different sample geometries.

In this analysis, the Combined Model was evaluated alongside the DSM UD and DSM Transverse Models. This inclusion was necessary because reducing the number of inputs for the full UD or Transverse Models would result in the number of outputs equalling the number of inputs, thereby eliminating the use of error minimisation techniques. By comparing these models, the robustness of the combined approach was further assessed, and its effectiveness in accommodating variations in input data was validated.

This sensitivity analysis focused on changes in the directional damping components and overall system damping to determine whether the results were significantly influenced by samples at the boundaries of the test range. The first phase examined the effects of removing the thinnest samples (2.0 mm) from the dataset, as illustrated in Figure 3.25.

### Chapter 3. Dynamic Mechanical Analysis for Damping Estimation

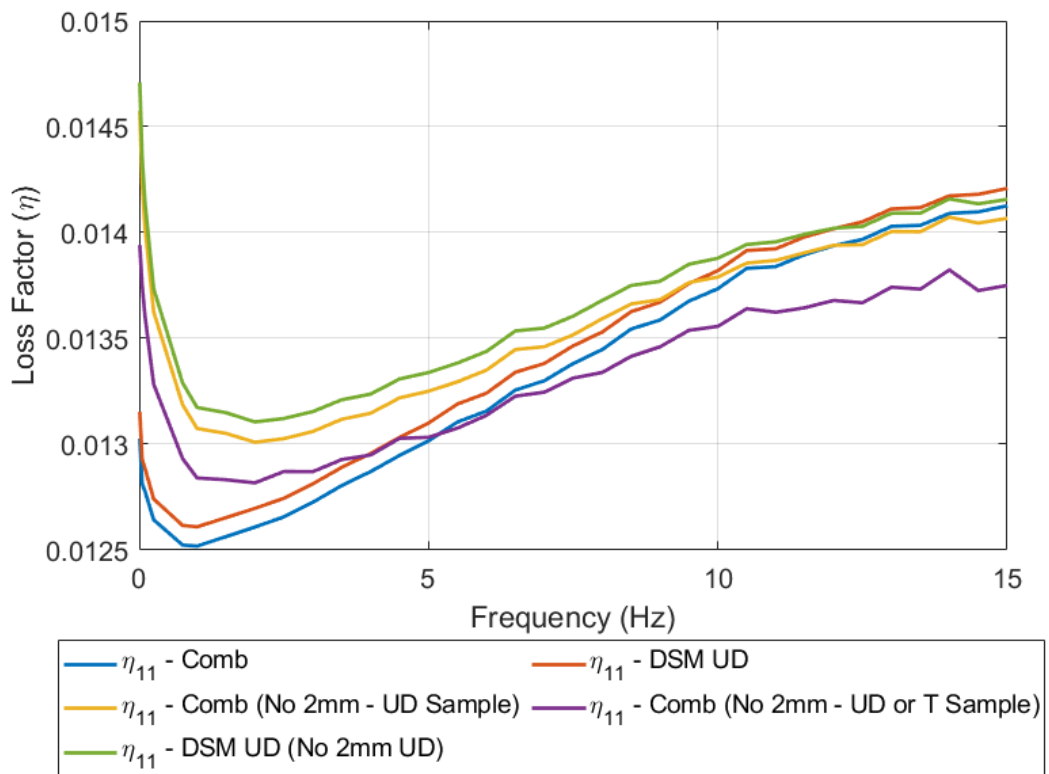


Figure 3.25:  $\eta_{11}$  Damping Characteristics - Comparison of the Combined Model (Comb), Combined Model without the 2 mm sample, DSM UD Model, and DSM UD Model without the 2 mm sample.

Figure 3.25 evaluates the impact of removing the 2.0 mm sample for the  $\eta_{11}$  damping characteristics and highlights the following observations:

- The removal of the 2.0 mm UD sample introduces only minor variations in the predictions at lower frequencies, with overall trends remaining consistent across models.
- The Combined Model without the 2.0 mm sample shows minimal deviations from the original Combined Model, indicating robust performance even when extreme data points were excluded.
- The DSM UD Model exhibited negligible sensitivity to the removal of the 2.0 mm sample, further validating the reliability of the directional damping

### Chapter 3. Dynamic Mechanical Analysis for Damping Estimation

components derived from the UD input.

- These findings suggested that both the Combined Model and the DSM models are not overly dependent on boundary data points and can effectively generalise across a range of sample geometries.

To complement the analysis of the  $\eta_{11}$  direction, the impact of removing the thinnest sample on the  $\eta_{22}$  direction was also examined. This allowed for a broader evaluation of the Combined Model's robustness when applied to the transverse direction, where damping is primarily influenced by strain energy in the 22 and 23 directions. Figure 3.26 illustrates the damping characteristics for  $\eta_{22}$  when the thinnest sample (2.0 mm) was excluded.

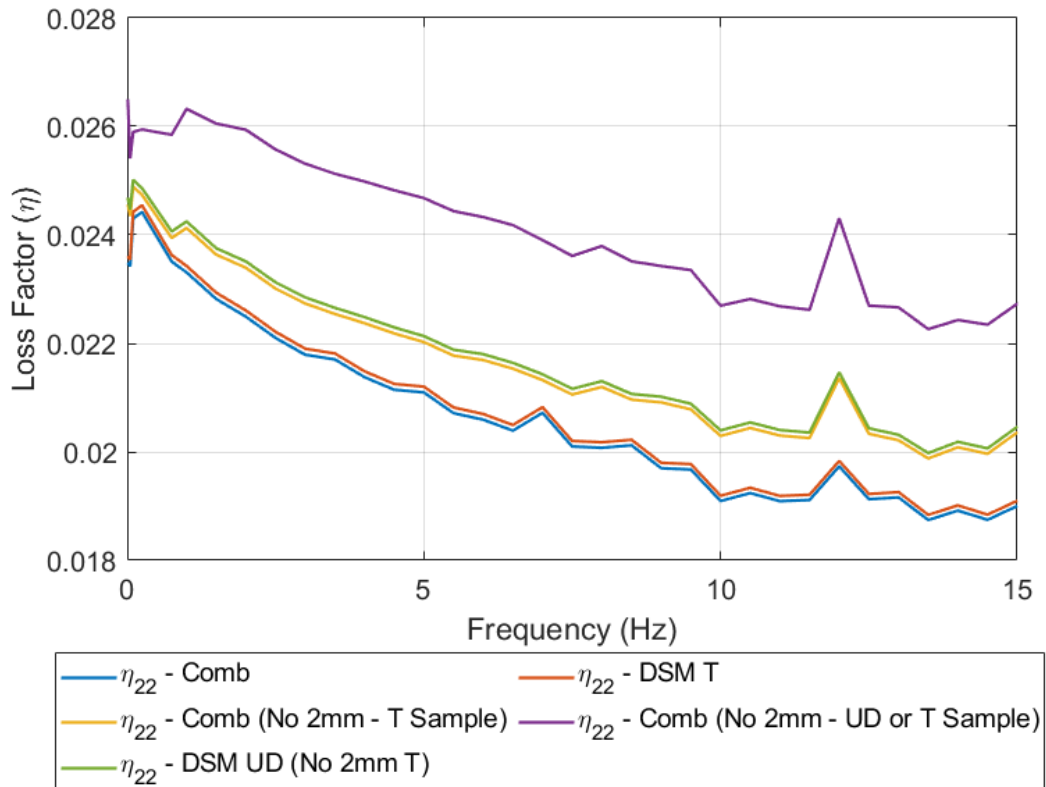


Figure 3.26:  $\eta_{22}$  Damping Characteristics - Removing 2 mm Sample: Comparison of the Combined Model (Comb), DSM Transverse Model, and adjusted models after removing the thinnest sample (2.0 mm).

### Chapter 3. Dynamic Mechanical Analysis for Damping Estimation

Figure 3.26 evaluates the impact of removing the 2.0 mm sample for the  $\eta_{22}$  damping characteristics and highlights the following observations:

- The Combined Model missing both 2.0 mm data sets (UD and transverse samples) showed a noticeable deviation, suggesting reduced accuracy when boundary samples were excluded. This deviation underscores the importance of including a broad range of data to improve model precision and reliability.
- When removing only the transverse 2.0 mm data set, the Combined Model demonstrated a variance of less than 5% compared to the full Combined Model, indicating a somewhat robust predictive capability.
- The exclusion of the transverse 2.0 mm sample, while slightly affecting accuracy, did not significantly compromise the model's ability to characterise damping behaviour in the  $\eta_{22}$  direction.

Next, the analysis shifted to evaluate the effect of excluding the thickest samples (4.0 mm) from the dataset. This evaluation sought to determine whether the trends observed during the removal of the thinnest samples were consistent or whether new insights emerge when the dataset's upper boundary was adjusted. By focusing on the  $\eta_{11}$  (fibre direction) and  $\eta_{22}$  (transverse direction) damping components, the robustness of the Combined Model, as well as the DSM UD and DSM Transverse Models, was further assessed.

Figures 3.27 and 3.28 present the results of this analysis. The plots compared the damping predictions from the full Combined Model with those obtained after removing the 4 mm UD and Transverse samples, as well as the predictions from the DSM UD and Transverse Models with their respective adjustments. These figures offer a detailed view of the effects of excluding the

thickest samples on the accuracy and consistency of the models.

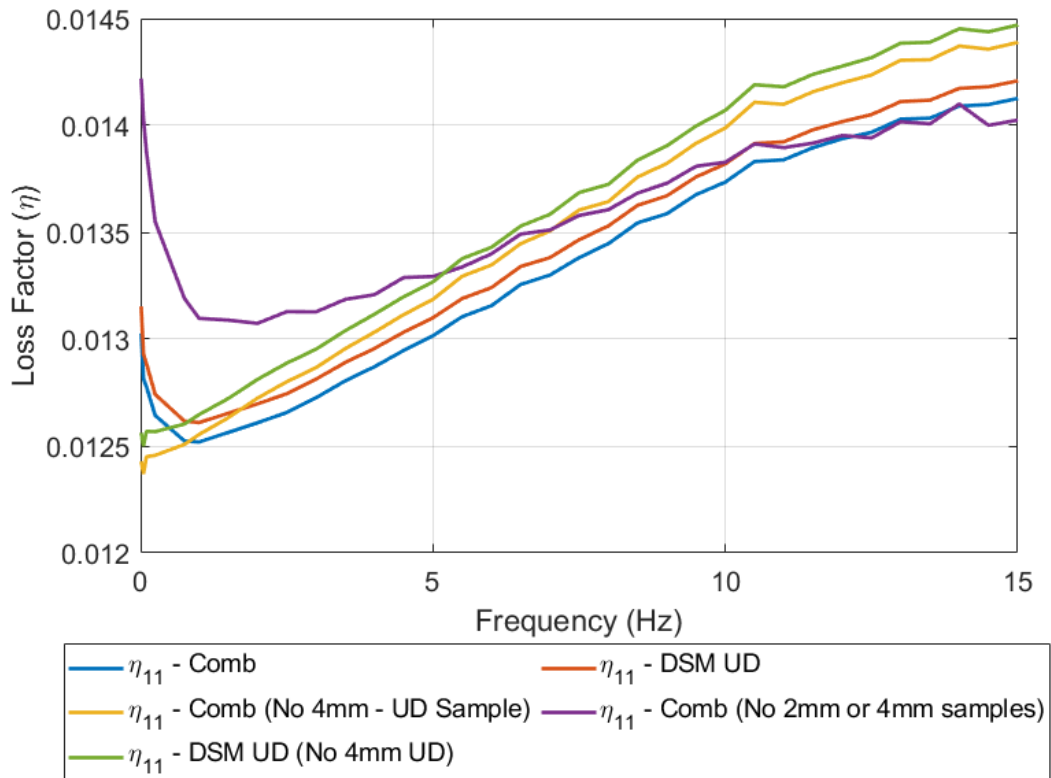


Figure 3.27:  $\eta_{11}$  Damping Characteristics - Comparison of the Combined Model (Comb), DSM UD Model, and Adjusted Models (4 mm sample removed).

Figure 3.27 evaluates the impact of removing the 4.0 mm sample on the  $\eta_{11}$  damping characteristics and highlights the following observations:

- The removal of the 4.0 mm sample generally had minimal impact on the models, with the exception of the Combined Model that excluded both 4.0 mm data points (UD and Transverse samples). This model was the poorest-performing in this comparison and struggled to capture the expected damping behaviour, particularly at frequencies below 1 Hz.
- Excluding the Combined Model without both 4.0 mm data points, the other models, including the Combined Model with the 4.0 mm Transverse sample removed and the DSM UD Model with the 4.0 mm

### Chapter 3. Dynamic Mechanical Analysis for Damping Estimation

UD sample removed, demonstrated strong consistency with the complete dataset.

- At frequencies below 1 Hz, the Combined Model and the UD Model without the 4.0 mm sample displayed slight deviations, failing to fully replicate the behaviour observed in the original dataset.

The analysis then examined the  $\eta_{22}$  damping characteristics to assess the impact of removing the 4.0 mm sample. The following discussion will assess the behaviour of the models under these conditions, as illustrated in Figure 3.28.

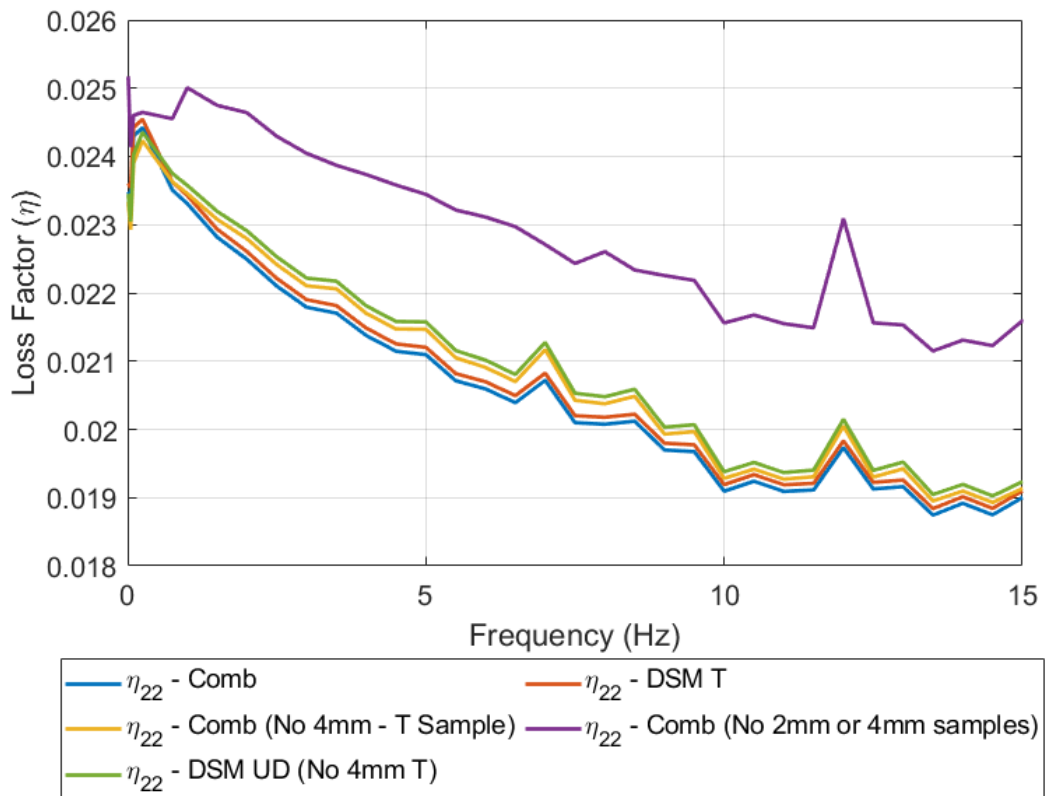


Figure 3.28:  $\eta_{22}$  Damping Characteristics - Comparison of the Combined Model (Comb), DSM Transverse Model, and Adjusted Models (4 mm sample removed).

Figure 3.28 illustrates the  $\eta_{22}$  damping characteristics and highlights the

### Chapter 3. Dynamic Mechanical Analysis for Damping Estimation

following observations:

- The Combined Model, when missing both 4.0 mm data points (UD and Transverse samples), deviated significantly from the expected trend and is the least reliable model in this comparison.
- The other adjusted models, including the Combined Model with the 4.0 mm Transverse sample removed and the DSM Transverse Model without the 4.0 mm sample, aligned closely with the more complete models, maintaining the expected behaviour.
- These adjusted models demonstrated minimal sensitivity to the exclusion of the 4.0 mm sample, showing that the removal of the thickest data point had a negligible impact on the accuracy of the predictions for the  $\eta_{22}$  direction.
- The results underscore the importance of including data from both sample types for reliable predictions, as highlighted by the poor performance of the Combined Model missing both 4.0 mm data points.

This section has examined the robustness of the combined, UD, and Transverse Models by selectively removing extreme data points, the thinnest (2.0 mm) and thickest (4.0 mm) samples. The following key conclusions are drawn from this analysis:

- The Combined Model demonstrated remarkable robustness when either the 2.0 mm or 4.0 mm sample was removed individually. However, its predictive accuracy diminishes significantly when both the number of samples in each direction is reduced to four, highlighting the importance of retaining a broad dataset.

### Chapter 3. Dynamic Mechanical Analysis for Damping Estimation

- The DSM UD and Transverse Models exhibited minimal sensitivity to the removal of either the 2.0 mm or 4.0 mm sample. Whilst these models maintained relative consistency with the more complete models, they showed a slightly greater dependence on the presence of the 2.0 mm sample, with minor deviations observed when this boundary sample was excluded.
- For the  $\eta_{22}$  damping characteristics, the exclusion of the 4.0 mm Transverse sample had a negligible effect on the models performance, provided that the 4.0 mm UD sample remains included. This finding underscores the complementary nature of the UD and Transverse inputs in the Combined Model.
- At very low frequencies (below 1 Hz), the exclusion of the 4.0 mm sample affected the ability of the Combined Model and the DSM UD Model to replicate the damping behaviour observed in the original dataset. This suggested that including the thickest sample was beneficial for capturing accurate damping characteristics in this frequency range.
- The findings confirmed that the models presented were generally robust and reliable, provided that extreme data points from both boundaries were not simultaneously removed. Including a broad range of sample geometries improves the model's generalisability and ensured accurate predictions across the entire frequency range.

This analysis highlighted that the removal of extreme data points, such as the thinnest (2.0 mm) or thickest (4.0 mm) samples, did not significantly alter the overall results. The models exhibited strong robustness and maintained consistent predictions across the majority of the dataset. However, it was observed that the removal of the 2.0 mm sample had a significant impact on the results compared to the 4.0 mm sample. This suggested that the inclusion

of thinner samples played a more critical role in achieving accurate predictions. Despite these variations, the Combined Model remained reliable and capable of generalising across a diverse range of sample geometries.

### 3.6 DMA Discussion

This study introduced an integrated FEA-assisted DMA methodology for quantifying the directional damping characteristics of carbon fibre composites. Its principal advantage lies in enabling the decomposition of global loss factors into distinct components associated with fibre-aligned, transverse, and shear directions. By computing strain energy contributions using ANSYS simulations and integrating them with experimental data, the approach improved the predictive accuracy of damping estimates, particularly in highly anisotropic UD composites.

The importance of accurate sample geometry was established early in the DMA campaign. Results demonstrated that while thickness variations within  $\sim 0.03$  mm had negligible impact on damping, deviations of 0.5 mm significantly skewed results. This justified the use of IMA-machined samples with a  $\sim 0.01$  mm tolerance. Such precision allowed experimental damping values to align more closely with theoretical predictions and improved model stability, particularly when used in combination with strain energy filtering.

A combined model was formulated, consolidating UD and transverse sample results into a full system of equations to estimate  $\eta_{11}, \eta_{12}, \eta_{22}, \eta_{23}$ . Strain energy contributions below 2% were excluded from the solution due to low sensitivity and high noise. The simplified version of this combined model, where only dominant energy directions were retained and scaled to 100%, yielded estimates within 1% of the full system, demonstrating both robustness

and computational efficiency.

The frequency dependence of damping was evident across all DMA results. For example,  $\eta_{11}$  increased from 0.0128 at 0.5 Hz to 0.0138 at 10 Hz, while  $\eta_{22}$  showed a reduction, consistent with the literature trend that transverse damping tends to diminish with frequency. This trend matched results from comparable studies, such as Bisagni and Catapano (2013), who investigated HexPly 8552/IM7 composites and also found orientation-dependent damping responses. Our values, though slightly higher, are considered reasonable given differences in fibre volume fraction, test temperature, and laminate architecture.

Table 3.11: Comparison of Loss Factors at Various Frequencies

<b>Material and Direction</b>	<b>0.5 Hz</b>	<b>1 Hz</b>	<b>10 Hz</b>
Carbon $\eta_{11}$ (Current Study)	0.0128	0.0125	0.0138
Carbon $\eta_{22}$ (Current Study)	0.0243	0.0235	0.0190
HexPly 0° [160]	0.007	0.0055	0.004
HexPly 90° [160]	0.0125	0.011	0.0075

These comparisons reinforce the credibility of the DMA results and show that despite differences in material type, the trends observed are consistent with established findings. The IM7 carbon fibre used by Bisagni et al. is renowned for its high stiffness and strength, making it ideal for applications that demand high durability and minimal deformation under stress, such as wind turbine blades. It exhibits slightly lower damping, likely due to higher stiffness and reduced internal friction at lower temperatures. Further comparative values are available in [165], which includes additional data on carbon and glass composites.

## Chapter 3. Dynamic Mechanical Analysis for Damping Estimation

Nonetheless, several limitations were noted. The FEA material properties relied on SGRE-provided data, which could not be independently verified. The boundary condition assumptions, such as negligible friction at supports, were based on manufacturer advice rather than measured contact responses, a common limitation in composite testing [166]. In addition, while sample thickness was well controlled, width tapering of  $\sim 0.1$  mm may have introduced slight inconsistencies, although these are likely insignificant when averaged correctly.

Finally, a strong regression fit and low residual error between modelled and experimental loss factors validated the methodology's utility. This approach is well-suited for refining damping predictions in numerical models for real structures, especially in cases where directional damping effects are of practical importance.

### **3.7 DMA Conclusion**

The FEA-assisted DMA method has demonstrated substantial improvements in quantifying damping in anisotropic composites. By accurately resolving fibre, transverse, and shear contributions, and accounting for sample geometry and strain energy distributions, the method offers a powerful tool for characterising material behaviour. The results align with the broader literature and suggest that such decomposition strategies could meaningfully inform wind turbine blade design and may be utilised to enhance the performance and lifespan of blades under operational loads. Future work should investigate additional approaches capable of evaluating damping in more structurally representative geometries and boundary conditions, as discussed in the following chapter.

# Chapter 4

## Experimental Modal Analysis for Damping Estimation

### 4.1 EMA Introduction

Although DMA offers a valuable insight into material-level viscoelastic properties and dynamic behaviour, it is limited to capturing micro-scale damping phenomena. In contrast, EMA can capture the global dynamic characteristics of larger test samples as well as complete structures. The integration of both methods provided complementary perspectives; DMA revealed the intrinsic material damping, while EMA captured the overall dynamic response. EMA is a well-established technique for determining the dynamic characteristics of structures, including natural frequencies, mode shapes, and damping ratios. Modal analysis, which forms the basis of EMA, decomposes a structure's vibrational response into its constituent modes, thereby providing detailed insight into its dynamic behaviour. In practice, EMA involves exciting the structure, often using a modal hammer or shaker, and measuring the resulting vibrations with high-precision sensors such as

## Chapter 4. Experimental Modal Analysis for Damping Estimation

accelerometers, strain gauges, or even non-contact methods. These measurements allow the construction of Frequency Response Functions (FRFs), from which key modal parameters, including damping ratios, can be extracted [167]. The accuracy of EMA is dependent on careful control of boundary conditions, excitation techniques, and data processing methods, making it a versatile approach applicable to both laboratory-scale specimens and full-scale structures.

In full-scale applications, EMA plays an important role in verifying design performance, monitoring structural health, and ensuring long-term durability across aerospace, automotive, and civil engineering industries. For instance, within the renewable energy sector, EMA has been effectively used to evaluate full-scale wind turbine blades, identifying key vibrational modes and quantifying damping characteristics [87]. This is particularly important because precise modal damping data are essential for predicting a blade's response to vibrational loads, maintaining stability, and extending fatigue life through affecting wind turbine blade design [18]. While traditional design has not focused on the contribution of structural damping, which arises from inherent material behaviour and internal friction, it is increasingly recognised for its potential to reduce fatigue loads and enhance blade durability [75, 168]. Thus, EMA not only provides the fundamental dynamic parameters needed for design and analysis but also serves as a key tool for advancing the safety, efficiency, and longevity of complex engineering systems.

Building on these foundational principles and large-scale applications, this chapter further explores the use of EMA to characterise the damping properties of composite materials used in wind turbine blades. Although EMA yields accurate modal parameters such as natural frequencies, mode shapes, and damping ratios, traditional EMA methods face several limitations.

## Chapter 4. Experimental Modal Analysis for Damping Estimation

Environmental influences (e.g., air damping and temperature variations) and sensitivity to boundary conditions can affect the vibrational response. In particular, these factors present significant challenges when attempting to isolate and extract structural or material damping, which is typically subtle and easily masked by external sources of energy dissipation. Additionally, issues in data acquisition, including the choice of excitation (impact hammers, shakers, or non-contact methods) and the specific post-processing techniques employed, can introduce inconsistencies in the extracted modal damping parameters.

To address these challenges and improve the reliability of material damping identification, a novel EMA test rig was designed and manufactured, employing a free-free boundary condition and facilitating testing under both ambient and vacuum environments. This approach reduced unintentional energy losses due to fixture and environmental effects, thereby enhancing the accuracy of the extracted damping data and improving the isolation of material damping contributions [56, 169, 170].

In the following sections, the background and development of EMA are examined. Next, we describe in detail the design and implementation of the novel EMA test rig. This rig utilised a modal hammer excitation method to capture the vibrational response via contact sensors (accelerometers and strain gauges). The resulting frequency response functions (FRFs) were post-processed using the Poly-reference Least Squares Complex Frequency (pLSCF) method, which enabled the extraction of key modal parameters, such as damping ratios. These extracted damping ratios can then be integrated into larger-scale models to predict the behaviour of a complete wind turbine blade.

## 4.2 EMA Background

The evolution of EMA spans several decades, transitioning from rudimentary vibration tests to today's sophisticated methods. Early modal testing emerged in the mid-20th century when engineers first sought to validate theoretical models by measuring the vibrational response of structures using basic transducers and analog equipment. The advent of digital signal processing, particularly the Fast Fourier Transform (FFT) in the 1960s and 1970s, revolutionised the field, enabling precise extraction of modal parameters from complex vibrational data [171].

Modern EMA utilises a range of excitation techniques, such as impact hammers, shakers, and non-contact methods, paired with advanced sensors to capture a structure's dynamic response. This data is then generally processed to construct FRFs and post-processed, from which natural frequencies, mode shapes, and damping ratios are derived. However, the technique's success hinges on meticulous experimental design; factors such as boundary conditions, environmental influences (e.g., temperature and air damping), and the specific excitation method can significantly affect the accuracy of the results.

Despite its strengths in capturing global dynamic behaviour, EMA faces challenges in isolating pure structural responses. Issues such as unwanted energy losses at supports and the influence of ambient conditions can obscure true modal characteristics. Recent advancements, including the implementation of free-free boundary conditions and testing under controlled (or even vacuum) environments, have addressed some of these limitations, enhancing the reliability of EMA data.

### **4.2.1 History of EMA in Composite Materials**

EMA has a rich history spanning over 50 years, evolving from rudimentary vibration tests to the sophisticated techniques utilised today. The earliest applications of what is now known as modal testing were developed to validate theoretical models of structural behaviour under dynamic loading, typically under steady-state excitation. In fact, the first documented modal testing methods can be traced back to the 1940s, when engineers performed vibration tests on aircraft structures aimed at supplementing their primary failure data with intermediate observations of input forces and corresponding responses [172]. The limitations of early transducers and signal conditioning equipment hampered these initial efforts. It was not until the advent of electronic devices and later digital computers that reliable measurements could be obtained. The widespread introduction of the fast Fourier transform (FFT) in the 1960s marked the true beginning of modern EMA [172].

In the early 1970s, pioneering work by Wright [173] on glass and carbon-reinforced polyester beams demonstrated the benefits of using free-free conditions, suspending the beams at their fundamental mode node, to reduce extraneous damping effects. Wright's method involved exciting the beams with a sinusoidal force and utilising an optical, contactless probe to capture the decay of oscillations. Building on these early efforts, Adams and Bacon [174] highlighted the critical importance of free-free vibration conditions to eliminate additional damping from supports. They introduced an electromagnetic excitation technique to measure carbon fibre-reinforced polymer beams' specific damping capacity (SDC). They noted that the relative mass of the coil and specimen significantly influenced the results. They later recommended performing tests in a vacuum to remove aerodynamic damping, a major source of dissipation in low-damping materials like

## Chapter 4. Experimental Modal Analysis for Damping Estimation

CFRP [175].

Throughout the 1970s and into the 1980s, further advancements were made. Guild and Adams [176] improved upon earlier methods by developing stiffer coil clamps to reduce uncertainties caused by clamping pressures. They refined both free–free and cantilever setups, although variations in boundary conditions and mass effects still resulted in some discrepancies. During the 1980s, Lin et al. [177] experimented with supported glass and carbon-reinforced epoxy plates using soft rubber foam supports to mitigate boundary condition effects. Their approach, which combined steady-state vibration with hammer impact testing and used non-contact transducers, provided improved estimates of SDC. Concurrently, Suarez et al. [178] introduced a more advanced impulse techniques using an electromagnetic shaker and eddy current probe to measure viscous damping ratios via the half-power bandwidth method, thus reducing leakage and enhancing accuracy.

The late 1980s saw a major breakthrough with the introduction of laser displacement sensors. Crane and Gillespie [179] developed an impulse technique apparatus that used these sensors, achieving high precision in displacement measurements and, consequently, in SDC estimation. This non-contact approach eliminated the mass-loading issues associated with conventional accelerometers. Maheri and Adams [180] later confirmed the advantages of laser vibrometry for accurate damping measurements, demonstrating its efficacy in free–free flexure tests by further reducing uncertainties related to mass effects and boundary conditions.

By the early 2000s, computational methods such as finite element analysis (FEA) began to be integrated with experimental damping measurements, further enhancing the accuracy and scope of EMA. For instance,

## Chapter 4. Experimental Modal Analysis for Damping Estimation

Kyriazoglou [181] proposed a hybrid simulation methodology that combined vibration tests, using magnets to excite the sample, in free–free flexure with laser vibrometry under vacuum conditions to eliminate aerodynamic damping effects. However, these advancements have not completely overcome persistent challenges in EMA, such as accurately replicating real-world boundary conditions and fully isolating intrinsic material damping from extraneous influences, including residual aerodynamic effects and measurement uncertainties. In recent years, techniques such as Operational Modal Analysis (OMA) have been developed, enabling in-situ damping measurements under real operational conditions without requiring controlled excitation. This is particularly beneficial for the health monitoring of large structures like wind turbine blades and aerospace components. Modern computational tools, often enhanced with machine learning algorithms, now facilitate real-time damping predictions and diagnostics [182].

These developments have shown the importance of precise experimental design, controlled testing environments, and integrating computational models with experimental data. The historical progression from early vibration tests to contemporary EMA techniques illustrates the continual refinement of methodologies to achieve higher accuracy and reliability. These lessons have been fundamental in the development of the EMA rig used in this thesis for medium-scale composite testing.

### **4.2.2 Application of EMA**

EMA is particularly valuable when the vibrational characteristics of a structure need to be experimentally determined, especially when theoretical or computational models, such as FEA, cannot effectively predict a material's damping behaviour. This is especially important for composite materials, as

## Chapter 4. Experimental Modal Analysis for Damping Estimation

their complex anisotropic behaviour can be challenging to model accurately [168]. Wind turbine blades, subjected to fluctuating dynamic loads, can benefit from EMA as it helps identify natural frequencies that may lead to resonance, potentially causing structural fatigue or failure [183]. Furthermore, EMA has been employed to detect defects in turbine blades by monitoring changes in modal parameters [183, 184].

The primary aim of EMA in this thesis was to determine the following modal properties:

- **Natural Frequencies:** The frequencies at which a structure will resonate. Resonance can amplify vibrational forces, leading to significant deformations and possible failure.
- **Mode Shapes:** These describe the deformation pattern of the structure at each natural frequency, highlighting areas of maximum stress or displacement.
- **Damping Ratios:** This parameter quantifies how quickly oscillations decay after dynamic excitation, which is critical to ensuring that vibrational forces do not cause excessive wear or instability [185].

By determining these properties, the performance and durability of wind turbine blades can be more accurately predicted, ensuring that they withstand operational conditions [168].

### 4.2.3 Excitation Methods Used in EMA

Various methods are employed to excite and measure structures' vibrational response during EMA, each offering specific advantages depending on the structure and testing conditions.

- **Impact Testing:** An impact hammer strikes the structure leading to the

## Chapter 4. Experimental Modal Analysis for Damping Estimation

excitation of modes, and the resulting vibrations are measured using accelerometers, strain gauges or laser vibrometers. This quick and efficient method is ideal for small to medium structures [168].

- **Shaker Testing:** A controlled excitation method, shakers provide continuous vibrational input over a range of frequencies. This method is better suited to larger or more complex structures that require precise input control [186].

In addition to these traditional methods, Operational Modal Analysis (OMA) allows for the determination of modal properties under normal operational conditions without requiring controlled excitation, which is helpful for in-situ testing [167, 187].

### 4.2.4 Post-Processing Methods

Post-processing in modal analysis involves extracting key parameters from measured data, such as natural frequencies, mode shapes, and damping ratios [188]. Depending on the availability of excitation input, two primary categories of modal analysis exist:

- **Experimental Modal Analysis (EMA)** – Utilises both input (excitation force) and output (structural response) data to determine modal properties. EMA is typically performed in controlled laboratory settings using shakers or impact hammers and is well suited for accurate parameter extraction in engineered systems.
- **Operational Modal Analysis (OMA)** – Also referred to as output-only modal analysis, OMA is used when input forces are unknown or difficult to measure. It is commonly applied in civil, aerospace, and offshore structures where environmental loads (e.g., wind or wave excitation) act

## Chapter 4. Experimental Modal Analysis for Damping Estimation

as ambient inputs.

Both EMA and OMA benefit from advanced post-processing techniques, which can be grouped accordingly:

### **Input-Output (EMA) Methods:**

- **Poly-reference Least Squares Complex Frequency-Domain (pLSCF / Polymax)** – A robust frequency-domain method that enhances the clarity of stabilisation diagrams and is widely used in structural dynamics research. Its least-squares optimisation effectively isolates physical modes from computational artefacts, making it particularly effective for complex structures such as wind turbine blades and composite materials [189].
- **Least-Squares Complex Exponential (LSCE)** – A time-domain method that fits decaying exponentials to impulse response data. LSCE is effective for lightly damped systems but may be less reliable in high-noise environments or systems with complex damping behaviour [190].
- **Eigensystem Realisation Algorithm (ERA)** – Another time-domain technique suited for input-output systems. ERA can simultaneously resolve multiple closely spaced modes and is effective for large systems with complex damping characteristics [107].

### **Output-Only (OMA) Methods:**

- **Stochastic Subspace Identification (SSI)** – A powerful time-domain OMA method used when excitation forces are unknown. It includes variants such as SSI-Covariance (SSI-Cov) and SSI-Data (SSI-DATA), and is especially effective for large-scale civil or offshore structures

## Chapter 4. Experimental Modal Analysis for Damping Estimation

under operational loads [191].

- **Frequency Domain Decomposition (FDD)** – A spectral peak-based OMA method that decomposes the output spectrum into principal components. It enables fast identification of modal frequencies and mode shapes, particularly in noisy environments [108].
- **Enhanced Frequency Domain Decomposition (EFDD)** – An improved version of FDD that estimates damping more accurately by using a time-domain reconstruction step following spectral decomposition [191].

Among these methods, the Polymax method (pLSCF) stands out as the preferred post-processing technique for this study. Its robust least-squares optimisation framework, compatibility with multiple-input multiple-output (MIMO) systems, and ability to generate clear stabilisation diagrams, particularly in the presence of closely spaced modes, make it especially well suited for analysing the complex dynamic behaviour of composite wind turbine blade structures [192].

This capability is particularly important when working with carbon fibre composite samples representative of spar cap materials, which exhibit significant anisotropy, directional damping behaviour, and densely packed modal frequencies. The Polymax method is highly effective at distinguishing true physical modes from computational artefacts, even in the presence of ambient noise, making it ideal for extracting subtle variations in structural damping [192, 193].

Furthermore, due to the nature of the testing carried out in this study, EMA is employed throughout this chapter. The availability of both input and output data allows for more precise identification of modal parameters, particularly damping ratios, while avoiding the assumptions and limitations inherent in

## Chapter 4. Experimental Modal Analysis for Damping Estimation

output-only techniques. As a result, the Polymax method, used in conjunction with EMA, offers the most reliable and accurate approach for meeting the high-resolution damping characterisation demands of this investigation [194].

### 4.2.4.1 Polymax (pLSCF) Method

The Polymax (Poly-reference Least-Squares Complex Frequency-Domain, or pLSCF) method is one of the most robust techniques for modal parameter estimation, particularly in noisy environments [195, 196]. It is widely used in experimental modal analysis due to the ability to produce transparent and interpretable stabilisation diagrams, essential for identifying the system's physical modes.

Polymax utilises a suitable matrix-fraction model to represent frequency response function (FRF) data. It applies a least-squares approach to estimate modal parameters, making it effective for handling multiple-input multiple-output (MIMO) systems [189]. The matrix fraction model equation can describe this approach [197]:

$$\mathbf{H}(\omega) = \mathbf{B}(\omega)\mathbf{A}(\omega)^{-1} \quad (4.1)$$

where  $\mathbf{H}(\omega)$  is the frequency response function, and  $\mathbf{B}(\omega)$  and  $\mathbf{A}(\omega)$  are polynomial matrices that describe the system in the frequency domain [198].

By analysing the FRF data, the Polymax method constructs stabilisation diagrams, where poles (representing potential modal frequencies) are identified and tracked across different model orders. In this diagram, stable poles (those that do not vary significantly with increasing model order) are associated with the physical modes of the structure. These modes are identified based on both frequency and damping stability

## Chapter 4. Experimental Modal Analysis for Damping Estimation

criteria [189, 195, 199]. The damping factor is computed using the equation:

$$\lambda_i = -\omega_i \xi_i \pm j\omega_i \sqrt{1 - \xi_i^2} \quad (4.2)$$

where  $\lambda_i$  represents the complex poles,  $\omega_i$  is the natural frequency, and  $\xi_i$  is the damping ratio [189].

Polymax offers a key advantage in resolving closely spaced modes, a recurring challenge in structures with complex damping behaviour, such as wind turbine blades and carbon composite spar caps. Traditional methods often struggle to differentiate genuine physical modes from spurious computational artefacts, but Polymax's robust least-squares optimisation effectively isolates these modes, even in noisy environments where signal interference is significant. This enhanced precision in modal characterisation makes Polymax ideally suited for applications requiring accurate damping estimation.

A hybrid stochastic-deterministic approach is sometimes employed to further enhance damping estimation, particularly under high-noise conditions. This involves incorporating Maximum Likelihood Estimation (MLE) prior to Polymax, which can improve the accuracy of damping ratio estimates while retaining the clarity of the stabilisation diagram [189].

Despite its advantages, the Polymax method is not without limitations. One notable challenge is its sensitivity to model order selection: overly low orders may omit physical modes, while overly high orders can introduce spurious poles, increasing the effort required during interpretation of the stabilisation diagram. Additionally, although Polymax is generally more intuitive than other frequency-domain methods, its implementation still demands user expertise in identifying stability trends and validating modal parameters. The method can

## Chapter 4. Experimental Modal Analysis for Damping Estimation

also be computationally intensive when applied to high-density or broadband FRF datasets, especially in large MIMO systems. Nonetheless, these limitations are well managed through the use of the MACEC toolbox, which offers built-in tools for order selection, pole validation, and mode shape visualisation, thereby mitigating much of the manual overhead typically associated with Polymax-based processing.

Using software tools such as the MACEC toolbox in MATLAB has further simplified the implementation of the Polymax method. MACEC allows users to generate stabilisation diagrams, plot mode shapes, and evaluate both deterministic and stochastic versions of the pLSCF method. The toolbox also supports the application of damping range criteria, helping to distinguish physical modes from spurious ones [191]. MACEC's ability to handle deterministic and stochastic data makes it highly suitable for large-scale structural analysis.

### **4.2.4.2 Justification for Selecting pLSCF in This Study**

Although the Polymax (pLSCF) method offers several advanced capabilities, not all of its strengths are strictly required for the conditions of this study. For instance, one of its key advantages is the ability to resolve closely spaced modes, a feature particularly valuable in structures with high modal density. However, in the current work, the mode spacing is sufficiently wide that this capability does not represent a limiting challenge.

Similarly, Polymax is known for its robustness in handling noisy measurement environments. Yet, due to the controlled laboratory conditions as will be discussed in Section 4.3, the signal-to-noise ratio in the collected data is relatively high. As a result, the method's noise resilience, while beneficial, is not critically needed.

## Chapter 4. Experimental Modal Analysis for Damping Estimation

Nonetheless, pLSCF remains the most appropriate choice for this investigation. Its ability to produce clear stabilisation diagrams, compatibility with MIMO systems, and support for both deterministic and stochastic formulations make it a widely adopted and well-validated method across academic and industrial contexts. Additionally, its seamless implementation in the MACEC toolbox ensures a reliable and reproducible workflow, with built-in tools for visualising mode stabilisation, assessing damping stability, and applying modal validation criteria.

In this context, the selection of pLSCF is not based solely on its advanced capabilities, but also on its established credibility, industry adoption, and ease of integration with the MACEC-based processing pipeline used throughout this study [191].

### 4.2.5 The MACEC Modal Analysis Toolbox

The MACEC toolbox is an open-source MATLAB-based framework designed for EMA [191]. Unlike commercial software, MACEC provides high transparency and control over data processing, enabling researchers to inspect intermediate steps, refine stabilisation criteria, and compare different modal analysis methods within a customisable MATLAB environment.

#### 4.2.5.1 Modal Analysis Methods in MACEC

MACEC implements a wide range of methodologies applicable to both Experimental and Operational Modal Analysis.

##### **EMA methods:**

- **Polymax (pLSCF)** – A frequency-domain technique offering both deterministic and stochastic implementations. Well suited for systems

## Chapter 4. Experimental Modal Analysis for Damping Estimation

with closely spaced modes when both input and output data are available.

### **OMA methods:**

- **Stochastic Subspace Identification (SSI)** – Includes data-driven (SSI-data, SSI-data/ref) and covariance-driven (SSI-cov, SSI-cov/ref) variants. Effective for output-only modal analysis in noisy or ambient environments.
- **Frequency Domain Decomposition (FDD)** – A non-parametric spectral method based on singular value decomposition of the output power spectral density. Ideal for rapid identification of modal frequencies and mode shapes.
- **Complex Mode Indication Function (CMIF)** – A visual method using singular values of the FRF matrix to identify closely spaced modes. Often used for mode separation; it does not estimate damping.

### **Hybrid method:**

- **Combined Subspace Identification (CSI, CSI-ref)** – A time-domain technique capable of handling mixed excitation conditions. By integrating both deterministic (input-output) and stochastic (output-only) subspace identification, CSI is particularly suited for partially instrumented or semi-operational environments where some inputs are known and others are not.

#### **4.2.5.2 Why MACEC Was Chosen for This Study**

For this research, which involves testing carbon composite samples representative of wind turbine spar cap materials, MACEC is particularly well-suited due to several reasons:

1. **Transparency and Control:** MACEC allows full access to the

## Chapter 4. Experimental Modal Analysis for Damping Estimation

underlying algorithms, enabling detailed inspection and modification of the modal identification process. This transparency is essential for research applications that require precise control over data processing.

2. **Customisation and Flexibility:** The ability to develop custom MATLAB scripts and integrate multiple modal analysis techniques in one environment makes MACEC highly adaptable, facilitating the comparative evaluation of different post-processing methods.
3. **Cost-Effectiveness:** MACEC offers a cost-effective alternative to proprietary software like Siemens Testlab, reducing financial barriers while maintaining high functionality.
4. **Methodological Variety:** MACEC supports both deterministic (pLSCF/Polymax) and stochastic (SSI, FDD) methods, providing a comprehensive suite of tools to extract modal parameters even in challenging, noisy conditions.

While proprietary solutions may offer a more integrated workflow, their closed nature limits algorithmic transparency and restricts detailed data manipulation. For applications requiring rigorous methodological control, such as the precise characterisation of damping in composite spar cap materials, MACEC is the preferred choice.

### 4.2.6 Advantages and Limitations of EMA

EMA offers several advantages, particularly in structural dynamics and damping estimation. One of the main strengths is the ability to provide accurate experimental data on modal properties, such as natural frequencies, mode shapes, and damping ratios, which are essential for validating theoretical or computational models like FEA. This is especially valuable in

## Chapter 4. Experimental Modal Analysis for Damping Estimation

composite structures, such as wind turbine blades, where dynamic performance directly impacts operational lifespan [168, 186]. Furthermore, EMA is non-destructive, making it ideal for applications where preserving structural integrity is essential, such as in the aerospace and renewable energy sectors [56, 194].

However, EMA is not without its challenges. One significant limitation is the sensitivity to environmental factors. Ambient conditions, such as air damping, temperature fluctuations, and humidity, which can influence the measured vibrational response. For example, air damping can introduce additional energy dissipation not inherent to the structure, potentially considerably increasing the apparent damping ratios. Tests conducted under non-controlled conditions may, therefore, overestimate the structural damping, leading to discrepancies when compared with theoretical predictions. Conducting tests in a vacuum can help isolate the intrinsic structural damping by eliminating aerodynamic contributions [184].

Another critical limitation is the influence of boundary conditions. Inadequate isolation of the test specimen from supports often results in energy losses that are mistakenly interpreted as part of the structure's inherent damping. This effect is particularly pronounced in cases where fixed or semi-rigid supports are used, as they can absorb vibrational energy and distort the modal response. Adopting a free-free boundary condition is a common strategy to mitigate these issues, as it minimises energy losses at the supports and enhances the accuracy of modal parameter estimation [168, 169, 194]. Nevertheless, slight misalignments or residual support effects can still affect the results, even with free-free setups. FEA was, therefore, integrated to allow for nodal location identification.

Data acquisition challenges also impact EMA outcomes. The choice of

## Chapter 4. Experimental Modal Analysis for Damping Estimation

excitation method, whether an impact hammer, shaker, or non-contact technique, directly influences the quality and repeatability of the measurements. For instance, impact force or sensor placement inconsistencies can lead to variability in the recorded Frequency Response Functions (FRFs). These variabilities, in turn, can cause discrepancies in the extracted modal parameters. In addition, advances in non-contact excitation methods, such as acoustic or electromagnetic excitation, offer potential improvements, though they are not yet widely used in all testing environments [169, 170]. However, acoustic methods are not possible in vacuum conditions.

Post-processing plays a crucial role in extracting reliable modal parameters from EMA data. While a wide range of algorithms exists, their applicability depends on the availability of input information and the quality of the data. This study employs the Polymax (pLSCF) method, a frequency-domain, input-output technique, as the preferred approach for post-processing. Polymax offers strong noise rejection, robustness to closely spaced modes, and generates clear stabilisation diagrams that facilitate reliable mode identification [167, 189]. Its least-squares optimisation framework minimises the impact of experimental uncertainty, making it especially valuable for assessing the low-damping contributions typical of carbon fibre composite spar caps. Additionally, its compatibility with multiple-input multiple-output (MIMO) systems enables high-fidelity characterisation of complex modal behaviour.

It is important to note that other popular post-processing methods, such as Stochastic Subspace Identification (SSI) and Frequency Domain Decomposition (FDD), are designed for Operational Modal Analysis (OMA), which is based on output-only data under ambient excitation. These methods

## Chapter 4. Experimental Modal Analysis for Damping Estimation

are not applicable in this study due to the availability of measured input forces via impact hammer excitation. Consequently, input-output techniques such as Polymax and ERA are more appropriate for extracting accurate damping characteristics in the context of Experimental Modal Analysis [194, 198, 200].

Although Polymax (pLSCF) offers several advantages in terms of clarity and robustness, it is not without challenges. One known limitation is its sensitivity to model order selection. Selecting too low an order may miss physical modes, while an excessively high order can introduce spurious poles that complicate interpretation. To mitigate this, a range of model orders was trialled, and stabilisation diagrams were reviewed to identify consistent poles across increasing model orders. Another common issue is the potential bias in damping estimation, particularly if the signal-to-noise ratio is low or if frequency resolution is insufficient. This was addressed in this study by ensuring high-quality FRFs through careful hammer impact placement, multiple averaged measurements, and ensuring free-free boundary conditions to minimise external damping contributions. This stepwise approach ensured confidence in the stability of extracted modal parameters and reflects established best practices in industrial and academic applications of Polymax [167, 192, 194].

Polymax also performs best when FRFs are clean and well-conditioned. In this work, efforts were made to maintain consistent excitation and precise sensor alignment, thereby reducing variability. Although the ability of Polymax to resolve very closely spaced modes is a key strength, in this thesis, the mode spacing was not critically narrow. Nevertheless, the method's transparency in modal pole tracking, compatibility with MIMO systems, and its established use in industry and research made it the most appropriate and reliable option. These measures ensured that the method's potential

drawbacks were effectively controlled and that its benefits could be fully leveraged for accurate damping characterisation [167, 194, 198].

### **4.2.7 Main Aims of Conducting EMA**

The primary aim of conducting EMA alongside DMA in this research was to develop a comprehensive understanding of the damping behaviour of composite materials used in wind turbine blades. While DMA provides a detailed insight into the viscoelastic properties of materials at the microstructural level, EMA allows for the assessment of dynamic behaviour at the structural scale. Together, these methods enable a deeper understanding of how material properties translate into performance under real-world conditions.

In Chapter 3, DMA was used to determine the stiffness, loss modulus, and resulting damping behaviour of composite materials under controlled conditions. These results can help to identify materials with favourable energy dissipation characteristics. However, the transition from material properties to structural performance requires a further understanding of how these characteristics influence the vibrational response of a full-scale structure like a wind turbine blade.

EMA is particularly suited for this purpose as it allows for the measurement of natural frequencies, mode shapes, and damping ratios. This makes it possible to assess how the damping properties identified through DMA affect the overall dynamic stability and performance of the structure under real-world conditions. By using both DMA and EMA, this research bridges the gap between small-scale material behaviour and large-scale structural performance, providing a holistic approach to optimising the damping characteristics of wind turbine blades.

### **4.3 Development of EMA Test Rig and Accompanying Methodology**

This section outlines the conceptualisation, design, and realisation of a novel EMA test rig, tailored to enhance the precision in estimating structural damping properties of materials employed in wind turbine blades. The rig was developed by the present author at the University of Strathclyde, Glasgow, primarily focusing on testing medium-scale samples under vacuum conditions to minimise external energy losses and isolate intrinsic damping characteristics.

The entire experimental setup, encompassed the vacuum chamber, a modular and adaptable frame, advanced force excitation methods, and associated apparatus, was designed, manufactured, assembled, and tested by the author. This hands-on approach ensured rigorous control over all experimental variables and testing conditions.

The theoretical foundation for the design of this experimental rig was derived from the principles discussed in Chapter 2. The design addresses key limitations inherent in standard EMA processes, ensuring enhanced accuracy and reliability in the characterisation of anisotropic and viscoelastic composite materials. The experimental protocol for this section is laid out in Appendix G. Figure 4.1 shows an EMA rig image to provide context to the rig development in this chapter.

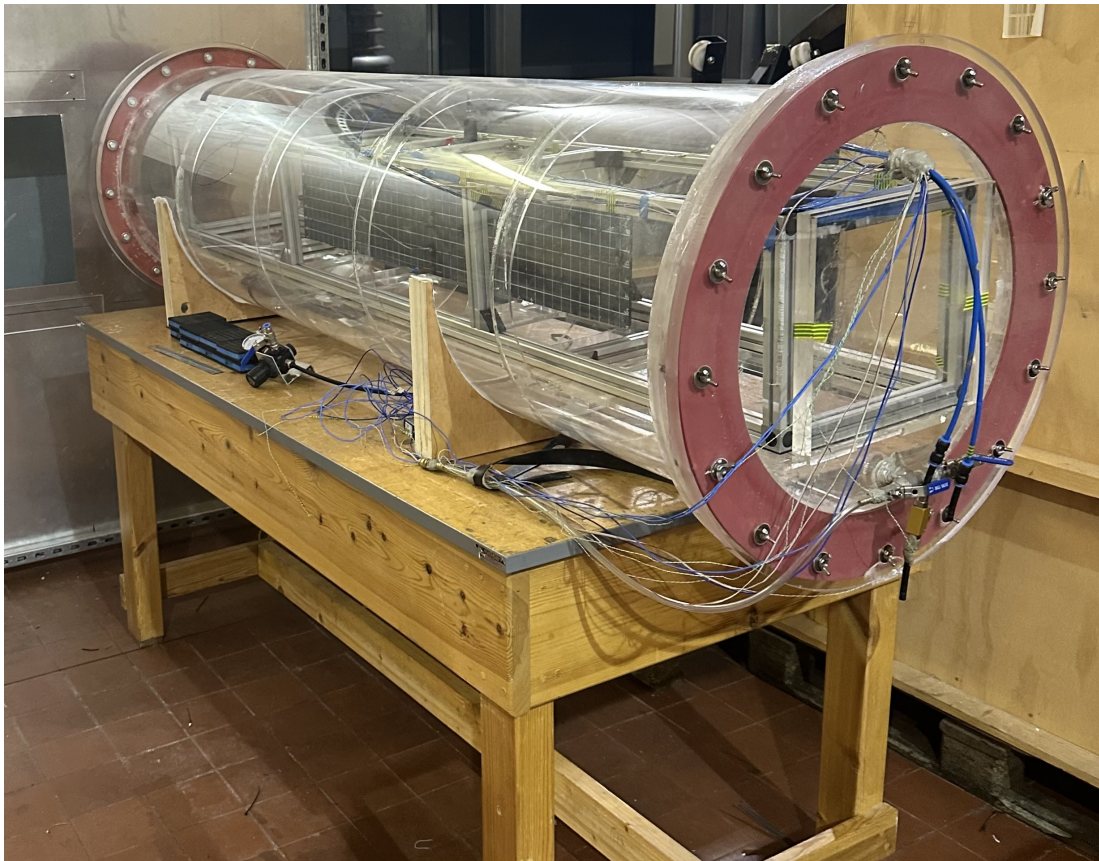


Figure 4.1: Isometric View Of EMA Rig

### 4.3.1 Requirements

The primary goal of the EMA test rig was to accurately capture modal damping, particularly at the first flexural mode of materials, within the frequency ranges typically observed in operational wind turbine blades. The first modern flexural mode with turbine blades generally has a low frequency (below 1 Hz) and is of interest to the industrial supervisor behind this project, SGRE. Because of this, the aim was to ideally keep the frequencies studied as close to this as possible. Additionally, the rig was designed to consider and quantify aerodynamic damping by comparing tests conducted in vacuum and air.

## Chapter 4. Experimental Modal Analysis for Damping Estimation

To achieve this, the rig was designed with the following additional considerations:

- **Sample Quality:** The sample must be checked to ensure no defects were present.
- **Free-Free Boundary Conditions:** Achieved using suspension systems to minimise energy losses at the sample supports.
- **Vacuum System Reliability:** A rotary vacuum pump was selected for achieving the -0.95 bar requirement, with additional sealing precautions to prevent leaks.
- **Sensor Calibration and Precision:** High-precision accelerometers and load cells were employed and calibrated to ensure consistent data accuracy.
- **Data Acquisition and Processing:** A high-resolution data acquisition system with a 2048 Hz sampling rate ensured the accurate capture of modal responses.
- **Flexibility in Sample Dimensions:** Designed to accommodate medium-scale composite panels up to 2 m in length.
- **Environmental Considerations:** While temperature and humidity were not actively controlled, all tests were conducted under standard laboratory conditions to minimise external variations.
- **Safety Protocols:** Includes pressure monitoring for vacuum integrity and protective barriers around the test setup to shield operators during testing.

These design considerations complement the requirements outlined in Table 4.1, ensuring the test rig could accommodate a variety of materials and

## Chapter 4. Experimental Modal Analysis for Damping Estimation

environmental conditions while providing reliable data.

Table 4.1: Design considerations for the EMA test rig.

<b>Design Variable</b>	<b>Specification / Requirement</b>
Material Compatibility	Suitable for composite and metallic samples
Boundary Conditions	Free-free (simulating unconstrained dynamic response)
Vacuum Capability	Minimum 95% vacuum (−0.95 bar) <sup>*1</sup>
Frequency Range	≤50 Hz <sup>*2</sup>
Primary Excitation Method	Remotely operated modal impact hammer
Hammer Strike Force Range	20–100 N
Modularity	Easily assembled/disassembled for configuration changes
Instrumentation Integration	Compatible with accelerometers and high-speed data logging

<sup>\*1</sup> Achieved using a single vacuum pump.

<sup>\*2</sup> First flexural mode is the primary focus due to industrial relevance.

These design considerations not only ensured the test rig's capability to capture reliable damping characteristics but also facilitated testing under controlled and repeatable conditions. Using a free-free boundary condition was critical for minimising energy loss during testing, while the vacuum requirement ensured that aerodynamic damping effects could be isolated. The modular design allowed for easy sample installation and reconfiguration, facilitating the testing of multiple samples and providing flexibility for future research needs.

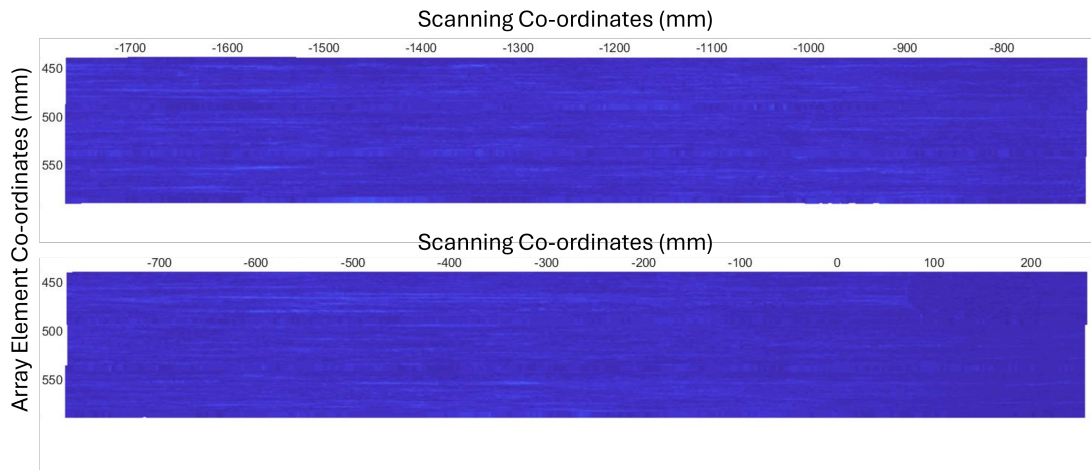
With these requirements met, it was essential to ensure the integrity of the samples to eliminate any influence of pre-existing defects on the test results.

### **4.3.2 Material Inspection Prior to Testing**

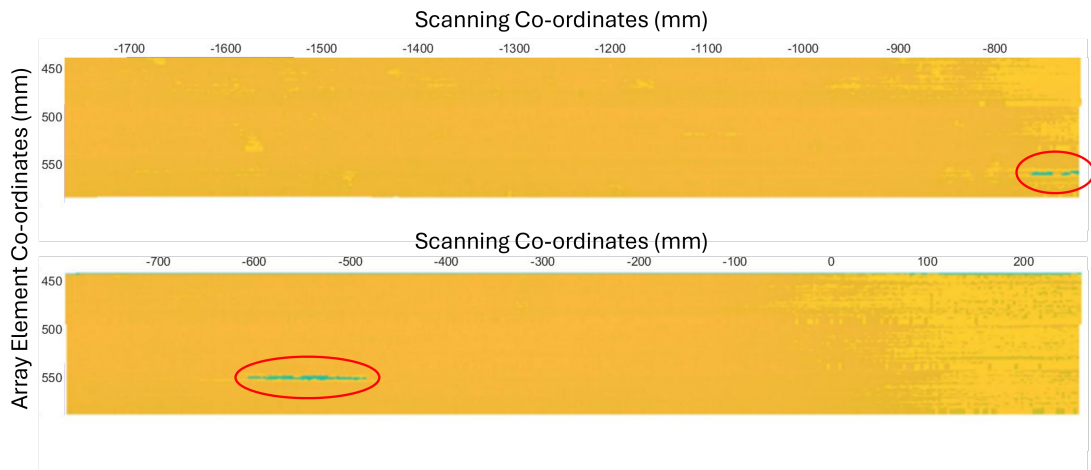
Before conducting any dynamic tests, it was essential to ensure that the materials used in the EMA tests were free from internal defects, such as small cracks or delamination, which could alter the structure's damping characteristics. Internal damage within the composite material could significantly impact internal friction and, consequently, the test results, leading to inaccurate estimations of damping ratios.

In accordance with methods outlined in previous studies on composite inspection [201–204], this inspection was conducted by Euan Duernberger, one of the authors of these referenced works, to ensure consistency and adherence to established protocols. An ultrasonic scanning technique was employed to inspect the composite samples before testing. This non-destructive evaluation method ensured that only defect-free samples were selected for the final testing pool, thereby preserving the reliability of the results. Ultrasonic scans were carefully reviewed to confirm the absence of any internal damage. Figure 4.2 presents examples of the scan results for one of the samples, with and without defects.

## Chapter 4. Experimental Modal Analysis for Damping Estimation



(a) Ultrasonic scan showing no defects.



(b) Ultrasonic scan showing regions of defects (highlighted in green).

Figure 4.2: Ultrasonic scans of composite samples. The top image (a) shows a defect-free sample, while the bottom image (b) shows a sample with defects (circled). The sample in (b) was removed from the testing pool.

As depicted in Figure 4.2, no defects were detected in four of the five scanned samples. Two-panel sections, representing the first and second halves of the sample, were scanned. The sample exhibiting defects was excluded from the pool to maintain the integrity of the test results. Although the detected defects were minor, the sample was eliminated to ensure the reliability of the testing

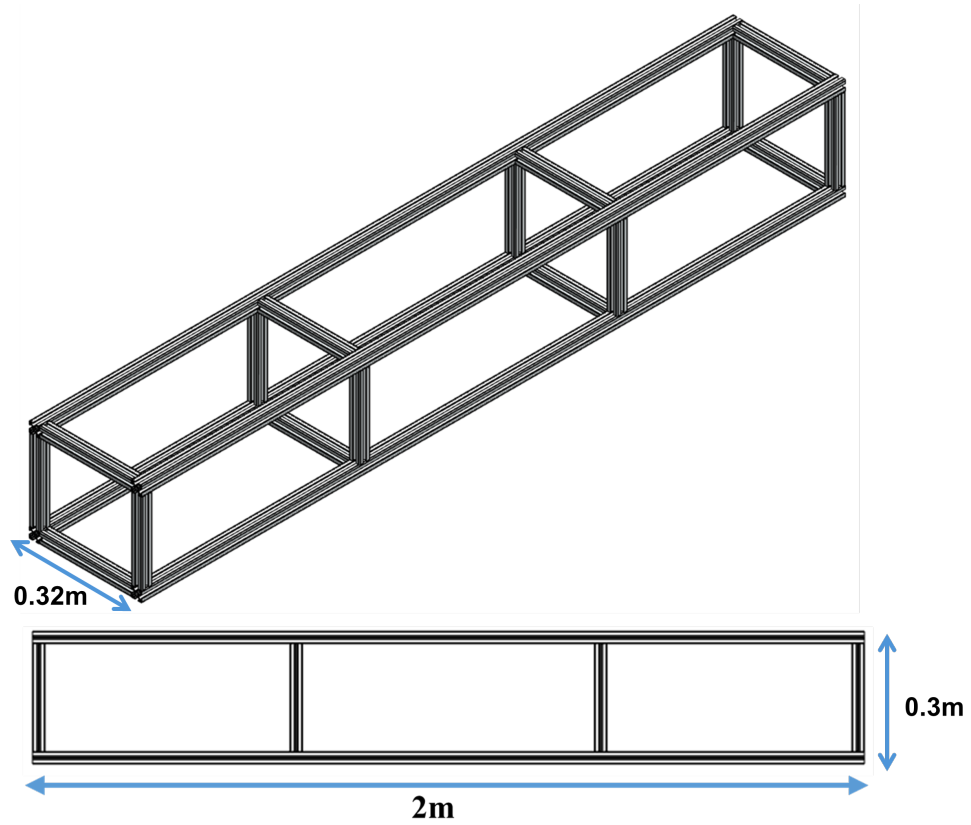
## Chapter 4. Experimental Modal Analysis for Damping Estimation

process. This inspection protocol, based on best practices from existing literature [201–204], ensured that the damping characteristics observed during testing were unaffected by pre-existing internal damage, thus enabling accurate and consistent results.

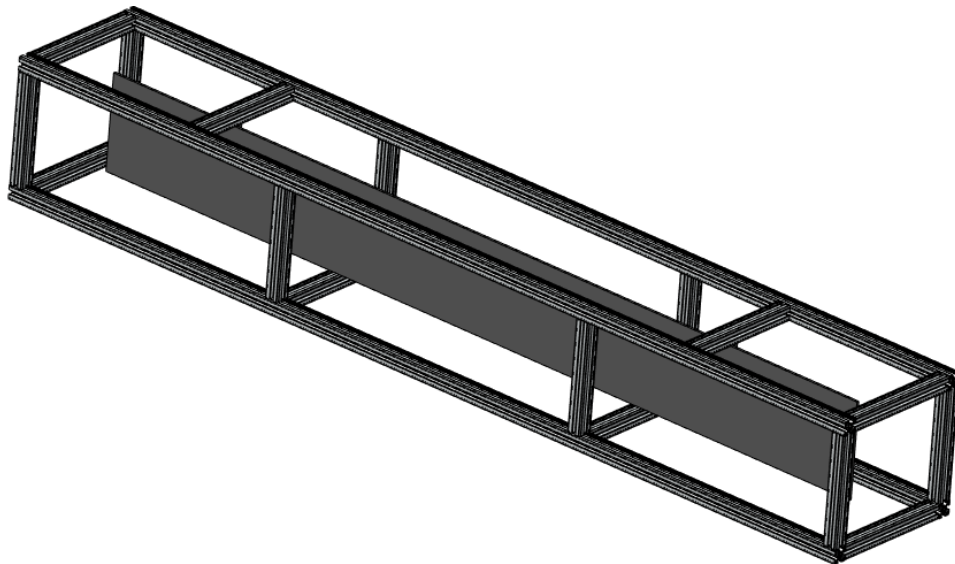
### **4.3.3 Testing Frame and Suspension Mechanism**

The test rig's suspension mechanism was designed to minimise energy loss during the tests. Research in the field has shown that energy can be lost through contact mechanisms, leading to inaccurately high damping values. To mitigate this, a free-free suspension system was selected to avoid the damping inaccuracies arising from fixed boundary conditions. This suspension method ensured that minimal energy was lost from the system, providing more accurate test results.

A modular frame was designed and constructed from aluminium profiles to provide rigidity and adaptability for different sample sizes. The frame allows for the suspension points of the sample to be selected and accommodates samples up to 2 m in length and 0.25 m in width. The frame was rigidly attached to a solid table mounted on a concrete floor to eliminate the influence of external vibrations on the test results. Figure 4.3 illustrates the frame design.



(a) Modular aluminium frame showing dimensions - made from aluminium struts



(b) Modular frame section - with 2m carbon sample suspended.

Figure 4.3: Modular frame design for the EMA test rig. (a) shows the frame only, while (b) shows the frame with the panel inserted.

## Chapter 4. Experimental Modal Analysis for Damping Estimation

FEA was used to determine the suspension points of the samples by identifying the nodal and anti-nodal regions for the first flexural mode of each sample. The nodal regions, which experienced minimal displacement during vibration, were chosen as the optimal suspension points to minimise energy loss through the suspension mechanism. Figure 4.4 shows an example of the FEA results for a sample, highlighting the nodal and anti-nodal locations.

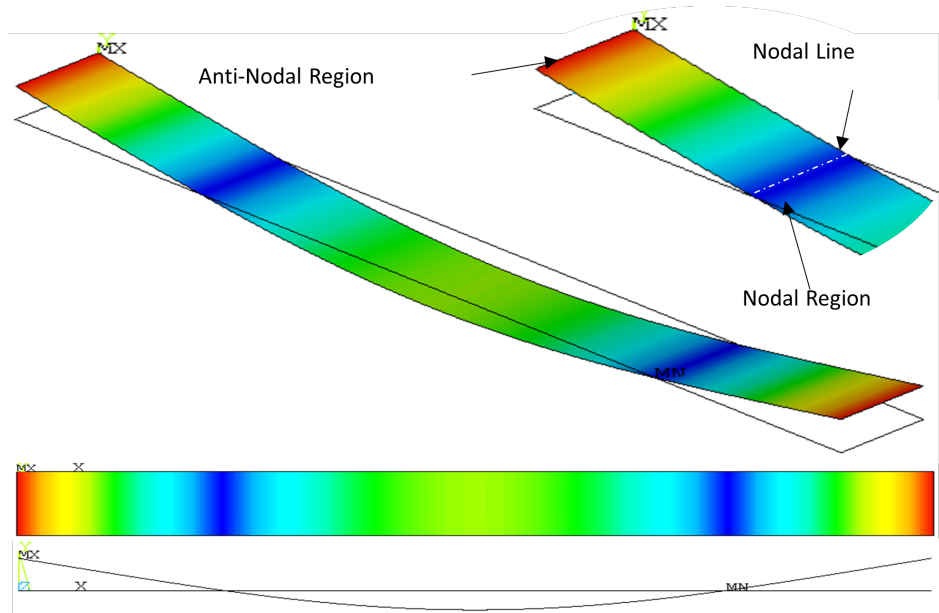


Figure 4.4: Modal FEA results showing the first flexural mode under free-free boundary conditions with element size of 0.25 mm. This image highlights nodal (low displacement - dark blue) and anti-nodal (high displacement- red) regions.

The test rig's suspension points were designed to be adjustable by sliding the top aluminium support profiles along the frame. This modular design enabled the testing of samples with various dimensions and material properties. After determining the optimal nodal locations for suspension, different suspension methods were evaluated through a comparative analysis based on the Frequency Response Function (FRF) generated during testing [205]. The sample mechanism can be seen isolated in Figure 4.5.

## Chapter 4. Experimental Modal Analysis for Damping Estimation

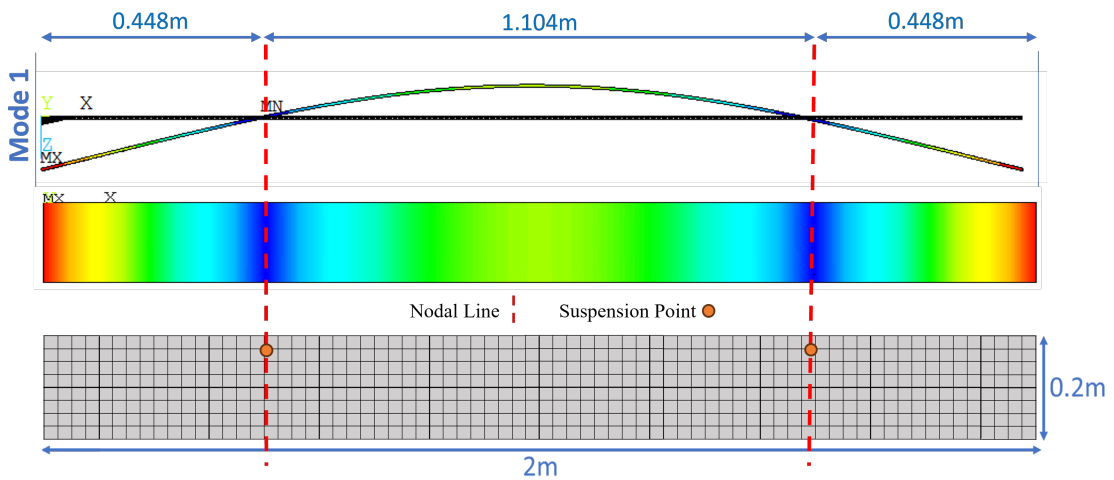


Figure 4.5: Sample showing support locations based on mode 1 deformation - blue locations represent minimum deflection of mode shape

The suspension points of the test rig were designed to be adjustable by sliding the top aluminium support profiles along the frame. This modular design enabled the testing of samples with various dimensions and material properties. After determining the optimal nodal locations for suspension, different suspension methods were evaluated through a comparative analysis based on the Frequency Response Function (FRF) generated during testing. The data acquisition was performed using Matlab with NI toolbox, with the code available in Appendix H

The following suspension methods were considered:

### Support Method:

- **Elastic Band Supports:** Provided flexible support.
- **Nylon Band Supports:** Provided rigid support.

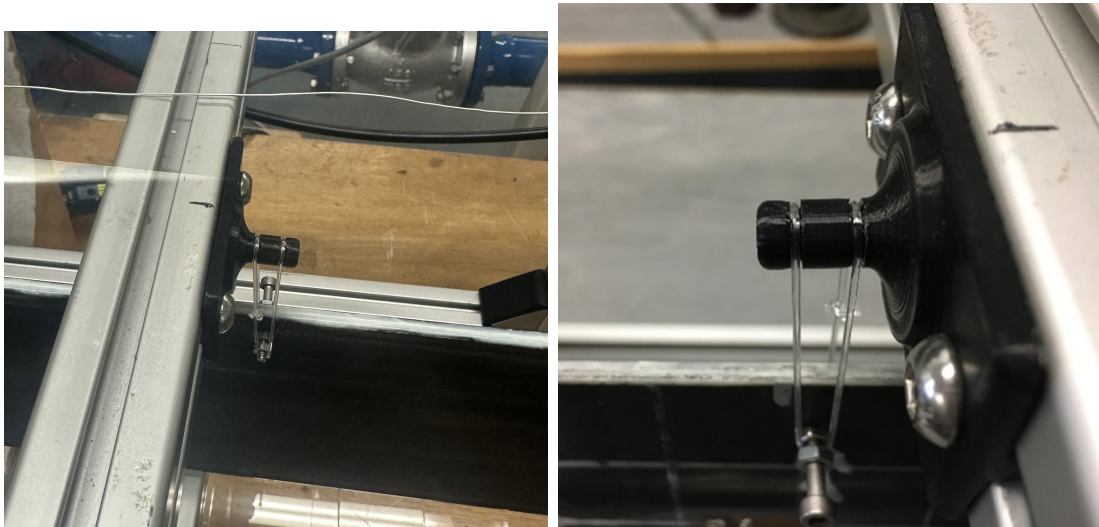
### Interface Methods Considered:

- **Band Only:** Offered minimal contact but lacked precise control, making it susceptible to unwanted motion.

## Chapter 4. Experimental Modal Analysis for Damping Estimation

- **Clamping Supports:** Offered a rigid hold but risked slipping and energy losses through friction at the contact points.
- **Single Pin Supports:** Allowed free rotational movement but required precise alignment to avoid off-axis motion and potential slipping.
- **Pin and Bolt Supports (with Clamping):** Combined pin supports with clamping for additional stability and adjustability.

Suspension methods that introduced unwanted peaks in the FRF, indicating additional energy losses or unwanted modes, were eliminated from consideration to ensure more accurate damping measurements. An example of a poor and good FRF are displayed in Appendix I. Experimenting determined that a combination of nylon string and pins with bolt supports provided the most stable suspension. The final suspension mechanism can be seen in Figure 4.6, where the top connector is also present.



(a) Updated suspension mechanism      (b) Zoomed view of the suspension point.

Figure 4.6: (a) Updated suspension mechanism, (b) Zoomed view of the suspension point.

The frequency response function (FRF) produced from testing revealed the

## Chapter 4. Experimental Modal Analysis for Damping Estimation

effectiveness of this optimised suspension method. Figure 4.7 shows the FRF results, with clear peaks corresponding to the first few modal frequencies of the sample. The absence of unknown peaks and the sharp magnitude of the first modal frequency indicated the success of this suspension method in minimising energy loss.

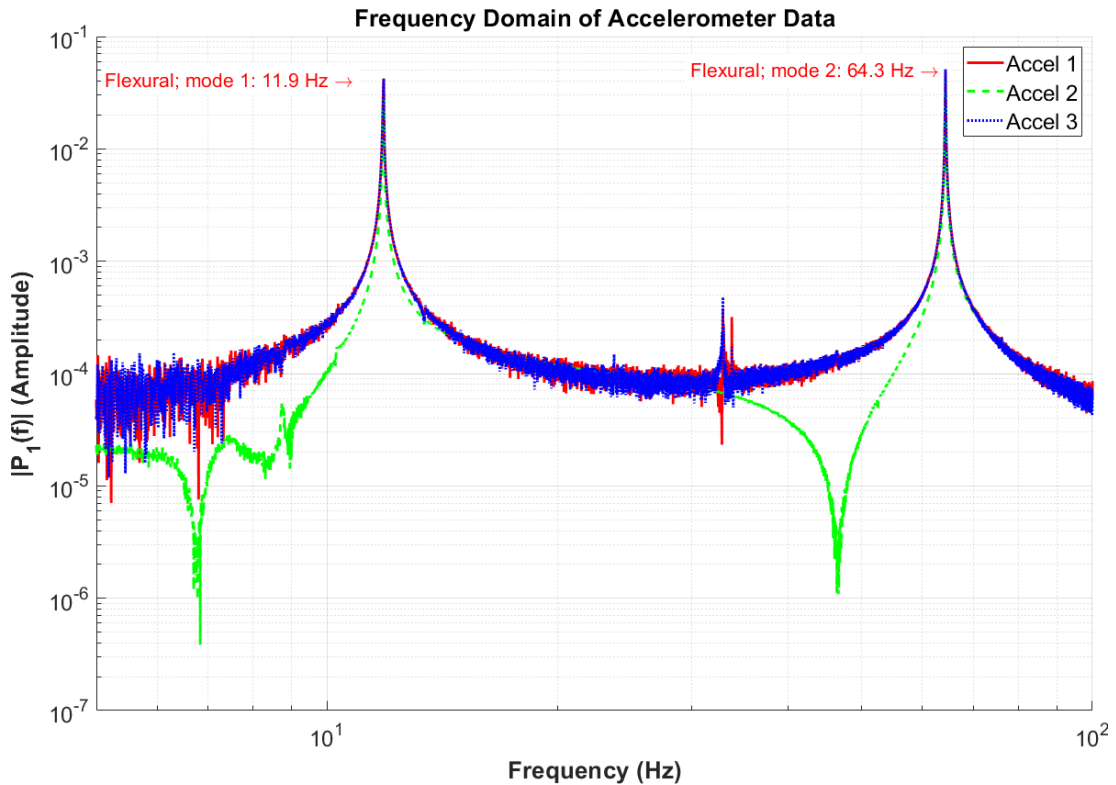


Figure 4.7: Frequency response function (FRF) of the unfiltered signals from the three accelerometers mounted along the test specimen. Peaks correspond to the first and second flexural modes, identified at 11.9 Hz and 64.3 Hz, respectively.

As seen in Figure 4.7, the magnitude of the response from the outer accelerometers (1 and 3) is consistently higher than that of the central accelerometer (2). This is expected, as the outer accelerometers were positioned near the antinodal regions of the first flexural mode, where displacement is maximal. In contrast, accelerometer 2 was located near a

## Chapter 4. Experimental Modal Analysis for Damping Estimation

nodal region, where displacement is minimal. This placement strategy, based on FEA predictions (see Figure 4.4), confirms the activation of the intended vibration mode and validates the effectiveness of the free-free suspension in preventing spurious energy dissipation.

The FRF also demonstrates a clean signal with well-defined peaks and minimal noise contamination, further supporting the quality of the test setup. While the Polymax (pLSCF) method was employed for modal parameter extraction (see Section 4.2.4.2), its advanced capabilities, such as resolving closely spaced modes and handling noisy data, were not strictly required under these conditions. Nonetheless, its compatibility with MIMO systems and seamless implementation via the MACEC toolbox made it the most appropriate choice for reliable and reproducible modal analysis.

In summary, the testing frame and suspension mechanism were carefully designed and optimised to ensure minimal energy loss, enabling accurate modal analysis. The modular frame and nodal-based suspension approach provided robust and repeatable testing conditions for characterising the damping behaviour of composite materials.

### **4.3.4 Sample Excitation Method**

Different excitation methods, both contact and non-contact, were considered to ensure consistent excitation during the testing process. However, since the test rig operates under vacuum conditions, a modal hammer with remote operation was decided to be the most appropriate excitation source.

During the initial stages of testing, it was found that the manual hammer strikes (Method A) lacked consistency and introduced errors due to double strikes. While data sorting by force ranges could have been implemented, it was determined that an automated mechanism would be required for testing

## Chapter 4. Experimental Modal Analysis for Damping Estimation

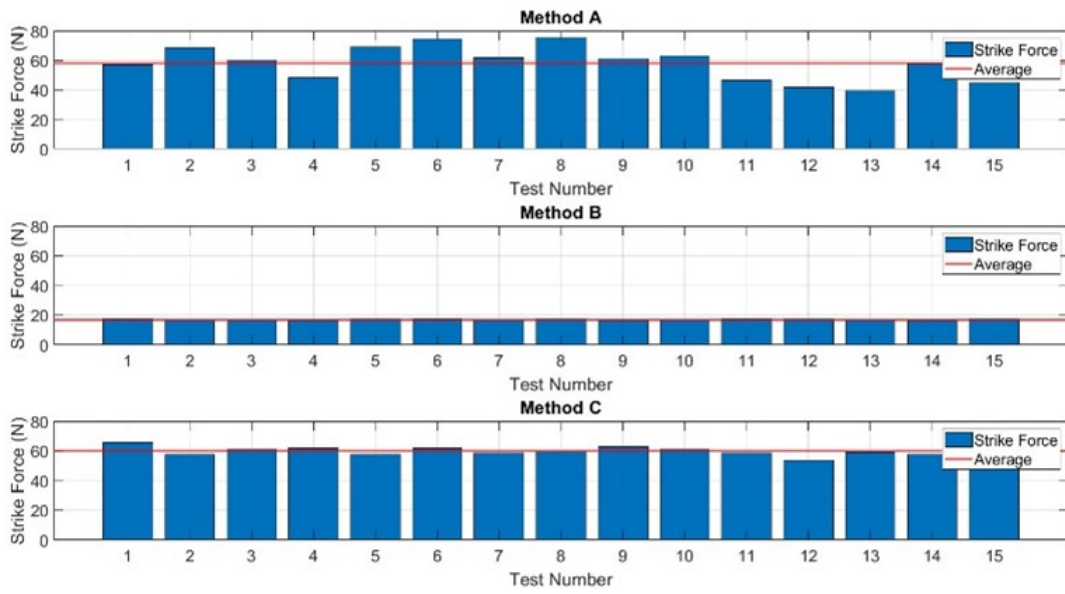
within a vacuum to provide more consistent strike data. This led to the investigation and comparison of two automated methods: solenoid-assisted strikes (Method B) and pneumatic-assisted strikes (Method C).

**Comparison of Excitation Methods** Three methods were evaluated:

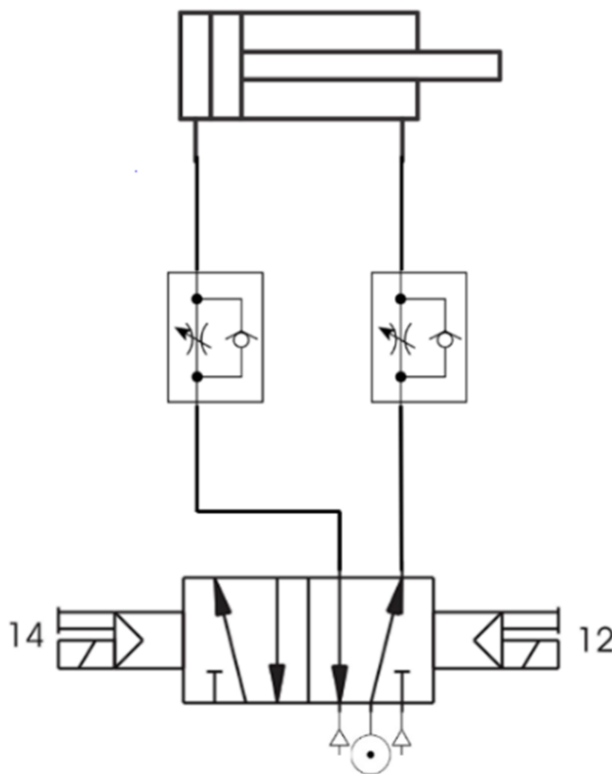
- **Method A:** Manual modal hammer strikes.
- **Method B:** Solenoid-assisted modal hammer strikes.
- **Method C:** Pneumatic-assisted modal hammer strikes.

Each method was assessed based on its consistency and the force it could generate. The target force for the tests was set to 60 N. As shown in Figure 4.8, Method A demonstrated a high level of inconsistency with a wide range of forces and a significant standard deviation. Additionally, manual strikes introduced double strikes, which compromised the accuracy of the results. In contrast, both Methods B and C were found to be more consistent. Still, Method B could not achieve the desired force levels, resulting in Method C being the most reliable option for consistent excitation.

## Chapter 4. Experimental Modal Analysis for Damping Estimation



(a) Comparison of excitation methods.



(b) Schematic of pneumatic-assisted excitation method.

Figure 4.8: Comparison of excitation methods (a) and the schematic of the selected pneumatic-assisted excitation method (b).

**Selected Pneumatic Striking System** The pneumatic system was chosen for its ability to generate consistent strikes at a wide range of forces. This system utilised a pneumatic piston actuator controlled by a 5/2 valve connected to an inlet air supply of 10 bar (which was important to remain consistent). The actuator was designed to strike the back of the modal hammer, which delivered the force to the sample without the pneumatic system directly contacting it. A schematic of this system is shown in Figure 4.8b.

The pneumatic-assisted hammer was equipped with restrictor valves, which allowed precise adjustment of the applied force, preventing double strikes and ensuring consistent excitation. To avoid multiple strikes, a 555-timer circuit was used to control the timing of the solenoid pulse, producing a short, controlled pulse to the actuator. This configuration eliminated the occurrence of double strikes during testing.

**Force Testing and Validation** The pneumatic system was rigorously tested to verify its ability to generate precise and repeatable forces. The results, summarised in Table 4.2, show that the system achieved a range of target forces with minimal error and acceptable standard deviations, indicating its suitability for testing under various force conditions.

## Chapter 4. Experimental Modal Analysis for Damping Estimation

Table 4.2: Force testing results for the pneumatic-assisted striking system.

Target (N)	Force	Average Force (N)	Error (%)	Standard Deviation (N)
30		29.10	0.97	0.28
40		40.57	1.02	0.41
50		49.70	1.34	0.67
60		60.13	0.35	0.21
70		71.54	0.92	0.66
80		79.72	0.31	0.24
90		89.85	1.14	1.02
100		98.70	2.42	2.38
110		109.32	3.58	3.91

As shown in Table 4.2, the pneumatic system demonstrated high accuracy across all target force levels, with errors ranging from 0.31% to 3.58% as the force level reached its upper bound. The results confirm the system's capability to provide consistent and reliable excitation forces, which are critical for accurate EMA testing.

**Pneumatic Setup in Operation** The final setup has the hammer installed at the back end of the test rig, as shown in Figure 4.9. The pneumatic-assisted system was mounted behind the modal hammer, using a 3D printed mount, ensuring the actuator disconnected from the hammer just before the strike occurred. This configuration enabled precise, controlled strikes at the sample's midpoint, delivering the required excitation force without introducing double strikes.

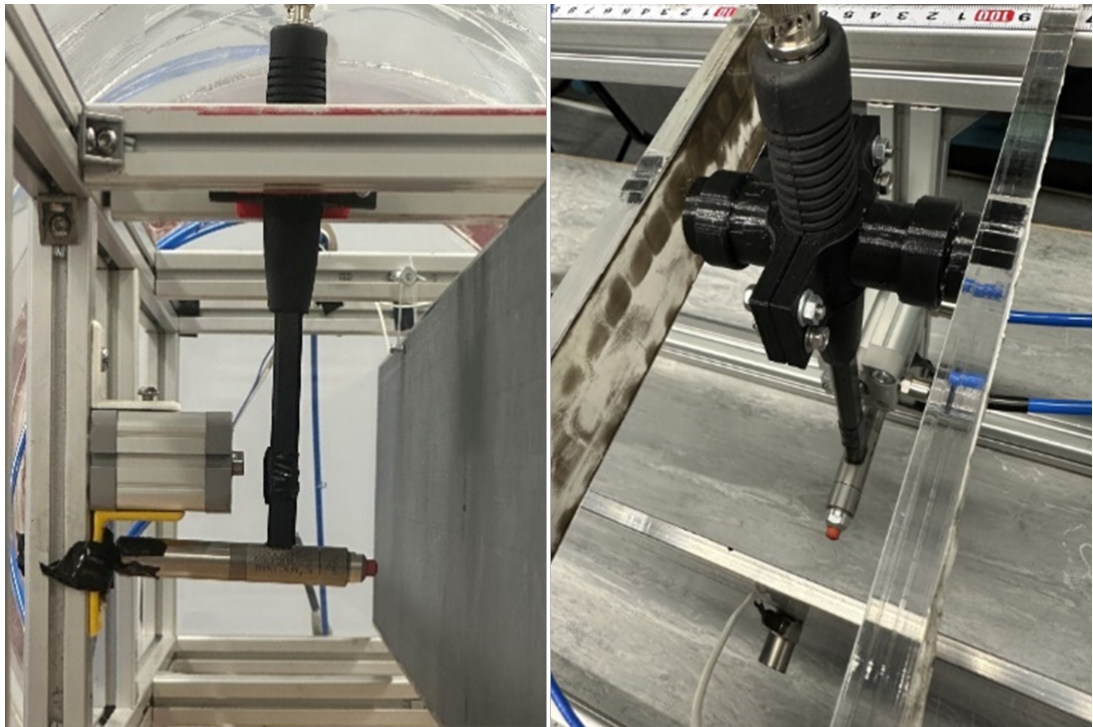


Figure 4.9: Full hammer setup for the EMA test rig.

### 4.3.5 Vacuum Chamber

The vacuum chamber was designed to eliminate aerodynamic damping effects, enabling the distinction between structural and aerodynamic damping in the tested samples [56]. The aerodynamic damping contributions can be removed entirely by conducting tests in a vacuum, allowing for more accurate measurements of the structural damping properties [206]. This setup also allowed the investigation of the effects of altering the strain rate on the damping characteristics of the sample.

The chamber was constructed from a 2.1 m acrylic cylinder with an outer diameter of 550 mm and a wall thickness of 6 mm. Four support stiffening rings were added along the cylinder to maintain structural integrity under vacuum conditions, with two additional rings placed at each end. The end

## Chapter 4. Experimental Modal Analysis for Damping Estimation

caps, made from 20 mm thick acrylic with an outer diameter of 650 mm, were bolted using an external mounting mechanism to ensure airtight seals and prevent leakage through the bolting methodology. The vacuum chamber design adhered to the pressure vessel design standards outlined in *PD5500: Specification for Unfired Pressure Vessels* [207]. Figure 4.10 shows the CAD model of the vacuum chamber.

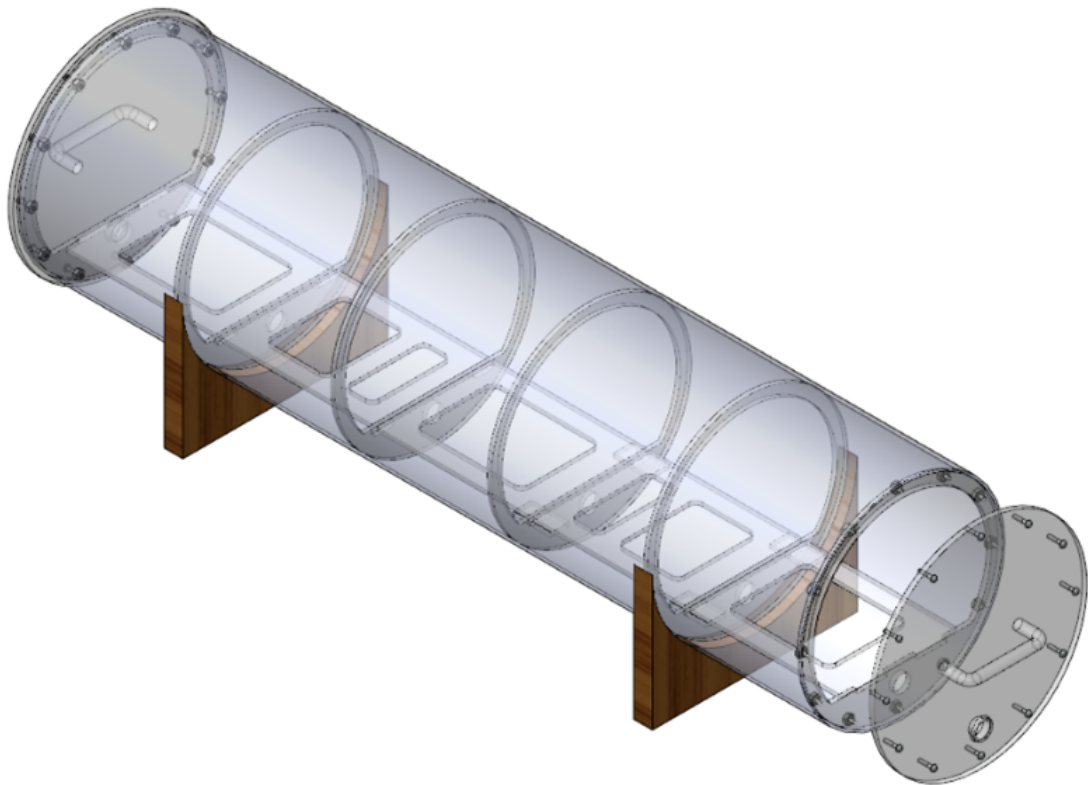


Figure 4.10: CAD model of the vacuum chamber for the EMA test rig.

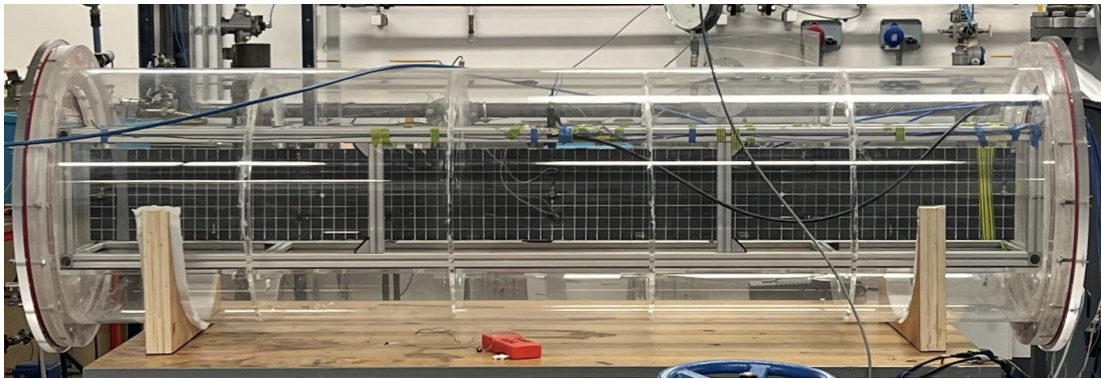
Two wooden saddle supports held the vacuum chamber rigidly, providing stability during testing. The end plates were equipped with fittings for connecting up to two vacuum pumps via a T-connector, gate valves, and quick disconnects for easy connection and disconnection of the pumps. A vacuum gauge and a pressure release valve were installed on one end plate. At the same time, the other end plate has cable glands for passing cables and the

## Chapter 4. Experimental Modal Analysis for Damping Estimation

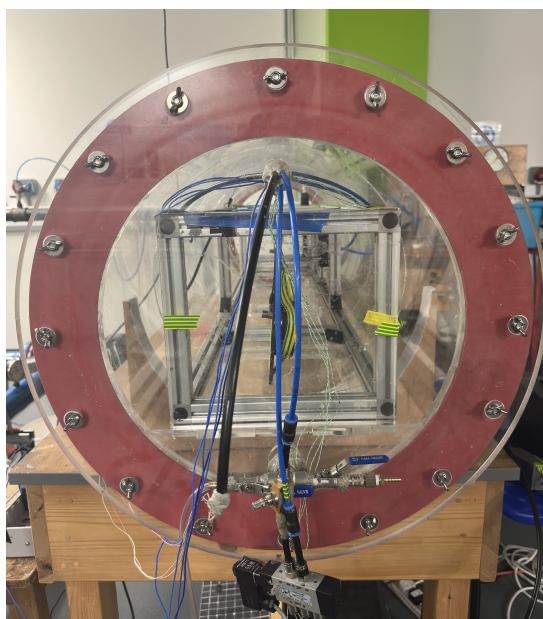
automated hammer striker's pressure system into the vacuum-controlled environment.

The chamber was designed to allow for easy removal of the modular frame between tests, ensuring the quick insertion and extraction of the frame and samples. A flat acrylic section was fitted inside the vacuum chamber to accommodate the frame. The design was modelled using SOLIDWORKS to ensure precision when manufacturing. All acrylic parts apart from the cylinder were cut in-house at the University of Strathclyde. These sections were cut to shape using a laser printer and connected using a rapid-bonding liquid acrylic adhesive. The complete vacuum chamber assembly, including the modular frame insertion, can be seen in Figure 4.11a.

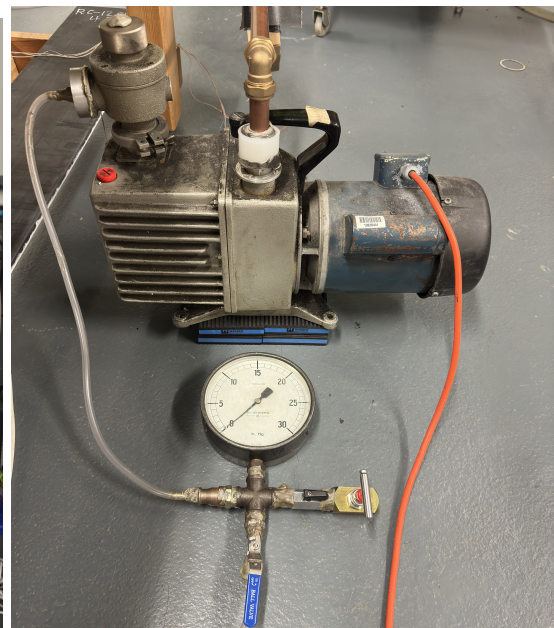
## Chapter 4. Experimental Modal Analysis for Damping Estimation



(a) Fully constructed vacuum chamber with modular frame setup for the EMA test rig.



(b) End-on view of the vacuum chamber



(c) Vacuum Pump on isolation pads

Figure 4.11: (a) Full vacuum chamber setup; (b) End-on view of the vacuum chamber; (c) Vacuum Pump on isolation pads

The structural integrity of the vacuum chamber was validated through calculations in accordance with *PD5500*, detailed in Appendix J.

### 4.3.6 Data Acquisition

The data acquisition system was an important component of the EMA setup and ensured the accurate capture of dynamic response data during testing. Three accelerometers were positioned at the anti-nodal points of the test samples and connected to a compact data acquisition (cDAQ) device using low-noise coaxial cables with microdot connectors at the accelerometer end and BNC connectors at the DAQ module. An example of this module can be seen in Figure 4.12, taken from [208]. In addition to accelerometers, strain gauges were installed to monitor strain in critical regions of the samples, providing a secondary data source to measure deformation. Strain measurements are vital as they allow for more meaningful comparisons between samples of varying material properties and sizes, ensuring that the material's response is assessed independently of the force applied during testing. Accelerometers primarily capture overall acceleration rather than direct local strain, they cannot reliably indicate the maximum strain within a sample. Therefore, incorporating strain gauges was essential for normalising the dynamic response data, thereby offering a more accurate and comparable metric for evaluating the damping characteristics of different materials.



Figure 4.12: NI cDAQ (NI 9189) with accelerometer module (NI 9234) - taken from [208]

## Chapter 4. Experimental Modal Analysis for Damping Estimation

Thermocouples were also employed to monitor the temperature of the samples during testing, as temperature variations can impact the material's damping characteristics. The K-type thermocouples were connected conventionally via an NI temperature module (NI 9211). The addition of the strain and temperature sensors provided a comprehensive set of measurements to capture the samples' complete dynamic response during testing. The placement of the sensors was carefully determined based on FEA results. Figure 4.4 illustrates the nodal and anti-nodal locations of the samples and the corresponding placement of accelerometers and strain gauges, which was crucial for ensuring accurate data collection during testing.

The placement of the accelerometers and strain gauges was validated through additional tests, where multiple strikes of the same magnitude were performed while adjusting sensor positions along the length of the beam. The results confirmed that the greatest acceleration and strain areas corresponded to the anti-nodal regions, as shown in Figure 4.4, validating the FEA predictions. This setup, combined with the pneumatic-assisted hammer, provided high accuracy and repeatability, ensuring reliable data acquisition across multiple measurement types throughout the testing process. The resultant positions may be viewed in Figure 4.13.

## Chapter 4. Experimental Modal Analysis for Damping Estimation

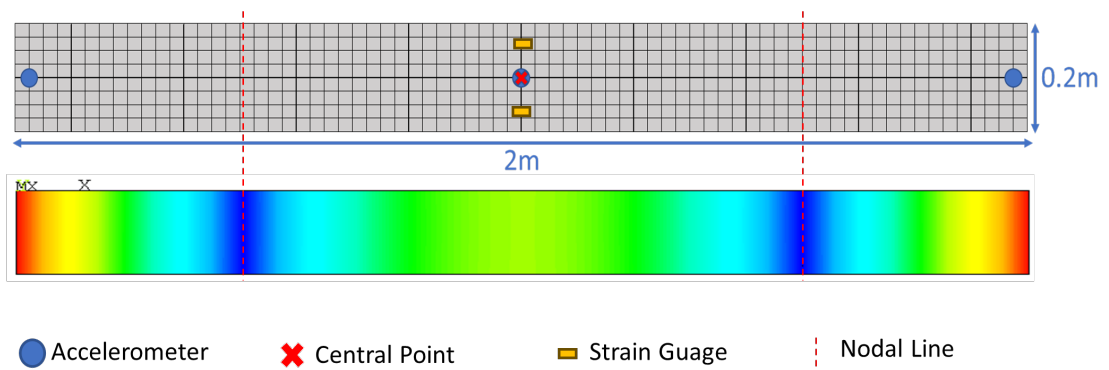


Figure 4.13: Placement of accelerometers and strain gauges at anti-nodal points for optimal data capture. Dark blue represents minimum deformation and transitions to red, representing maximum deformation.

The force applied by the impact hammer and the corresponding acceleration responses of the three accelerometers are shown in Figure 4.14. This figure demonstrates the dynamic response captured during testing, highlighting the impact's transient nature and the structure's subsequent decaying vibration.

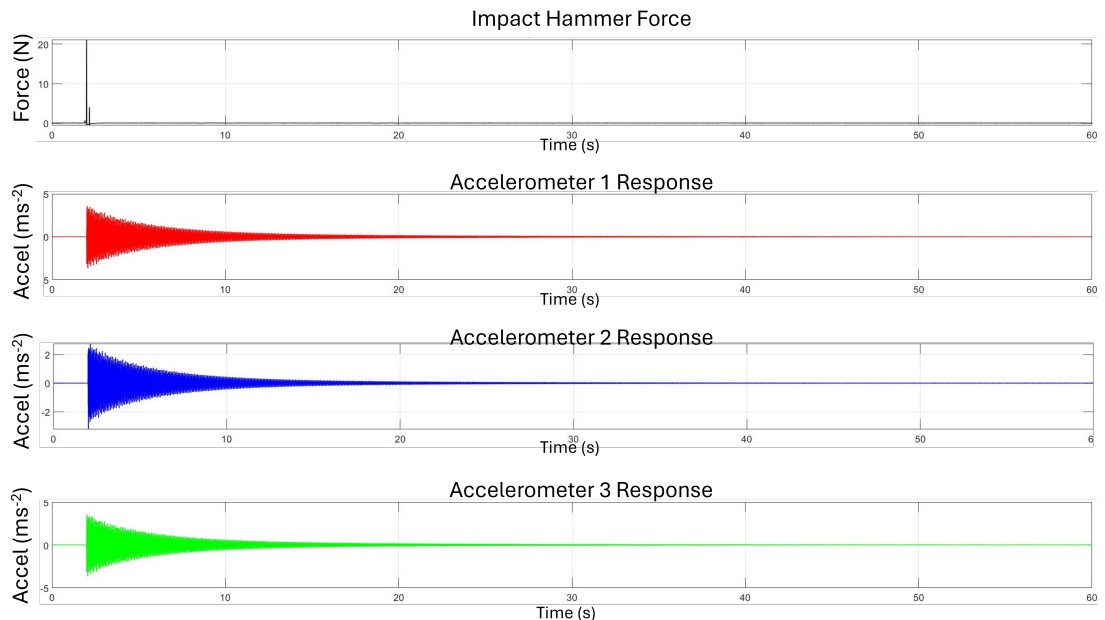
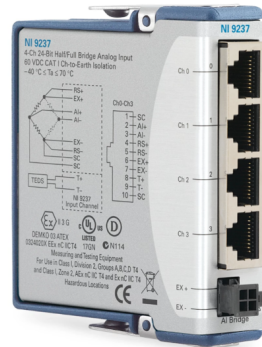


Figure 4.14: Impact test data showing the force applied by the hammer and the responses of Accelerometer 1, 2, and 3.

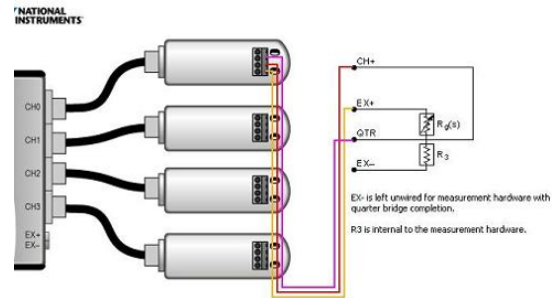
## Chapter 4. Experimental Modal Analysis for Damping Estimation

The strain gauges were connected to the data acquisition (cDAQ) system through an NI 9237 strain gauge module, which is specifically designed to measure signals from strain gauges and load cells with high accuracy. In this setup, a quarter-bridge configuration was employed to capture the strain data.

To facilitate quarter-bridge completion, an NI 9944 bridge completion module was used in conjunction with the NI 9237. The NI 9944 module provides a precise  $R_g$  resistor, enabling the accurate measurement of strain in the quarter-bridge configuration. Figures 4.15 show the NI 9237 strain gauge module and the quarter-bridge wiring configuration with the NI 9944, respectively [208] (Taken from [209]).



(a) NI 9237 strain gauge module for connecting strain gauges in a quarter-bridge configuration.



(b) Wiring diagram for the quarter-bridge strain gauge setup, showing the connection of the NI 9944 bridge completion module with the NI 9237.

Figure 4.15: (a) NI 9237 strain gauge module for connecting strain gauges; (b) Wiring diagram for quarter-bridge setup with NI 9944 bridge completion module.

[(a) NI 9237 strain gauge module for connecting strain gauges; (b) Wiring diagram for quarter-bridge setup with NI 9944 bridge completion module. - Taken from [209]]

Table 4.3 summarises the hardware setup used for data acquisition within the EMA experimental setup.

## Chapter 4. Experimental Modal Analysis for Damping Estimation

Table 4.3: Data acquisition hardware for EMA testing.

<b>Component</b>	<b>Model</b>
cDAQ	NI 9189
Accelerometer Modules	NI 9234
Strain Gauge Module	NI 9237
Temperature Module	NI 9211
Accelerometers	PCB 353B03 (3)
Strain Gauges	120-ohm Uni-Axial Gauge (2)
Thermocouples	K Type (4)
Modal Hammer	PCB 086C03
Accelerometer Cables	Low-noise BNC cables - 5m (3)*
Modal Hammer Cable	Low-noise BNC cable - 5m

\*The accelerometer BNC cable features a Microdot connection on the accelerometer end.

Real-time data acquisition was performed using MATLAB in conjunction with the NI toolbox. This facilitated the collection of dynamic response data from the accelerometers, strain gauges, and thermocouples with a data acquisition rate of 2048 Hz (well above the frequency of interest within this experiment). The MATLAB interface allowed for efficient data handling and visualisation during testing, ensuring data points from mistaken experiments could be discarded (e.g. fault during strike).

Using strain measurements was particularly valuable, allowing for a more appropriate comparison between samples with different geometries or setups. While force applied by the modal hammer could vary slightly between tests, strain data provided a normalised metric, making it easier to assess each sample's accurate excitation metrics. This was especially important when comparing different suspension mechanisms near the start of the object, where the force-to-strain relationship can differ significantly - allowing for direct comparison between different geometries with constant strain.

### 4.3.7 Post-Processing

Post-processing was conducted using the MACEC toolbox within MATLAB, which is specifically designed for extracting modal parameters such as natural frequencies, mode shapes, and damping ratios from measured vibration data. The toolbox, developed by KU Leuven, provides extensive functionalities for data visualisation, system model identification, and modal characteristics determination. Integrating the NI toolbox in MATLAB during data acquisition allowed for seamless real-time data capture and provided a strong foundation for post-processing and advanced analysis of the collected data.

The first step in the post-processing workflow was creating a nodal model within the MACEC toolbox. This nodal model mapped the physical locations of accelerometers and the force cell onto corresponding nodes in the system. Figure 4.16 shows the nodal model used in this study, where nodes 2, 8, and 14 represent the accelerometer locations, and node 8 corresponds to the force cell. This geometrical model was used to bind the collected acceleration and force data to specific locations within the test structure, allowing for the accurate extraction of modal parameters based on these sensor placements.

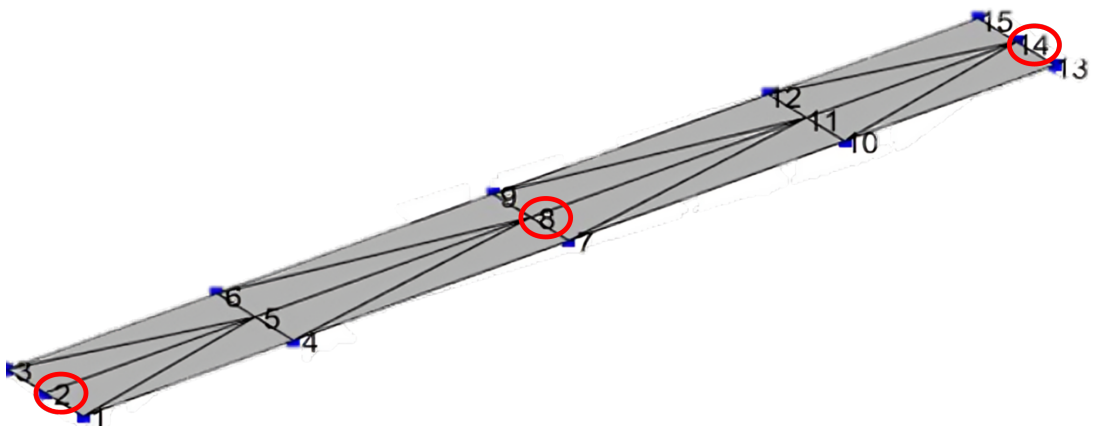


Figure 4.16: Nodal model showing accelerometer and force cell locations.

## Chapter 4. Experimental Modal Analysis for Damping Estimation

Once the nodal model was established, the collected force and acceleration data were imported into the MACEC toolbox. The appropriate sample rate was set to ensure accurate signal processing, after which the data was bound to the nodes within the created model. This step allowed for the precise allocation of measurements to the relevant physical points on the structure, ensuring that modal analysis was performed concerning the real sensor placements.

The Polymax (PLSCF) method was then applied to process the force and acceleration data. This method was required for generating stabilisation diagrams, which visually represent the stable modes of the structure across a range of frequencies. These stabilisation diagrams were used to identify modes that remained stable over multiple model orders, filtering out spurious modes. An example of a stabilisation diagram generated during testing is shown in Figure 4.17.

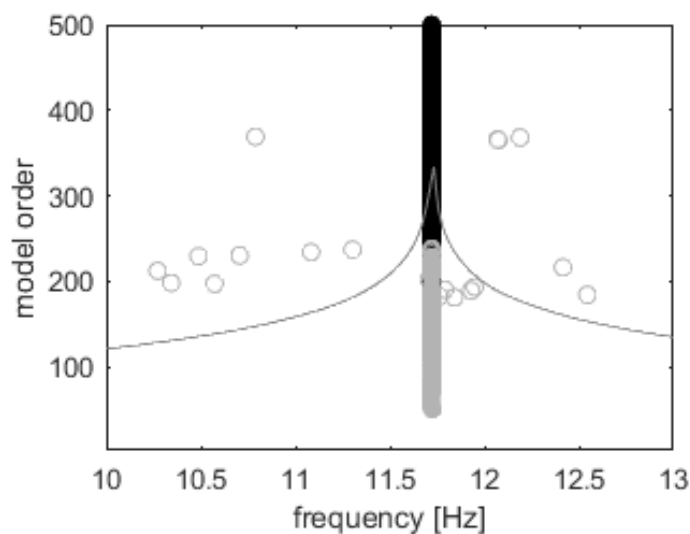


Figure 4.17: Stabilisation diagram generated using Polymax (PLSCF) method - for 2 m x 20 cm x 5 mm sample - dark circles represent stable modes

Once the stabilisation diagram was generated, several key filtering metrics

## Chapter 4. Experimental Modal Analysis for Damping Estimation

were applied to ensure the selection of real and stable modes. These metrics not only evaluate the consistency of the extracted modes but also mitigate the influence of measurement noise and numerical errors, thereby enhancing the reliability of the modal parameters. Specifically:

- *Modal Assurance Criteria (MAC)*: This metric assessed the consistency of mode shapes across different frequency ranges. MAC values close to 1 indicate a high degree of similarity, confirming the physical relevance and repeatability of the modes.
- *Modal Phase Collinearity (MPC)*: MPC was used to filter out spurious modes by ensuring that the phase of the mode shapes remains collinear. This is particularly important in reducing the impact of noise and in automating the mode selection process.
- *Modal Phase Deviation (MPD)*: MPD detected significant deviations in phase across mode shapes, providing an additional check on the stability and validity of the extracted modal parameters.

Collectively, these filtering metrics enabled automated mode selection and minimise uncertainties arising from environmental and experimental conditions, ensuring that only robust, physically meaningful modes were utilised in subsequent analyses and model updates. By applying these criteria, only the most stable and accurate modes, particularly those corresponding to the first modal frequency, were retained. Once these stable modes were identified, the system provided the final modal parameters (modal frequencies, mode shapes, and damping ratios), which were then used to evaluate the dynamic behaviour of the carbon composite samples.

To further validate the selected modes, the resultant mode shape was viewed for the initial 2 m, 5 mm carbon sample, showing the dynamic deformation of

## Chapter 4. Experimental Modal Analysis for Damping Estimation

the sample at the first modal frequency. Figure 4.18 provides an example of a visualised mode, which helped verify the accuracy of the extracted modal shapes and damping characteristics.

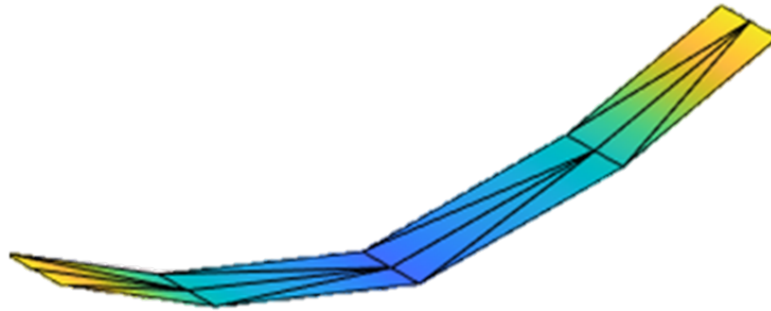


Figure 4.18: Mode shape visualisation at the first modal frequency 11.7 Hz

Using the extracted modal parameters from the stabilisation diagrams and mode shape visualisations, the structural damping of the carbon samples was evaluated. The first modal frequency was used as the reference point for extracting damping ratios, providing a benchmark for comparing the damping properties of the carbon composite samples. This method confirmed the effectiveness of the EMA test rig in capturing accurate modal data across different testing conditions.

### 4.4 EMA Results

This section presents the findings from the EMA testing program, focusing on evaluating the damping characteristics of composite materials used in wind turbine blades. The test program involved testing all samples in both atmospheric and vacuum conditions to isolate aerodynamic damping effects. The tested samples included:

- 2 m x 20 cm x 5 mm Pultruded Carbon Fibre Composite Sample

## Chapter 4. Experimental Modal Analysis for Damping Estimation

- 2 m x 20 cm x 2.5 mm Pultruded Carbon Fibre Composite Sample (Milled)
- 1.2 m x 20 cm x 5 mm Pultruded Carbon Fibre Composite Sample (Cut)

This chapter presents the measured sample thickness results, the FEA validation outcomes, and the experimentally derived damping properties of all samples tested. In the following subsections, a detailed analysis compares the damping characteristics of each sample, highlighting the effects of environmental conditions, such as atmospheric versus vacuum testing and varying excitation forces, on damping behaviour.

These findings support a more accurate understanding of the dynamic properties of composite materials by ensuring that only true material damping is captured via measurement. They will also contribute to the development of larger-scale wind turbine blade models with improved damping characterisation.

### **4.4.1 Results from EMA Testing of UD Pultruded Carbon Fibre Composite (2 m x 20 cm x 5 mm)**

This section presents the results obtained from the EMA of the unidirectional (UD) pultruded carbon fibre composite sample, which has dimensions of 2 m x 20 cm x 5 mm. The study focused on evaluating the material's damping properties at its first flexural mode and assessing the consistency of the sample's geometric properties.

#### **4.4.1.1 Sample Geometry Consistency**

Prior to conducting the EMA testing, the consistency of the sample's geometry was evaluated and displayed via two methods. The first is a heat

## Chapter 4. Experimental Modal Analysis for Damping Estimation

map, which visually represents the thickness uniformity across the length and width of the composite panel. Figure 4.19 illustrates the heat map, confirming the consistent thickness of the sample, which is needed for ensuring accurate modal analysis and reliable damping results.

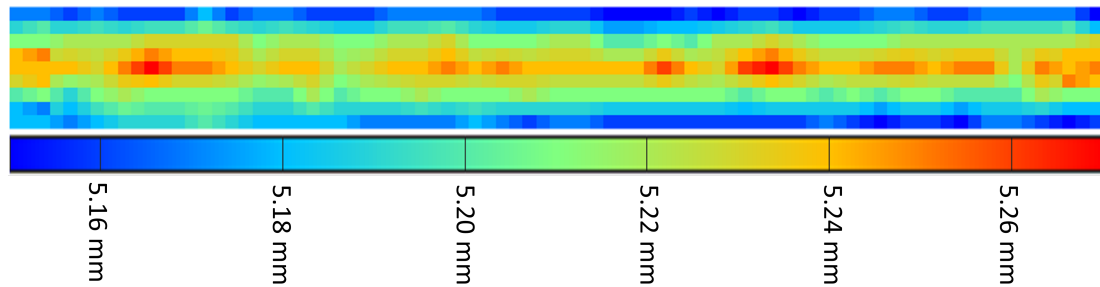
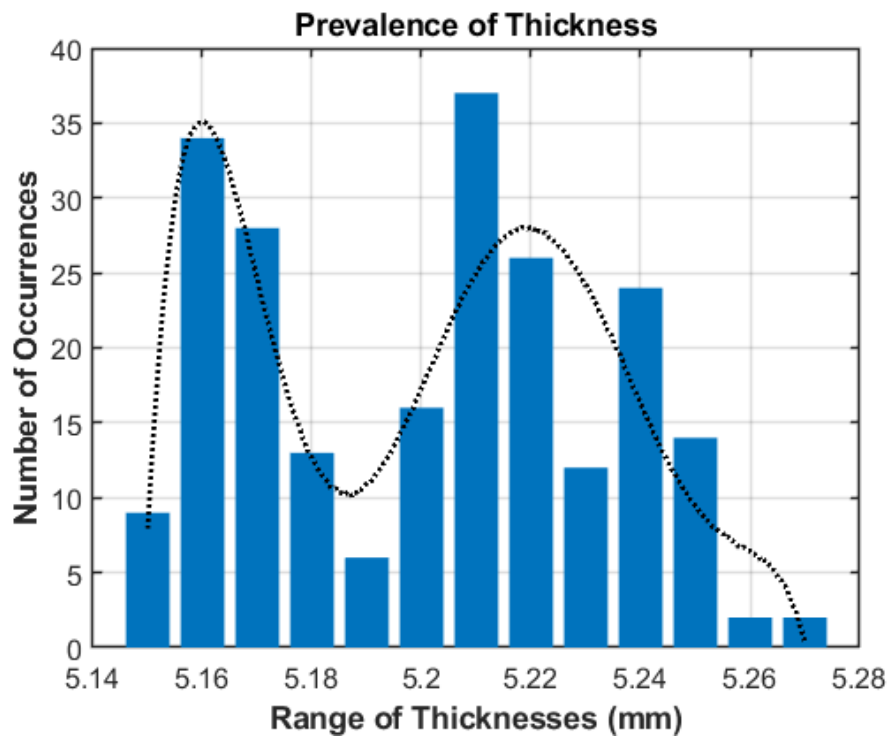


Figure 4.19: Heat map showing the consistency of the sample geometry for the 2 m x 20 cm x 5 mm UD pultruded carbon fibre composite.

A statistical analysis of the thickness distribution was performed, as shown in Figure 4.20a, providing further evidence of the sample's geometric consistency. The target thickness was 5.00 mm, with an average of 5.20 mm and a standard deviation of 0.03 mm. The range of thicknesses is presented in the graph, showing that the majority of the sample thicknesses fall within a narrow range, supporting the uniformity of the material.



(a) Distribution of sample thicknesses.

Statistic	Value
Target Thickness (mm)	5.00
Measured Average (mm)	5.20
Standard Deviation (mm)	0.03
Maximum Thickness (mm)	5.27
Minimum Thickness (mm)	5.15

(b) Thickness statistics of the composite sample.

Figure 4.20: Statistical evaluation of the sample's geometry, showing the thickness distribution (a) and summary of geometric data (b).

The results indicate that the composite sample exhibits a high degree of thickness uniformity. With a measured average thickness of 5.20 mm, a standard deviation of 0.03 mm, and a range spanning from 5.15 mm to 5.27 mm, the overall thickness variation is minimal (approximately  $\pm 0.06$  mm from the average). This level of consistency was essential for minimising geometric

## Chapter 4. Experimental Modal Analysis for Damping Estimation

variability in modal analysis and ensuring that the derived damping measurements were reliable.

### **4.4.1.2 Modal Testing, Stabilisation Diagram, and Frequency Validation**

The stabilisation diagram was generated using the deterministic Polymax (pLSCF) method, as shown in Figure 4.17. To ensure the accuracy of the selected mode, additional filtering criteria were applied to the stabilisation diagram data:

- Damping values were required to be positive.
- Modal Assurance Criteria (MAC) values needed to be greater than 0.92.
- Modal Phase Collinearity (MPC) values needed to be greater than 0.92.
- Modal Phase Deviation (MPD) values had to be less than 10.

A multifunctional script, displayed in Appendix K, was used to optimise MAC and MPC values while minimising MPD, allowing only the most stable modes to be selected for final analysis. The stabilisation diagram for this experiment was shown previously in Figure 4.17, and the associated mode shape is shown in Figure 4.21

## Chapter 4. Experimental Modal Analysis for Damping Estimation

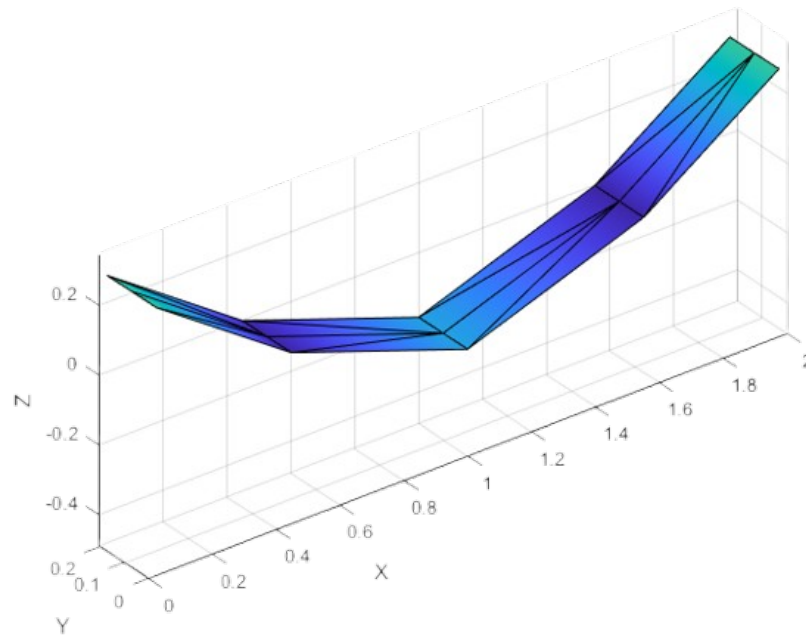


Figure 4.21: Mode shape of the stable first flexural mode identified using the Polymax (pLSCF) method.

The FEA and experimentally determined stable mode frequencies can be evaluated in Table 4.4.

Table 4.4: Comparison of FEA-predicted frequency and EMA-obtained modal frequency.

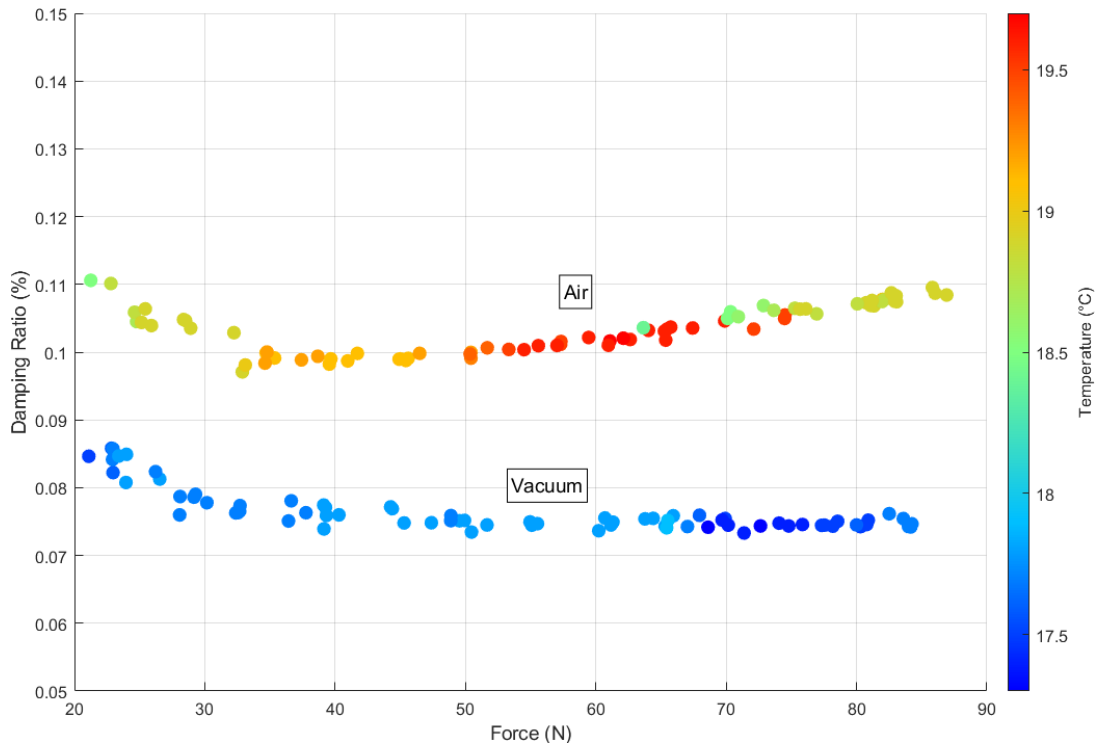
<b>Method</b>	<b>First Flexural Mode Frequency (Hz)</b>
FEA Prediction	11.89
EMA Result	11.73

The refined modes' results were then used to extract the composite's mode shapes, modal frequencies, and damping ratios. The close correlation between the FEA-predicted and experimentally obtained frequencies confirms the accuracy of the EMA testing, resulting in a reliable assessment of the damping properties at the first flexural mode.

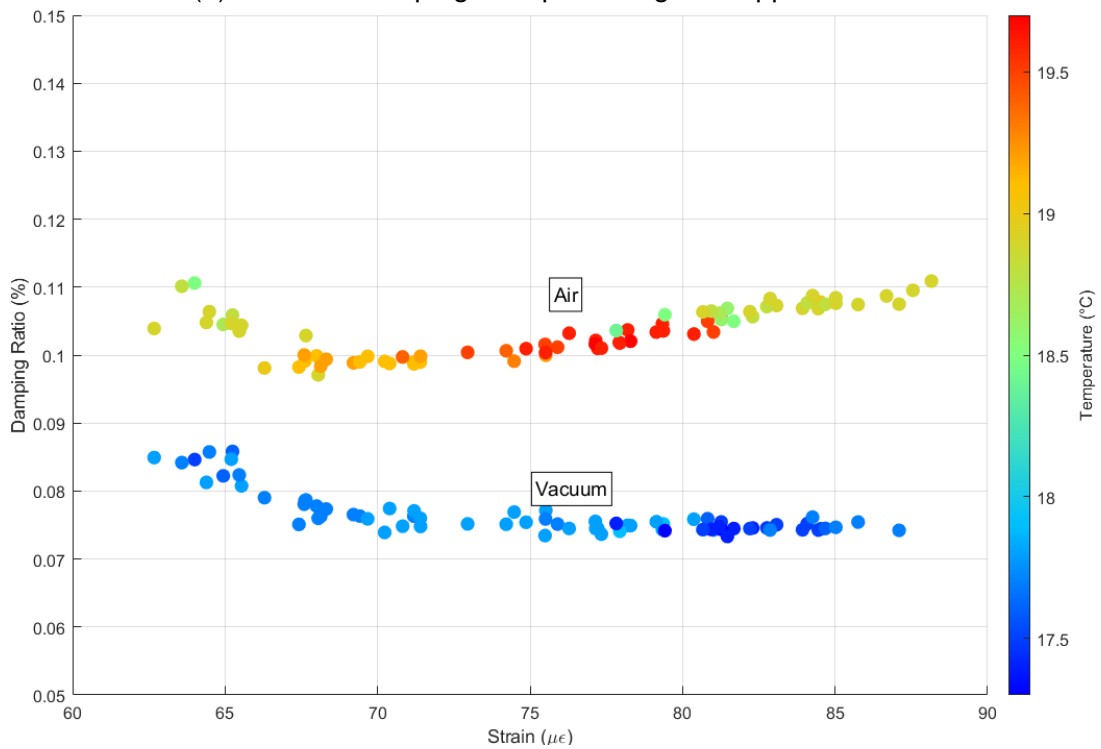
#### **4.4.1.3 Damping Analysis**

To evaluate the influence of different testing environments on the damping ratio, force and strain sweeps were conducted in both air and vacuum conditions. The damping ratios were plotted against both applied force and strain for each condition, with temperature variations recorded during the tests. These variations are shown in Figure 4.22, which presents the damping results concerning force and strain.

## Chapter 4. Experimental Modal Analysis for Damping Estimation



(a) Effect on damping ratio plotted against applied force.



(b) Effect on damping ratio plotted against strain.

Figure 4.22: Effect of applied force, strain, and temperature on damping ratios for the 5 mm carbon fibre composite sample in air and vacuum environments  
205

## Chapter 4. Experimental Modal Analysis for Damping Estimation

As seen in Figure 4.22, the damping ratio is consistently higher in air compared to vacuum across all force and strain levels. This behaviour can be attributed to the presence of aerodynamic damping, which is eliminated in vacuum conditions. The temperature variations recorded during testing are also displayed in the figure, with temperatures ranging between 17.5°C and 19.5°C. While efforts were made to maintain a constant temperature, slight variations occurred during the testing process and are shown as part of the analysis.

Under vacuum conditions, the damping ratio remained lower and more stable, as expected, due to the absence of aerodynamic contributions. This finding highlighted the importance of controlling environmental conditions during EMA to isolate the material's structural damping.

The comparison of the damping properties between air and vacuum environments provides further insights into the damping mechanisms at play in the composite sample. By eliminating aerodynamic damping, the vacuum environment allows for a more accurate assessment of the material's intrinsic structural damping properties. Additionally, by plotting against strain in Figure 4.22b, the relationship between strain and damping further clarifies the strain dependency of damping under different environmental conditions.

From previous work, seen in Chapter 3 within this thesis, the frequency impacts the damping results obtained. Methods for varying the frequency results were investigated. These possibilities included thinning down the sample to reduce the sample's natural frequency or shortening the length of the sample to increase the natural frequency. An additional method that was considered was using point masses attached to the sample to reduce the sample's natural frequency. The method was first attempted in the sample thickness investigation.

#### 4.4.2 Results from EMA Testing of Milled UD Pultruded Carbon Fibre Composite (2 m x 20 cm x 2.5 mm)

This report presents the results obtained from the EMA of the UD pultruded carbon fibre composite sample, initially sized at 2 m x 20 cm x 5 mm. The sample was milled down to a thickness of 2.5 mm using a CNC machine at the National Manufacturing Institute Scotland (NMIS). The machine can be seen in Figure 4.23

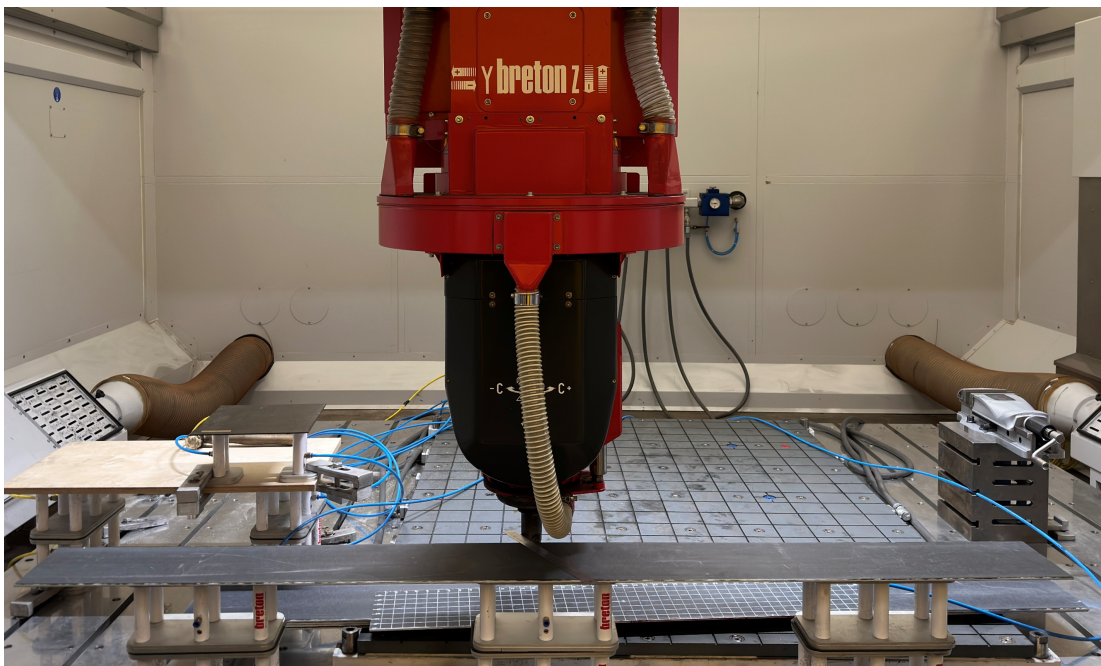


Figure 4.23: NMIS CNC Machine, with carbon fibre milling tool and CFRP 2 m CFRP sample

##### 4.4.2.1 Sample Geometry Consistency

As with the original sample, the geometry consistency of the milled composite was assessed. A heat map, shown in Figure 4.24, illustrates the thickness uniformity across the length and width of the milled sample, confirming its geometric consistency, which is important for accurate modal analysis and

## Chapter 4. Experimental Modal Analysis for Damping Estimation

reliable damping results.

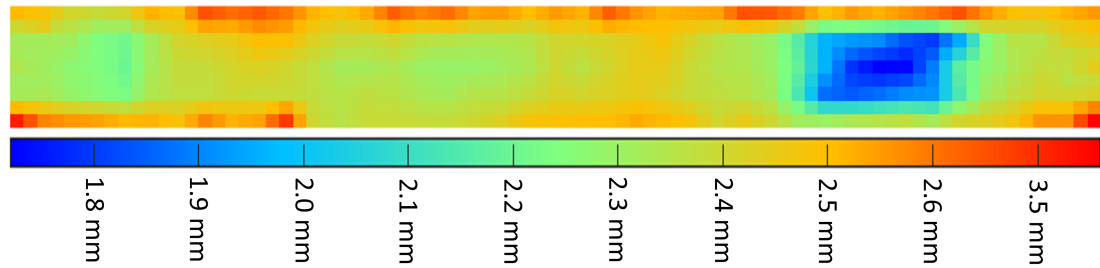
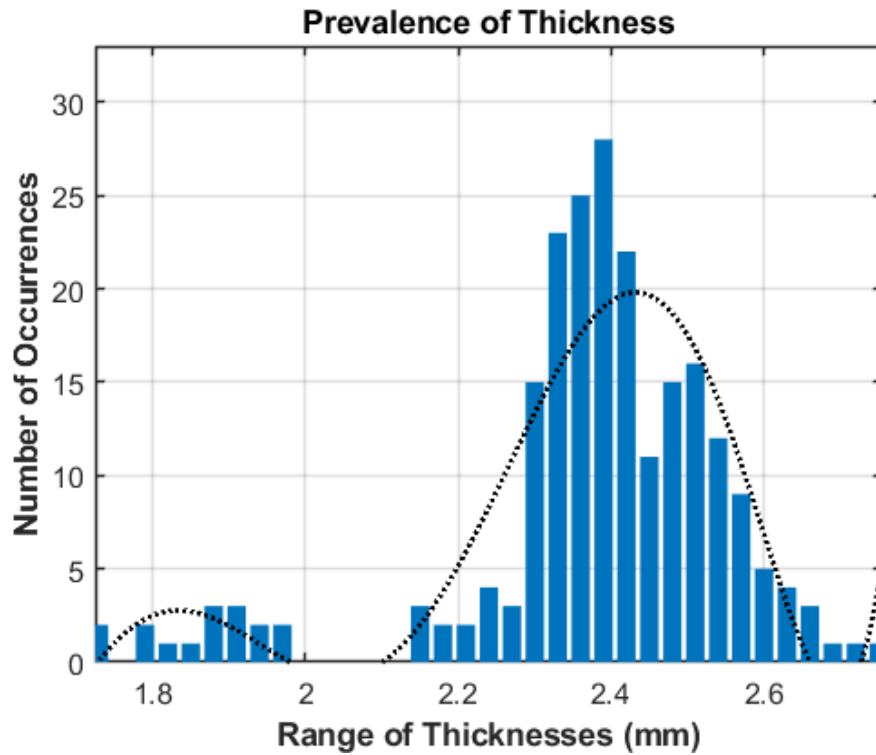


Figure 4.24: Heat map showing the consistency of the sample geometry for the 2 m x 20 cm x 2.5 mm milled UD pultruded carbon fibre composite.

Additionally, a statistical analysis of the thickness distribution was conducted, summarised in Figure 4.25. The target thickness for this sample was 2.5 mm, with an average measured thickness of 2.37 mm and a standard deviation of 0.18 mm. The results indicate that while the sample's thickness distribution is slightly broader than the target, the deviations remain minimal, confirming the material's relative uniformity.



(a) Distribution of sample thicknesses.

Statistic	Value
Target Thickness (mm)	2.50
Measured Average (mm)	2.37
Standard Deviation (mm)	0.18
Maximum Thickness (mm)	2.76
Minimum Thickness (mm)	1.72

(b) Thickness statistics of the milled composite sample.

Figure 4.25: Statistical evaluation of the milled sample's geometry, showing the thickness distribution (a) and summary of geometric data (b).

The statistical evaluation indicated that the milled composite sample had a measured average thickness of 2.37 mm  $\pm$  0.18 mm, with individual measurements ranging from 1.72 mm to 2.76 mm. Although this represents a greater variation compared to the target thickness of 2.50 mm, the overall

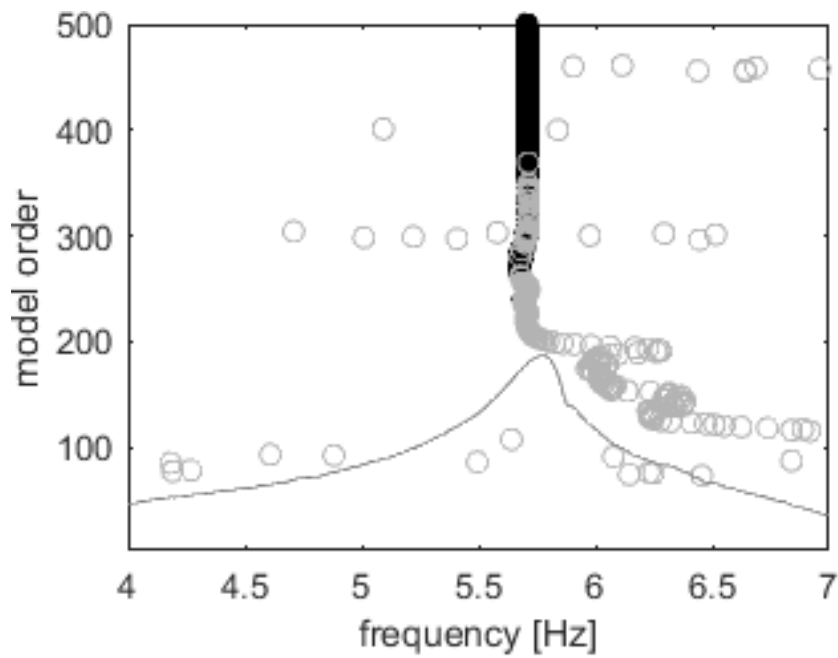
## Chapter 4. Experimental Modal Analysis for Damping Estimation

uniformity remained relatively consistent for reliable modal analysis, even though the increased variability may introduce slight discrepancies in the damping results.

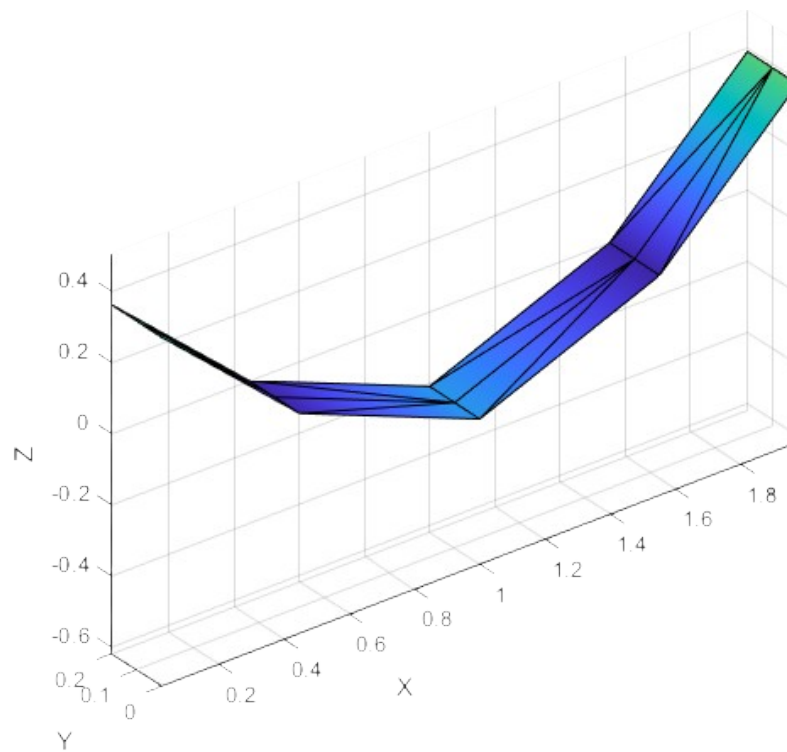
### **4.4.2.2 Modal Testing, Stabilisation Diagram, and Frequency Validation**

The stabilisation diagram for the 2.5 mm milled sample was generated using the deterministic Polymax (pLSCF) method, as shown in Figure 4.26. The same frequency and stability filtering criteria, as applied in the 5 mm sample analysis, were used here to ensure the accuracy of the selected mode. After applying these criteria, the stabilisation diagram and validated mode shape for the first flexural mode of the 2.5 mm sample are presented side by side in Figure 4.26.

Chapter 4. Experimental Modal Analysis for Damping Estimation



(a) Stabilisation diagram using Polymax (pLSCF).



(b) Mode shape of the stable first flexural mode.

Figure 4.26: (a) Stabilisation diagram generated using the deterministic Polymax (pLSCF) method; (b) Mode shape of the stable mode identified after applying filtering criteria for the 2.5 mm sample. (Both were produced with MACEC)

## Chapter 4. Experimental Modal Analysis for Damping Estimation

The comparison of frequencies for the FEA-predicted and experimentally determined stable mode is shown in Table 4.5.

Table 4.5: Comparison of FEA-predicted frequency and EMA-obtained modal frequency for the 2.5mm sample.

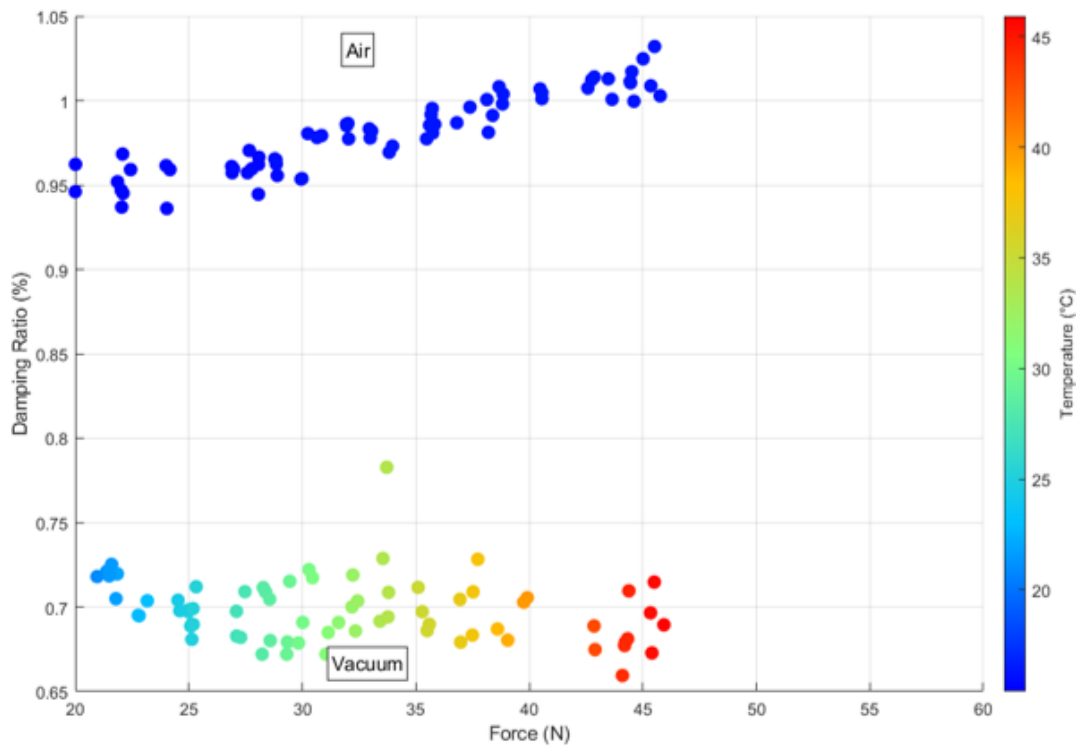
<b>Method</b>	<b>First Flexural Mode Frequency (Hz)</b>
FEA Prediction	5.95
EMA Result	5.83

The processed data was then used to extract the composite's mode shapes, modal frequencies, and damping ratios. The close correlation between the FEA-predicted and experimentally obtained frequencies for the 2.5 mm sample confirms the reliability of the EMA testing, allowing for an accurate assessment of the damping properties at the first flexural mode.

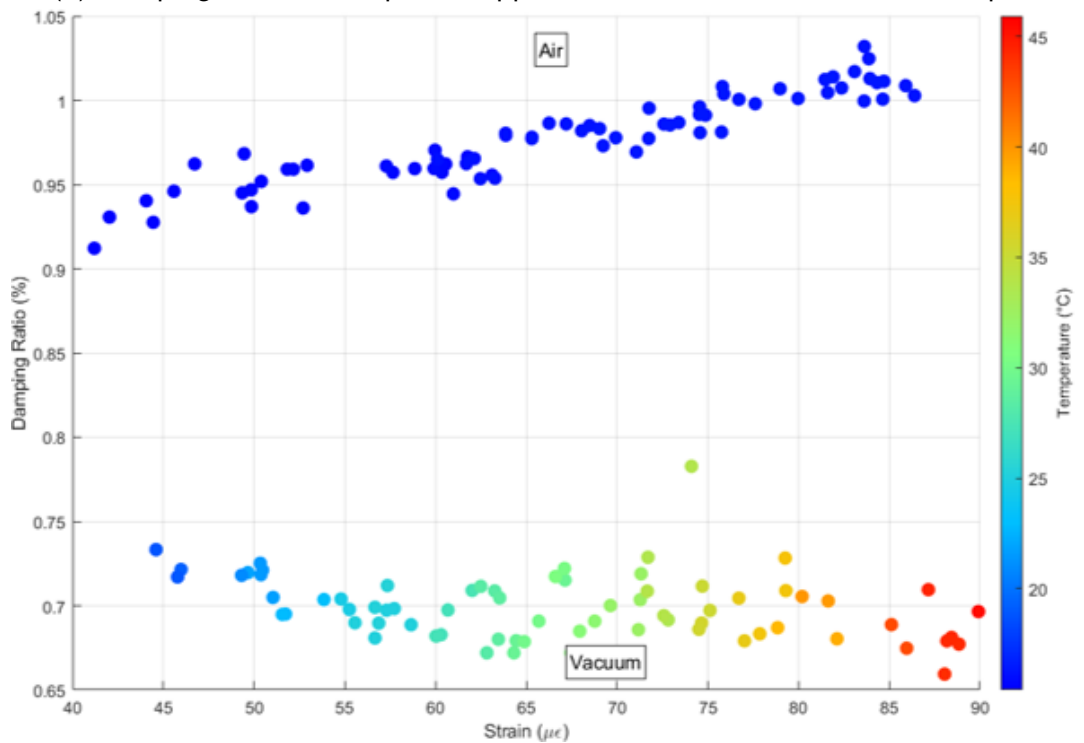
### **4.4.2.3 Damping Analysis**

For the milled 2.5 mm sample, force and strain sweeps were again conducted under both air and vacuum conditions to evaluate the damping ratio, with temperature variations recorded throughout the tests. The results are presented in Figure 4.27, showing the damping ratios plotted against applied force and strain, respectively.

## Chapter 4. Experimental Modal Analysis for Damping Estimation



(a) Damping ratio with respect to applied force for the milled 2.5 mm sample.



(b) Damping ratio with respect to strain for the milled 2.5 mm sample.

Figure 4.27: Effect of applied force, strain, and temperature on damping ratios for the 2.5 mm milled carbon fibre composite in air and vacuum environments.

## Chapter 4. Experimental Modal Analysis for Damping Estimation

As shown in Figure 4.27, the damping ratios measured under air and vacuum conditions are notably higher for the milled 2.5 mm sample compared to the original 5 mm sample. While microcracks or surface damage induced during the CNC milling process are likely contributors to the increased damping, the reduction in thickness itself may also play a significant role. Reducing a structure's thickness alters its flexural stiffness, affecting modal frequencies and the associated damping mechanisms, such as internal friction and interlaminar shear stresses. Thinner composite sections typically exhibit increased flexibility, potentially resulting in higher internal damping due to enhanced interlaminar friction or altered energy dissipation pathways.

Moreover, the CNC milling process inherently introduces additional microstructural imperfections, such as surface roughness, fibre breakage, and microcracking, which increase internal friction and, consequently, structural damping. Distinguishing between damping increases caused by structural scale effects (i.e., thickness reduction) and microstructural damage from milling is challenging with the current experimental setup. Therefore, attributing the observed damping increase exclusively to milling-induced defects may oversimplify the complex interplay of factors involved.

As in the 5 mm sample, damping ratios remain consistently higher under air conditions compared to vacuum conditions, highlighting aerodynamic damping contributions. This disparity further validates the vacuum environment's effectiveness in isolating structural damping from aerodynamic effects.

Additionally, the relatively flat gradient of damping ratios with respect to strain and force (Figure 4.27) indicates that internal damping mechanisms dominate in vacuum conditions, with minimal strain dependence observed (even though the variability seems to increase within this test scenario).

## Chapter 4. Experimental Modal Analysis for Damping Estimation

In summary, the findings for the milled 2.5 mm sample highlight the complexities involved in damping characterisation following thickness modification. Both structural scale effects and milling-induced microstructural defects significantly impact damping behaviour, making it difficult to isolate the precise cause of increased damping. Consequently, CNC milling as a method of thickness modification poses clear limitations for reliable damping characterisation. Alternative manufacturing or machining techniques that minimise microstructural damage should be explored in future work to better understand the individual contributions of structural scale effects and microstructural integrity to damping characteristics.

### 4.4.3 Results from EMA Testing of UD Pultruded Carbon Fibre Composite - Shortened (1.2 m x 20 cm x 5 mm)

#### 4.4.3.1 Sample Geometry Consistency

As with the previous samples, the geometry consistency of the 5 mm thickness 1.2 m sample was assessed. A heat map, shown in Figure 4.28, illustrates the thickness uniformity across the length and width of the sample, confirming its geometric consistency, which is important for accurate modal analysis and reliable damping results.

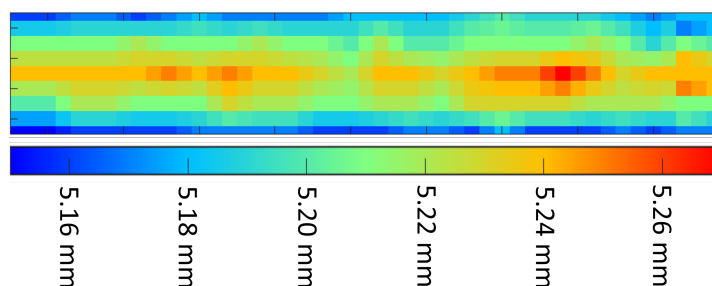
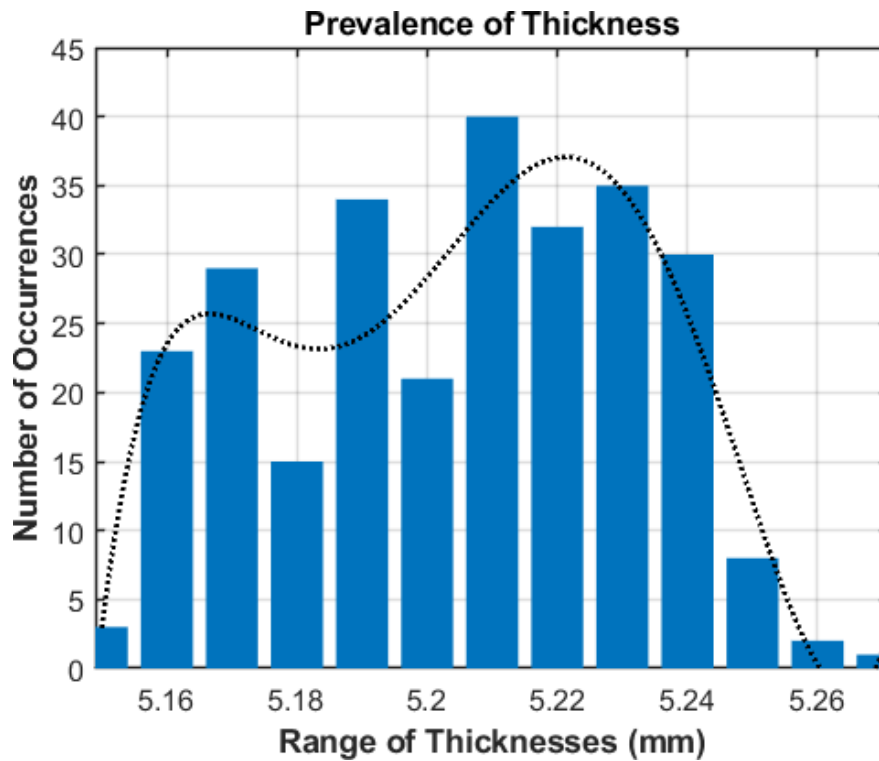


Figure 4.28: Heat map showing the consistency of the sample geometry for the 1.2 m x 20 cm x 5 mm UD pultruded carbon fibre composite.

#### Chapter 4. Experimental Modal Analysis for Damping Estimation

Additionally, a statistical analysis of the thickness distribution was conducted and summarised in Figure 4.29. The target thickness for this sample was 5.00 mm, with an average measured thickness of 5.19 mm and a standard deviation of 0.04 mm. The range of thicknesses is presented in the graph, showing that the majority of the sample's thicknesses fall within a narrow range, supporting the uniformity of the material.



(a) Distribution of sample thicknesses.

Statistic	Value
Target Thickness (mm)	5.00
Measured Average (mm)	5.19
Standard Deviation (mm)	0.04
Maximum Thickness (mm)	5.26
Minimum Thickness (mm)	5.12

(b) Thickness statistics of the 1.2 m composite sample.

Figure 4.29: Statistical evaluation of the 1.2 m sample’s geometry, showing the thickness distribution (a) and summary of geometric data (b).

The statistical evaluation shows that the 1.2 m composite sample has a measured average thickness of 5.19 mm ± 0.04 mm, with individual measurements ranging from 5.12 mm to 5.26 mm. This level of uniformity is closely aligned with the target thickness of 5.00 mm and supports the

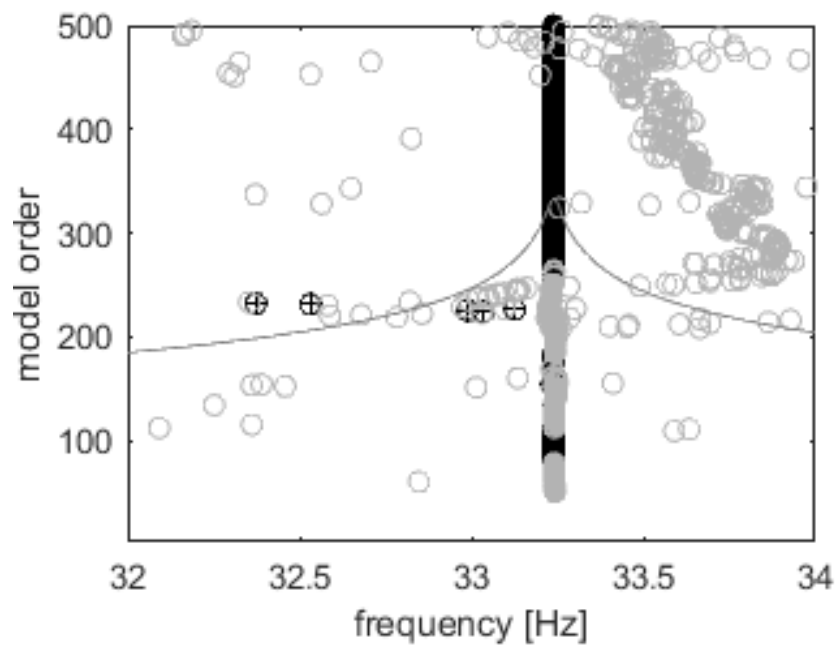
reliability of the modal analysis and damping measurements.

#### **4.4.3.2 Modal Testing, Stabilisation Diagram, and Frequency Validation**

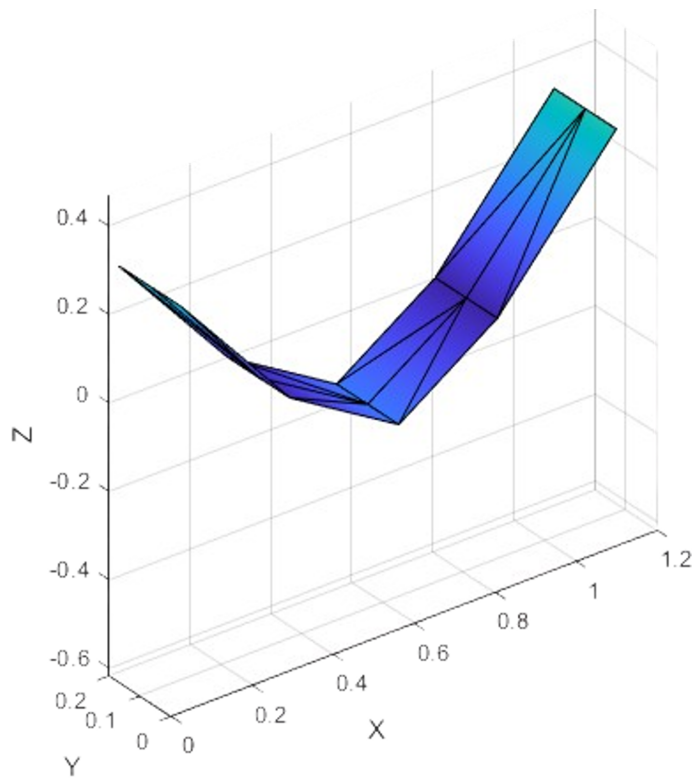
The stabilisation diagram for the 1.2 m x 20 cm x 5 mm pultruded carbon fibre composite sample was generated using the deterministic Polymax (pLSCF) method. The results are shown in Figure 4.30. As in previous samples, an initial frequency filter was applied to isolate the first flexural mode, focusing on modal orders within a  $\pm 0.5$  Hz range of the predicted FEA frequency.

The stabilisation diagram and corresponding mode shape of the first flexural mode, validated through the filtering criteria, are presented in Figure 4.30.

Chapter 4. Experimental Modal Analysis for Damping Estimation



(a) Stabilisation diagram using Polymax (pLSCF)



(b) Mode shape of the stable first flexural mode.

Figure 4.30: (a) Stabilisation diagram generated using the deterministic Polymax (pLSCF) method; (b) Mode shape of the stable mode identified for the 1.2 m sample (Both Generated from MACEC)

## Chapter 4. Experimental Modal Analysis for Damping Estimation

The comparison of frequencies for the FEA-predicted and experimentally determined stable mode is shown in Table 4.6.

Table 4.6: Comparison of FEA-predicted frequency and EMA-obtained modal frequency for the 1.2m sample.

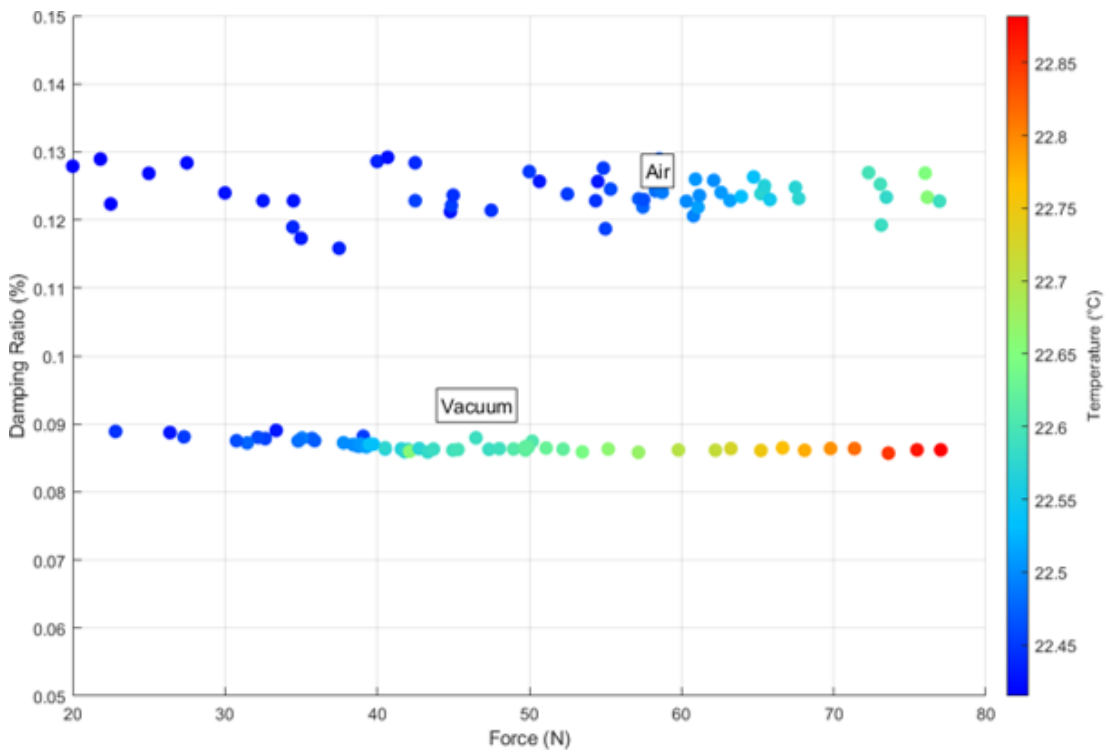
<b>Method</b>	<b>First Flexural Mode Frequency (Hz)</b>
FEA Prediction	33.02
EMA Result	33.23

The close correlation between the FEA-predicted and experimentally obtained frequencies confirms the consistency of the EMA testing for this sample. This correlation, along with the stability of the filtered mode shape, supports the reliability of the damping measurements at the first flexural mode.

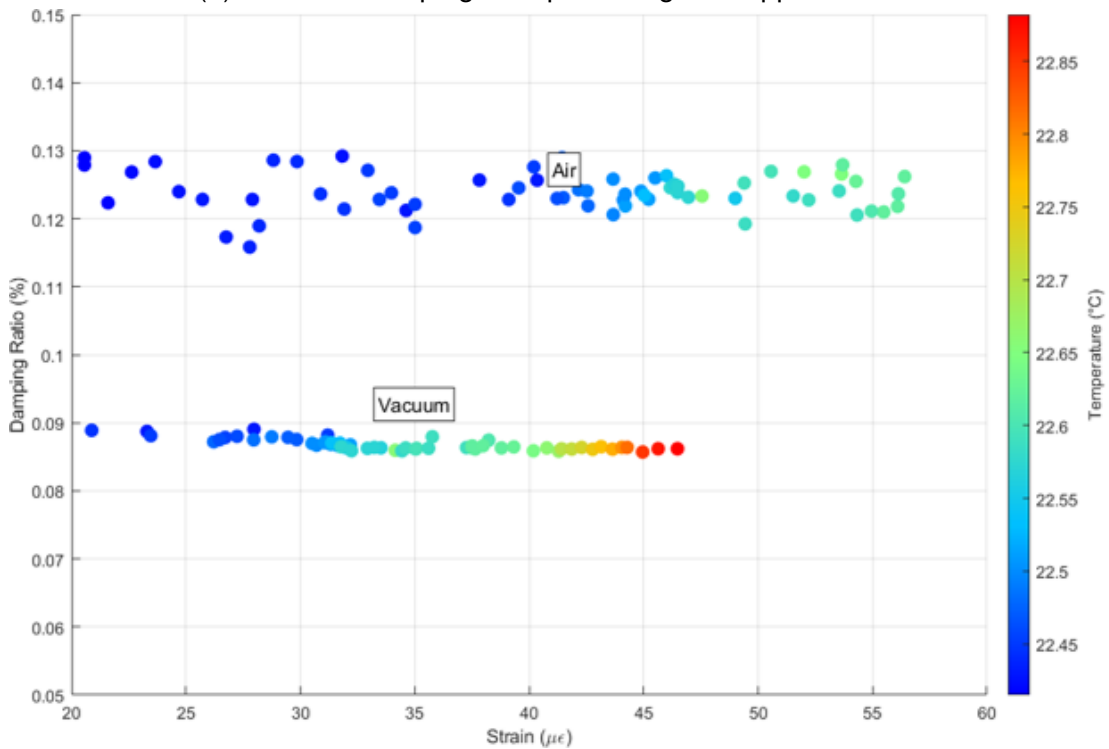
### 4.4.3.3 Damping Analysis

To assess the damping characteristics of the 5 mm, 1.2 m UD pultruded carbon fibre composite sample, force and strain sweeps were performed under both air and vacuum conditions. This approach allowed for a comparison between the damping contributions of the structural material alone (in vacuum) and with additional aerodynamic damping (in air). The damping ratios, plotted against applied force and strain, with temperature variations recorded during the tests, are shown in Figure 4.31.

## Chapter 4. Experimental Modal Analysis for Damping Estimation



(a) Effect on damping ratio plotted against applied force.



(b) Effect on damping ratio plotted against strain.

Figure 4.31: Effect of applied force, strain, and temperature on damping ratios for the shortened 1.2 m carbon fibre composite in air and vacuum.

## Chapter 4. Experimental Modal Analysis for Damping Estimation

As observed in Figure 4.31, the damping ratio in air conditions is consistently higher than in vacuum, similar to the previous samples. This is due to the aerodynamic damping present in air, which is eliminated in vacuum conditions. The results for the 1.2 m sample demonstrate a noticeable increase in damping magnitude compared to the previous 2 m sample, which may be attributed to the increase in natural frequency.

Temperature variations recorded during testing ranged from 17.5°C to 19.5°C and were consistent with those in previous samples. While minor, these were monitored to ensure damping values were not skewed by thermal influences.

In vacuum conditions, the damping response was not only lower but also more stable, confirming the benefit of controlled environments for isolating material behaviour. Interestingly, although the 1.2 m sample's shorter length may reduce aerodynamic effects, the observed damping increase appears more closely tied to the shift in modal frequency. This highlights that frequency, rather than length alone, may be the dominant factor influencing damping magnitude.

These results reflect the complex interplay between geometry, mode shape, and environmental influences. While shorter specimens like the 1.2 m sample are structurally stiffer and operate at higher frequencies, these characteristics can inherently alter the damping response. Therefore, any observed increase in damping should not be solely attributed to geometric changes, but rather considered in the context of modal dynamics and strain distribution. This reinforces the need to treat damping trends with caution when comparing across different sample sizes and boundary conditions.

In summary, the shortened 1.2 m sample exhibits a consistent damping pattern relative to prior tests, with an increased damping magnitude that is likely driven by elevated modal frequencies. The combination of air and

vacuum tests confirms the necessity of controlling both geometry and environment when evaluating the damping properties of pultruded composite structures.

#### **4.4.4 Comparison of Vacuum Damping Results for 1.2 m and 2 m Samples - Vacuum Conditions**

To evaluate the effect of natural frequency on the damping characteristics under vacuum conditions, a comparison was made between the 1.2 m and 2 m samples, both with a thickness of 5 mm. This comparison focuses on the damping ratios obtained from strain and force sweeps, which provide insight into how sample length influences the damping behaviour of the composite material.

The damping ratio as a function of applied force is presented in Figure 4.32. Consistent with the strain results, the 1.2 m sample demonstrates a higher damping ratio across all force levels compared to the 2 m sample. The force sweep results further reinforce the observation that a shorter sample length, resulting in higher frequency excitation, leads to increased damping. This phenomenon could be attributed to the effect that frequency/environment has upon damping characterisation.

## Chapter 4. Experimental Modal Analysis for Damping Estimation

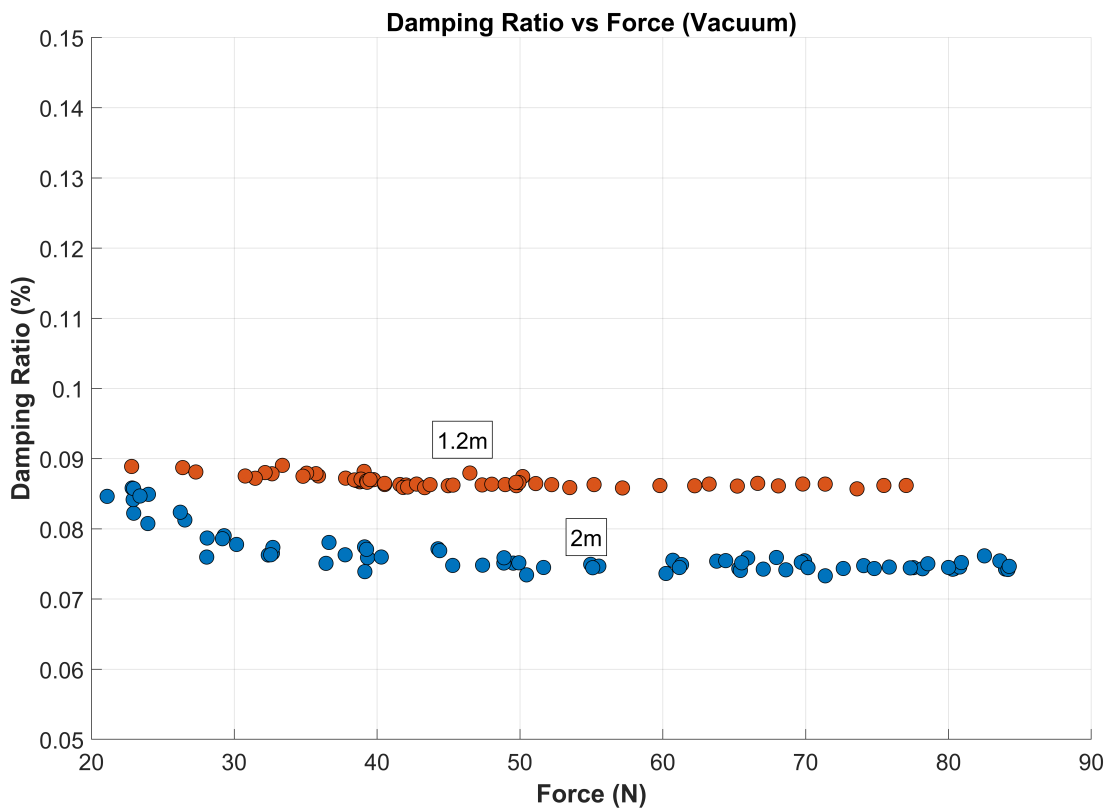


Figure 4.32: Damping ratio comparison between 1.2 m and 2 m samples in vacuum, plotted against the applied force. The 1.2 m sample consistently exhibits higher damping ratios.

Similarly, Figure 4.33 shows the damping ratio plotted against strain for both the 1.2 m and 2 m samples under vacuum. As seen in the figure, the 1.2 m sample exhibits a consistently higher damping ratio across the range of applied strains compared to the 2 m sample. This trend again shows that the increased frequency of the shorter sample results in higher damping. Additionally, it is noted that temperature changes occurred during testing due to unavoidable laboratory relocations, affecting temperature control. Although temperature could not be perfectly managed due to it not being possible to be conducted within an environmental chamber, its potential impact on damping results is acknowledged.

## Chapter 4. Experimental Modal Analysis for Damping Estimation

It can be noted that there is a temperature variation within this comparison due to the inability to control lab testing temperatures. Putting this variation into context, a 10°C increase in temperature for the DMA experiment (from 30-40°C) resulted in an approximate increase in damping of 4.5%. Assuming a linear relationship, the 4°C increase in this test would be less than a 2% effect.

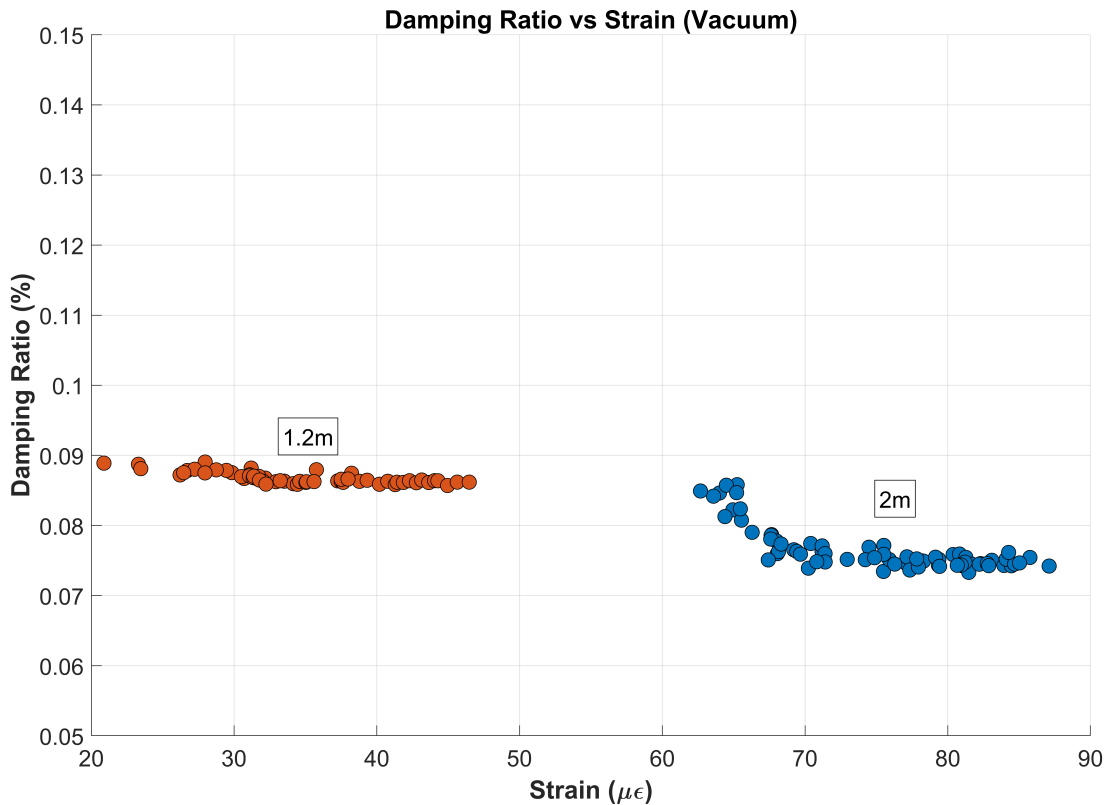


Figure 4.33: Damping ratio comparison between 1.2 m and 2 m samples in vacuum, plotted against strain. The 1.2 m sample shows a higher damping ratio than the 2 m sample across the strain range.

The comparison between the 1.2 m and 2 m samples under vacuum conditions suggests that the higher natural frequency leads to higher damping ratios. This finding aligns with the hypothesis that an increase in the natural frequency due to altered modal properties may enhance the material's damping behaviour. These results provide valuable insights into the influence of natural frequency

## Chapter 4. Experimental Modal Analysis for Damping Estimation

on the damping characteristics of composite materials, particularly in a vacuum environment where aerodynamic damping is eliminated.

### 4.4.5 Comparison of Damping Results Across Frequencies

To support a comparative understanding of the damping characteristics across different modal frequencies, the average damping ratios for the 1.2 m and 2 m samples were extracted from the stable (linear) regions of their vacuum test results. These values are plotted in Figure 4.34, which illustrates the experimentally observed damping ratios without any extrapolation.

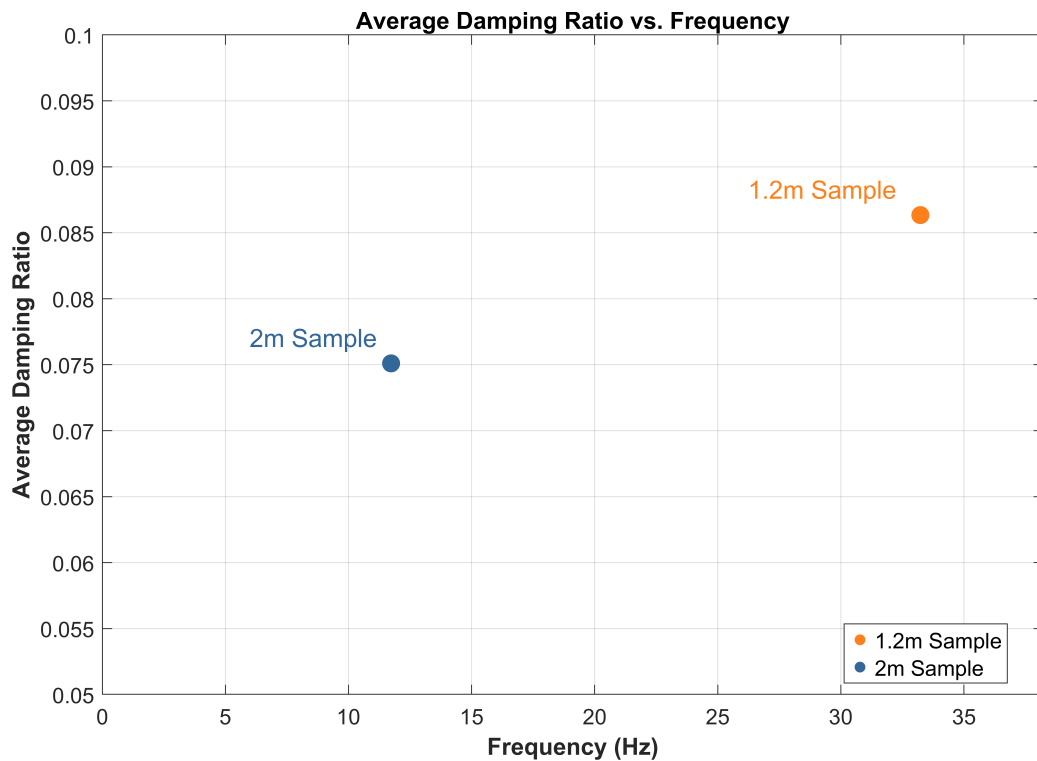


Figure 4.34: Average damping ratios of the 1.2 m and 2 m UD pultruded carbon fibre composite samples tested under vacuum conditions.

As shown in Figure 4.34, the shorter 1.2 m sample exhibited a higher damping ratio than the longer 2 m sample. While no extrapolation is made,

## Chapter 4. Experimental Modal Analysis for Damping Estimation

this difference suggests a possible trend whereby damping may reduce with decreasing frequency. This aligns with behaviour previously observed in DMA testing, where higher frequencies were generally associated with greater internal damping.

However, with only two data points, no definitive conclusions can be drawn regarding the functional relationship between frequency and damping ratio. Rather than fitting a mathematical trend, this comparison serves to illustrate the directionality of change that might be expected in composite structures with varying modal frequencies.

Further experimental work would be necessary to verify the presence and nature of such a trend, ideally through testing additional samples across a broader range of lengths and corresponding natural frequencies.

### **4.4.6 Impact of Frequency Variation on Damping Behaviour through Added Mass**

To examine the effect of altering the natural frequency of the test sample, additional masses were introduced to the 1.2 m composite beam. This approach was selected as it offered a practical alternative to changing the sample length or suspension configuration. The added masses were positioned symmetrically around the centre of the beam, aligned with the expected antinode of the first flexural mode, with 0.3 kg copper blocks clamped 1.5 cm from both the top and bottom faces. Initial tests using adhesive tape to fix the masses led to artificially high damping due to relative motion. This was resolved by drilling and mechanically clamping the masses through the specimen, as illustrated in Figure 4.35.

## Chapter 4. Experimental Modal Analysis for Damping Estimation

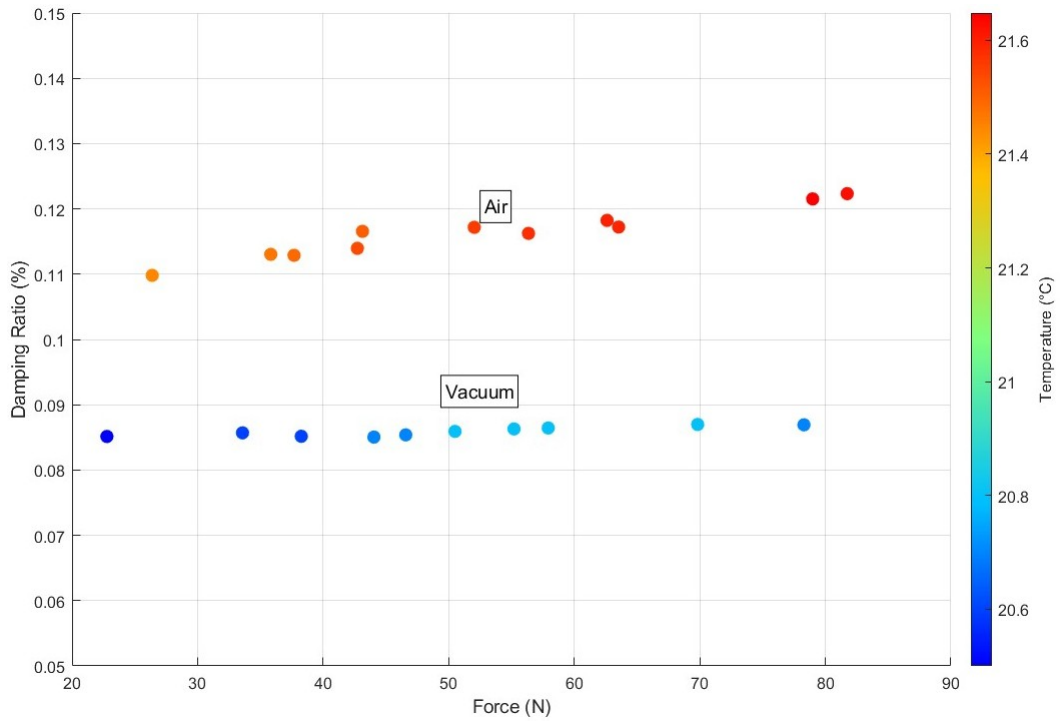


(a) Front view of clamped masses (b) Closer angle of the mass attachments (c) Side detail of the copper mass clamps

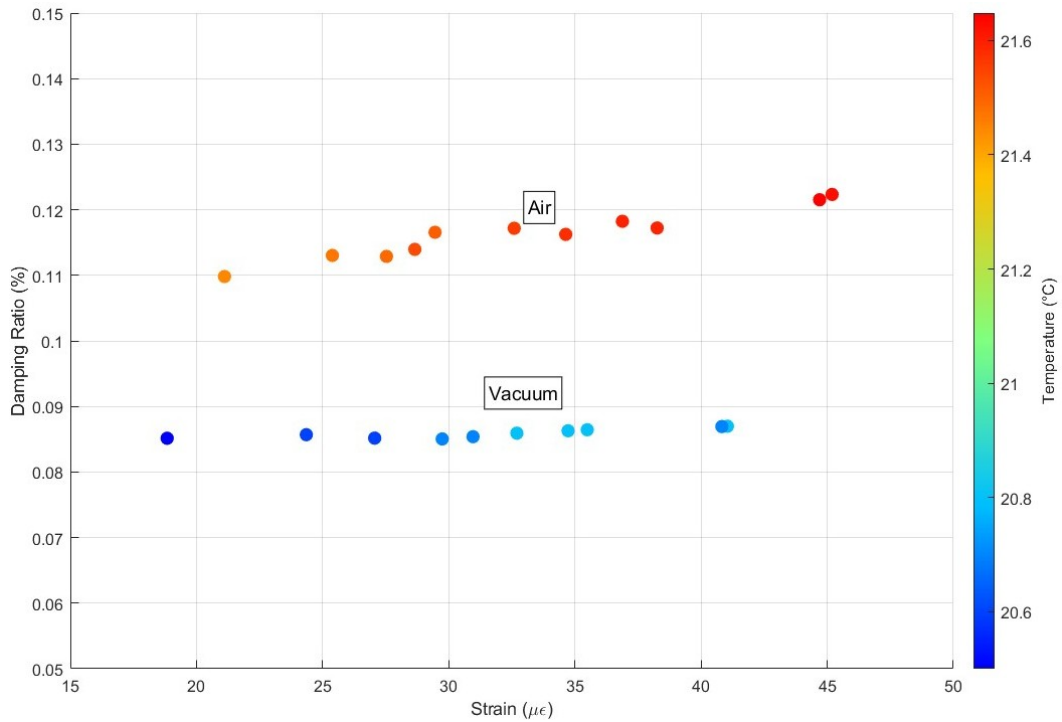
Figure 4.35: Final approach for added masses: Copper masses drilled and clamped through the composite sample to ensure secure attachment and stable frequency modification.

Figure 4.36 shows the damping results for the added-mass configuration. As before, force and strain sweeps were conducted in both air and vacuum conditions to assess damping behaviour.

## Chapter 4. Experimental Modal Analysis for Damping Estimation



(a) Effect on damping ratio plotted against applied force.



(b) Effect on damping ratio plotted against strain.

Figure 4.36: Damping ratio for the 1.2 m x 20 cm x 5 mm composite sample in air and vacuum with added masses, showing applied force, strain, and temperature variations.

## Chapter 4. Experimental Modal Analysis for Damping Estimation

The addition of mass reduced the first natural frequency from 33.2 Hz to approximately 30.9 Hz, as confirmed by both FEA and experimental modal analysis. This shift is consistent with expectations given the increased inertia. A reduction in the damping ratio of approximately 0.5% was also observed in vacuum conditions when compared to the original 1.2 m sample without added mass.

While only a limited number of data points are available, plotting the vacuum damping values across frequencies (Figure 4.37) shows that the added mass configuration falls in line with the general trend observed across the three configurations. This supports the hypothesis that damping decreases slightly as frequency reduces. However, no quantitative extrapolation has been applied, as the limited dataset is insufficient to support a rigorous model.

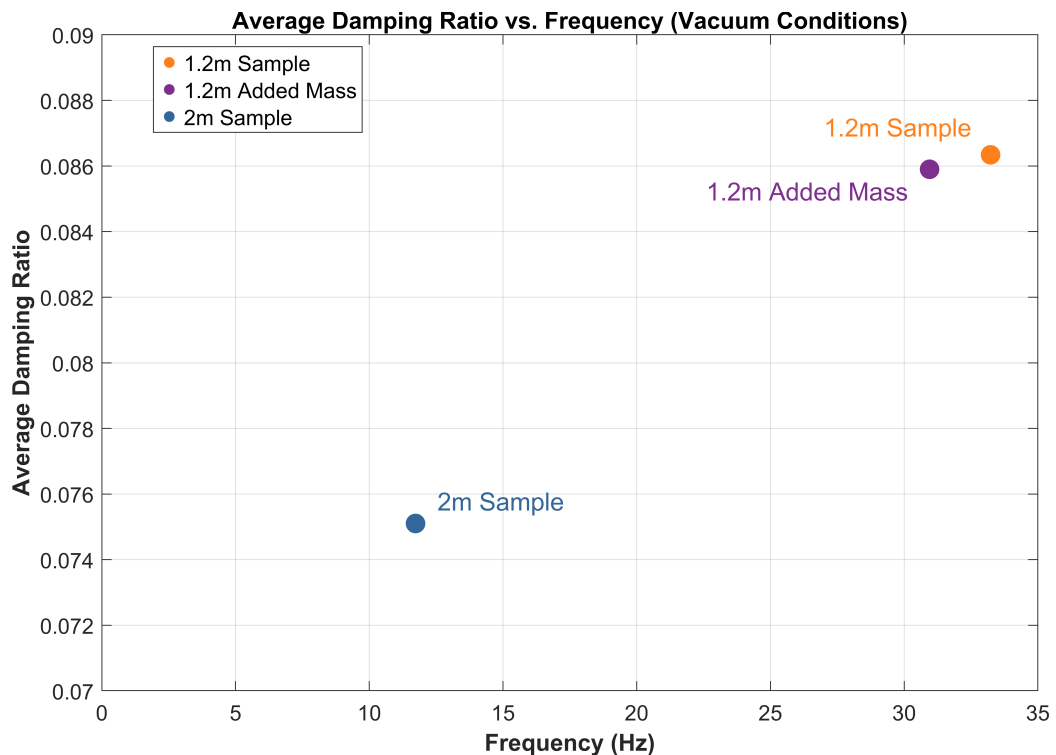


Figure 4.37: Extrapolated damping trend across frequencies based on average damping ratios from 1.2 m and 2 m samples under vacuum with Added Mass Configuration

## Chapter 4. Experimental Modal Analysis for Damping Estimation

These results demonstrate the feasibility of using clamped masses to modify natural frequency without introducing significant additional damping. Although this study was not designed to exhaustively characterise the effects of added mass, the consistency of modal behaviour and damping response supports its suitability as a method for targeted frequency adjustment in future experimental campaigns.

### 4.5 Comparison Between DMA and EMA Results

Within this Chapter, EMA was employed to characterise the dynamic behaviour of larger carbon fibre composite samples, specifically focusing on accurately estimating their natural frequencies, mode shapes, and damping ratios. Initial studies using conventional EMA techniques identified significant shortcomings, especially when characterising materials with inherently low damping, such as carbon fibre composites, identified through the review in Section 4.2.6. External energy losses, including boundary conditions and aerodynamic damping, could erroneously be interpreted as intrinsic material damping.

To overcome these issues, a bespoke EMA test rig was developed with features specifically designed to address the identified limitations:

- **Medium-Scale Sample Testing:** Accommodates medium-sized composite structures.
- **Vacuum Environment Testing:** Eliminates aerodynamic damping, isolating structural damping.
- **Nodal Suspension System:** Minimises boundary interaction energy losses.

## Chapter 4. Experimental Modal Analysis for Damping Estimation

- **Automated Excitation:** Pneumatic-assisted impact hammer provides consistent and repeatable excitation.
- **Comprehensive Data Acquisition:** Integrated sensors (accelerometers, strain gauges, thermocouples) accurately capture dynamic responses.
- **Modular Design:** Allows testing of various materials and structural configurations.

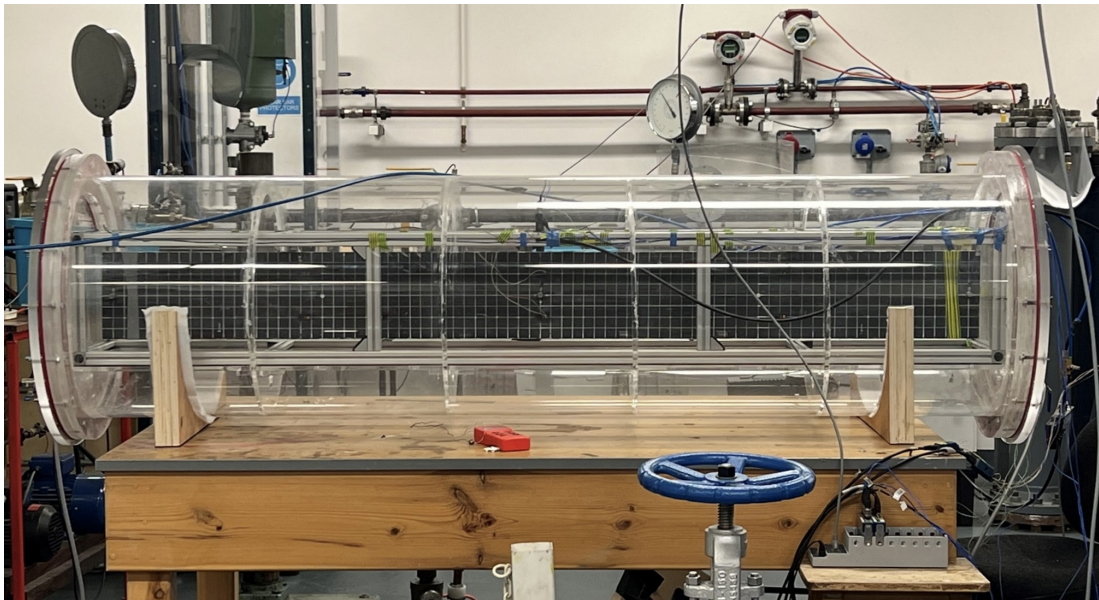
The developed setup is illustrated in Figure 4.38.

## Chapter 4. Experimental Modal Analysis for Damping Estimation



(a) Automated striker mechanism.

(b) Data Acquisition setup.



(c) Full assembly including vacuum chamber with sample.

Figure 4.38: EMA setup highlighting striker, DAQ, and complete vacuum chamber configuration.

Modal parameters were extracted using the robust Poly-reference Least-Squares Complex Frequency domain (PolyMAX) method, chosen for its precision in identifying physical modes and minimising noise-induced errors.

## Chapter 4. Experimental Modal Analysis for Damping Estimation

Key experimental results are summarised in Table 4.7.

Table 4.7: Summary of EMA Damping Results

Sample	Frequency (Hz)	Temperature (° C)	Strain ( $\mu\epsilon$ )	Damping Ratio (%)
2m 5mm Carbon UD (Air)	11.73	18.9	65	0.104
		19.2	70	0.099
		19.4	75	0.100
		19.6	80	0.105
		18.8	85	0.108
2m 5mm Carbon UD (Vacuum)	11.73	17.7	65	0.084
		17.9	70	0.075
		17.8	75	0.075
		17.8	80	0.075
		18.5	85	0.075
1.2m 5mm Carbon UD (Air)	33.23	22.4	25	0.123
		22.4	30	0.123
		22.4	35	0.124
		22.5	40	0.124
		22.6	45	0.124
1.2m 5mm Carbon UD (Vacuum)	33.23	22.4	25	0.089
		22.4	30	0.088
		22.4	35	0.087
		22.5	40	0.087
		22.6	45	0.087
Predicted 1 Hz UD (Vacuum)	1.00	N/A	N/A	0.069

*Note: Predicted EMA data is an estimate Figure 4.34 based on the current data present*

Key insights from these EMA findings include:

- **Aerodynamic Damping Impact:** Vacuum testing significantly reduced aerodynamic damping, highlighting its importance in accurate damping characterisation. Samples tested in air consistently exhibited higher

## Chapter 4. Experimental Modal Analysis for Damping Estimation

damping ratios due to aerodynamic energy losses, validating the inclusion of vacuum conditions as essential for isolating intrinsic structural damping. This result underscores the capability of the developed rig to minimise external influences and accurately reflect material behaviour.

- **Frequency-Damping Relationship:** Higher-frequency samples consistently showed increased damping ratios, mirroring observations from the DMA programme where greater excitation frequencies were associated with elevated damping. This agreement between two independent experimental techniques strengthens confidence in the derived trends and validates the use of both approaches in characterising frequency-dependent damping properties.
- **Low-Frequency Prediction:** The predicted damping ratio at 1 Hz was derived as a preliminary estimate using a fitted extrapolation of current EMA results. While useful for early-stage assessment, more accurate low-frequency damping predictions would require a broader frequency sweep across multiple sample geometries and layups to capture the full behaviour of frequency-sensitive damping.

Overall, these findings demonstrate the effectiveness of the developed EMA test rig and methodology in characterising the structural damping of carbon fibre composites. The ability to control environmental factors, ensure consistent excitation, and employ advanced post-processing techniques such as PolyMAX resulted in robust and meaningful damping data. These insights contributed to the broader understanding of material behaviour and support future improvements in wind turbine blade design and other structural applications.

To enable a direct and meaningful comparison between the damping results

## Chapter 4. Experimental Modal Analysis for Damping Estimation

obtained from EMA and those derived via DMA, it was necessary to unify the damping metrics. EMA typically yields damping ratios ( $\zeta$ ), whereas DMA provides the loss factor ( $\eta$ ) derived from the phase lag between stress and strain. To bridge this gap, Specific Damping Capacity (SDC,  $\Psi$ ) was used as a common parameter.

The relationships between these damping representations are summarised in Equation 4.3, reproduced from the literature [41]:

$$\eta = \frac{\Psi}{2\pi} = \frac{E''}{E'} = \frac{\Delta}{\pi} = \tan \delta = 2\zeta\sqrt{1 - \zeta^2} \quad (4.3)$$

These equivalences offer a theoretical basis for conversion, but their practical application is subject to limitations. Environmental conditions such as temperature, excitation frequency, and even humidity can influence results, making one-to-one conversion between methods potentially misleading if these variables are not adequately controlled.

Nevertheless, by rearranging Equation 4.3, a unified form to compute Specific Damping Capacity from either loss factor or damping ratio is given as:

$$\Psi = 2\pi\eta = 4\pi\zeta\sqrt{1 - \zeta^2} \quad (4.4)$$

*Note: In some cases,  $1 - \zeta^2$  may be considered negligible but it will be considered for this analysis*

The comparison results are summarised in Table 4.8.

Chapter 4. Experimental Modal Analysis for Damping Estimation

Table 4.8: Summary of EMA Damping Results

Sample	Frequency (Hz)	Temperature (° C)	Strain ( $\mu\epsilon$ )	Damping Ratio/ Loss Factor	SDC $\Psi$
EMA - 2m 5mm Carbon UD (Air)	11.73	18.9	65	0.104	1.300
		19.2	70	0.099	1.238
		19.4	75	0.100	1.250
		19.6	80	0.105	1.312
		18.8	85	0.105	1.312
EMA - 2m 5mm Carbon UD (Vacuum)	11.73	17.7	65	0.084	1.052
		17.9	70	0.075	0.940
		17.8	75	0.075	0.940
		17.8	80	0.075	0.940
		18.5	85	0.075	0.940
EMA - 1.2m 5mm Carbon UD (Air)	33.23	22.4	25	0.123	1.534
		22.4	30	0.123	1.534
		22.4	35	0.124	1.546
		22.5	40	0.124	1.546
		22.6	45	0.124	1.546
EMA - 1.2m 5mm Carbon UD (Vacuum)	33.23	22.4	25	0.089	1.114
		22.4	30	0.088	1.102
		22.4	35	0.087	1.089
		22.5	40	0.087	1.089
		22.6	45	0.087	1.089
EMA - Predicted 1 Hz UD (Vacuum)	1.00	19.0	N/A	0.069	0.865
EMA - Predicted 10 Hz UD (Vacuum)	10.00	19.0	N/A	0.074	0.927
EMA - Predicted 30 Hz UD (Vacuum)	10.00	19.0	N/A	0.085	1.064
DMA $\eta_{11}$ UD (Air)	1.00	30	100	0.0125	0.079
DMA $\eta_{11}$ UD (Air)	10.00	30	100	0.0138	0.087
DMA $\eta_{22}$ UD (Air)	1.00	30	100	0.0235	0.148
DMA $\eta_{22}$ UD (Air)	10.00	30	100	0.0190	0.119
DMA $\eta_{11}$ Predicted UD (Air)	30.00	30	100	0.01669	0.1049

*Note: Predicted EMA data from Figure 4.34, DMA 30 Hz result predicted from fitting line to  $\eta_{11}$  via Figure 3.21*

## Chapter 4. Experimental Modal Analysis for Damping Estimation

The key findings from this comparison were:

- Frequency matching was attempted across the datasets; however, due to laboratory constraints, it was impossible to align temperature conditions perfectly. The weights from accelerometers and strain gauges were also unable to be accounted for, though they were minimised through hardware selection. This introduces some variability into the comparisons.
- A comparison between DMA loss factors and EMA damping ratios reveals notable discrepancies. This is likely because DMA quantifies the stress–strain phase lag, while EMA measures vibrational energy dissipation, meaning that each technique inherently captures different aspects of damping.
- Specific Damping Capacity ( $\Psi$ ) offers a unified metric that directly compares the methods. However, it also underscores the limitations of interchangeably using loss factor or damping ratio without accounting for external factors such as temperature and excitation frequency. This can be seen through comparison of results from both methodologies and industry data.
- While the absolute values of Specific Damping Capacity ( $\Psi$ ) from DMA and EMA do not match, the ratio between them remains relatively consistent across the tested frequency range. At 1 Hz, the ratio of DMA  $\eta_{11}$  to EMA-predicted is 0.0913 (0.079/0.865), at 10 Hz, the ratio is 0.0939 (0.087/0.927), and at 30 Hz, the ratio is 0.0986 (0.1049/1.064). This small variation suggests that while direct numerical comparisons are not straightforward, a frequency-dependent correction factor may be viable if external influences such as temperature and strain levels are well accounted for.

## Chapter 4. Experimental Modal Analysis for Damping Estimation

In summary, the observed differences indicate that while both DMA and EMA provide valuable insights into material damping, they are sensitive to different physical phenomena. This suggests that direct numerical comparisons between DMA loss factors and EMA damping ratios must be interpreted with caution, especially when environmental influences can also cause discrepancies. A unified metric like Specific Damping Capacity is essential for more meaningful cross-method evaluations, but is not always appropriate to convert to.

### 4.6 Discussion and Conclusion

This section examines the significance of the EMA results presented in this chapter. The experimental programme has yielded valuable insights into the damping characteristics of carbon fibre composites used in offshore wind turbine blades. Key findings are discussed, the performance of the custom EMA rig is evaluated, and the implications for blade modelling and design are considered. Additionally, the results are compared with those obtained using DMA (Chapter 3), providing a broader understanding of damping behaviour across different length scales and experimental contexts.

#### 4.6.1 Key Findings

The EMA testing demonstrated several important aspects related to damping characterisation and the effectiveness of the developed experimental setup:

- **Impact of Vacuum Conditions:** Testing under vacuum significantly reduced aerodynamic damping, enabling a clearer characterisation of intrinsic structural damping in carbon fibre composites.
- **Material and Geometry Influence:** Milled samples were found

## Chapter 4. Experimental Modal Analysis for Damping Estimation

unsuitable due to potential damage during the milling process, which likely affected their structural integrity. In contrast, cut samples maintained their integrity while allowing for modal frequency adjustments. Added masses were also a potential method for frequency alterations.

- **Excitation and Response Reliability:** The pneumatic-assisted excitation system proved effective, providing consistent excitation forces across tests. Reliable modal responses were consistently observed, validating both the force application mechanism and the data acquisition process.

### 4.6.2 Evaluation of the EMA Test Rig

The custom-built EMA rig achieved its primary objectives, including accurate force excitation, stable and repeatable boundary conditions, and high-fidelity modal response capture. Several aspects were particularly important in ensuring test quality:

- The use of free–free boundary conditions reduced boundary influence on measured modes, improving the reliability of damping estimates.
- Vacuum chamber integration effectively removed aerodynamic contributions and demonstrated the rig’s suitability for isolating structural damping.
- Modular design features facilitated rapid and consistent sample mounting, improving experimental throughput and consistency.

The overall flexibility and robustness of the rig suggest strong potential for continued use in both research and industrial contexts focused on composite structural characterisation.

### **4.6.3 Sample Size - Thickness & Consistency**

Reliable damping characterisation via EMA depends not only on instrumentation and rig performance, but also critically on the geometric consistency of the test specimens. This study paid particular attention to maintaining uniform thickness and precise sample dimensions to minimise unintended variation in dynamic response.

Statistical analyses of thickness measurements (see Figures 4.20 and 4.29) confirmed that most specimens exhibited deviations of less than 0.05 mm, ensuring that observed modal behaviour was primarily governed by material properties rather than manufacturing inconsistencies. Averaging thickness data across multiple points per sample allowed the FEA models to incorporate realistic geometries, thereby improving the accuracy of frequency validation.

The influence of sample length on modal behaviour was also evident. The 1.2 m samples consistently exhibited higher natural frequencies and slightly elevated damping ratios compared to the 2 m specimens. These trends are attributable to changes in strain energy distribution and boundary condition sensitivity associated with sample length. Notably, the 2 m specimens achieved an aspect ratio of approximately 400:1, concentrating strain energy almost exclusively along the fibre direction. This geometric characteristic reinforces the interpretation that the damping values obtained through EMA predominantly reflect longitudinal (fibre-direction) behaviour.

Although some variability in sample dimensions is inevitable, the rigorous preparation protocols and dimensional verification procedures adopted in this research ensured that such factors did not meaningfully compromise the reliability of the damping measurements. Nonetheless, future work could benefit from tighter control over fabrication tolerances and further automation

of thickness measurement to reduce residual uncertainty.

#### **4.6.4 Comparison with DMA Results**

A direct comparison between the EMA and DMA results, presented in Section 4.5, underscores the complementary nature of the two techniques in characterising damping within fibre-reinforced composites.

EMA was particularly sensitive to damping in the fibre direction due to the very high aspect ratio of the specimens—up to 400 for the 2 m samples—leading to strain energy distributions almost entirely aligned with the longitudinal axis. As such, the damping values obtained from EMA testing primarily reflected energy dissipation mechanisms active along the fibre direction, with negligible contributions from transverse or through-thickness deformation modes.

In contrast, DMA tests involved much shorter specimens (e.g., 50 mm in length with 4 mm thickness), resulting in significantly lower aspect ratios (as low as 12.5). This enabled a more uniform strain field and greater sensitivity to viscoelastic and interfacial damping phenomena occurring across all material directions, including the matrix-dominated transverse and out-of-plane directions that EMA could not resolve.

This divergence in directional sensitivity highlights the value of combining both methods: EMA delivers structural-scale insights into modal damping and energy dissipation along principal stiffness directions under representative boundary conditions, while DMA offers precise, material-level measurements of frequency- and temperature-dependent damping associated with the microstructural phases. When used together, the methods bridge the micro-to-macro scale, offering a more holistic understanding of damping in composite wind turbine blades.

## Chapter 4. Experimental Modal Analysis for Damping Estimation

Furthermore, the use of Specific Damping Capacity ( $\Psi$ ) as a unifying metric in Section 4.5 enabled a first-order comparison between DMA and EMA results. While absolute values differed, the relative trends with frequency remained consistent, validating both techniques within their domains. Deviations arose due to several controllable and uncontrollable factors. EMA samples exhibited extremely high aspect ratios, concentrating strain along the fibre direction and limiting detection of transverse and matrix-related damping effects that were better captured in lower-aspect-ratio DMA specimens. Frequencies of excitations differed due to experimental setup processes. Temperature control also differed: DMA tests were isothermal, whereas EMA was subject to ambient variation. Additionally, EMA tests in vacuum excluded aerodynamic damping, unlike DMA, which operated in air. Despite these differences, the comparative use of  $\Psi$  illustrated that each method responds to distinct aspects of damping behaviour.

In conclusion, this chapter has demonstrated the value of the EMA testing methodology in characterising the structural damping behaviour of unidirectional carbon fibre composites. When used in conjunction with DMA, the approach bridges micro- and macro-scale damping mechanisms, laying the foundation for improved blade modelling and design optimisation. Further investigation and refinement of these approaches could extend their application to hybrid laminates, curved geometries, and in-field structural health monitoring.

# Chapter 5

## Conclusions

This thesis addressed the primary research question:

*How can the damping of anisotropic composites be accurately characterised through experimental methods, considering their directional property dependence, and therefore be effectively represented in numerical models to enhance wind turbine blade design?*

The integration of theoretical, experimental, and numerical methodologies, specifically DMA, FEA-assisted DMA, and EMA, has successfully advanced the understanding and accuracy of damping characterisation for anisotropic composite materials used in wind turbine blades.

### 5.1 Research Structure

The research presented in this thesis was systematically structured into four main chapters, each specifically addressing aspects of the primary research question outlined previously:

## Chapter 5. Conclusions

- **Chapter 1 – Introduction:** Outlined the motivation for investigating structural damping in wind turbine blades, emphasising its significance in enhancing structural performance and blade longevity. Additionally, it clearly defined the scope, objectives, and contributions of the research.
- **Chapter 2 – Damping Fundamentals:** Provided essential theoretical foundations on damping mechanisms specific to composite materials, introducing key concepts such as viscoelastic damping, energy dissipation, and relevant mathematical models. These concepts established the necessary theoretical basis for subsequent experimental and numerical investigations.
- **Chapter 3 – Dynamic Mechanical Analysis:** Evaluated DMA techniques, highlighting their limitations in characterising anisotropic materials such as carbon fibre composites. To address these challenges, a novel FEA-assisted DMA methodology was developed, enabling accurate decomposition of directional damping components. This approach successfully accounted for shear effects, environmental factors, and sensitivity to sample preparation, significantly enhancing the accuracy of directional damping quantification.
- **Chapter 4 – Experimental Modal Analysis:** Investigated EMA as a robust experimental technique for characterising structural damping within multi-degree-of-freedom composite structures. A custom EMA test rig was designed, manufactured, and validated, incorporating features such as a modular vacuum chamber, automated modal excitation, and high-precision instrumentation. Experimental results provided valuable insights into the influence of environmental conditions, excitation levels, and geometric configurations on damping characteristics, with validation supported by finite element analyses.

## Chapter 5. Conclusions

Additionally, EMA and DMA results were compared using an analytical conversion approach as introduced in Section 3.2.2.1.

This structured approach facilitated a comprehensive examination of damping characterisation, enabling detailed insight into both material-level and structural-level damping behaviours critical for wind turbine blade design.

## 5.2 Summary of Main Contributions

The principal contributions of this thesis, aligned with the development of the research chapters, are summarised below:

### 1. Development of a Novel FEA-assisted DMA Methodology (Chapter 3):

- Proposed and validated an FEA-assisted approach for decomposing directional damping contributions in unidirectional carbon fibre composites using standard three-point bending DMA tests.
- Enabled quantification of damping contributions from fibre-aligned, transverse, and shear directions by analysing strain energy distributions through multiple numerical models.
- Demonstrated that high-precision geometric tolerances ( $\pm 0.01$  mm) are critical for reliable damping characterisation, especially in low-frequency ranges of interest to SGRE.
- Identified frequency-dependent damping trends and established the minimum damping response near 0.25 Hz, providing insight into low-mode behaviour relevant to offshore blade design.

### 2. Design and Validation of a Custom EMA Testing Framework

**(Chapter 4):**

- Designed and built a modular EMA test rig featuring nodal suspension, vacuum environmental control, and automated pneumatic excitation to isolate intrinsic structural damping.
- Demonstrated that vacuum conditions can reduce aerodynamic damping by up to 30%, enabling clearer identification of material damping characteristics in large-scale composite specimens.
- Achieved repeatable modal responses across multiple specimens and validated experimental frequencies through FEA, confirming the rig's accuracy and reliability.

**3. Enhanced Understanding of Directional and Frequency-Dependent Damping (Chapters 3 & 4):**

- Showed consistent trends between DMA and EMA results across frequency, supporting the physical validity of both techniques within their respective domains.
- Confirmed that EMA primarily captures fibre-aligned damping due to the extreme aspect ratios of tested specimens, while DMA captures broader viscoelastic behaviour across all directions.

**4. Introduction of Specific Damping Capacity as a Comparative Metric (Section 4.5):**

- Introduced Specific Damping Capacity ( $\psi$ ) as a unifying metric for comparing loss factors and damping ratios obtained from DMA and EMA respectively.
- Highlighted the limitations of directly equating damping ratio and loss factor, particularly under varying environmental conditions,

excitation frequencies, and strain energy distributions.

### 5.3 Key Conclusions

The integration of DMA, FEA-assisted DMA, and EMA has enabled a multi-scale understanding of damping behaviour in unidirectional carbon fibre composites. The following conclusions can be drawn from the findings:

- **Directional Damping Behaviour:** Fibre-aligned damping dominates in EMA results due to the high aspect ratio of tested specimens (up to 400:1), whereas DMA captures a more comprehensive response including shear and transverse effects, especially in shorter specimens (AR as low as 12.5 within the testing in Chapter 3).
- **Frequency and Environmental Sensitivities:** Both DMA and EMA revealed frequency-dependent damping behaviour, with damping increasing with excitation frequency. However, comparisons between the techniques must consider environmental influences such as vacuum vs ambient air, temperature stability and more, as discussed in Chapter 3 and Chapter 4.
- **Metric Interpretation:** The adoption of Specific Damping Capacity ( $\psi$ ) in Section 4.5 enabled a consistent, though first-order, comparison between loss factors and damping ratios. The results highlight the limitations of interchangeably using these metrics without adjusting for excitation mode, frequency range, and environmental effects.
- **Validation and Model Integration:** Integration with FEA models confirmed that the damping behaviour observed experimentally could be translated to numerical models, particularly when supported by detailed strain energy analysis (Chapter 3).

- **Guidelines for DMA and EMA experiment have been shown:** Within Chapter 3 and 4, recommendation for experimental setup have been advised.

Taken together, these findings confirm that a combined DMA and EMA framework is useful for fully characterising the damping of anisotropic composite materials, addressing both micro-scale viscoelasticity and macro-scale structural response.

## **5.4 Implications for Wind Turbine Blade Design**

The validated damping parameters and methodologies developed in this thesis directly support the design and optimisation of wind turbine blades. Accurate directional damping characterisation, particularly crucial in edgewise bending where aerodynamic effects are minimal, significantly enhances vibration control, fatigue resistance, and structural reliability in next-generation offshore wind turbines. Furthermore, the experimental and analytical frameworks presented here are directly transferable to future blade development programmes, providing a robust foundation for more predictive and resilient composite structures.

## **5.5 Limitations of the Present Study**

While the methodologies developed and applied in this thesis significantly advance the understanding of damping in anisotropic composite materials, several limitations should be acknowledged to contextualise the findings and guide future improvements.

## DMA-Specific Limitations

DMA, particularly in the three-point bending configuration, provided high-resolution measurements of viscoelastic behaviour but was subject to the following constraints:

- **Geometric and Boundary Assumptions:** The test setup assumes uniform bending and ideal boundary conditions, which can be compromised by slight misalignments or imperfections in clamping and support. Additionally, the assumed isotropy of strain energy distribution within each test mode does not hold for highly anisotropic materials.
- **Environmental Sensitivity:** DMA results are highly sensitive to ambient temperature and humidity. While tests were conducted at controlled temperatures, no thermal sweep tests were included. Therefore, the damping behaviour reported is valid only within the tested environmental window. Further to this humidity could not be controlled with the equipment available.
- **Frequency Limitations:** The test frequency range (0.01–10 Hz) was selected based on SGRE's interest in low-mode dynamic behaviour, but excludes the higher frequencies at which additional damping mechanisms may become active.
- **Material Homogeneity Assumptions in FEA:** The FEA-assisted DMA models assume perfect material homogeneity and perfect bonding at ply interfaces. Local flaws or interfacial debonding are not captured in the numerical model and could lead to under- or overestimation of transverse and shear damping contributions.

## EMA-Specific Limitations

EMA provided system-scale damping measurements but also presented several constraints:

- **Directional Bias of Strain Energy:** Due to the high aspect ratio of EMA specimens (up to 400), strain energy was almost exclusively aligned with the fibre direction. This limits the ability of EMA to capture transverse and shear damping contributions, which were more effectively measured via DMA. However, this allows for the isolation of fibre direction damping, which is of more interest within this study.
- **Vacuum and Free-Free Assumptions:** Although vacuum testing removed aerodynamic damping, it introduced practical limitations in setup repeatability, vacuum quality, and measurement accessibility. Additionally, perfect free-free boundary conditions are approximated rather than fully achieved, potentially affecting modal accuracy.
- **Frequency Sweep and Data Availability:** This analysis focused primarily on the first mode of vibration (Mode 1). Accurately characterising frequency-dependent damping would require additional testing across a broader range of samples and modal configurations. As such, the results presented in this thesis represent specific modal scenarios, with generalisation to other modes or frequencies necessitating further experimental data.

## Comparative Limitations: Use of Specific Damping Capacity

( $\psi$ )

Section 4.5 introduced the Specific Damping Capacity ( $\psi$ ) as a unifying metric to facilitate the comparison between DMA and EMA results. While this

## Chapter 5. Conclusions

approach provided useful trends:

- **Absolute Values Are Not Directly Comparable:** DMA and EMA operate under fundamentally different excitation types, boundary conditions, and response scales. The absolute  $\psi$  values are therefore not interchangeable.
- **Method-Specific Sensitivities:** DMA is more sensitive to viscoelastic phase lag and temperature effects, whereas EMA captures geometric and structural damping more prominently. These distinctions must be accounted for when interpreting relative trends.
- **Frequency and Temperature Discrepancy:** Although trends in damping with frequency were similar, the exact correspondence is limited due to differing frequency ranges and lack of temperature sweeps in DMA.

### Generalisability and Material Scope

This research focused exclusively on unidirectional carbon fibre composites relevant to SGRE's offshore wind turbine blades. While many insights are transferable:

- **Multi-orientation Laminates Not Studied Directly:** Although predictive models (e.g., Ni–Adams, Adams–Maheri) were considered, experimental validation of these models on full laminates was beyond the scope of this work. Further expansion of these models to a 3D model would also be of interest.
- **Manufacturing Variability:** All specimens were produced under controlled conditions using industrial-grade UD prepregs. The influence of defects such as porosity, voids, or fibre misalignment remains to be

explored.

These limitations do not undermine the core findings but highlight areas where further development is necessary to broaden the robustness and application of the proposed methodologies.

## 5.6 Future Work

The work presented in this thesis has established a solid foundation for damping characterisation in anisotropic composites, particularly those used in wind turbine blades. Building on these findings, several avenues for future research are proposed to improve methodological robustness, broaden applicability, and address the limitations outlined in the previous section.

- **Expanded Material Systems:** Future studies should explore the damping behaviour of hybrid laminates and multi-material systems, including carbon–glass hybrids and composite–metal combinations. This would provide insight into the interaction of different constituent materials and their contribution to overall energy dissipation.
- **Broader Environmental Testing:** Systematic investigations of damping under varying temperatures, humidity levels, and long-term cyclic exposure are recommended. Incorporating thermal sweep testing in DMA and EMA under environmental conditioning would enhance understanding of operational degradation and inform temperature-dependent modelling.
- **Scale-Up and Component-Level Validation:** Applying the developed methodologies to larger-scale specimens, such as spar caps or blade cross-sections, would help validate scalability. This would also serve as a bridge between coupon-level characterisation and full-scale blade

## Chapter 5. Conclusions

simulations.

- **Enhanced Comparative Methodology:** Future work should establish more robust guidelines for comparing DMA and EMA-derived parameters. This includes developing refined conversion frameworks between loss factor, damping ratio, and Specific Damping Capacity ( $\psi$ ), accounting for frequency, boundary conditions, and environmental effects. Experimental cross-validation of damping across shared frequencies and conditions would further enhance interpretability.
- **Improved Material Prediction :** Expand upon the Tsai-Chang model mentioned in Section 2.6.1 for use with 3D composite structures for more accurate composite damping estimation.
- **Extended Frequency Characterisation:** EMA and DMA studies could benefit from a broader frequency spectrum. This would better simulate blade excitation profiles encountered in practice.

By addressing these areas, future research can build on the experimental frameworks, models, and data interpretation techniques developed in this thesis. This would contribute to more robust and generalisable models of damping in composite structures and further support the design of longer-lasting, vibration-resistant wind turbine blades.

In summary, this thesis establishes a validated and scalable framework for accurately characterising directional damping in anisotropic composites, specifically tailored to wind turbine blade applications. Through innovative experimental methods, rigorous numerical modelling, and careful analysis of damping metrics, this research addresses key challenges in reliably representing composite damping in structural design. The methodologies developed not only advance blade design practices but are also transferable

## Chapter 5. Conclusions

to other composite structures across energy, aerospace, and civil engineering industries. As the demand for lighter, more durable, and dynamically robust composite structures grows, the contributions from this thesis offer a robust foundation for future research and industrial implementation.

# Bibliography

- [1] Global Wind Energy Council. Wind energy in the uk: June 2021, 2021.
- [2] Keshani Attanayake, Isuru Wickramage, Udul Samarasinghe, Yasangi Ranmini, Sandali Ehalapitiya, Ruwan Jayathilaka, and Shanta Yapa. Renewable energy as a solution to climate change: Insights from a comprehensive study across nations. *PLOS ONE*, 2024.
- [3] Yanan Zhao, Shijing Liang, Yi Liu, Tim R. McVicar, Cesar Azorin-Molina, Lihong Zhou, Robert J.H. Dunn, Sonia Jerez, Yingzuo Qin, Xinrong Yang, Jiayu Xu, and Zhenzhong Zeng. Global assessment of spatiotemporal changes of frequency of terrestrial wind speed. *Environmental Research Letters*, 18, 4 2023.
- [4] International Renewable Energy Agency (IRENA). Renewable capacity statistics 2024. <https://www.irena.org/Publications/2024/Mar/Renewable-capacity-statistics-2024>, 2024. Accessed: February 26, 2025.
- [5] Global Wind Energy Council (GWEC). Global wind report 2023. <https://gwec.net/global-wind-report/>, 2023. Accessed: February 26, 2025.
- [6] Sara C. Pryor, Rebecca J. Barthelmie, Melissa S. Bukovsky, L. Ruby

## Bibliography

- Leung, and Koichi Sakaguchi. Climate change impacts on wind power generation, 12 2020.
- [7] Jiaxing Wang, Yu Liu, and Zhenhao Zhang. Fatigue damage and reliability assessment of wind turbine structure during service utilizing real-time monitoring data. *Buildings*, 14(11), 2024.
- [8] Nikolay Krasimirov Dimitrov. *Structural Reliability of Wind Turbine Blades: Design Methods and Evaluation*. Phd thesis, Technical University of Denmark, 2013.
- [9] D. I. Chortis, N. A. Chrysochoidis, and D. A. Saravanos. Damped structural dynamics models of large wind-turbine blades including material and structural damping. In *Journal of Physics: Conference Series*, volume 75. Institute of Physics Publishing, 6 2007.
- [10] Povl Brøndsted, Hans Lilholt, and Aage Lystrup. Composite materials for wind power turbine blades. *Annual Review of Materials Research*, 35:505–538, 2005.
- [11] Haoming Liu, Suxiang Yang, Wei Tian, Min Zhao, Xiaoling Yuan, and Bofeng Xu. Vibration reduction strategy for offshore wind turbines. *Applied Sciences*, 10(17), 2020.
- [12] R Vinayaravi, K Jayaraj, D Kumaresan, and AK Asraff. Study on energy dissipation mechanism of an impact damper system. *Journal of Computational and Nonlinear Dynamics*, 17(4):041003, 2022.
- [13] Tai Hong Cheng, Ming Ren, Zhen Zhe Li, and Yun De Shen. Vibration and damping analysis of composite fiber reinforced wind blade with viscoelastic damping control. *Advances in Materials Science and Engineering*, 2015, 2015.

## Bibliography

- [14] Seher Ahsan Khalid, Abdul Munem Khan, and Owaisur Rahman Shah. A numerical study into the use of auxetic structures for structural damping in composite sandwich core panels for wind turbine blades. *Journal of Energy Resources Technology, Transactions of the ASME*, 144, 3 2022.
- [15] K. Thomsen, J. T. Petersen, E. Nim, S. Øye, and B. Petersen. A method for determination of damping for edgewise blade vibrations. *Wind Energy*, 3:233–246, 10 2000.
- [16] Yentl Swolfs. Perspective for fibre-hybrid composites in wind energy applications. *Materials*, 10(11):1281, 2017.
- [17] Suryans Chamoli and Adrian Gambier. Active edgewise blade damping control of large wind turbines by using the pitch controller and an interval observer. In *Actuators*, volume 13, page 58. MDPI, 2024.
- [18] Biswajit Basu, Zili Zhang, and Søren R.K. Nielsen. Damping of edgewise vibration in wind turbine blades by means of circular liquid dampers. *Wind Energy*, 19:213–226, 2 2016.
- [19] Baher Pishbahar and Hamed Moradi. Active control of the edgewise vibrations in wind turbine blade by optimization of the number and locations of the intermediate actuators. *International Journal of Dynamics and Control*, 11:1230–1246, 6 2023.
- [20] Khawla Essassi, Ayman Ayachi, Nabih Feki, Anas Bouguecha, Fakher Chaari, and Mohamed Haddar. Mechanical characterization of glass fibers–reinforced composites for wind turbine blades applications. In *International Conference Design and Modeling of Mechanical Systems*, pages 901–908. Springer, 2021.
- [21] Hanwei Teng, Shujian Li, Zheng Cao, Shuang Li, Changping Li, and Tae Jo Ko. Carbon fiber composites for large-scale wind turbine blades:

## Bibliography

- Applicability study and comprehensive evaluation in china. *Journal of Marine Science and Energy*, 2023.
- [22] Bing Cai, Zhenghong Yao, Xiaowen Zhang, Changyou Li, Xu Liu, Xiaorong Zhang, Ziyi Wang, and Ce Zhang. Damping model of fiber reinforced composites and factors affecting damping and dynamic response. *Applied Composite Materials*, 28(5):1451–1476, 2021.
- [23] Georgios Sieros, Dora Lekou, Dimitrios Chortis, Panagiotis Chaviaropoulos, Xabier Munduate, Amaia Irisarri, Helge Aa. Madsen, Anders Yde, Kasper Thomsen, Marco Stettner, Maarten Reijerkerk, Francesco Grasso, Ronald Savenije, Gerard Schepers, and Casper F. Andersen. Avatar reference blade design. Technical Report D1.2, AVATAR Project, ECN Wind Energy, January 2015. Deliverable D1.2 of the AVATAR Project, FP7-ENERGY-2013-1, Grant Agreement No. 608396.
- [24] Christophe Floreani, Fergus Cuthill, Jeffrey Steynor, James Maguire, Edward D McCarthy, Maarten J Niessink, Sandro Di Noi, Lukas Wittevrongel, Tomas Flanagan, and Conchur MO Bradaigh. Testing of 6m hybrid glass/carbon fibre powder epoxy composite wind blade demonstrator. *Sampe Journal*, 3, 2021.
- [25] Cagri Kocan and Gökhan Osman Özgen. Investigation of the effect of structural damping on wind turbine wind-induced fatigue loads. *Mechanics Based Design of Structures and Machines*, 52:680–705, 2024.
- [26] Giannis Serafeim, Dimitris Manolas, Vasilis Riziotis, and Panagiotis Chaviaropoulos. Wind turbine blade design optimization for reduced lcoe, focusing on design-driving loads due to storm conditions. *Fluids*,

## Bibliography

7:280, 2022.

- [27] Wenxian Yang, Zhike Peng, Kexiang Wei, and Wenye Tian. Structural health monitoring of composite wind turbine blades: challenges, issues and potential solutions. *IET Renewable Power Generation*, 11(4):411–416, 2017.
- [28] A. Treviso, B. Van Genechten, D. Mundo, and M. Tournour. Damping in composite materials: Properties and models. *Composites Part B: Engineering*, 78:144–152, 2015.
- [29] Yasser Hamed Elmoghazy, Babak Safaei, Mohammed Asmael, Saeid Sahmani, Qasim Zeeshan, and Zhaoye Qin. Computational modelling and analysis of effect of viscoelastic materials on damping and vibrational behaviors of composite structures—an extensive review. *Archives of Computational Methods in Engineering*, 31:2611–2662, 2024.
- [30] Brandon Lee Ennis, Christopher Lee Kelley, Brian Thomas Naughton, Robert E Norris, Sujit Das, Dominic Lee, and Dave Miller. Optimized carbon fiber composites in wind turbine blade design. Technical report, Sandia National Lab.(SNL-NM), Albuquerque, NM (United States); Oak Ridge . . . , 2019.
- [31] Brandon Lee Ennis, Ryan James Clarke, Joshua Paquette, Robert E Norris, Sujit Das, David A Miller, and Daniel D Samborsky. Optimized carbon fiber composites in wind turbine blade design: Follow-on studies. Technical report, Sandia National Lab.(SNL-NM), Albuquerque, NM (United States); Oak Ridge . . . , 2023.
- [32] Manjeet Rani, Priyanka Choudhary, Venkata Krishnan, and Sunny Zafar. A review on recycling and reuse methods for carbon fiber/glass

## Bibliography

- fiber composites waste from wind turbine blades. *Composites part B: engineering*, 215:108768, 2021.
- [33] Leon Mishnaevsky, Kim Branner, Helga Nørgaard Petersen, Justine Beauson, Malcolm McGugan, and Bent F. Sørensen. Materials for wind turbine blades: An overview. *Materials*, 10, 11 2017.
- [34] R Chandra, SP Singh, and K Gupta. Experimental evaluation of damping of fiber-reinforced composites. *Journal of Composites Technology and Research*, 25(2):1–12, 04 2003.
- [35] Jean Marie Berthelot, Mustapha Assarar, Youssef Sefrani, and Abderrahim El Mahi. Damping analysis of composite materials and structures. *Composite Structures*, 85:189–204, 10 2008.
- [36] Jingyu Zhai, Xinyuan Song, Anyang Xu, Yugang Chen, and Qingkai Han. Dislocation damping and defect friction damping in magnesium: molecular dynamics study. *Metals and Materials International*, 27:1458–1468, 2021.
- [37] Zhi Tang and Y. Yan. A review on the damping properties of fiber reinforced polymer composites. *Composites Part B: Engineering*, 182:107675, 2020.
- [38] Xiaodong Liu. Damping mathematical modelling and dynamic responses for frp laminated composite plates with polymer matrix. *Composite Interfaces*, 25(10):911–931, 2018.
- [39] L Gaul and A Schmidt. Experimental determination and modeling of material damping. *VDI BERICHTE*, 2003:17, 2007.
- [40] F ; Wang, J ; Liao, C ; Huang, H ; Yu, J ; Yan, H Li, Fei Wang, Jianbin Liao, Chaoming Huang, Hongliang Yu, Jin Yan, and Hanlin Li. Study on the

## Bibliography

- damping dynamics characteristics of a viscoelastic damping material. *Processes* 2022, Vol. 10, Page 635, 10:635, 3 2022.
- [41] Hasan Koruk and Srinath Rajagopal. A comprehensive review on the viscoelastic parameters used for engineering materials, including soft materials, and the relationships between different damping parameters. *Sensors*, 24(18):6137, 2024.
- [42] Dharun Vadugappatty Srinivasan and Anastasios P. Vassilopoulos. Manufacturing and toughening effects on the material properties of wind turbine blade adhesives. *Polymer Testing*, 116, 12 2022.
- [43] Akhil P Mathew and B Tech Scholar. Structural analysis of composite wind turbine blade. *International Research Journal of Engineering and Technology*, 2018.
- [44] Biswajit Basu, Zili Zhang, and Søren RK Nielsen. Damping of edgewise vibration in wind turbine blades by means of circular liquid dampers. *Wind Energy*, 19(2):213–226, 2016.
- [45] Zhigao Dang, Zhaoyong Mao, and Baowei Song. Underwater noise reduction of offshore wind turbines through vibration isolation. In *Global Oceans 2020: Singapore–US Gulf Coast*, pages 1–4. IEEE, 2020.
- [46] Jie Meng and Dagang Sun. Research on vibration suppression of wind turbine blade with a multi-layer porous damping structure based on bamboo wall microstructure. *Journal of the Brazilian Society of Mechanical Sciences and Engineering*, 43(3):153, 2021.
- [47] Giannis Serafeim, Dimitris Manolas, Vasilis Riziotis, and Panagiotis Chaviaropoulos. Wind turbine blade design optimization for reduced lcoe, focusing on design-driving loads due to storm conditions. *Fluids*, 7(8), 2022.

## Bibliography

- [48] José M Gutiérrez, Rodrigo Astroza, Francisco Jaramillo, Marcos Orchard, and Marcelo Guarini. Correction: Evolution of modal parameters of composite wind turbine blades under short-and long-term forced vibration tests. *Journal of Civil Structural Health Monitoring*, 14(5):1371–1371, 2024.
- [49] N. Saba, M. Jawaid, Othman Y. Alothman, and M. T. Paridah. A review on dynamic mechanical properties of natural fibre reinforced polymer composites, 3 2016.
- [50] Alan T Nettles. Basic mechanics of laminated composite plates. Technical report, NASA, 1994.
- [51] Humphrey Hardy. *Isotropic Materials*, pages 55–62. Springer International Publishing, Cham, 2022.
- [52] William D. Callister and David G. Rethwisch. *Materials Science and Engineering: An Introduction*. Wiley, 8th edition, 2010.
- [53] Dipen Kumar Rajak, Pratiksha H Wagh, and Emanoil Linul. Manufacturing technologies of carbon/glass fiber-reinforced polymer composites and their properties: A review. *Polymers*, 13(21):3721, 2021.
- [54] Sefiu Adekunle Bello. Carbon-fiber composites: Development, structure, properties, and applications. *Handbook of Nanomaterials and Nanocomposites for Energy and Environmental Applications*, pages 63–84, 2021.
- [55] S. J. Hwang and R. F. Gibson. Micromechanical Modeling of Damping in Discontinuous Fiber Composites Using a Strain Energy/Finite Element Approach. *Journal of Engineering Materials and Technology*, 109:47–52, 01 1987.

## Bibliography

- [56] Euan Brough, David Nash, Abbas Mehrad Kazemi Amiri, Philippe Couturier, and Vitor Luiz Reis. Development of a test rig for improved estimation of structural damping of wind turbine composite materials. In *ASME Aerospace Structures, Structural Dynamics, and Materials Conference*, volume 87141, page V001T01A026. American Society of Mechanical Engineers, 2023.
- [57] I Gyunal, VN Paimushin, VA Firsov, and VM Shishkin. Identification of the damping properties of rigid isotropic materials by studying the damping flexural vibrations of test specimens. *Mechanics of Solids*, 52:200–211, 2017.
- [58] Biao Wei, Mingyu Chen, Lizhong Jiang, Yujie Yu, and Haozheng Min. Equivalence of bilinear hysteresis and viscous damping energy dissipation. *Journal of Testing and Evaluation*, 52(1), 2024.
- [59] Tareq Al-Hababi, Maosen Cao, Bassiouny Saleh, Nizar Faisal Alkayem, and Hao Xu. A critical review of nonlinear damping identification in structural dynamics: Methods, applications, and challenges. *Sensors*, 20(24):7303, 2020.
- [60] Ying Gao, Yibin Li, Yi Hong, Hongming Zhang, and Xiaodong He. Modeling of the damping properties of unidirectional carbon fibre composites. *Polymers and Polymer Composites*, 19(2-3):119–122, 2011.
- [61] Bryan Harris. *Engineering Composite Materials*. The Institute of Materials, 1999.
- [62] S. G. Advani and E. M. Sozer. *Process Modeling in Composites Manufacturing*. CRC Press, 2nd edition, 2010.

## Bibliography

- [63] Harshavardhan N. Jayaraman, Justine Beauson, Malcolm McGugan, and Bent F. Sørensen. Materials for wind turbine blades: An overview. *Materials*, 10(11):1285, 2017.
- [64] Seungjin Han and DDL Chung. Mechanical energy dissipation using carbon fiber polymer–matrix structural composites with filler incorporation. *Journal of Materials Science*, 47:2434–2453, 2012.
- [65] Arash Afshar, Maen Alkhader, Chad S Korach, and Fu-Pen Chiang. Synergistic effects of fatigue and marine environments on carbon fiber vinyl-ester composites. *Journal of Engineering Materials and Technology*, 137(4):041002, 2015.
- [66] Weiwei Jiao, Wenbo Liu, Fan Yang, Long Jiang, Weicheng Jiao, and Rongguo Wang. Improving the interfacial property of carbon fiber/vinyl ester resin composite by grafting modification of sizing agent on carbon fiber surface. *Journal of Materials Science*, 52(23):13812–13828, 2017.
- [67] MoonHeui Han, WangGeun Song, and Doo-Won Kim. Sizing-agent control of the high-focusing and spread-ability of a melt-spun polyacrylonitrile-based carbon fiber and its interfacial shear strength. *Carbon Letters*, pages 1–7, 2024.
- [68] João Ramôa Correia. Pultrusion of advanced composites. In Elsevier Ltd, editor, *Advanced Fiber-Reinforced Polymer (FRP) Composites for Structural Applications*, chapter 7, pages 138–167. Elsevier, 2023.
- [69] K Abdurrohman, T Satrio, NL Muzayadah, and Teten. A comparison process between hand lay-up, vacuum infusion and vacuum bagging method toward e-glass ew 185/lycal composites. In *Journal of Physics: Conference Series*, volume 1130, page 012018. IOP Publishing, 2018.

## Bibliography

- [70] M. Hancioglu, E. M. Sozer, and S. G. Advani. Comparison of in-plane resin transfer molding and vacuum-assisted resin transfer molding 'effective' permeabilities based on mold filling experiments and simulations. *Journal of Reinforced Plastics and Composites*, 39(1–2):31–44, 2020.
- [71] CJ Creighton and TW Clyne. The compressive strength of highly-aligned carbon-fibre/epoxy composites produced by pultrusion. *Composites Science and Technology*, 60(4):525–533, 2000.
- [72] KN Verghese, NS Broyles, JJ Lesko, RM Davis, and JS Riffle. Pultruded carbon fiber/vinyl ester composites processed with different fiber sizing agents. part ii: enviro-mechanical durability. *Journal of materials in civil engineering*, 17(3):334–342, 2005.
- [73] Z Hashin. Analysis of the effects of fiber anisotropy on the properties of carbon and graphite fiber composites. In *Mechanical Behavior of Anisotropic Solids/Comportment Mécanique des Solides Anisotropes: Proceedings of the Euromech Colloquium 115 Villard-de-Lans, June 19–22, 1979/Colloque Euromech 115 Villard-de-Lans, 19–22 juin 1979*, pages 407–408. Springer, 1982.
- [74] Dimitris A Saravanos and Christos C Chamis. Unified micromechanics of damping for unidirectional fiber reinforced composites. Technical report, NASA Lewis Research Centre Cleveland, OH, United States, 1989.
- [75] A. Treviso, B. van Genechten, D. Mundo, and M. Tournour. Damping in composite materials: Properties and models. *Composites B: Engineering*, 78:144–152, 2015.
- [76] Y Qiu, Y Zhang, et al. Research on damping performance and strength of the composite e-glass fiber laminates. *Scientific Reports*, 11:18711,

## Bibliography

2021.

- [77] Mohammad Rouhi Moghanlou, Ali Mahmoudi, MM Khonsari, and G Li. A comparison of damping-based methods to identify damage to carbon-fiber-reinforced polymers laminates subjected to low-velocity impact. *Journal of Composite Materials*, 58(3):401–417, 2024.
- [78] S Mohanty, H Mankodi, and K S Pandya. Multiscale simulation and experimental analysis of damping in composite structures. *Composite Structures*, 295:115871, 2022.
- [79] Feng Li, Hongqiang Li, Rui Bai, Yanhong Liu, and Zhiwen Zhu. Experimental and numerical investigation on the influence factors of damage interference in patch-repaired cfrp laminates. *Polymers*, 15(6):1403, 2023.
- [80] R. Chandra, S.P. Singh, and K. Gupta. Damping studies in fiber-reinforced composites - a review. *Composite Structures*, 46:41–51, 2003.
- [81] C.T. Sun. Integrated mechanics for the passive damping of polymer-matrix composites. Technical report, NASA Technical Reports Server (NTRS), 2021. NASA/TM-2021-220172.
- [82] H. Yang, Y. Zhang, and X. Liu. Effects of interfacial dynamics on the damping of biocomposites. *Nature*, 15:1249–1257, 2023.
- [83] Xin-Yu Lu, Si-Yu Guo, Yan-Gao Hu, and Thomas Böhlke. Study of the effect of interfacial damage and friction on stress transfer in short fiber-reinforced composites. *European Journal of Mechanics - A/Solids*, 102:105408, 2024.

## Bibliography

- [84] S. Graham Kelly. *Mechanical Vibrations: Theory and Applications*. Cengage Learning, si edition edition, 2012.
- [85] A. A. Shabana. *Theory of Vibration: An Introduction*. Springer, 3rd edition, 2019.
- [86] Ray W. Clough and Joseph Penzien. *Dynamics of Structures*. Computers and Structures, Inc., third edition edition, 2003.
- [87] Anil K. Chopra. *Dynamics of Structures: Theory and Applications to Earthquake Engineering*. Pearson, 4th edition, 2015.
- [88] Rong Chen, Haitao Luo, Hongguang Wang, and Weijia Zhou. Topology optimization of partial constrained layer damping treatment on plate for maximizing modal loss factors. *Composites and Advanced Materials*, 30:26349833211034879, 2021.
- [89] Yi Hua, Ananth Ram Mahanth Kasavajhala, and Linxia Gu. Elastic–plastic analysis and strength evaluation of adhesive joints in wind turbine blades. *Composites Part B: Engineering*, 44(1):650–656, 2013.
- [90] Abdollah Malekjafarian, Soroosh Jalilvand, Paul Doherty, and David Igoe. Foundation damping for monopile supported offshore wind turbines: A review, 5 2021.
- [91] Tony Burton, David Sharpe, Nick Jenkins, and Ervin Bossanyi. *Wind energy handbook*, 2011.
- [92] Vikram K. Kinra and Alan Wolfenden. *M3D, mechanics and mechanisms of material damping* Vikram K. Kinra and Alan Wolfenden, eds. ASTM STP ; 1169. American Society for Testing Materials, Philadelphia, Pa, 1992.

## Bibliography

- [93] Patrick Kelly. Viscoelasticity. [https://pkel015.connect.amazon.auckland.ac.nz/SolidMechanicsBooks/Part\\_I/BookSM\\_Part\\_I/10\\_Viscoelasticity/10\\_Viscoelasticity\\_Complete.pdf](https://pkel015.connect.amazon.auckland.ac.nz/SolidMechanicsBooks/Part_I/BookSM_Part_I/10_Viscoelasticity/10_Viscoelasticity_Complete.pdf), 2012. Accessed: 2024-07-29.
- [94] E. J. Graesser and C. R. Wong. The relationship of traditional damping measures for materials with high damping capacity. Technical Report DTRC-SME-91/05, David Taylor Research Center, Bethesda, MD, 1991. Available at: <https://apps.dtic.mil/sti/pdfs/ADA235347.pdf>.
- [95] A. Alipour and F. Zareian. Study rayleigh damping in structures: Uncertainties and treatments. In *14th World Conference on Earthquake Engineering*, Beijing, China, 2008.
- [96] Anil K Chopra and Frank McKenna. Modeling viscous damping in nonlinear response history analysis of buildings for earthquake excitation. *Earthquake Engineering & Structural Dynamics*, 45(2):193–211, 2016.
- [97] Zuzana Murčinková, Imrich Vojtko, Michal Halapi, and Mária Šebestová. Damping properties of fibre composite and conventional materials measured by free damped vibration response. *Advances in Mechanical Engineering*, 11(5):1687814019847009, 2019.
- [98] EP Petrov and DJ Ewins. Effects of damping and varying contact area at blade-disk joints in forced response analysis of bladed disk assemblies. *Journal of Turbomachinery*, 2006.
- [99] L. E. Goodman and R. A. Klumpp. Studies of interface damping. Technical report, NASA Technical Note D-5709, 1970.
- [100] Kevin P Menard and Noah Menard. *Dynamic mechanical analysis*. CRC press, 2020.

## Bibliography

- [101] TA Instruments. *Dynamic Mechanical Analysis (DMA) - A Guide*, 2022. Accessed: 2024-09-28.
- [102] Leonard Meirovitch. *Fundamentals of Vibrations*. Waveland Press, Inc., 2001.
- [103] Bertha A. Olmos and Jose M. Roesset. Evaluation of the half-power bandwidth method to estimate damping in systems without real modes. *Earthquake Engineering & Structural Dynamics*, 39:1671–1686, 2010.
- [104] Carlo Rainieri and Giovanni Fabbrocino. *Operational Modal Analysis of Civil Engineering Structures*. Springer, 2014.
- [105] Hamed Hasani and Francesco Freddi. Operational modal analysis on bridges: A comprehensive review. *Infrastructures*, 8(12), 2023.
- [106] Gregory H. James and Thomas G. Carne. The natural excitation technique for modal parameter extraction from operating wind turbines. Technical Report SAND95-2622, Sandia National Laboratories, 1995.
- [107] Peter Van Overschee and Bart De Moor. *Subspace Identification for Linear Systems*. Springer US, 1996.
- [108] R. Brincker, L. Zhang, and P. Andersen. Modal identification of output-only systems using frequency domain decomposition. *Smart Materials and Structures*, 10(3):441–445, 2001.
- [109] Gregory H. James, Thomas G. Carne, and Jon P. Lauffer. The natural excitation technique (next) for modal parameter extraction from operating structures. *Modal Analysis*, 10(4):260–277, 1993.
- [110] Edwin Reynders. Uncertainty quantification in operational modal analysis. *Mechanical Systems and Signal Processing*, 28:500–514, 2012.

## Bibliography

- [111] Bart Peeters and Guido De Roeck. Reference-based stochastic subspace identification for output-only modal analysis. *Mechanical Systems and Signal Processing*, 13(6):855–878, 1999.
- [112] Filipe Manuel Rodrigues Leite de Magalhães. *Operational modal analysis for testing and monitoring of bridges and special structures*. PhD thesis, Universidade do Porto (Portugal), 2010.
- [113] Christof Devriendt, Filipe Magalhães, Wout Weijtjens, Gert De Sitter, Álvaro Cunha, and Patrick Guillaume. Structural health monitoring of offshore wind turbines using automated operational modal analysis. *Structural Health Monitoring*, 13(6):644–659, 2014.
- [114] Carlo Rainieri and Giovanni Fabbrocino. Operational modal analysis of civil engineering structures. *Springer, New York*, 142:143, 2014.
- [115] Randall Allemang and Peter Avitabile. *Handbook of experimental structural dynamics*, 2022.
- [116] David J Ewins. *Modal testing: theory, practice and application*. John Wiley & Sons, 2009.
- [117] Bart Peeters and Herman Van Der Auweraer. Polymax: a revolution in operational modal analysis.
- [118] M. Böswald, D. Göge, U. Füllekrug, and Y. Govers. A review of experimental modal analysis methods with respect to their applicability to test data of large aircraft structures. In *Proceedings of ISMA2006: International Conference on Noise and Vibration Engineering*, volume 5, pages 2461–2482, 2006.
- [119] Kenneth G McConnell. *Vibration testing: theory and practice*. John Wiley & Sons, 1995.

## Bibliography

- [120] Kjær Brüel. Applicability limits of operational modal analysis to operational wind turbines. <https://www.bksv.com/doc/bn0923.pdf>, 2017.
- [121] RG Ni and RD Adams. The damping and dynamic moduli of symmetric laminated composite beams—theoretical and experimental results. *Journal of Composite Materials*, 18(2):104–121, 1984.
- [122] RD Adams and MR Maheri. Dynamic flexural properties of anisotropic fibrous composite beams. *Composites Science and Technology*, 50(4):497–514, 1994.
- [123] Jia-Lin Tsai and Nai-Ren Chang. 2-d analytical model for characterizing flexural damping responses of composite laminates. *Composite Structures*, 89(3):443–447, 2009.
- [124] Steven Eric Zeltmann, Keerthana A Prakash, Mrityunjay Doddamani, and Nikhil Gupta. Prediction of modulus at various strain rates from dynamic mechanical analysis data for polymer matrix composites. *Composites Part B: Engineering*, 120:27–34, 2017.
- [125] LibreTexts Team. Dynamic mechanical analysis (dma). <https://chem.libretexts.org>, 2024. Accessed: 2024-11-18.
- [126] Sudeshna Patra, Pulickel M Ajayan, and Tharangattu N Narayanan. Dynamic mechanical analysis in materials science: The novice’s tale. *Oxford Open Materials Science*, 1(1):itaa001, 2021.
- [127] Naheed Saba, Mohammad Jawaid, Othman Y Alothman, and MT Paridah. A review on dynamic mechanical properties of natural fibre reinforced polymer composites. *Construction and Building Materials*, 106:149–159, 2016.

## Bibliography

- [128] Sanjay Mavinkere Rangappa, Jyotishkumar Parameswaranpillai, Suchart Siengchin, and Sabu Thomas. *Handbook of Epoxy/Fiber Composites*. Springer, Singapore, 2022.
- [129] Somen K Bhudolia, Pavel Perrotey, and Sunil C Joshi. Enhanced vibration damping and dynamic mechanical characteristics of composites with novel pseudo-thermoset matrix system. *Composite Structures*, 179:502–513, 2017.
- [130] CSMF Costa, AC Fonseca, AC Serra, and JFJ Coelho. Dynamic mechanical thermal analysis of polymer composites reinforced with natural fibers. *Polymer Reviews*, 56(2):362–383, 2016.
- [131] Dharun Vadugappatty Srinivasan and Anastasios P. Vassilopoulos. Manufacturing and toughening effects on the material properties of wind turbine blade adhesives. *Polymer Testing*, 116:107770, 2022.
- [132] Mettler Toledo. *Thermal Analysis of Composites: Applications Handbook*, 2024. Accessed: October 24, 2024.
- [133] A.K. Saha, S. Das, D. Bhatta, and B.C. Mitra. Study of jute fiber reinforced polyester composites by dynamic mechanical analysis. *Journal of Applied Polymer Science*, 71:1505–1513, 1999.
- [134] F. Mortensen, P. Beran, and K. Parker. Analysis of properties of fiber composites with anisotropic stiffness and damping. *Journal of Applied Mechanics*, 46(3):543–548, 1979.
- [135] N. Rajini, J.T. Winowlin Jappes, P. Jeyaraj, S. Rajakarunakaran, and C. Bennet. Dynamic mechanical analysis and free vibration behavior in chemical modifications of coconut sheath/nano-clay reinforced hybrid polyester composite. *Journal of Composite Materials*, 47(24):3105–3121, 2013.

## Bibliography

- [136] Hongliang Yu, Jin Yan, and Hanlin Li. Study on the damping dynamics characteristics of a viscoelastic damping material. *Processes*, 10(4):635, 2022.
- [137] Pasakorn Sengsri, Chayut Ngamkhanong, Andre Luis Oliveira de Melo, and Sakdirat Kaewunruen. Experimental and numerical investigations into dynamic modal parameters of fiber-reinforced foamed urethane composite beams in railway switches and crossings. *Vibration*, 3(3):174–188, 2020.
- [138] Jeong-Ho Kim and GH Paulino. Isoparametric graded finite elements for nonhomogeneous isotropic and orthotropic materials. *J. Appl. Mech.*, 69(4):502–514, 2002.
- [139] William Finnegan, Yadong Jiang, Nicolas Dumergue, Peter Davies, and Jamie Goggins. Investigation and validation of numerical models for composite wind turbine blades. *Journal of Marine Science and Engineering*, 9(5):525, 2021.
- [140] JJ Aklonis and WJ MacKnight. Introduction to polymer viscoelasticity. 1983. *A Wiley-Interscience Publication: New York*, 2024.
- [141] J. D. Ferry. *Viscoelastic Properties of Polymers*. Wiley, New York, 2nd edition, 1965.
- [142] TA Instruments. *Dynamic Mechanical Analysis (DMA) Brochure*, 1976.
- [143] Dma: Applications in polymer composites. <https://ctherm.com/resources/webinars/dma-applications-in-polymer-composites/>, 2024. Accessed: October 24, 2024.
- [144] Gary Foster. What is dynamic mechanical analysis (dma)? <https://coventivecomposites.com/explainers/>

## Bibliography

- what-is-dynamic-mechanical-analysis-dma/, 2018. Accessed: October 24, 2024.
- [145] Dma testing | dynamic mechanical analysis | smithers. <https://www.smithers.com/services/testing/polymer/dma-testing>, 2024. Accessed: October 24, 2024.
- [146] Aggelos Koutsomichalis, Thomas Kalampoukas, and Dionysios E. Mouzakis. Mechanical testing and modeling of the time–temperature superposition response in hybrid fiber reinforced composites. *Polymers*, 13(7), 2021.
- [147] Stelios K. Georgantzinis, Georgios I. Giannopoulos, Konstantinos Stamoulis, and Stylianos Markolefas. Composites in aerospace and mechanical engineering. *Materials*, 16(22):7230, 2023.
- [148] TA Instruments. *DMA 850 Product Specifications*. Accessed: October 24, 2024.
- [149] Veryst Engineering. Dynamic mechanical analysis (dma). <https://www.veryst.com/services/testing/material-test-library/dynamic-mechanical-analysis-dma>, 2024. Accessed: October 24, 2024.
- [150] TA Instruments. *Introduction to Dynamic Mechanical Analysis and its Application to Testing of Polymer Solids*, 2024.
- [151] TA Instruments. *Q850 Dynamic Mechanical Analyzer (DMA) Brochure*, 2018. Accessed: 2024-11-18.
- [152] TA Instruments. *Q850 Dynamic Mechanical Analyzer: Getting Started Guide*, 2019. Accessed: 2024-11-18.

## Bibliography

- [153] F Duc, P. E. Bourban, and J.-A A.E. Månson. Damping performance of flax fibre composites. In *16th European Conference on Composite Materials, ECCM 2014*, pages 1–7, 2014.
- [154] Polymer Chemistry Characterization Lab. Dynamic mechanical analysis (dma). <https://pcc1.chem.ufl.edu/dma/>. Accessed: 2024-10-01.
- [155] Vikram K. Kinra and Alan Wolfenden. *M3D: Mechanics and Mechanisms of Material Damping*. ASTM International, West Conshohocken, PA, 1992.
- [156] MV Pathan, S Patsias, JA Rongong, and VL Tagarielli. Measurements and predictions of the viscoelastic properties of a composite lamina and their sensitivity to temperature and frequency. *Composites Science and Technology*, 149:207–219, 2017.
- [157] IMA Materialforschung und Anwendungstechnik GmbH. IMA Dresden: The Full Service Test Center. <https://www.ima-dresden.de/en/>. Accessed: 2024-07-30.
- [158] P. S. Valvo. The effects of shear on mode ii delamination: A critical review. *Frattura ed Integrità Strutturale*, 44:123–139, 2018.
- [159] Serge Abrate. Impact on laminated composite materials: recent advances. *Applied Mechanics Reviews*, 47(11):517–544, 1994.
- [160] Chiara Bisagni and Eduardo Catapano. Strain energy method to model composite structures damping. In *54th AIAA/ASME/ASCE/AHS/ASC Structures, Structural Dynamics, and Materials Conference*, 2013.
- [161] Mathias Kliem, Marvin Rüppel, Jan Høgsberg, Christian Berggreen, and Sina Baier. Damping properties of non-conductive composite materials

## Bibliography

- for applications in power transmission pylons. *Journal of Composite Materials*, 52:3601–3619, 11 2018.
- [162] Riccardo Vescovini. A procedure for the evaluation of damping effects in composite laminated structures. *Journal of Composite Structures*, X(Y):1–12, 2023.
- [163] ANSYS Inc. *ANSYS Contact Technology Guide: Contact Stiffness and Penetration*, 2009. Release 12.1 Documentation.
- [164] ASME. Standard for verification and validation in computational fluid dynamics and heat transfer. <https://www.asme.org/codes-standards/find-codes-standards/standard-for-verification-and-validation-in-computational-fluid-dynamics-2009>. ASME V&V 20-2009.
- [165] Matthias Klaerner, Mario Wuehrl, Lothar Kroll, and Steffen Marburg. Modelling and fea-simulation of the anisotropic damping of thermoplastic composites. *Advances in Aircraft and Spacecraft Science*, 3:331–349, 7 2016.
- [166] Łukasz Pyrzowski, Krzysztof Sobczyk, and Jacek Chróścielewski. Impact of boundary conditions on the behavior of thin-walled laminated angle column under uniform shortening. *Materials*, 14(11):2732, 2021.
- [167] J. Vanwalleghem, I. de Baere, M. Loccufier, and W. van Paepegem. External damping losses in measuring the vibration damping properties in lightly damped specimens using transient time-domain methods. *Journal of Sound and Vibration*, 333(6):1596–1611, 2014.
- [168] M. Rueppel, J. Rion, C. Dransfeld, C. Fischer, and K. Masania. Damping of carbon fibre and flax fibre angle-ply composite laminates. *Composites Science and Technology*, 146:1–9, 2017.

## Bibliography

- [169] C. A. Geweth, S. K. Baydoun, F. Saati, K. Sepahvand, and S. Marburg. Effect of boundary conditions in the experimental determination of structural damping. *Mechanical Systems and Signal Processing*, 146, 2021.
- [170] D. A. Pereira, T. A. M. Guimarães, H. B. Resende, and D. A. Rade. Numerical and experimental analyses of modal frequency and damping in tow-steered cfrp laminates. *Composite Structures*, 244, 2020.
- [171] DJ Ewins. Encyclopedia of vibration, mode of vibration, 2001.
- [172] SG Braun, DJ Ewins, Singiresu S Rao, and AW Leissa. Encyclopedia of vibration: Volumes 1, 2, and 3. *Appl. Mech. Rev.*, 55(3):B45–B45, 2002.
- [173] G. Wright. The dynamic properties of glass and carbon fibre reinforced plastic beams. *Journal of Sound and Vibration*, 21:205–212, 1972.
- [174] R. Adams and D. Bacon. Measurement of the flexural damping capacity and dynamic young's modulus of metals and reinforced plastics. *Journal of Physics D: Applied Physics*, 6:27–41, 1973.
- [175] R. Adams and D. Bacon. The dynamic properties of unidirectional fibre reinforced composites in flexure and torsion. *Journal of Composite Materials*, 7:53–67, 1973.
- [176] F. Guild and R. Adams. A new technique for the measurement of the specific damping capacity of beams in flexure. *Journal of Physics E: Scientific Instruments*, 14:355–363, 1981.
- [177] D. Lin, R. Ni, and R. Adams. Prediction and measurement of the vibrational damping parameters of carbon and glass fibre-reinforced plastics plates. *Journal of Composite Materials*, 18:132–152, 1984.

## Bibliography

- [178] S. Suarez, R. Gibson, and L. Deobald. Random and impulse techniques for measurements of damping in composite materials. *Experimental Techniques*, 8:19–24, 1984.
- [179] R. M. Crane and J. W. Gillespie. Damping loss factor determination of glass and graphite fiber composites. *David Taylor Research Center Technical Report*, 1989.
- [180] M. Maheri and R. Adams. Finite-element prediction of modal response of damped layered composite panels. *Composites Science and Technology*, 55:13–23, 1995.
- [181] C. Kyriazoglou and F. Guild. Finite element prediction of damping of composite gfrp and cfrp laminates a hybrid formulation vibration damping experiments and rayleigh damping. *Composites Science and Technology*, 66:487–498, 2006.
- [182] Sahar Hassani, Mohsen Mousavi, and Amir H. Gandomi. Structural health monitoring in composite structures: A comprehensive review. *Sensors*, 22(1), 2022.
- [183] Rachel Henderson, Fae Azhari, and Anthony Sinclair. Natural frequency transmissibility for detection of cracks in horizontal axis wind turbine blades. *Sensors*, 24(14):4456, 2024.
- [184] L. Tartibu M. Abdulraheem, A. Kilfoil. A simplified wind turbine blade crack identification using experimental modal analysis (ema). *International Journal of Renewable Energy Research (IJRER)*, 10(4):1223–1231, 2020.
- [185] X. Liu, L. Liu, and C. Liu. Review of the typical damage and damage-detection methods of large wind turbine blades. *MDPI Sensors*, 21(5):3542, 2023.

## Bibliography

- [186] R.D. Adams and D. Bacon. *Dynamic Testing of Materials and Structures*. Butterworth-Heinemann, Oxford, UK, 1973.
- [187] S. Gade. Operational modal analysis: Basics, examples, and exercises. *Brüel & Kjær Technical Review*, 2000.
- [188] Texas A&M University. *The Fundamentals of Modal Testing*.
- [189] M. El-Kafafy, P. Guillaume, B. Peeters, and P. Verboven. Polymax plus: An extension of the polymax algorithm. *Conference Proceedings of the Society for Experimental Mechanics Series*, pages 91–105, 2013.
- [190] G. H. James, T. G. Carne, and J. P. Lauffer. The natural excitation technique (next) for modal parameter extraction from operating wind turbines. Technical Report SAND2001-1767, Sandia National Laboratories, 2001.
- [191] Edwin Reynders, Mattias Schevenels, and Guido De Roeck. *MACEC 3.4 - The MATLAB Toolbox for Experimental and Operational Modal Analysis - User's Manual*. KU Leuven, Department of Civil Engineering, Structural Mechanics Section, 2021.
- [192] B. Peeters, H. Van der Auweraer, P. Guillaume, and G. De Roeck. The polymax frequency-domain method: A new standard for modal parameter estimation? *Shock and Vibration*, 11(3-4):395–409, 2004.
- [193] B. Peeters and G. De Roeck. Stochastic system identification for operational modal analysis: A review. *Journal of Dynamic Systems, Measurement, and Control*, 123(4):659–667, 2001.
- [194] D. J. Ewins. *Modal Testing: Theory, Practice and Application*. Research Studies Press, 2nd edition, 2000.

## Bibliography

- [195] M El-Kafafy, B Peeters, T De Troyer, and P Guillaume. Polymax plus estimator: better estimation of the modal parameters and their confidence bounds. In *Proceedings of international noise and vibration conference ISMA*, 2014.
- [196] Bart Peeters, Mahmoud El-kafafy, and Patrick Guillaume. The new polymax plus method: confident modal parameter estimation even in very noisy cases. In *Proceedings of the ISMA*, pages 2801–2813, 2012.
- [197] Bart Peeters, Geert Lowet, Herman Van der Auweraer, and Jan Leuridan. A new procedure for modal parameter estimation. *Sound and Vibration*, 38(1):24–29, 2004.
- [198] B. Peeters, P. Guillaume, P. Verboven, and H. Van der Auweraer. Polymax: A revolution in operational modal analysis. In *Proceedings of the 22nd International Modal Analysis Conference (IMAC)*, Dearborn, MI, USA, 2004.
- [199] Chang-Sheng Lin. Modified polymax for parametric estimation of structures with modal interference. *Proceedings*, 2(18):1077, 2018.
- [200] R. Brincker and C. Ventura. *Introduction to Operational Modal Analysis*. Wiley, 2015.
- [201] Vedran Tunukovic, Shaun McKnight, Ehsan Mohseni, S Gareth Pierce, Richard Pyle, Euan Duernberger, Charalampos Loukas, Randika KW Vithanage, David Lines, Gordon Dobie, et al. Automated deep learning for defect detection in carbon fibre reinforced plastic composites. In *50th Annual Review of Progress in Quantitative Nondestructive Evaluation*, 2023.
- [202] Euan Duernberger, Charles MacLeod, and Dave Lines. Fibre volume fraction screening of pultruded carbon fibre reinforced polymer panels

## Bibliography

based on analysis of anisotropic ultrasonic sound velocity. *Composites Part B: Engineering*, 254:110577, 2023.

- [203] Vedran Tunukovic, Shaun McKnight, Ehsan Mohseni, S Gareth Pierce, Richard Pyle, Euan Duernberger, Charalampos Loukas, Randika KW Vithanage, David Lines, Gordon Dobie, et al. A study of machine learning object detection performance for phased array ultrasonic testing of carbon fibre reinforced plastics. *NDT & E International*, 144:103094, 2024.
- [204] Euan Duernberger. *Advanced Non-Destructive Testing of Blade Manufacturing Defects*. Doctoral thesis, University of Strathclyde, 2023. Accessed: 29 October 2024.
- [205] NTI Audio. Fast fourier transformation fft - basics, 2022.
- [206] R.D. Adams and F. Guild. Modal testing of large structures in vacuum: A new approach. In *Proceedings of the 5th International Conference on Modal Analysis*, pages 108–115, 1984.
- [207] British Standard. Bs 5500, specification for unfired fusion welded pressure vessels, 1997.
- [208] National Instruments. Ni 9237 getting started guide, 2024. Accessed: November 11, 2024.
- [209] National Instruments. Connecting strain gauges to ni-9237 using accessories ni-9926/9944/9945, 2023. Accessed: November 11, 2024.

# Appendix A

## Derivations of Damping Models

### Matrix Definitions

**Q Matrix:** A stiffness matrix is used to describe the elastic behaviour of a ply under loading conditions. The reduced stiffness matrix is defined as:

$$Q_{ij} = \begin{bmatrix} Q_{11} & Q_{12} & 0 \\ Q_{12} & Q_{22} & 0 \\ 0 & 0 & Q_{66} \end{bmatrix} \quad (\text{A.1})$$

where:

$$Q_{11} = \frac{E_{11}}{1 - \nu_{12}^2 \frac{E_{22}}{E_{11}}}, \quad Q_{12} = \frac{\nu_{12} E_{11} E_{22}}{E_{11} - \nu_{12}^2 E_{22}}, \quad Q_{22} = \frac{E_{22}}{1 - \nu_{12}^2 \frac{E_{22}}{E_{11}}}, \quad Q_{66} = G_{12} \quad (\text{A.2})$$

To account for the fibre orientation angle  $\theta$  of a ply, the stiffness matrix must be transformed using the following expressions:

## Appendix A. Derivations of Damping Models

$$\begin{aligned}
\bar{Q}_{11} &= Q_{11} \cos^4(\theta) + 2(Q_{12} + 2Q_{66}) \cos^2(\theta) \sin^2(\theta) + Q_{22} \sin^4(\theta) \\
\bar{Q}_{12} &= Q_{12}(\cos^4(\theta) + \sin^4(\theta)) + (Q_{11} + Q_{22} - 4Q_{66}) \cos^2(\theta) \sin^2(\theta) \\
\bar{Q}_{16} &= (\bar{Q}_{11} - \bar{Q}_{12} - 2\bar{Q}_{66}) \cos^3(\theta) \sin(\theta) - (\bar{Q}_{22} - \bar{Q}_{12} - 2\bar{Q}_{66}) \cos(\theta) \sin^3(\theta) \\
\bar{Q}_{22} &= Q_{11} \sin^4(\theta) + 2(Q_{12} + 2Q_{66}) \cos^2(\theta) \sin^2(\theta) + Q_{22} \cos^4(\theta) \\
\bar{Q}_{26} &= (\bar{Q}_{11} - \bar{Q}_{12} - 2\bar{Q}_{66}) \cos(\theta) \sin^3(\theta) - (\bar{Q}_{22} - \bar{Q}_{12} - 2\bar{Q}_{66}) \cos^3(\theta) \sin(\theta) \\
\bar{Q}_{66} &= (Q_{11} + Q_{22} - 2Q_{12} - 2Q_{66}) \cos^2(\theta) \sin^2(\theta) + Q_{66}(\cos^4(\theta) + \sin^4(\theta))
\end{aligned} \tag{A.3}$$

This yields the transformed stiffness matrix:

$$\bar{Q}_{ij} = \begin{bmatrix} \bar{Q}_{11} & \bar{Q}_{12} & \bar{Q}_{16} \\ \bar{Q}_{12} & \bar{Q}_{22} & \bar{Q}_{26} \\ \bar{Q}_{16} & \bar{Q}_{26} & \bar{Q}_{66} \end{bmatrix} \tag{A.4}$$

**C Matrix:** The lamina stiffness matrix, involving engineering constants  $E_L$ ,  $E_T$ ,  $G_{LT}$ , and  $\nu_{LT}$ , is defined as:

$$C_{ij} = \begin{bmatrix} C_{11} & C_{12} & 0 \\ C_{12} & C_{22} & 0 \\ 0 & 0 & C_{66} \end{bmatrix} \tag{A.5}$$

where:

$$C_{11} = \frac{E_L}{1 - \nu_{LT}^2 \frac{E_T}{E_L}}, \quad C_{22} = \frac{E_T}{1 - \nu_{LT}^2 \frac{E_T}{E_L}}, \quad C_{12} = \nu_{LT} C_{22}, \quad C_{66} = G_{LT} \tag{A.6}$$

## Appendix A. Derivations of Damping Models

The normalised flexural compliance is given by:

$$C_{ij}^* = \frac{1}{D_{ij}^*} = C_{ij}h^* \quad (\text{A.7})$$

### Ni-Adams Model Derivation

In this derivation, two coordinate systems are used: the global coordinate system (e.g., 1-direction) and the fibre coordinate system (e.g., x-direction). It is crucial to distinguish between them. For instance, a ply oriented at 90 degrees relative to the global 1-axis has its stress in the transverse (y) direction, while a ply aligned with the global 1-axis shares the same orientation as the fibre x-axis.

Each ply in the laminate has its own stress and strain relationships, expressed using the constitutive equation:

$$\begin{bmatrix} \sigma_1 \\ \sigma_2 \\ \sigma_6 \end{bmatrix}_k = \begin{bmatrix} Q_{11} & Q_{12} & Q_{16} \\ Q_{12} & Q_{22} & Q_{26} \\ Q_{16} & Q_{26} & Q_{66} \end{bmatrix}_k \begin{bmatrix} \varepsilon_1 \\ \varepsilon_2 \\ \varepsilon_6 \end{bmatrix}_k \quad (\text{A.8})$$

where  $Q_{ij}$  are the stiffness matrix components for the  $k$ -th layer.

**Stress and Strain in the Fibre Coordinate System** For the  $k$ -th layer, the stress and strain in the fibre reference axis are:

$$\varepsilon_x^k = \frac{zM_x}{h^*}(c^2C_{11}^* + csC_{16}^*), \quad \sigma_x^k = \frac{zM_x}{h^*}c^2(Q_{11}^k C_{11}^* + Q_{12}^k C_{12}^* + Q_{16}^k C_{16}^*) \quad (\text{A.9})$$

## Appendix A. Derivations of Damping Models

$$\varepsilon_y^k = \frac{zM_x}{h^*}(s^2 C_{11}^* - cs C_{16}^*), \quad \sigma_y^k = \frac{zM_x}{h^*} s^2 (Q_{11}^k C_{11}^* + Q_{12}^k C_{12}^* + Q_{16}^k C_{16}^*) \quad (\text{A.10})$$

$$\gamma_{xy}^k = -\frac{zM_x}{h^*}(2cs C_{11}^* - (c^2 - s^2) C_{16}^*), \quad \sigma_{xy}^k = \frac{zM_x}{h^*}(-cs)(Q_{11}^k C_{11}^* + Q_{12}^k C_{12}^* + Q_{16}^k C_{16}^*) \quad (\text{A.11})$$

where  $c = \cos(\theta_k)$  and  $s = \sin(\theta_k)$ .

**Specific Damping Capacity (SDC)** According to the strain energy method, the specific damping capacity ( $\psi$ ) is the ratio of energy dissipation ( $\Delta U$ ) to the total energy stored ( $U$ ) in the material:

$$\psi = \frac{\Delta U}{U} = \psi_1 + \psi_2 + \psi_{12} \quad (\text{A.12})$$

The total energy dissipation per cycle is given by:

$$\Delta U = \Delta U_1 + \Delta U_2 + \Delta U_{12} \quad (\text{A.13})$$

**Energy Dissipation Derivation** The energy dissipation per cycle in the fibre direction is calculated as:

$$\Delta U_1 = 2\psi_L \int_0^{L/2} \int_0^{h/2} \sigma_x \varepsilon_x dz dx \quad (\text{A.14})$$

Substituting the stress and strain relations yields:

## Appendix A. Derivations of Damping Models

$$\Delta U_1 = \frac{2\psi_L}{(h^*)^2} \int_0^{L/2} M_x^2 dx \int_0^{h/2} [c^2(Q_{11}^k C_{11}^* + Q_{12}^k C_{12}^* + Q_{16}^k C_{16}^*)][(c^2 C_{11}^* + cs C_{16}^*)] z^2 dz \quad (\text{A.15})$$

**Total Strain Energy** The total strain energy stored in the composite is:

$$U = \int_0^{L/2} M_1 k_1 dx = \frac{C_{11}^*}{h^*} \int_0^{L/2} M_x^2 dx \quad (\text{A.16})$$

**SDC in the Fibre Direction** The specific damping capacity in the fibre direction is then:

$$\psi_1 = \frac{\Delta U_1}{U} = \frac{2\psi_L}{C_{11}^* h^*} \int_0^{h/2} [c^2(Q_{11}^k C_{11}^* + Q_{12}^k C_{12}^* + Q_{16}^k C_{16}^*)][(c^2 C_{11}^* + cs C_{16}^*)] z^2 dz \quad (\text{A.17})$$

By considering uniform lamina layers, the integration becomes a summation:

$$\psi_1 = \frac{8\psi_L}{(C_{11}^* N)^3} \sum_{k=1}^{N/2} [c^2(Q_{11}^k C_{11}^* + Q_{12}^k C_{12}^* + Q_{16}^k C_{16}^*)][(c^2 C_{11}^* + cs C_{16}^*)] W_k \quad (\text{A.18})$$

where  $W_k = k^3 - (k - 1)^3$ .

**Transverse and Shear Directions** Using similar derivations, the SDC in the transverse and in-plane shear directions can be expressed as:

$$\psi_2 = \frac{8\psi_T}{(C_{11}^* N)^3} \sum_{k=1}^{N/2} [s^2(Q_{11}^k C_{11}^* + Q_{12}^k C_{12}^* + Q_{16}^k C_{16}^*)][(s^2 C_{11}^* - cs C_{16}^*)] W_k \quad (\text{A.19})$$

## Appendix A. Derivations of Damping Models

$$\psi_{12} = \frac{8\psi_{LT}}{(C_{11}^*N)^3} \sum_{k=1}^{N/2} [cs(Q_{11}^k C_{11}^* + Q_{12}^k C_{12}^* + Q_{16}^k C_{16}^*)][(2csC_{11}^* - (c^2 - s^2)C_{16}^*)]W_k \quad (\text{A.20})$$

This derivation highlights the relationship between the stress-strain components in the fibre and global coordinates and how these contribute to the damping properties in different directions.

### Adams-Maheri Model Derivation

The Adams-Maheri model extends the prediction of damping by incorporating boundary conditions and transforming stress-strain relationships to account for various loading scenarios. The model utilises the transformation of stress and strain from the global coordinate system (e.g., 1-2) to the local fibre coordinate system (e.g., x-y). The transformed stress and strain relationships allow for a more accurate damping calculation, especially in anisotropic composite materials like those used in wind turbine blades.

**Transformation Relations** The transformation between the global and fibre coordinate systems is described by:

$$\{\sigma_i\} = [T_{ij}]_{\sigma} \{\sigma_{x,y}\}, \quad \{\varepsilon_i\} = [T_{ij}]_{\varepsilon} \{\varepsilon_{x,y}\} \quad (\text{A.21})$$

where:

$$\{\sigma_{x,y}\} = \begin{pmatrix} \sigma_x \\ \sigma_y \\ \sigma_{xy} \end{pmatrix}, \quad \{\varepsilon_{x,y}\} = \begin{pmatrix} \varepsilon_x \\ \varepsilon_y \\ \gamma_{xy} \end{pmatrix} \quad (\text{A.22})$$

## Appendix A. Derivations of Damping Models

The stress-strain relationship is given by:

$$\{\sigma_i\} = [Q_{ij}]\{\varepsilon_j\} \quad (\text{A.23})$$

The inverse transformations are:

$$\{\sigma_x\} = [T_{ij}]_{\sigma}^{-1}\{\sigma_i\}, \quad \{\varepsilon_x\} = [T_{ij}]_{\varepsilon}^{-1}\{\varepsilon_i\} \quad (\text{A.24})$$

**Off-Axis Stiffness Matrix** The off-axis stiffness matrix  $[Q_{ij}]$  can be defined in terms of the transformation matrices:

$$[Q_{ij}] = [T_{ij}]_{\sigma}[Q_{(x,y)}][T_{ij}]_{\varepsilon}^{-1} \quad (\text{A.25})$$

This allows for the derivation of the stress-strain relationship in the transformed coordinate system:

$$\{\sigma_i\} = [T_{ij}]_{\sigma}[Q_{(x,y)}][T_{ij}]_{\varepsilon}^{-1}\{\varepsilon_j\} \quad (\text{A.26})$$

**Strain Energy Method** According to the strain energy method, the specific damping capacity (SDC) is defined as the ratio of energy dissipation per cycle to the total stored energy:

$$\psi = \frac{\Delta U_x}{U} + \frac{\Delta U_y}{U} + \frac{\Delta U_{xy}}{U} \quad (\text{A.27})$$

For the damping in the fibre direction, the energy dissipation per cycle is:

$$\Delta U_x = \frac{1}{2} \int_v \psi_L \varepsilon_x \sigma_x dv \quad (\text{A.28})$$

Substituting the transformed components gives:

$$\Delta U_x = \frac{1}{2} \int_v \psi_L [[T_{ij}]_{\varepsilon}^{-1}\{\varepsilon_j\}][c^2 \sigma_1] dv \quad (\text{A.29})$$

## Appendix A. Derivations of Damping Models

Implementing  $\sigma_1 = [Q_{ij}^k]\{\varepsilon_j\}$ , we get:

$$\Delta U_x = \frac{1}{2} \int_v \psi_L [[T_{ij}]_\varepsilon^{-1} \{\varepsilon_j\}] [c^2 [Q_{ij}^k] \{\varepsilon_j\}] dv \quad (\text{A.30})$$

By further substituting  $\{\varepsilon_j\} = \{X_j\}z$ , the expression simplifies to:

$$\Delta U_x = \frac{1}{2} \int_v \psi_L [[T_{ij}]_\varepsilon^{-1} \{X_j\}z] [c^2 [Q_{ij}^k] \{X_j\}z] dv \quad (\text{A.31})$$

For a beam of unit width, this becomes:

$$\Delta U_x = 2 \int_0^{L/2} M_1^2 dx \int_0^{h/2} \psi_L [T_{ij}]_\varepsilon^{-1} [C_{ij}] [Q_{ij}^k] [C_{ij}] c^2 z^2 dz \quad (\text{A.32})$$

**Damping Equations** The derived specific damping capacity in the fibre direction is given by:

$$\psi_x = \frac{8\psi_L}{C_{11}^* N^3} \sum_{k=1}^{N/2} \left[ c^2 (c^2 C_{11}^* + s^2 C_{12}^* + cs C_{16}^*) \right] \times \left[ Q_{11}^k C_{11}^* + Q_{12}^k C_{12}^* + Q_{16}^k C_{16}^* \right] W_k \quad (\text{A.33})$$

Similarly, the damping capacities in the transverse and shear directions are:

$$\psi_y = \frac{8\psi_T}{C_{11}^* N^3} \sum_{k=1}^{N/2} \left[ s^2 (s^2 C_{11}^* + c^2 C_{12}^* - cs C_{16}^*) \right] \times \left[ Q_{11}^k C_{11}^* + Q_{12}^k C_{12}^* + Q_{16}^k C_{16}^* \right] W_k \quad (\text{A.34})$$

$$\psi_{xy} = \frac{8\psi_{LT}}{C_{11}^* N^3} \sum_{k=1}^{N/2} \left[ cs (2cs C_{11}^* - 2cs C_{12}^* - (c^2 - s^2) C_{16}^*) \right] \times \left[ Q_{11}^k C_{11}^* + Q_{12}^k C_{12}^* + Q_{16}^k C_{16}^* \right] W_k \quad (\text{A.35})$$

where  $c$  and  $s$  represent  $\cos(\theta)$  and  $\sin(\theta)$ , respectively, and  $W_k$  represents the weight factors for the summation.

## Tsai-Chang Model Derivation

The Tsai-Chang model extends the analysis of multi-layer composites, providing a more comprehensive estimation of damping properties by considering in-plane stress components. The model is particularly effective for complex layups where interactions between layers play a significant role.

**Energy Dissipation and Damping Capacities** The total energy dissipated by the material per cycle is expressed as the sum of contributions from the fibre direction, transverse direction, and in-plane shear:

$$\Delta U = \Delta U_1 + \Delta U_2 + \Delta U_{12} \quad (\text{A.36})$$

and the corresponding specific damping capacity (SDC) is given by:

$$\psi = \psi_1 + \psi_2 + \psi_{12} \quad (\text{A.37})$$

**Damping in Different Directions** The energy dissipated in each direction is calculated as:

$$\Delta U_1 = \frac{1}{2} \int_v \psi_L \varepsilon_1 \sigma_1 dv, \quad \Delta U_2 = \frac{1}{2} \int_v \psi_T \varepsilon_2 \sigma_2 dv, \quad \Delta U_{12} = \frac{1}{2} \int_v \psi_{LT} \gamma_{12} \sigma_{12} dv \quad (\text{A.38})$$

where  $\varepsilon_1$ ,  $\varepsilon_2$ , and  $\gamma_{12}$  are the strains, and  $\sigma_1$ ,  $\sigma_2$ , and  $\sigma_{12}$  are the stresses in the fibre, transverse, and shear directions, respectively.

**Transformation of Strains and Stresses** Using the coordinate transformation relations, the energy dissipation in the fibre direction can be

## Appendix A. Derivations of Damping Models

written as:

$$\Delta U_1 = \frac{1}{2} \int_v \psi_L \left[ c^2 \varepsilon_x + s^2 \varepsilon_y + cs \gamma_{xy} \right] \left[ c^2 \sigma_x + s^2 \sigma_y + 2cs \sigma_{xy} \right] dv \quad (\text{A.39})$$

with:

$$\varepsilon_x = z \frac{C_{11}^*}{h^*} M_x, \quad \sigma_x = \frac{zM_x}{h^*} \left( \bar{Q}_{11}^k C_{11}^* + \bar{Q}_{12}^k C_{12}^* + \bar{Q}_{16}^k C_{16}^* \right) \quad (\text{A.40})$$

$$\varepsilon_y = z \frac{C_{12}^*}{h^*} M_x, \quad \sigma_y = \frac{zM_x}{h^*} \left( \bar{Q}_{12}^k C_{11}^* + \bar{Q}_{22}^k C_{12}^* + \bar{Q}_{26}^k C_{16}^* \right) \quad (\text{A.41})$$

$$\gamma_{xy} = z \frac{C_{16}^*}{h^*} M_x, \quad \sigma_{xy} = \frac{zM_x}{h^*} \left( \bar{Q}_{16}^k C_{11}^* + \bar{Q}_{26}^k C_{12}^* + \bar{Q}_{66}^k C_{16}^* \right) \quad (\text{A.42})$$

**Damping Equations** The specific damping capacities in the different directions can be derived as:

$$\begin{aligned} \psi_1 = & \frac{8\psi_L}{C_{11}^* N^3} \sum_{k=1}^{N/2} \left[ c^2 C_{11}^* + s^2 C_{12}^* + cs C_{16}^* \right] \times \left[ c^2 (\bar{Q}_{11}^k C_{11}^* + \bar{Q}_{12}^k C_{12}^* + \bar{Q}_{16}^k C_{16}^*) \right. \\ & \left. + s^2 (\bar{Q}_{12}^k C_{11}^* + \bar{Q}_{22}^k C_{12}^* + \bar{Q}_{26}^k C_{16}^*) + 2cs (\bar{Q}_{16}^k C_{11}^* + \bar{Q}_{26}^k C_{12}^* + \bar{Q}_{66}^k C_{16}^*) \right] W_k \quad (\text{A.43}) \end{aligned}$$

$$\begin{aligned} \psi_2 = & \frac{8\psi_T}{C_{11}^* N^3} \sum_{k=1}^{N/2} \left[ s^2 C_{11}^* + c^2 C_{12}^* - cs C_{16}^* \right] \times \left[ s^2 (\bar{Q}_{11}^k C_{11}^* + \bar{Q}_{12}^k C_{12}^* + \bar{Q}_{16}^k C_{16}^*) \right. \\ & \left. + c^2 (\bar{Q}_{12}^k C_{11}^* + \bar{Q}_{22}^k C_{12}^* + \bar{Q}_{26}^k C_{16}^*) + 2cs (\bar{Q}_{16}^k C_{11}^* + \bar{Q}_{26}^k C_{12}^* + \bar{Q}_{66}^k C_{16}^*) \right] W_k \quad (\text{A.44}) \end{aligned}$$

$$\psi_{12} = \frac{8\psi_{LT}}{C_{11}^* N^3} \sum_{k=1}^{N/2} \left[ 2cs C_{11}^* - 2cs C_{12}^* - (c^2 - s^2) C_{16}^* \right] \times \left[ cs (\bar{Q}_{11}^k C_{11}^* + \bar{Q}_{12}^k C_{12}^* + \bar{Q}_{16}^k C_{16}^*) \right]$$

## Appendix A. Derivations of Damping Models

$$-cs(\bar{Q}_{12}^k C_{11}^* + \bar{Q}_{22}^k C_{12}^* + \bar{Q}_{26}^k C_{16}^*) - (c^2 - s^2)(\bar{Q}_{16}^k C_{11}^* + \bar{Q}_{26}^k C_{12}^* + \bar{Q}_{66}^k C_{16}^*)] W_k \quad (\text{A.45})$$

where  $c$  and  $s$  represent  $\cos(\theta)$  and  $\sin(\theta)$ , respectively, and  $\bar{Q}$  terms represent the transformed reduced stiffness matrix components of each layer  $k$ .

## Summary of Model Derivations

These models build upon foundational theories of composite material behaviour, each refining the approach to predict damping more accurately. The Ni-Adams model emphasises interlaminar effects, while the Adams-Maheri model refines boundary conditions. The Tsai-Chang model further advances the understanding of multi-layer, multi-orientation composites, providing a more comprehensive framework for estimating damping behaviour.

Including these derivations in the appendix provides a theoretical foundation for the models used in the analysis and design of wind turbine blades, ensuring that the detailed mathematical principles behind their application are accessible for future research and validation.

# Appendix B

## DMA Sample Dimensions

Table B.1: Summary of DMA0 Sample Dimensions

Sample	Length (mm)	Avg. Width (mm)	Width SD (mm)	Avg. Thickness (mm)	Thickness SD (mm)
DMA0_1.0mm_1	50	5.098	0.0114	1.010	0.0000
DMA0_1.0mm_2	50	5.132	0.0100	1.008	0.0045
DMA0_1.0mm_3	50	5.088	0.0000	1.010	0.0000
DMA0_1.5mm_1	50	5.100	0.0081	1.500	0.0000
DMA0_1.5mm_2	50	5.092	0.0081	1.500	0.0000
DMA0_1.5mm_3	50	5.078	0.0110	1.500	0.0000
DMA0_2.0mm_1	50	5.110	0.0000	2.000	0.0000
DMA0_2.0mm_2	50	5.124	0.0054	2.004	0.0045
DMA0_2.0mm_3	50	5.132	0.0054	2.000	0.0000
DMA0_2.5mm_1	50	5.104	0.0054	2.500	0.0000
DMA0_2.5mm_2	50	5.126	0.0054	2.492	0.0045
DMA0_2.5mm_3	50	5.120	0.0054	2.500	0.0000
DMA0_3.0mm_1	50	5.090	0.0000	3.010	0.0000
DMA0_3.0mm_2	50	5.084	0.0050	3.000	0.0000
DMA0_3.0mm_3	50	5.070	0.0000	3.008	0.0045
DMA0_3.5mm_1	50	5.090	0.0050	3.500	0.0000
DMA0_3.5mm_2	50	5.080	0.0000	3.500	0.0000
DMA0_3.5mm_3	50	5.072	0.0100	3.500	0.0000
DMA0_4.0mm_1	50	5.090	0.0000	3.990	0.0000
DMA0_4.0mm_2	50	5.104	0.0082	3.990	0.0000
DMA0_4.0mm_3	50	5.108	0.0100	3.990	0.0000
DMA0_4.5mm_1	50	5.092	0.0082	4.500	0.0000
DMA0_4.5mm_2	50	5.112	0.0100	4.500	0.0000
DMA0_4.5mm_3	50	5.096	0.0100	4.500	0.0000

Appendix B. DMA Sample Dimensions

Table B.2: Summary of DMA90 Sample Dimensions

Sample	Length (mm)	Avg. Width (mm)	Width SD (mm)	Avg. Thickness (mm)	Thickness SD (mm)
DMA90_1.0mm_1	50	5.124	0.0110	1.000	0.0045
DMA90_1.0mm_2	50	5.089	0.0052	1.004	0.0000
DMA90_1.0mm_3	50	5.113	0.0000	1.000	0.0000
DMA90_1.5mm_1	50	5.096	0.0074	1.500	0.0045
DMA90_1.5mm_2	50	5.109	0.0096	1.503	0.0000
DMA90_1.5mm_3	50	5.103	0.0081	1.500	0.0000
DMA90_2.0mm_1	50	5.118	0.0000	2.000	0.0045
DMA90_2.0mm_2	50	5.102	0.0056	2.002	0.0000
DMA90_2.0mm_3	50	5.117	0.0058	2.000	0.0000
DMA90_2.5mm_1	50	5.107	0.0054	2.500	0.0045
DMA90_2.5mm_2	50	5.121	0.0057	2.502	0.0000
DMA90_2.5mm_3	50	5.099	0.0050	2.500	0.0000
DMA90_3.0mm_1	50	5.105	0.0000	3.000	0.0045
DMA90_3.0mm_2	50	5.119	0.0051	3.002	0.0000
DMA90_3.0mm_3	50	5.111	0.0000	3.000	0.0000
DMA90_3.5mm_1	50	5.123	0.0052	3.500	0.0045
DMA90_3.5mm_2	50	5.120	0.0000	3.500	0.0000
DMA90_3.5mm_3	50	5.115	0.0102	3.500	0.0000
DMA90_4.0mm_1	50	5.114	0.0000	4.000	0.0045
DMA90_4.0mm_2	50	5.104	0.0081	4.000	0.0000
DMA90_4.0mm_3	50	5.108	0.0101	4.000	0.0000
DMA90_4.5mm_1	50	5.098	0.0080	4.500	0.0045
DMA90_4.5mm_2	50	5.112	0.0100	4.500	0.0000
DMA90_4.5mm_3	50	5.106	0.0102	4.500	0.0000

# Appendix C

## MATLAB Code: FEA 1-5 mm

### Sample Test

```
1 clc;
2 close all;
3 clear all;
4
5 tic
6
7 %% Setup
8 % Define the range and step for average thicknesses
9 min_thickness = 0.0001;
10 max_thickness = 0.0001;
11 thickness_step = 0.0001;
12
13 % Generate a vector of thicknesses from min_thickness to
    max_thickness with the specified step
14 average_thicknesses = min_thickness:thickness_step:max_thickness;
15 iterations = floor((max_thickness - min_thickness) /
    thickness_step) + 1;
16
17 % Initialize the progress bar
18 h = waitbar(0, 'Processing...');
19 aa = 0;
20
21 % Loop over the average thickness values
22 for i = min_thickness:thickness_step:max_thickness
```

## Appendix C. MATLAB Code: FEA 1-5 mm Sample Test

```
23     aa = aa + 1;
24
25     % Update the progress bar
26     waitbar((aa-1)/iterations, h, sprintf('Progress: %d/%d', aa
27         -1, iterations));
28
29     % Read in Baseline Text File
30
31     S = readlines('solid_detailed_script_DN_UD.txt');
32
33     % Define strain value
34     strainValue = 0.000100;    % x microstrain
35     S{19} = sprintf('*SET,STRAIN,%f', strainValue);    % Set
36         strain in ANSYS script
37     S{15} = sprintf('*SET,THK,%f', i);    %
38         Thickness sweep
39     S{25} = sprintf('*SET,Rotate,180');    % 0 for UD,
40         90 for transverse
41
42     % Save the modified script to a new file
43     filename_x = sprintf('TEST_Pause_%d.txt', aa);
44     fileID = fopen(filename_x, 'w');
45     if fileID == -1
46         error('Cannot open file for writing');
47     end
48     for k = 1:numel(S)
49         fprintf(fileID, '%s\n', S(k));
50     end
51     fclose(fileID);
52     fclose('all');
53
54     % Run ANSYS in batch mode
55     disp(['SET_ANS_CONSEC=YES&SET_ANSYS_LOCK=OFF&SET_
56         KMP_STACKSIZE=10240k&"C:\Program Files\ANSYS Inc\v231\
57         ansys\bin\winx64\ANSYS231"-b-np16-i', filename_x, '-
```



## Appendix C. MATLAB Code: FEA 1-5 mm Sample Test

```
74
75     %% Manual Strain Energy Calculation
76     Strain_Dens_11{aa,:} = (0.5*Stress_Input{aa,:}(:,2)).*
        Strain_Input{aa,:}(:,2);
77     Strain_Dens_22{aa,:} = (0.5*Stress_Input{aa,:}(:,3)).*
        Strain_Input{aa,:}(:,3);
78     Strain_Dens_12{aa,:} = (0.5*Stress_Input{aa,:}(:,4)).*
        Strain_Input{aa,:}(:,4);
79     Strain_Dens_13{aa,:} = (0.5*Stress_Input{aa,:}(:,5)).*
        Strain_Input{aa,:}(:,5);
80     Strain_Dens_23{aa,:} = (0.5*Stress_Input{aa,:}(:,6)).*
        Strain_Input{aa,:}(:,6);
81     Strain_Dens_33{aa,:} = (0.5*Stress_Input{aa,:}(:,7)).*
        Strain_Input{aa,:}(:,7);
82
83     Strain_Energy_11{aa,:} = Strain_Dens_11{aa,:}.*(Volume_M{aa
        ,:}(:,2));
84     Strain_Energy_22{aa,:} = Strain_Dens_22{aa,:}.*(Volume_M{aa
        ,:}(:,2));
85     Strain_Energy_12{aa,:} = Strain_Dens_12{aa,:}.*(Volume_M{aa
        ,:}(:,2));
86     Strain_Energy_13{aa,:} = Strain_Dens_13{aa,:}.*(Volume_M{aa
        ,:}(:,2));
87     Strain_Energy_23{aa,:} = Strain_Dens_23{aa,:}.*(Volume_M{aa
        ,:}(:,2));
88     Strain_Energy_33{aa,:} = Strain_Dens_33{aa,:}.*(Volume_M{aa
        ,:}(:,2));
89
90     Strain_Energy_11_TOT{aa,:} = sum(Strain_Energy_11{aa,:});
91     Strain_Energy_22_TOT{aa,:} = sum(Strain_Energy_22{aa,:});
92     Strain_Energy_12_TOT{aa,:} = sum(Strain_Energy_12{aa,:});
93     Strain_Energy_13_TOT{aa,:} = sum(Strain_Energy_13{aa,:});
94     Strain_Energy_23_TOT{aa,:} = sum(Strain_Energy_23{aa,:});
95     Strain_Energy_33_TOT{aa,:} = sum(Strain_Energy_33{aa,:});
```

## Appendix C. MATLAB Code: FEA 1-5 mm Sample Test

```

96
97 SEND_E_TOTAL_TOT{aa,:} = Strain_Energy_11_TOT{aa,:}(:,1) +
    ...
98                               Strain_Energy_22_TOT{aa,:}(:,1) +
    ...
99                               Strain_Energy_12_TOT{aa,:}(:,1) +
    ...
100                              Strain_Energy_13_TOT{aa,:}(:,1) +
    ...
101                              Strain_Energy_23_TOT{aa,:}(:,1) +
    ...
102                              Strain_Energy_33_TOT{aa,:}(:,1);
103
104 SE11_Perc{aa,:} = ((Strain_Energy_11_TOT{aa,:}) /
    SEND_E_TOTAL_TOT{aa,:}) * 100;
105 SE22_Perc{aa,:} = ((Strain_Energy_22_TOT{aa,:}) /
    SEND_E_TOTAL_TOT{aa,:}) * 100;
106 SE12_Perc{aa,:} = ((Strain_Energy_12_TOT{aa,:}) /
    SEND_E_TOTAL_TOT{aa,:}) * 100;
107 SE13_Perc{aa,:} = ((Strain_Energy_13_TOT{aa,:}) /
    SEND_E_TOTAL_TOT{aa,:}) * 100;
108 SE23_Perc{aa,:} = ((Strain_Energy_23_TOT{aa,:}) /
    SEND_E_TOTAL_TOT{aa,:}) * 100;
109 SE33_Perc{aa,:} = ((Strain_Energy_33_TOT{aa,:}) /
    SEND_E_TOTAL_TOT{aa,:}) * 100;
110
111 SENE_perc{aa,:} = [SE11_Perc{aa,:}, SE22_Perc{aa,:},
    SE12_Perc{aa,:}, ...
112                    SE13_Perc{aa,:}, SE23_Perc{aa,:},
    SE33_Perc{aa,:}];
113
114 min_strain_x{aa,:} = min(N_Strain{aa, 1}(:,2));
115 max_strain_x{aa,:} = max(N_Strain{aa, 1}(:,2));
116

```

## Appendix C. MATLAB Code: FEA 1-5 mm Sample Test

```
117     min_strain_x_ms{aa,:} = min(N_Strain{aa, 1}(:,2)) * 100000;
118     max_strain_x_ms{aa,:} = max(N_Strain{aa, 1}(:,2)) * 100000;
119
120     result_matrix(1,aa) = i;
121     result_matrix(2,aa) = SE11_Perc{aa};
122     result_matrix(3,aa) = SE22_Perc{aa};
123     result_matrix(4,aa) = SE12_Perc{aa};
124     result_matrix(5,aa) = SE13_Perc{aa};
125     result_matrix(6,aa) = SE23_Perc{aa};
126     result_matrix(7,aa) = SE33_Perc{aa};
127 end
128
129 % Close the progress bar
130 close(h);
131 toc
132
133 % Post-processing and plotting code continues here...
```

Listing C.1: MATLAB Code for FEA 1-5mm Sample Test

# Appendix D

## ANSYS APDL Code: Baseline Implementation

```
1  !%%ANSYS SCRIPT MODIFIED FOR DIRECT CONTACT BETWEEN BEAM AND
    SUPPORTS
2
3  /clear ,all
4
5  !/pnum ,line ,1
6  !/pnum ,area ,1
7  !/pnum ,volume ,1
8
9  /PREP7
10 /TITLE ,UD Carbon Coupon Analysis
11 *SET ,L ,64e-3
12 *SET ,LSUPP ,7e-3
13 *SET ,LSPAN ,L-(2*LSUPP)
14 *SET ,W ,5e-3
15 *SET ,THK ,0.004
16 *SET ,n1 ,4
17 *SET ,LT ,THK/n1
18 *SET ,ESIZE ,0.25e-3
19 *SET ,STRAIN ,0.000100
20 *SET ,Pois ,0.25
21 *SET ,CIRCR ,2e-3
22 *SET ,C_DISP ,(STRAIN*(LSPAN**2))/(12*THK)
23 *SET ,NSUBST ,5
```

## Appendix D. ANSYS APDL Code: Baseline Implementation

```
24 *SET,F_COEF,0.0001
25 *SET,Rotate,180
26
27 ! Define material properties - of Sample
28 MP,EX,1,XXXXXX
29 MP,EY,1,XXXXXX
30 MP,EZ,1,XXXXXX
31 MP,GXY,1,XXXXXX
32 MP,GYZ,1,XXXXXX
33 MP,GXZ,1,XXXXXX
34 MP,PRXY,1,XXXXXX
35 MP,PRYZ,1,XXXXXX
36 MP,PRXZ,1,XXXXXX
37 MP,DENS,1,XXXXXX
38 TREF,XXXXXX
39
40 ! Define material properties - nearly incompressible cylinder
41 MP,EX,2,2.1e12
42 MP,EY,2,2.1e12
43 MP,EZ,2,2.1e12
44 MP,GXY,2,1.05e12
45 MP,GYZ,2,1.05e12
46 MP,GXZ,2,1.05e12
47 MP,PRXY,2,0.4999
48 MP,PRYZ,2,0.4999
49 MP,PRXZ,2,0.4999
50 MP,DENS,2,1600
51
52 /VIEW,1,1,1,1
53
54 ! Element type for sample (Material 1)
55 ET,1,SOLID185
56 KEYOPT,1,2,2
57 KEYOPT,1,3,0
```

## Appendix D. ANSYS APDL Code: Baseline Implementation

```
58 KEYOPT,1,6,0
59
60 ! Element type for cylinders (Supports)
61 ET,2,SOLID187
62 KEYOPT,2,1,0
63 KEYOPT,2,2,0
64 KEYOPT,2,3,0
65 KEYOPT,2,9,0
66
67 ANTYPE,0
68
69 ! GEOMETRY BUILD (USING KEYPOINTS)
70 K,1,0,0,0
71 K,2,0,THK,0
72
73 ! CREATE LINES FOR CROSS SECTIONS
74 *SET,a,(n1+2)
75 l,1,2
76 ldiv,1,,,n1
77
78 k,a,0,0,W
79 l,1,a
80
81 ! CREATE AREAS (FROM GENERATED KEYPOINTS X-SECTIONS)
82 adrag,all,,,,,a-1
83
84 ! BUILD SINGLE LINE FOR SWEEP DISTANCE
85 ! CREATE LINES FOR DRAG
86 *SET,b,(n1+1)*2+1
87 k,(b+1),(L),0,0
88 l,1,(b+1)
89
90 ! BUILD TWO SPAN SUPPORTS AND ACTUATOR ARM (LINES + AREAS + SWEEP
    DISTANCE LINE)
```

## Appendix D. ANSYS APDL Code: Baseline Implementation

```
91
92 *GET ,Lnum ,Line ,0 ,num ,max
93 *GET ,Lnum1 ,Line ,0 ,num ,max
94
95 ! SUPPORT 1 - Adjusted for Direct Contact
96 k ,2000 ,LSUPP , -CIRCR ,0-1e-3
97 k ,2001 ,LSUPP , -CIRCR ,W-1e-3
98 CIRCLE ,2000 ,CIRCR ,2001
99 AL ,Lnum1+1 ,Lnum1+2 ,Lnum1+3 ,Lnum1+4
100 k ,2002 ,LSUPP , -CIRCR ,W+1e-3
101 l ,2000 ,2002
102
103 ! SUPPORT 2 - Adjusted for Direct Contact
104 k ,3000 ,L-LSUPP , -CIRCR ,0-1e-3
105 k ,3001 ,L-LSUPP , -CIRCR ,W-1e-3
106 CIRCLE ,3000 ,CIRCR ,3001
107 AL ,Lnum1+6 ,Lnum1+7 ,Lnum1+8 ,Lnum1+9
108 k ,3002 ,L-LSUPP , -CIRCR ,W+1e-3
109 l ,3000 ,3002
110
111 ! CENTRAL ACTUATOR CYLINDER
112 k ,4000 ,L/2 ,THK+CIRCR ,0-1e-3
113 k ,4001 ,L/2 ,THK+CIRCR ,W-1e-3
114 CIRCLE ,4000 ,CIRCR ,4001
115 AL ,Lnum1+11 ,Lnum1+12 ,Lnum1+13 ,Lnum1+14
116 k ,4002 ,L/2 ,THK+CIRCR ,W+1e-3
117 l ,4000 ,4002
118
119 ! SWEEP ALL AREAS INTO VOLUMES
120 ! SWEEP SAMPLE VOLUMES
121 LOCAL ,11 ,0 ,0 ,0 ,0 ,0 ,0 ,Rotate ! Rotate local coordinate system 90
    degrees about the Y-axis
122 CSYS ,11
123 ESYS ,11 ! Apply the local coordinate system to the elements
```

## Appendix D. ANSYS APDL Code: Baseline Implementation

```
124 ETYPE,1
125 Type,1
126 Mat,1
127 *SET,c,Lnum-2
128 *DO,kk,1,nl,1
129 vdrag,kk,,,,,Lnum
130 *ENDDO
131 ESYS,0 ! Revert to the global coordinate system
132 CSYS,0
133
134 ! Create volumes for supports
135 ETYPE,2
136 Type,2
137 Mat,2
138 vdrag,nl+1,,,,,Lnum1+5
139 vdrag,nl+2,,,,,Lnum1+10
140 vdrag,nl+3,,,,,Lnum1+15
141
142 ! Glue Sample Volumes
143 CSYS,11
144 ESYS,11 ! Apply the local coordinate system to the elements
145 ETYPE,1
146 Type,1
147 Mat,1
148 ALLSEL
149 vsel,s,LOC,Y,0,THK
150 vglu,all
151 ALLSEL
152 ESYS,0 ! Revert to the global coordinate system
153 CSYS,0
154
155 ! Meshing
156 CSYS,11
157 ESYS,11 ! Apply the local coordinate system to the elements
```

## Appendix D. ANSYS APDL Code: Baseline Implementation

```
158 ALLSEL
159 esize,(ESIZE)
160 vsel,s,LOC,Y,0,THK
161 vmesh,all
162 ALLSEL
163 ESYS,0 ! Revert to the global coordinate system
164 CSYS,0
165
166 ! Mesh support volumes - cylinders
167 ETYPE,2
168 TYPE,2
169 MAT,2
170 esize,(ESIZE)
171 VMESH,N1+1,N1+3,1
172
173 /REP,FAST
174 /replot
175
176 !Apply Boundary Conditions
177
178 ! Z-SUPPORT AT FIRST SUPPORT LINE (APPLIED TO SAMPLE) - Adjusted
179 ALLSEL
180 VSEL,S,VOLU,,1
181 *DO,kk,n1+4,n1+6,1
182     VSEL,A,VOLU,,kk
183 *ENDDO
184 NSLV,S,1
185 NSEL,r,LOC,X,LSUPP-(ESIZE/2),LSUPP+(ESIZE/2)
186 NSEL,r,LOC,Y,0,(ESIZE/2)
187 NSEL,r,LOC,Z,0-(ESIZE/2),0+(ESIZE/2)
188 D,ALL,UZ,0
189
190 ! Z-SUPPORT AT SECOND SUPPORT LINE (APPLIED TO SAMPLE) - Adjusted
191 ALLSEL
```

## Appendix D. ANSYS APDL Code: Baseline Implementation

```
192 VSEL , S , VOLU , , 1
193 *DO , kk , n1+4 , n1+6 , 1
194     VSEL , A , VOLU , , kk
195 *ENDDO
196 NSLV , S , 1
197 NSEL , r , LOC , X , L-LSUPP-(ESIZE/2) , L-LSUPP+(ESIZE/2)
198 NSEL , r , LOC , Y , 0 , (ESIZE/2)
199 NSEL , r , LOC , Z , 0-(ESIZE/2) , 0+(ESIZE/2)
200 D , ALL , UZ , 0
201
202 ! X-SUPPORT AT MID SECTION A (APPLIED TO SAMPLE)
203 ALLSEL
204 VSEL , S , VOLU , , 1
205 *DO , kk , n1+4 , n1+6 , 1
206     VSEL , A , VOLU , , kk
207 *ENDDO
208 NSLV , S , 1
209 NSEL , r , LOC , X , L/2-(ESIZE/2) , (L/2)+(ESIZE/2)
210 NSEL , r , LOC , Y , (THK/2)-(ESIZE/2) , (THK/2)+(ESIZE/2)
211 NSEL , r , LOC , Z , -(ESIZE/2) , (ESIZE/2)
212 D , ALL , UX , 0
213
214 ! X-SUPPORT AT MID SECTION B (APPLIED TO SAMPLE)
215 ALLSEL
216 VSEL , S , VOLU , , 1
217 *DO , kk , n1+4 , n1+6 , 1
218     VSEL , A , VOLU , , kk
219 *ENDDO
220 NSLV , S , 1
221 NSEL , r , LOC , X , L/2-(ESIZE/2) , (L/2)+(ESIZE/2)
222 NSEL , r , LOC , Y , (THK/2)-(ESIZE/2) , (THK/2)+(ESIZE/2)
223 NSEL , r , LOC , Z , W-(ESIZE/2) , W+(ESIZE/2)
224 D , ALL , UX , 0
225
```

## Appendix D. ANSYS APDL Code: Baseline Implementation

```
226 ! APPLY SUPPORT TO SPAN SUPPORTS (SUPPORT 1)
227 ALLSEL
228 VSEL,S,VOLU,,n1+1
229 NSLV,S,VOLU
230 NSEL,r,LOC,X,LSUPP-(ESIZE/4),LSUPP+(ESIZE/4)
231 NSEL,r,LOC,Y,-CIRCR-(ESIZE/4),-CIRCR+(ESIZE/4)
232 D,ALL,UX,0
233 D,ALL,UY,0
234 D,ALL,UZ,0
235
236 ! APPLY SUPPORTS TO SPAN SUPPORTS (SUPPORT 2)
237 ALLSEL
238 VSEL,A,VOLU,,n1+2
239 NSLV,S,VOLU
240 NSEL,r,LOC,X,L-LSUPP-(ESIZE/4),L-LSUPP+(ESIZE/4)
241 NSEL,r,LOC,Y,-CIRCR-(ESIZE/4),-CIRCR+(ESIZE/4)
242 D,ALL,UX,0
243 D,ALL,UY,0
244 D,ALL,UZ,0
245
246 ! APPLY DISPLACEMENT TO CENTRAL CYLINDER
247 ALLSEL
248 VSEL,A,VOLU,,n1+3
249 NSLV,S,VOLU
250 NSEL,r,LOC,Y,THK+CIRCR-(ESIZE/2),THK+CIRCR+(ESIZE/2)
251 NSEL,r,LOC,X,(L/2)-(ESIZE/2),(L/2)+(ESIZE/2)
252 D,ALL,UX,0
253 D,ALL,UZ,0
254 D,ALL,UY,-C_DISP
255
256 !-----
257 ! Creating contact pairs
258
259 ! Define contact manager for various entities
```

## Appendix D. ANSYS APDL Code: Baseline Implementation

```
260 CM,_CONTACT,AREA
261 /COM, CONTACT PAIR CREATION - START
262 CM,_NODECM,NODE
263 CM,_ELEMCM,ELEM
264 CM,_KPCM,KP
265 CM,_LINECM,LINE
266 CM,_AREACM,AREA
267 CM,_VOLUCM,VOLU
268
269 ! Save current graphic settings
270 /GSAV,cwz,gsav,,temp
271
272 ! Define material properties and element types
273 MP,MU,1,F_COEF
274 MAT,1
275 R,3
276 REAL,3
277 ET,3,170
278 ET,4,174
279 KEYOPT,4,9,0
280 KEYOPT,4,10,0
281 R,3,
282 RMORE,
283 RMORE,,0
284 RMORE,0
285
286 ! Generate the target surface (Bottom Supports)
287 ALLSEL
288 ASEL,S,LOC,Y,-CIRCR,-(ESIZE/4)
289
290 ! Assign target surface to a component
291 CM,_TARGET,AREA
292
293 ! Define element type and real constant for target surface
```

## Appendix D. ANSYS APDL Code: Baseline Implementation

```
294 TYPE , 3
295 NSLA , S , 1
296 ESLN , S , 0
297 ESLL , U
298 ESEL , U , ENAME , , 188 , 189
299 NSLE , A , CT2
300
301 ! Create target surface elements
302 ESURF
303
304 ! Remove target elements from _ELEMCM
305 CMSEL , S , _ELEMCM
306
307 ! Generate the contact surface (Bottom of sample)
308 ALLSEL
309 ASEL , S , LOC , Y , -(ESIZE/4) , (ESIZE/4)
310
311 ! Assign contact surface to a component
312 CM , _CONTACT , AREA
313
314 ! Define element type and real constant for contact surface
315 TYPE , 4
316 NSLA , S , 1
317 ESLN , S , 0
318 NSLE , A , CT2
319 ! Create contact surface elements
320 ESURF
321
322 ! Clear all selections
323 ALLSEL
324
325 ! Plot the created contact and target surfaces
326 ESEL , ALL
327 ESEL , S , TYPE , , 3
```

## Appendix D. ANSYS APDL Code: Baseline Implementation

```
328 ESEL , A , TYPE , , 4
329 ESEL , R , REAL , , 3
330 /PSYMB , ESYS , 1
331 /PNUM , TYPE , 1
332 /NUM , 1
333 EPLOTT
334
335 ! Clean up the unnecessary components
336 ESEL , ALL
337 ESEL , S , TYPE , , 3
338 ESEL , A , TYPE , , 4
339 ESEL , R , REAL , , 3
340 CMSEL , A , _NODECM
341 CMDEL , _NODECM
342 CMSEL , A , _ELEMCM
343 CMDEL , _ELEMCM
344 CMSEL , S , _KPCM
345 CMDEL , _KPCM
346 CMSEL , S , _LINECM
347 CMDEL , _LINECM
348 CMSEL , S , _AREACM
349 CMDEL , _AREACM
350 CMSEL , S , _VOLUCM
351 CMDEL , _VOLUCM
352
353 ! Restore graphic settings
354 /GRES , cwz , gsav
355
356 ! Delete the _TARGET and _CONTACT components
357 CMDEL , _TARGET
358 CMDEL , _CONTACT
359
360 /COM , CONTACT PAIR CREATION - END
361
```

## Appendix D. ANSYS APDL Code: Baseline Implementation

```
362 !-----
363 ! Creating the second contact pair
364
365 ! Define contact manager for various entities
366 CM,_TARGET,AREA
367 /COM, CONTACT PAIR CREATION - START
368 CM,_NODECM,NODE
369 CM,_ELEMCM,ELEM
370 CM,_KPCM,KP
371 CM,_LINECM,LINE
372 CM,_AREACM,AREA
373 CM,_VOLUCM,VOLU
374
375 ! Save current graphic settings
376 /GSAV,cwz,gsav,,temp
377
378 ! Define material properties and element types
379 MP,MU,1,F_COEF
380 MAT,1
381 R,4
382 REAL,4
383 ET,5,170
384 ET,6,174
385 KEYOPT,6,9,0
386 KEYOPT,6,10,0
387 R,4,
388 RMORE,
389 RMORE,,0
390 RMORE,0
391
392 ! Generate the target surface (Top Central Cylinder)
393 ALLSEL
394 ASEL,S,LOC,Y,THK+(ESIZE/4),THK+CIRCR
395 ! Assign target surface to a component
```

## Appendix D. ANSYS APDL Code: Baseline Implementation

```
396 CM, _TARGET, AREA
397
398 ! Define element type and real constant for target surface
399 TYPE, 5
400 NSLA, S, 1
401 ESLN, S, 0
402 ESLL, U
403 ESEL, U, ENAME, , 188, 189
404 NSLE, A, CT2
405
406 ! Create target surface elements
407 ESURF
408
409 ! Remove target elements from _ELEMCM
410 CMSEL, S, _ELEMCM
411
412 ! Generate the contact surface (Top of Sample)
413 ALLSEL
414 ASEL, S, LOC, Y, THK-(ESIZE/4), THK+(ESIZE/4)
415 ! Assign contact surface to a component
416 CM, _CONTACT, AREA
417
418 ! Define element type and real constant for contact surface
419 TYPE, 6
420 NSLA, S, 1
421 ESLN, S, 0
422 NSLE, A, CT2
423 ! Create contact surface elements
424 ESURF
425
426 ! Clear all selections
427 ALLSEL
428
429 ! Plot the created contact and target surfaces
```

## Appendix D. ANSYS APDL Code: Baseline Implementation

```
430 ESEL , ALL
431 ESEL , S , TYPE , , 5
432 ESEL , A , TYPE , , 6
433 ESEL , R , REAL , , 4
434 /PSYMB , ESYS , 1
435 /PNUM , TYPE , 1
436 /NUM , 1
437 EPLOTT
438
439 ! Clean up the unnecessary components
440 ESEL , ALL
441 ESEL , S , TYPE , , 5
442 ESEL , A , TYPE , , 6
443 ESEL , R , REAL , , 4
444 CMSEL , A , _NODECM
445 CMDEL , _NODECM
446 CMSEL , A , _ELEMCM
447 CMDEL , _ELEMCM
448 CMSEL , S , _KPCM
449 CMDEL , _KPCM
450 CMSEL , S , _LINECM
451 CMDEL , _LINECM
452 CMSEL , S , _AREACM
453 CMDEL , _AREACM
454 CMSEL , S , _VOLUCM
455 CMDEL , _VOLUCM
456
457 ! Restore graphic settings
458 /GRES , cwz , gsav
459
460 ! Delete the _TARGET and _CONTACT components
461 CMDEL , _TARGET
462 CMDEL , _CONTACT
463
```

## Appendix D. ANSYS APDL Code: Baseline Implementation

```
464 /COM, CONTACT PAIR CREATION - END
465
466 ! Start solution phase
467 /SOL
468 TIME,1
469 NLGEOM,1
470 KBC,0
471 !NSUBST,30,100,30
472 autots,on
473 OUTRES,ERASE
474 OUTRES,ALL,ALL
475
476 ! Solve
477 FINI
478 /SOLU
479 SOLVE
480 FINI
481
482 !-----
483 ! POSTPROCESS
484 /POST1
485 ALLSEL
486 RSYS,SOLU
487 SET,LAST
488
489 ! LOOP FOR OUTPUTS
490 aa=-LT
491 bb=0
492 *DO,IL,0,nl,1
493     ALLSEL
494     rsys,solu
495     esel,s,CENT,Y,aa,bb
496     /HEAD,off,off,off,off,off,off
497     ! Strain
```

## Appendix D. ANSYS APDL Code: Baseline Implementation

```
498     ETABLE , VOLUME , VOLU
499     ETABLE , E11 , EPT0 , X
500     ETABLE , E22 , EPT0 , Y
501     ETABLE , E12 , EPT0 , XY
502     ETABLE , E13 , EPT0 , XZ
503     ETABLE , E23 , EPT0 , YZ
504     ETABLE , E33 , EPT0 , Z
505     ! Stress
506     ETABLE , S11 , S , X
507     ETABLE , S22 , S , Y
508     ETABLE , S12 , S , XY
509     ETABLE , S13 , S , XZ
510     ETABLE , S23 , S , YZ
511     ETABLE , S33 , S , Z
512     ! Strain Energy Density
513     ETABLE , SENDA11 , SEND , ELASTIC , X
514     ETABLE , SENDA22 , SEND , ELASTIC , Y
515     ETABLE , SENDA12 , SEND , ELASTIC , XY
516     ETABLE , SENDA13 , SEND , ELASTIC , XZ
517     ETABLE , SENDA23 , SEND , ELASTIC , YZ
518     ETABLE , SENDA33 , SEND , ELASTIC , Z
519     /output , Volume_L_%IL% , txt
520     /Format , 6 , , 20 , 8 , , 240
521     PRETAB , Volume
522     /output
523     /output , Strain_L_%IL% , txt
524     /Format , 6 , , 20 , 8 , , 240
525     PRETAB , E11 , E22 , E12 , E13 , E23 , E33
526     /output
527     /output , Stress_L_%IL% , txt
528     /Format , 6 , , 20 , 10 , , 240
529     PRETAB , S11 , S22 , S12 , S13 , S23 , S33
530     /output
531     /output , StrainDout_L_%IL% , txt
```

## Appendix D. ANSYS APDL Code: Baseline Implementation

```
532 /Format ,6 , ,20 ,10 , ,240
533 PRETAB ,SENDA11 ,SENDA12 ,SENDA22 ,SENDA13 ,SENDA23 ,SENDA33
534 /output
535 aa=aa+LT
536 bb=bb+LT
537 *ENDDO
538
539 ALLSEL
540 ESEL ,TYPE ,1
541 rsys ,solu
542 /HEAD ,off ,off ,off ,off ,off ,off
543 ! Strain
544 ETABLE ,VOLUMET ,VOLU
545 ETABLE ,E11T ,EPT0 ,X
546 ETABLE ,E22T ,EPT0 ,Y
547 ETABLE ,E12T ,EPT0 ,XY
548 ETABLE ,E13T ,EPT0 ,XZ
549 ETABLE ,E23T ,EPT0 ,YZ
550 ETABLE ,E33T ,EPT0 ,Z
551 ! Stress
552 ETABLE ,S11T ,S ,X
553 ETABLE ,S22T ,S ,Y
554 ETABLE ,S12T ,S ,XY
555 ETABLE ,S13T ,S ,XZ
556 ETABLE ,S23T ,S ,YZ
557 ETABLE ,S33T ,S ,Z
558 ! Strain Energy Density
559 ETABLE ,SENDA11T ,SEND ,ELASTIC ,X
560 ETABLE ,SENDA22T ,SEND ,ELASTIC ,Y
561 ETABLE ,SENDA12T ,SEND ,ELASTIC ,XY
562 ETABLE ,SENDA13T ,SEND ,ELASTIC ,XZ
563 ETABLE ,SENDA23T ,SEND ,ELASTIC ,YZ
564 ETABLE ,SENDA33T ,SEND ,ELASTIC ,Z
565 /output ,Volume_VOLUME_TOT ,txt
```

## Appendix D. ANSYS APDL Code: Baseline Implementation

```
566 /Format ,6 , ,20,8 , ,240
567 PRETAB ,VOLUMET
568 /output
569 /output ,Strain_VOLUME_TOT ,txt
570 /Format ,6 , ,20,8 , ,240
571 PRETAB ,E11T ,E22T ,E12T ,E13T ,E23T ,E33T
572 /output
573 /output ,Stress_VOLUME_TOT ,txt
574 /Format ,6 , ,20,10 , ,240
575 PRETAB ,S11T ,S22T ,S12T ,S13T ,S23T ,S33T
576 /output
577 /output ,StrainDout_VOLUME_TOT ,txt
578 /Format ,6 , ,20,10 , ,240
579 PRETAB ,SENDA11T ,SENDA12T ,SENDA22T ,SENDA13T ,SENDA23T ,SENDA33T
580 /output
581
582 NSOL ,2,ALL,U,X ! Extract nodal displacement in X-direction
583 NSOL ,3,ALL,U,Y ! Extract nodal displacement in Y-direction
584 NSOL ,4,ALL,U,Z ! Extract nodal displacement in Z-direction
585 PRNSOL ,U ! Print nodal displacement results
586
587 NSOL ,5,ALL,EPTO,X ! Extract nodal strain in X-direction
588 NSOL ,6,ALL,EPTO,Y ! Extract nodal strain in Y-direction
589 NSOL ,7,ALL,EPTO,Z ! Extract nodal strain in Z-direction
590 NSOL ,8,ALL,EPTO,XY ! Extract nodal strain in XY-plane
591 NSOL ,9,ALL,EPTO,YZ ! Extract nodal strain in YZ-plane
592 NSOL ,10,ALL,EPTO,XZ ! Extract nodal strain in XZ-plane
593 PRNSOL ,EPTO ! Print nodal strain results
594
595 /OUTPUT ,Nodal_Strain ,txt
596 PRNSOL ,EPTO
597 /OUTPUT
598
599 NSOL ,5,ALL,EPTOX,X ! Extract nodal strain in X-direction
```

## Appendix D. ANSYS APDL Code: Baseline Implementation

```
600 /OUTPUT ,Nodal_Strain_x ,txt
601 PRNSOL ,EPTOX
602 /OUTPUT
603
604 FINI
```

Listing D.1: ANSYS APDL Code Modified for Direct Contact Between Beam and Supports

# Appendix E

## Strain Energy Study

Table E.1: UD Test - Strain values and corresponding displacements for different microstrains and selected thicknesses.

Thickness (mm)	0.50	1.00	1.50	2.00	2.50	3.00	3.50	4.00	4.50	5.00
<b>Span (mm)</b>	50									
<b>Microstrain</b>	50									
$U_{11}\%$	99.532	98.278	96.249	93.385	89.808	85.602	80.938	75.942	70.811	65.615
$U_{22} + U_{33}\%$	0.040	0.067	0.158	0.384	0.789	1.389	2.213	3.234	4.462	5.845
$U_{12} + U_{13}\%$	0.429	1.655	3.593	6.230	9.403	13.009	16.849	20.825	24.727	28.540
Displacement ( $\mu\text{m}$ )	20.83	10.42	6.94	5.21	4.17	3.47	2.98	2.60	2.31	2.08
<b>Microstrain</b>	100									
$U_{11}\%$	99.531	98.277	96.248	93.384	89.807	85.600	80.934	75.937	70.805	65.608
$U_{22} + U_{33}\%$	0.040	0.067	0.158	0.385	0.790	1.390	2.215	3.236	4.466	5.849
$U_{12} + U_{13}\%$	0.429	1.655	3.593	6.231	9.404	13.010	16.851	20.827	24.729	28.543
Displacement ( $\mu\text{m}$ )	41.67	20.83	13.89	10.42	8.33	6.94	5.95	5.21	4.63	4.17
<b>Microstrain</b>	150									
$U_{11}\%$	99.531	98.277	96.248	93.384	89.807	85.600	80.935	75.938	70.807	65.611
$U_{22} + U_{33}\%$	0.040	0.067	0.158	0.385	0.789	1.390	2.214	3.235	4.465	5.848
$U_{12} + U_{13}\%$	0.429	1.655	3.593	6.231	9.403	13.010	16.850	20.826	24.728	28.542
Displacement ( $\mu\text{m}$ )	62.50	31.25	20.83	15.63	12.50	10.42	8.93	7.74	6.94	6.25
<b>Microstrain</b>	200									
$U_{11}\%$	99.531	98.277	96.248	93.384	89.806	85.599	80.934	75.937	70.805	65.608
$U_{22} + U_{33}\%$	0.040	0.067	0.158	0.385	0.790	1.390	2.215	3.236	4.466	5.849
$U_{12} + U_{13}\%$	0.429	1.655	3.593	6.231	9.404	13.010	16.851	20.827	24.729	28.543
Displacement ( $\mu\text{m}$ )	83.33	41.67	27.78	20.83	16.67	13.89	11.90	10.42	9.26	8.33
<b>Microstrain</b>	250									
$U_{11}\%$	99.531	98.277	96.248	93.384	89.806	85.599	80.933	75.935	70.804	65.606
$U_{22} + U_{33}\%$	0.040	0.068	0.158	0.385	0.790	1.391	2.216	3.237	4.467	5.850
$U_{12} + U_{13}\%$	0.429	1.655	3.593	6.231	9.404	13.011	16.851	20.827	24.730	28.543
Displacement ( $\mu\text{m}$ )	104.17	52.08	34.72	26.04	20.83	17.36	14.88	13.02	11.57	10.42

\* For thicknesses  $\geq 5$  mm, Eq. 3.7 is said to be more appropriate than the one used for these data.

# Appendix F

## Equation Derivation

In this appendix, we derive the equation for  $\delta$  in terms of  $\epsilon_x$ ,  $L$ ,  $t$ , and  $\nu$ .

Starting with the original TA provided equation:

$$\epsilon_x = \frac{6\delta t}{2L^2 \left[ 1 + \frac{6}{10}(1 + \nu) \left( \frac{t}{L} \right)^2 \right]} \quad (\text{F.1})$$

To align with the FEA framework, where  $L$  represents the full span, this equation is rewritten as:

$$\epsilon_x = \frac{3\delta t}{\left( \frac{L}{2} \right)^2 \left[ 1 + \frac{3}{5}(1 + \nu) \left( \frac{2t}{L} \right)^2 \right]} \quad (\text{F.2})$$

Multiplying through by the denominator to eliminate the fraction gives:

$$\epsilon_x \left( \frac{L}{2} \right)^2 \left[ 1 + \frac{3}{5}(1 + \nu) \left( \frac{2t}{L} \right)^2 \right] = 3\delta t \quad (\text{F.3})$$

Squaring  $\frac{L}{2}$  gives  $\frac{L^2}{4}$ , which is then distributed within the bracket:

$$\epsilon_x \frac{L^2}{4} \left[ 1 + \frac{3}{5}(1 + \nu) \left( \frac{4t^2}{L^2} \right) \right] = 3\delta t \quad (\text{F.4})$$

## Appendix F. Equation Derivation

Expanding the terms inside the bracket results in:

$$\epsilon_x \frac{L^2}{4} \left[ 1 + \frac{12t^2(1 + \nu)}{5L^2} \right] = 3\delta t \quad (\text{F.5})$$

Distributing  $\frac{L^2}{4}$  across the terms in the bracket yields:

$$\epsilon_x \left[ \frac{L^2}{4} + \frac{12t^2(1 + \nu)}{20} \right] = 3\delta t \quad (\text{F.6})$$

Dividing through by  $3t$  isolates  $\delta$ :

$$\epsilon_x \left[ \frac{L^2}{12t} + \frac{12t(1 + \nu)}{60} \right] = \delta \quad (\text{F.7})$$

Finding a common denominator for the terms inside the bracket gives:

$$\epsilon_x \left[ \frac{5L^2}{60t} + \frac{12t(1 + \nu)}{60} \right] = \delta \quad (\text{F.8})$$

Combining the terms results in:

$$\epsilon_x \left[ \frac{5L^2 + 12t^2(1 + \nu)}{60t} \right] = \delta \quad (\text{F.9})$$

Finally, simplifying gives the expression for  $\delta$ :

$$\delta = \epsilon_x \frac{5L^2 + 12t^2(1 + \nu)}{60t} \quad (\text{F.10})$$

This equation expresses  $\delta$  in terms of  $\epsilon_x$ ,  $L$ ,  $t$ , and  $\nu$ , accounting for the geometric and material properties relevant to the damping behaviour.

# Appendix G

## EMA Test Protocol with Vacuum Chamber

This appendix outlines the detailed Experimental Modal Analysis (EMA) test protocol with a vacuum chamber, including safety precautions, equipment setup, test procedures, and post-test steps. Prior to using this equipment, users must have lab access permission, complete a risk assessment, and arrange an induction with a trained operator.

### Pre-Test Procedure

1. **Safety Notice:** Do not operate this equipment in the presence of untrained personnel.
2. Ensure that the air supply is switched off and disconnected at the wall.
3. Verify that the valve at the regulator is off.
4. Confirm that the power for the vacuum pump, the data acquisition system (DAQ), and the pneumatic power supply is switched off.
5. Perform a visual inspection of the vacuum chamber to ensure there are no cracks in the material.
6. Mount the sample in the test rig outside the vacuum chamber.

## Appendix G. EMA Test Protocol with Vacuum Chamber

7. Affix accelerometers to the sample using wax.
8. Ensure that the blue BNC cable is connected to the modal hammer.
9. Remove one endplate of the vacuum chamber by loosening the wing nuts and carefully removing the acrylic endplate.
10. Carefully place the test rig into the vacuum chamber, ensuring that no strain is imposed on the cables.
11. Replace the endplate onto the vacuum chamber, ensuring the red gasket is correctly installed between the chamber and the endplate.
12. Place washers and hand-tighten the wing nuts on every mounting bolt (do not use tools to avoid damaging the acrylic).
13. Connect the accelerometers and modal hammer to the NI9234 DAQ hardware as per Table G.1.

Table G.1: DAQ Connection Details

Component	Label	Connection
Modal Hammer	Blue Wire	Device 1, Port 0
Accelerometer 1	(No Label)	Device 1, Port 1
Accelerometer 2	Black	Device 1, Port 2
Accelerometer 3	Green/Yellow	Device 2, Port 0

## Equipment Setup

1. Connect an Ethernet cable between the PC and the DAQ.
2. Turn on the power for the DAQ and the 24VDC power supply for pneumatics using the designated ON/OFF switch.
3. Connect the inlet connection to the wall air supply and turn it on.

## Appendix G. EMA Test Protocol with Vacuum Chamber

4. Verify that the pressure at the regulator is less than 9 bar, then turn on the valve at the regulator.
5. Pressurise the vacuum chamber.
6. Attach the vacuum pump to the designated vacuum pump connection and turn on the corresponding valve.
7. Ensure all outlet valves are closed.
8. Turn on the vacuum pump and observe the pressure gauge; the pressure should decrease gradually.
9. Listen for any signs of leaks.
10. When the target pressure is reached (maximum vacuum pressure: -0.85 bar), turn off the vacuum pump. This process typically takes approximately 40 minutes.
11. Turn off the valve at the vacuum pump connection.

## Test Procedure

1. Open the `Data_Acquisition_3_accel_add_new.m` MATLAB script on the PC.
2. Run the script.
3. After an audible beep, press the Striker Actuation Switch once.
4. Adjust the pneumatic cylinder extension time using the Pulse Length Adjustment control.
5. Modify the force of extension and retraction of the cylinders via the Flow Restrictors as necessary.

## Appendix G. EMA Test Protocol with Vacuum Chamber

6. Once the test is complete, the force data will be reported in MATLAB. Adjust the Extension Flow Restrictor accordingly to achieve the desired force.

### **Post-Test Procedure**

1. Turn on the outlet valve and wait until the pressure gauge returns to atmospheric pressure.
2. Turn off the air supply at the wall.
3. Press the Striker Actuation Switch several times until the pneumatic cylinder ceases movement, ensuring the system is depressurised.
4. Disconnect the air supply at the wall.

**Note:** Never leave the vacuum pump operating unattended.

# Appendix H

## MATLAB Code: EMA Data Acquisition

```
1 %% Reset
2 close all
3 clc
4 clear all
5
6 %% Set Duration
7 duration = 200; % seconds
8 Set_Count = 1; % seconds
9
10 %% Create DAQ Session and List Devices
11 s = daq("ni");
12 d = daqlist("ni");
13 dq = s;
14
15 % Identify Module Types
16 id9234 = contains(d.Model, "9234");
17 id9219 = contains(d.Model, "9219");
18 id9237 = contains(d.Model, "9237");
19
20 % Extract Device IDs
21 deviceId = d.DeviceID(id9234);
22 deviceId_acc = deviceId(1);
23
24 deviceId_2 = d.DeviceID(id9219);
```

## Appendix H. MATLAB Code: EMA Data Acquisition

```
25 deviceId_strain = deviceId_2(1);
26
27 % Set Sampling Rate
28 s.Rate = 2048; % Hz
29
30 %% Add Input Channels
31 % Force Channel (Channel 0)
32 ch0 = addinput(s, deviceId_acc, "ai0", "IEPE");
33
34 % Acceleration Channels (Channels 1 to 3)
35 ch1 = addinput(s, deviceId_acc, "ai1", "IEPE");
36 ch2 = addinput(s, deviceId_acc, "ai2", "IEPE");
37 ch3 = addinput(s, deviceId_acc, "ai3", "IEPE");
38
39 %% Set Sensitivity Values
40 Sensitivity_Hammer = 2.25/1000; % V/N
41 Sensitivity_CH1 = 10.07/1000; % V/g (model 35)
42 Sensitivity_CH2 = 99.6/1000; % V/g (model 49)
43 Sensitivity_CH3 = 10.13/1000; % V/g (model 35)
44
45 beep on
46
47 %% Start Data Acquisition Loop
48 Length_accel = 0;
49 Continue = 1;
50 Reading_number = 0;
51
52 while Continue > 0.5
53     disp('-----')
54     Continue = input('To Continue Analysis Type "1", To Stop Type
55                     "0": ');
56     disp('-----')
57     if Continue > 0.5
```

## Appendix H. MATLAB Code: EMA Data Acquisition

```
58     % Countdown before acquisition
59     disp('-----3-----')
60     pause(Set_Count);
61     disp('-----2-----')
62     pause(Set_Count);
63     disp('-----1-----')
64     pause(Set_Count);
65     disp('-----START-----')
66     beep
67     data = read(s, seconds(duration));
68     beep
69     disp('-----STOP-----')
70
71     % Convert timetable to table and rename variables
72     T = timetable2table(data);
73     data_2 = renamevars(T, ["Time", "cDAQ9189-1E050FFMod1_ai0",
74         "...", "cDAQ9189-1E050FFMod1_ai1", "cDAQ9189-1E050FFMod1_ai2",
75         "...", "cDAQ9189-1E050FFMod1_ai3"], ...
76         ["Time", "CDAQ_Hammer", "CDAQ_Ai_1", "CDAQ_Ai_2", "CDAQ_Ai_3"]);
77     data_2.Time = seconds(data_2.Time);
78
79     %% Process Data
80     Hammer_force = data_2.CDAQ_Hammer / Sensitivity_Hammer;
81     test_A1 = data_2.CDAQ_Ai_1 / Sensitivity_CH1;
82     test_A2 = data_2.CDAQ_Ai_2 / Sensitivity_CH2;
83     test_A3 = data_2.CDAQ_Ai_3 / Sensitivity_CH3;
84
85     % Find Peak in Hammer Force
86     [Check_Peaks, peak_loc] = findpeaks(Hammer_force, 'MinPeakDistance', 1, 'MinPeakHeight', 10);
87     if ~isempty(peak_loc)
88         peak_time = data_2.Time(peak_loc(1)); % first peak
```

## Appendix H. MATLAB Code: EMA Data Acquisition

```
88         start_time = peak_time - 0.25;
89         end_time = peak_time + 0.25;
90         range_indices = find(data_2.Time >= start_time &
91                               data_2.Time <= end_time);
92         time_range = data_2.Time(range_indices);
93         hammer_force_range = Hammer_force(range_indices);
94         figure
95         plot(time_range, hammer_force_range);
96         title("Hammer CHO around the peak")
97         ylabel("Force (N)")
98         xlabel("Time (s)")
99         Peak_Number = numel(Check_Peaks);
100        disp('
101              -----
102              ')
103        disp(Peak_Number)
104        disp(Check_Peaks)
105        disp('
106              -----
107              ')
108    else
109        disp('No peaks were found with the given criteria.')
110    end
111
112    pause(5)
113
114    % Plot all channels
115    figure
116    subplot(4,1,1);
117    plot(data_2.Time, Hammer_force);
118    title("Hammer CHO")
119    ylabel("Force (N)")
120    xlabel("Time (s)")
121    subplot(4,1,2);
```

## Appendix H. MATLAB Code: EMA Data Acquisition

```
117     plot(data_2.Time, test_A1);
118     title("Accelerometer CH1")
119     ylabel("Acceleration (g)")
120     xlabel("Time (s)")
121     subplot(4,1,3);
122     plot(data_2.Time, test_A2);
123     title("Accelerometer CH2")
124     ylabel("Acceleration (g)")
125     xlabel("Time (s)")
126     subplot(4,1,4);
127     plot(data_2.Time, test_A3);
128     title("Accelerometer CH3")
129     ylabel("Acceleration (g)")
130     xlabel("Time (s)")
131
132     %% Save Data Based on User Input
133     disp('
134         -----
135     ')
136     Data_save = input('Save Data = 1, Discard = 0: ');
137     disp('
138         -----
139     ')
140     if Data_save > 0.5
141         data_out_1(1,:) = Hammer_force;
142         data_out_1(2,:) = test_A1;
143         data_out_1(3,:) = test_A2;
144         data_out_1(4,:) = test_A3;
145         disp('
146             -----
147         ')
148         disp('Reading Number Completed')
149         Reading_number = Reading_number + 1;
150         disp(Reading_number)
```

## Appendix H. MATLAB Code: EMA Data Acquisition

```
145         disp('
           -----
           ')
146         data_out{Reading_number, :} = data_out_1;
147     end
148     pause(5)
149 end
150 end
151
152 %% Save and Organise Acquired Data
153 data_out_T1 = data_out{1,1};
154 T1(1:4,:) = data_out_T1;
155 save('T1.mat', 'T1')
156
157 data_out_T2 = data_out{2,1};
158 T2(1:4,:) = data_out_T2;
159 save('T2.mat', 'T2')
160
161 data_out_T3 = data_out{3,1};
162 T3(1:4,:) = data_out_T3;
163 save('T3.mat', 'T3')
164
165 data_out_T4 = data_out{4,1};
166 T4(1:4,:) = data_out_T4;
167 save('T4.mat', 'T4')
168
169 data_out_T5 = data_out{5,1};
170 T5(1:4,:) = data_out_T5;
171 save('T5.mat', 'T5')
172
173 data_out_T6 = data_out{6,1};
174 T6(1:4,:) = data_out_T6;
175 save('T6.mat', 'T6')
176
```

## Appendix H. MATLAB Code: EMA Data Acquisition

```
177 data_out_T7 = data_out{7,1};
178 T7(1:4,:) = data_out_T7;
179 save('T7.mat','T7')
180
181 data_out_T8 = data_out{8,1};
182 T8(1:4,:) = data_out_T8;
183 save('T8.mat','T8')
184
185 data_out_T9 = data_out{9,1};
186 T9(1:4,:) = data_out_T9;
187 save('T9.mat','T9')
188
189 data_out_T10 = data_out{10,1};
190 T10(1:4,:) = data_out_T10;
191 save('T10.mat','T10')
192
193 data_out_T11 = data_out{11,1};
194 T11(1:4,:) = data_out_T11;
195 save('T11.mat','T11')
196
197 data_out_T12 = data_out{12,1};
198 T12(1:4,:) = data_out_T12;
199 save('T12.mat','T12')
200
201 data_out_T13 = data_out{13,1};
202 T13(1:4,:) = data_out_T13;
203 save('T13.mat','T13')
204
205 data_out_T14 = data_out{14,1};
206 T14(1:4,:) = data_out_T14;
207 save('T14.mat','T14')
208
209 data_out_T15 = data_out{15,1};
210 T15(1:4,:) = data_out_T15;
```

## Appendix H. MATLAB Code: EMA Data Acquisition

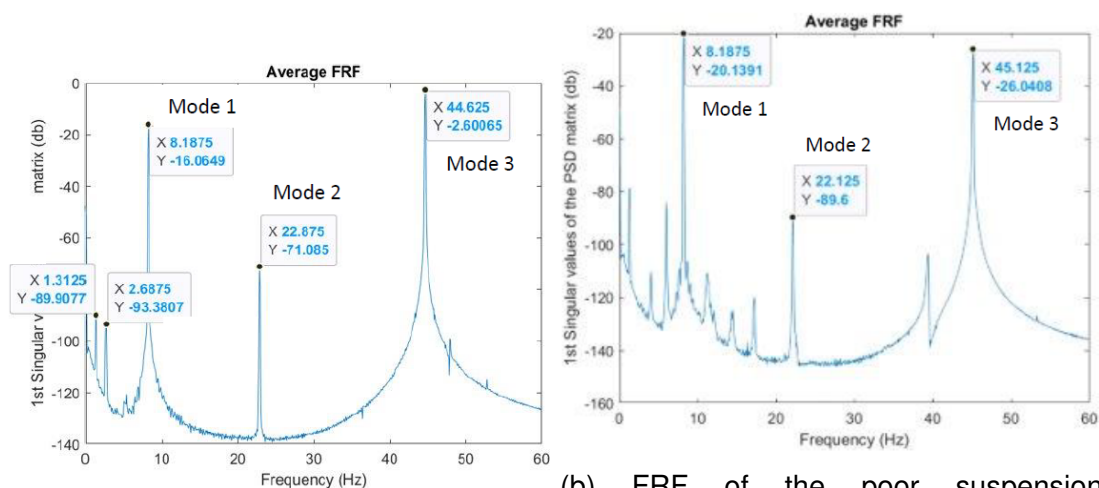
```
211 save('T15.mat','T15')
212
213 data_out_T16 = data_out{16,1};
214 T16(1:4,:) = data_out_T16;
215 save('T16.mat','T16')
216
217 %% Concatenate and Save Final Results
218 resultCell = cat(1, T1, T2, T3, T4, T5, T6, T7, T8, T9, T10, T11,
    T12, T13, T14, T15, T16);
219 reorderedResult = resultCell(:, [2 1 3 5 6 7 4]);
220 save('reorderedResult.mat','reorderedResult')
```

Listing H.1: Data Acquisition for EMA using MACEC via the pISCF method

# Appendix I

## FRF Response of Suspension Mechanisms

The following figures compare the FRFs of the selected and poor suspension mechanisms, illustrating the impact of suspension quality on mode identification.



(a) FRF of the selected suspension mechanism, exhibiting additional lateral mechanism. (b) FRF of the poor suspension mechanism.

Figure I.1: Comparison of the FRFs for the selected and poor suspension mechanisms, highlighting differences in mode identification and additional undesired modes.

# Appendix J

## Vacuum Chamber Validation Calculations

This appendix outlines the detailed design calculations for the vacuum chamber, adhering to the guidelines of *PD5500: Specification for Unfired Pressure Vessels*. The vacuum chamber was designed to operate at a maximum vacuum of -0.9 bar, removing aerodynamic damping effects and enabling accurate measurements of structural damping properties.

### 1. Design Requirements

The following design parameters were specified for the vacuum chamber:

- Outer Diameter ( $D_o$ ) = 550 mm
- Length ( $L$ ) = 2100 mm
- Wall Thickness ( $e_{final}$ ) = 6 mm
- Design Pressure ( $P$ ) = 0.1 N/mm<sup>2</sup> (vacuum up to -0.9 bar)

The material chosen for the chamber is acrylic, with the following properties:

- Modulus of Elasticity ( $E_{acrylic}$ ) = 3.2 GPa
- Yield Strength ( $\sigma_y$ ) = 69 MPa

## Appendix J. Vacuum Chamber Validation Calculations

The allowable design stress ( $f$ ) at room temperature is calculated as a fraction of the material's yield strength:

$$f = \frac{\sigma_y}{1.5} = \frac{69 \text{ MPa}}{1.5} = 46 \text{ N/mm}^2 \quad (\text{J.1})$$

### 2. Cylinder Wall Thickness

To determine the required wall thickness, the following formula from *PD5500* is used for external pressure vessels:

$$e_{cylinder} = \frac{P \cdot D_o}{2f - P} \quad (\text{J.2})$$

Substituting the known values:

$$e_{cylinder} = \frac{0.1 \cdot 550}{2 \cdot 46 - 0.1} = 0.597 \text{ mm} \quad (\text{J.3})$$

A 6 mm wall thickness was selected due to it being in excess of the specified result, and a manufacturable component.

### 3. Check Thickness without Support Rings

The vacuum chamber design was evaluated to determine if it can operate safely without stiffening rings under external pressure. The following calculations were performed based on the chamber's geometric and material properties.

#### Initial Properties

- Cylinder Length ( $L_{cyl}$ ) = 2100 mm

## Appendix J. Vacuum Chamber Validation Calculations

- Shape Factor ( $s$ ) = 1.4

**Calculate  $\frac{L}{2R}$  and  $\frac{2R}{e}$ , and Find  $\varepsilon$  from the Graph**

$$a = \frac{L_{cyl}}{D_o} = \frac{2100}{550} = 3.818 \quad (\text{J.4})$$

$$b = \frac{D_o}{e_{final}} = \frac{550}{6} = 91.667 \quad (\text{J.5})$$

From the referenced graph [207]:

$$\varepsilon_1 = 0.00046 \quad (\text{J.6})$$

**Find Allowable External Pressure without Rings (Early Estimations)** The following equations are used to estimate the allowable external pressure:

$$P_{y1} = \frac{s \cdot f \cdot e_{final}}{\frac{D_o}{2}} = \frac{1.4 \cdot 46 \cdot 6}{275} = 1.405 \text{ N/mm}^2 \quad (\text{J.7})$$

$$P_{m1} = \frac{E_{acrylic} \cdot e_{final} \cdot \varepsilon_1}{\frac{D_o}{2}} = \frac{3200 \cdot 6 \cdot 0.00046}{275} = 0.032 \text{ N/mm}^2 \quad (\text{J.8})$$

The ratio  $K_1$  is calculated as:

$$K_1 = \frac{P_{m1}}{P_{y1}} = \frac{0.032}{1.405} = 0.023 \quad (\text{J.9})$$

**Calculate  $\Delta_1$  and Modified  $\Delta_{1mod}$**  The value of  $\Delta_1$  is obtained as:

$$\Delta_1 = 0.0075 \quad (\text{J.10})$$

For  $\Delta_{1mod}$ , we assume:

$$\Delta_{1mod} = \Delta_1 \cdot 2 = 0.015 \quad (\text{J.11})$$

## Appendix J. Vacuum Chamber Validation Calculations

**Final Allowable Pressure** ( $P_{a1}$ ) The final allowable pressure without stiffening rings is:

$$P_{a1} = \Delta_{1mod} \cdot P_{y1} = 0.015 \cdot 1.405 = 0.021 \text{ N/mm}^2 \quad (\text{J.12})$$

**Note:** This must be greater than the design pressure of 0.1 N/mm<sup>2</sup>.

**The design does not satisfy the pressure requirements without stiffeners.**

Stiffening rings are therefore necessary to ensure safe operation under the specified conditions.

### 4. Interstiffening Rings

The design of interstiffening rings was evaluated to ensure the vacuum chamber meets safety requirements under external pressure. Below are the detailed calculations.

#### Ring Information

- Number of Supports = 4
- Stiffener Spacing:

$$L_{stiff} = \frac{L_{cyl}}{\text{Number\_supports} + 1} = \frac{2100}{4 + 1} = 420 \text{ mm} \quad (\text{J.13})$$

- Width of Stiffener in Contact with Shell ( $b$ ) = 10 mm
- Poisson's Ratio ( $\nu$ ) = 0.3

#### Radius Information

## Appendix J. Vacuum Chamber Validation Calculations

- Mean Radius:

$$R_o = \frac{D_o}{2} = \frac{550}{2} = 275 \text{ mm} \quad (\text{J.14})$$

- Outer Radius of Shell:

$$R = R_o - \frac{e_{final}}{2} = 275 - \frac{6}{2} = 272 \text{ mm} \quad (\text{J.15})$$

- Inner Radius:

$$D_i = D_o - 2 \cdot e_{final} = 550 - 2 \cdot 6 = 538 \text{ mm} \quad (\text{J.16})$$

- Outer Radius of Stiffener:

$$R_{outer} = \frac{D_i}{2} = \frac{538}{2} = 269 \text{ mm} \quad (\text{J.17})$$

- Thickness of Support Ring ( $T_{support}$ ) = 30 mm

- Inner Radius of Stiffener:

$$R_{inner} = R_{outer} - T_{support} = 269 - 30 = 239 \text{ mm} \quad (\text{J.18})$$

- Mean Radius of Stiffener:

$$R_s = \frac{R_{outer} + R_{inner}}{2} = \frac{269 + 239}{2} = 254 \text{ mm} \quad (\text{J.19})$$

### Calculate $\alpha$

$$\alpha = \frac{1.28}{\sqrt{R \cdot e_{final}}} = \frac{1.28}{\sqrt{272 \cdot 6}} = 31.685 \text{ m}^{-1} \quad (\text{J.20})$$

$$\alpha \cdot L_{stiff} = 31.685 \cdot 0.42 = 13.308 \quad (\text{J.21})$$

## Appendix J. Vacuum Chamber Validation Calculations

### Area Calculations

- Stiffener Area:

$$A_s = \pi \cdot (R_{outer}^2 - R_{inner}^2) = \pi \cdot (269^2 - 239^2) = 4.788 \times 10^4 \text{ mm}^2 \quad (\text{J.22})$$

- Modified Stiffener Area:

$$A = \frac{R^2 \cdot A_s}{R_s^2} = \frac{272^2 \cdot 4.788 \times 10^4}{254^2} = 5.49 \times 10^4 \text{ mm}^2 \quad (\text{J.23})$$

### Evaluate Parameters $N$ and $G$

$$N_{comp} = \frac{\cosh(\alpha \cdot L_{stiff}) - \cos(\alpha \cdot L_{stiff})}{\sinh(\alpha \cdot L_{stiff}) + \sin(\alpha \cdot L_{stiff})} = 1 \quad (\text{J.24})$$

$$G_{comp} = \frac{2 \left[ \sinh\left(\frac{\alpha \cdot L_{stiff}}{2}\right) \cdot \cos\left(\frac{\alpha \cdot L_{stiff}}{2}\right) + \cosh\left(\frac{\alpha \cdot L_{stiff}}{2}\right) \cdot \sin\left(\frac{\alpha \cdot L_{stiff}}{2}\right) \right]}{\sinh(\alpha \cdot L_{stiff}) + \sin(\alpha \cdot L_{stiff})} = 3.337 \times 10^{-3} \quad (\text{J.25})$$

### Calculate $B$ and $\gamma$ Values

$$B = \frac{2 \cdot e_{final} \cdot N_{comp}}{\alpha \cdot [A + (b \cdot e_{final})]} = \frac{2 \cdot 6 \cdot 1}{31.685 \cdot [5.49 \times 10^4 + (10 \cdot 6)]} = 6.89 \times 10^{-3} \quad (\text{J.26})$$

$$\gamma = \frac{A \cdot \left(1 - \frac{\nu}{2}\right)}{(A + b \cdot e_{final}) \cdot (1 + B)} = \frac{5.49 \times 10^4 \cdot \left(1 - \frac{0.3}{2}\right)}{(5.49 \times 10^4 + 10 \cdot 6) \cdot (1 + 6.89 \times 10^{-3})} = 0.843 \quad (\text{J.27})$$

### Check Yield Pressure

$$P_{y2} = \frac{s \cdot f \cdot e_{final}}{R \cdot (1 - \gamma \cdot G_{comp})} = \frac{1.4 \cdot 46 \cdot 6}{272 \cdot (1 - 0.843 \cdot 3.337 \times 10^{-3})} = 1.425 \text{ N/mm}^2 \quad (\text{J.28})$$

## Appendix J. Vacuum Chamber Validation Calculations

**Evaluate  $\varepsilon$**  To evaluate  $\varepsilon_2$ , the following values are calculated:

$$\frac{L_{stiff}}{2R} = \frac{420}{2 \cdot 272} = 0.772 \quad (\text{J.29})$$

$$\frac{2R}{e_{final}} = \frac{2 \cdot 272}{6} = 90.667 \quad (\text{J.30})$$

From the graph (Figure J.1), for  $\frac{L_{stiff}}{2R} = 0.772$  and  $\frac{2R}{e_{final}} = 90.667$ :

$$\varepsilon_2 = 0.002 \quad (\text{J.31})$$

## Appendix J. Vacuum Chamber Validation Calculations

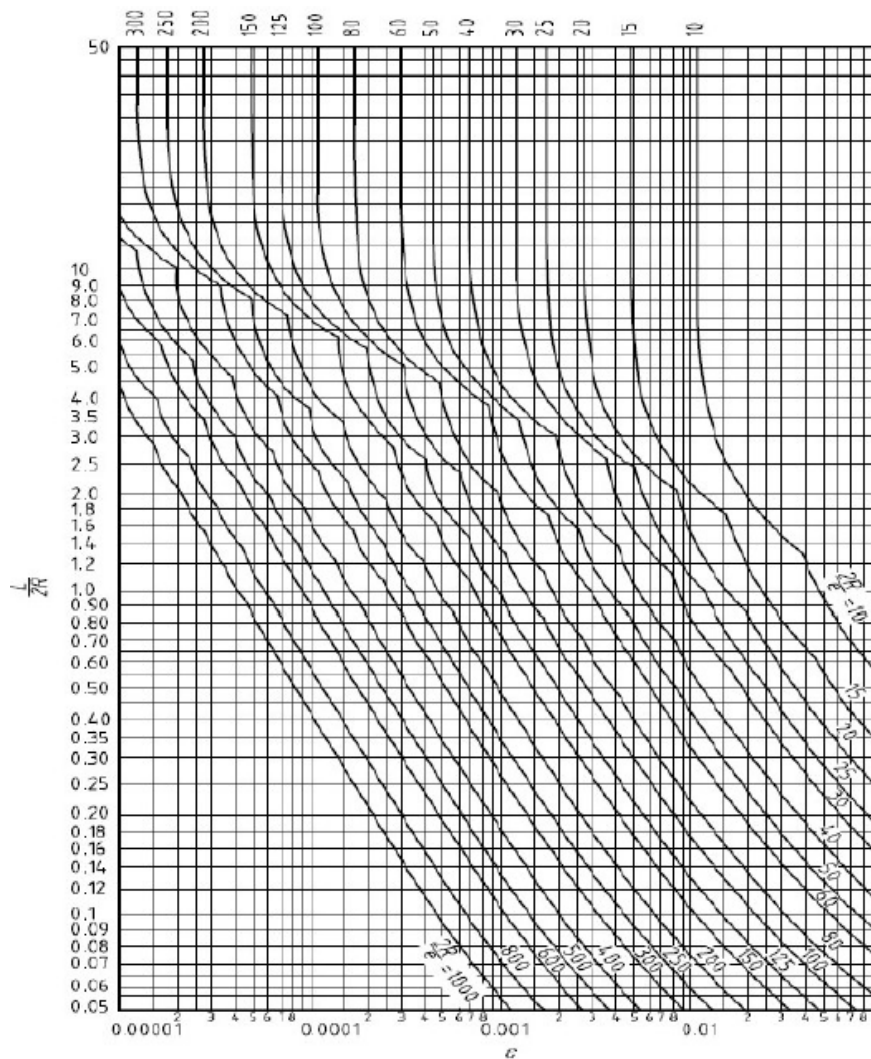


Figure J.1: Graph for evaluating  $\epsilon_2$  based on  $\frac{L_{stiff}}{2R}$  and  $\frac{2R}{e_{final}}$

Figure taken from [207]

**Check Instability Pressure** The instability pressure is calculated using the formula:

$$P_{m2} = \frac{E_{acrylic} \cdot e_{final} \cdot \epsilon_2}{R} \quad (J.32)$$

Substituting the values:

$$P_{m2} = \frac{3200 \cdot 6 \cdot 0.002}{272} = 0.141 \text{ N/mm}^2 \quad (J.33)$$

## Appendix J. Vacuum Chamber Validation Calculations

This value must exceed the design pressure of 0.1 N/mm<sup>2</sup>.

The ratio  $K_2$  is then determined:

$$K_2 = \frac{P_{m2}}{P_{y2}} = \frac{0.141}{1.425} = 0.099 \quad (\text{J.34})$$

**Determine  $\Delta$**  From the graph (Figure J.2), the value of  $\Delta_2$  is found:

$$\Delta_2 = 0.035 \quad (\text{J.35})$$

Assuming  $\Delta_{2mod}$ :

$$\Delta_{2mod} = 2 \cdot \Delta_2 = 2 \cdot 0.035 = 0.07 \quad (\text{J.36})$$

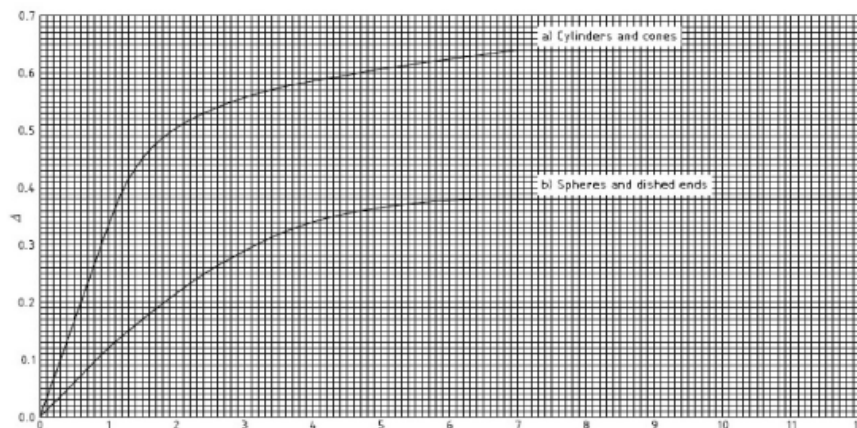


Figure J.2: Graph for determining  $\Delta_2$  for cylindrical shells under external pressure

Figure taken from [207]

**Allowable Pressure** The allowable pressure is calculated as:

$$P_{a2} = \Delta_{2mod} \cdot P_{y2} = 0.07 \cdot 1.425 = 0.1 \text{ N/mm}^2 \quad (\text{J.37})$$

Since  $P_{a2}$  exceeds the design pressure of 0.1 N/mm<sup>2</sup>, this solution is valid.

## 4. Flat End Thickness Equation

This section outlines the calculation of the required thickness for the flat end of the vacuum chamber, ensuring it meets safety requirements under the specified design conditions.

### Calculation Inputs

- Coefficient ( $C$ ): 0.41 (simply supported/flexible)
- Outer Diameter ( $D_o$ ): 550 mm
- Nominal Design Stress for Flat End ( $f$ ): 100 N/mm<sup>2</sup>

**Thickness of Flat End** The thickness of the flat end ( $e_{end}$ ) is calculated using the following equation:

$$e_{end} = C \cdot D_o \cdot \sqrt{\frac{P}{f}} \quad (\text{J.38})$$

Substituting the given values:

$$e_{end} = 0.41 \cdot 550 \cdot \sqrt{\frac{0.1}{100}} = 7.131 \times 10^{-3} \text{ m} \quad (\text{J.39})$$

$$e_{end} = 7.131 \text{ mm} \quad (\text{J.40})$$

An end plate thickness of 10 mm is therefore sufficient:

$$e_{endmod} = 10 \text{ mm} \quad (\text{J.41})$$

## 5. Bolt Spacing

This section calculates the required bolt spacing for the vacuum chamber's flat end plate to ensure structural integrity under the specified conditions.

### Calculation Inputs

- Modulus of Elasticity at Design Temperature ( $E_{end}$ ): 190000 N/mm<sup>2</sup> (assumed for steel bolts)
- Bolt Outside Diameter ( $d_b$ ): 10 mm (to be confirmed)
- Gasket Factor ( $m$ ): 3 (value to be verified)

**Bolt Spacing Calculation** The bolt spacing ( $t_B$ ) is determined using the following equation:

$$t_B = 2 \cdot d_b + \left( \frac{E_{end}}{200000} \right)^{0.25} \cdot \left( \frac{6 \cdot e_{endmod}}{m + 0.5} \right) \quad (\text{J.42})$$

Substituting the given values:

$$t_B = 2 \cdot 10 + \left( \frac{190000}{200000} \right)^{0.25} \cdot \left( \frac{6 \cdot 10}{3 + 0.5} \right) \quad (\text{J.43})$$

$$t_B = 20 + (0.974) \cdot \left( \frac{60}{3.5} \right) \quad (\text{J.44})$$

$$t_B = 20 + (0.974) \cdot 17.143 = 20 + 16.696 = 36.696 \text{ mm} \quad (\text{J.45})$$

Convert to meters:

$$t_B = 115.173 \text{ mm} \quad (\text{J.46})$$

The calculated bolt spacing is  $t_B = 115.173$  mm. However, for simplicity and standardisation, the bolt spacing was set to 100 mm for the final design. This

## Appendix J. Vacuum Chamber Validation Calculations

adjustment ensures uniformity and sufficient clamping force for the gasket while maintaining the structural integrity of the end plate.

This detailed calculation validates the vacuum chamber's structural integrity according to the *PD5500* standards for unfired pressure vessels. The stiffening rings, end plate design, and bolt spacing calculations demonstrate that the design can safely withstand the maximum operating vacuum of -0.9 bar, eliminating aerodynamic damping and ensuring accurate structural damping measurements.

# Appendix K

## MATLAB Code: EMA Post-processing via MACEC using pLSCF Method

```
1 %% Reset
2 clc;
3 close all;
4 clear all;
5
6 %% MACEC version 3.4
7 % Copyright KU Leuven, Structural Mechanics Section
8 % https://bwk.kuleuven.be/bwm/macec
9 % run("Force_fix.m")
10
11 %% Input
12 % Ensure these numbers are correct
13 F_mode_1 = 11.7; % Target frequency of data for mode 1
14 % F_mode_1 = 32.8; % Target frequency for mode 2
15 % F_mode_1 = 64.2; % Target frequency for mode 3
16 variance_fq = 0.75;
17
18 Sampling_rate = 2048; % Sampling rate of DAQ
19 Number_Tests = 50; % Number of tests to calculate
20 damping for
```

## Appendix K. MATLAB Code: EMA Post-processing via MACEC using pLSCF Method

```
21 start_modal = 50;
22 end_modal = 500;
23 modal_param = start_modal:1:end_modal;    % Modal orders
      calculated
24
25 % Input Geometry Files - Grid, slave and beam file
26 gridfile = 'C:\Users\xgb14157\OneDrive_\University_of_\
      Strathclyde\5th_Year_Project_2022\5_\EMA\Results\Data_\
      Processing_\Matlab_EFFT\MACEC\BASIC_GRID_Mode1.asc';
27 slavefile = 'C:\Users\xgb14157\OneDrive_\University_of_\
      Strathclyde\5th_Year_Project_2022\5_\EMA\Results\Data_\
      Processing_\Matlab_EFFT\MACEC\BASIC_SLAVE.asc';
28 beamfile = 'C:\Users\xgb14157\OneDrive_\University_of_\
      Strathclyde\5th_Year_Project_2022\5_\EMA\Results\Data_\
      Processing_\Matlab_EFFT\MACEC\BASIC_SURFACE.asc';
29
30 tic;
31
32 %% Start loop
33 for i = 1:Number_Tests
34     % Construct filename for current test
35     filename = sprintf(['C:/Users/xgb14157/OneDrive_\University_\
      of_\Strathclyde/' ...
36         '5th_Year_Project_2022_\Copy/1_\New_Results/Final/' ...
37         'C-5mm-Force_Test-(SGM1W)(CRAF)-AllN-Model-Air//T%d_upd.\
      mat'], i);
38     file = strvcats(filename);
39     ext = strvcats('mat');
40
41     %% Data Read and Filtering
42     % Read the data and sampling frequency
43     x = input2mcsignal(file, ext, Sampling_rate);
44
45     % Modify magnitudes if required
```

## Appendix K. MATLAB Code: EMA Post-processing via MACEC using pLSCF Method

```
46     sens = [1; 1; 1; 1];
47     ampl = [1; 1; 1; 1];
48     db = [0; 0; 0; 0];
49
50     % Allocate data types and label each channel
51     types = cell_(strvcat('force','acc','acc','acc'));
52     labels = cell_(strvcat('ForceA1A2A3','A1','A2','A3'));
53
54     for par = 1:1
55         cnvdats{par} = volt2xa(x{par}, sens', ampl', db', types',
56             labels');
57     end
58     predats = cnvdats;
59
60     % Remove DC offset
61     for par = 1:1
62         predats{par} = detrend(predats{par}, 'constant');
63     end
64
65     % Allocate channels to pre-defined nodes and directions
66     node_num = [8; 2; 8; 14];
67     meas_dir = [0 -90; 0 90; 0 90; 0 90];
68
69     %% System Identification - Part 1
70     predat = predats{1};
71     [h1frf, freqscale] = H1estimate(predat, 2, 'rect', [1], [2 3
72         4], 'fs');
73     H_meas = h1frf;
74
75     %% System Identification - Part 2
76     chanelout = [2 3 4];
77     rmfd = RMFDcalc(H_meas, 'pLSCF', modal_param, chanelout,
78         [1], [], freqscale, 0, round(Sampling_rate));
```

## Appendix K. MATLAB Code: EMA Post-processing via MACEC using pLSCF Method

```
77     %% Modal Analysis
78     [node_num, meas_dir, quants, chan_outin, ampl_outin, refs] =
        identsel(node_num, meas_dir, predat.quantity', rmfd.
        chanelout, rmfd.chanselin, rmfd.refs);
79     sysmat = rmfd2sysmat(rmfd);
80     allmodes = stable_propmodpar(sysmat, predat.dt, chan_outin,
        ampl_outin, quants);
81
82     selnrs_old = [];
83     selnrs_new = [];
84
85     %% Preallocate memory for results
86     All_results = cell(numel(modal_param), 7);
87     All_results_B = zeros(numel(modal_param), 7);
88
89     for order1 = modal_param
90         [modenr, yes, selnrs_new] = modfind(allmodes, F_mode_1,
            order1, selnrs_old);
91         stabmodes = stabpick(allmodes, selnrs_new);
92         a = order1 - modal_param(1) + 1;
93         All_results{a,1} = stabmodes.o;
94         All_results{a,2} = stabmodes.f;
95         All_results{a,3} = stabmodes.xi;
96         All_results{a,4} = stabmodes.m;
97         All_results{a,5} = stabmodes.mac;
98         All_results{a,6} = stabmodes.mpc;
99         All_results{a,7} = stabmodes.mpd;
100        All_results_B(a,:) = [stabmodes.o, stabmodes.f, stabmodes
            .xi, 0, stabmodes.mac, stabmodes.mpc, stabmodes.mpd];
101    end
102
103    %% Filter Data
104    toKeep_11 = All_results_B(:,2) >= F_mode_1 - variance_fq &
        All_results_B(:,2) <= F_mode_1 + variance_fq;
```

## Appendix K. MATLAB Code: EMA Post-processing via MACEC using pLSCF Method

```
105     All_results_B_1 = All_results_B(toKeep_11, :);
106
107     toKeep12 = cell2mat(All_results(:,2)) >= F_mode_1 - 1 &
           cell2mat(All_results(:,2)) <= F_mode_1 + 1;
108     All_results_1 = All_results(toKeep12, :);
109
110     % Filter 2 - Damping positive
111     toKeep_21 = All_results_B_1(:,3) > 0;
112     All_results_B_2 = All_results_B_1(toKeep_21, :);
113     toKeep22 = cell2mat(All_results_1(:,3)) > 0;
114     All_results_2 = All_results_1(toKeep22, :);
115
116     % Filter 3 - MPC
117     toKeep_31 = All_results_B_2(:,6) >= 0.92;
118     All_results_B_3 = All_results_B_2(toKeep_31, :);
119     toKeep32 = cell2mat(All_results_2(:,6)) >= 0.92;
120     All_results_3 = All_results_2(toKeep32, :);
121
122     % Filter 4 - MPD
123     toKeep_41 = All_results_B_3(:,7) <= 10;
124     All_results_B_4 = All_results_B_3(toKeep_41, :);
125     toKeep42 = cell2mat(All_results_3(:,7)) <= 6;
126     All_results_4 = All_results_3(toKeep42, :);
127
128     %% Sort and Order Data
129     norm_co26 = All_results_B_4(:,6) / max(All_results_B_4(:,6));
130     norm_co27 = (max(All_results_B_4(:,7)) - All_results_B_4(:,7)
           + min(All_results_B_4(:,7))) / (max(All_results_B_4(:,7))
           - min(All_results_B_4(:,7)));
131     combined_score_2 = norm_co26 + norm_co27;
132     [~, order_2] = sort(combined_score_2, 'descend');
133     sorted_data_2 = All_results_B_4(order_2, :);
134     Final_Data_2 = sorted_data_2(1:10, :);
135
```

## Appendix K. MATLAB Code: EMA Post-processing via MACEC using pLSCF Method

```
136     for aa = 1:10
137         for bb = 1:size(All_results,2)
138             Final_Test{aa,bb} = All_results{Final_Data_2(aa,1) -
                start_modal + 1, bb};
139         end
140     end
141
142     %% Read Result
143     Stored_Results{i,:} = Final_Test;
144     fprintf('Completed %d out of %d loops.\n', i, Number_Tests);
145 end
146
147 %% Select best result for each test
148 for x = 1:i
149     Final_Result{x,:}(1,:) = Stored_Results{x,:}(1,:);
150 end
151
152 toc
153
154 %% Save Results
155 save('Stored_Results.mat', 'Stored_Results');
156 save('Final_Result.mat', 'Final_Result');
157
158 %% Concatenate and Reorder Data
159 resultCell = cat(1, Final_Result{:}); % Concatenate along the
    first dimension
160 reorderedResult = resultCell(:, [2 1 3 5 6 7 4]);
161 save('reorderedResult.mat', 'reorderedResult');
```

Listing K.1: EMA Results Processing Using MACEC via the pLSCF Method